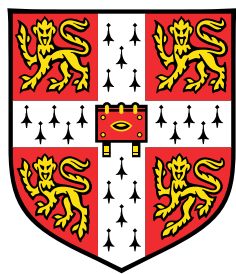


Acoustic Scattering in Sheared Flow



David Iain Baker

Supervisor: Professor Nigel Peake

Department of Applied Mathematics and Theoretical Physics
University of Cambridge

This dissertation is submitted for the degree of

Doctor of Philosophy

St. Catharine's College

April 2019

Declaration

This dissertation is the result of my own work and includes nothing which is the outcome of work done in collaboration except as declared in the Preface and specified in the text.

It is not substantially the same as any that I have submitted, or, is being concurrently submitted for a degree or diploma or other qualification at the University of Cambridge or any other University or similar institution except as declared in the Preface and specified in the text. I further state that no substantial part of my dissertation has already been submitted, or, is being concurrently submitted for any such degree, diploma or other qualification at the University of Cambridge or any other University or similar institution except as declared in the Preface and specified in the text.

David Iain Baker
April 2019

Acknowledgements

The work contained within the thesis would not have been possible without the assistance, patience and support of friends, family and colleagues over the past four years.

Firstly, thanks must be given to my supervisor, Prof. Nigel Peake, for his guidance and direction, both when work was going well and during more difficult phases of my research, and the provision of the final encouragement needed to pull everything together. His contributions were supported by presentations to and work with all members of the Waves Group here in DAMTP: my contemporaries Owen and Peter (to whom I hope I was a bearable officemate); and the experience of Lorna, Ed, Anastasia, James and James, Ridhwaan, Doran and Stephen, who could draw on their work to enhance my own. Also, the inspiration of the fresh younger faces of the Waves Group in Matthew, Chris, Georg and Mungo, made the final stages of my thesis the most enjoyable of the entire process. Finally, I would like to mention the contributions and discussions with William Devenport and Ian Clark of Virginia Tech, who gave me the confidence that I could contribute to the field.

Beyond the academic support of the group, the support of friends and family, both within Cambridge and beyond, have been critical for keeping me working away. My parents, for always giving me a place to get away and being two friends always willing to talk; my brother for leading the way in his own work and ensuring I left my house from time to time. To Sid and Simon and Anthony, for not getting fed up of my temperamental hours and for making a home a pleasure to return to after a tough day of work.

And to Lizzie, who saw both the worst and the best, and somehow hasn't run away quite yet.

Finally, I should like to thank DAMTP and EPSRC for hosting and funding my research, and to St. Catharine's College for providing me a home and a place to belong for the past eight years.

Abstract

Airframe noise, the noise of an aircraft in flight not due to the engine or other mechanical devices, is often a major contribution to the sound heard from an aircraft during landing approach. Over the past few decades certification requirements have gradually tightened, reaching the point where the required noise reductions cannot be achieved through reducing engine noise alone. There are, similarly, restrictions on the noise output of wind turbines to reduce their impacts on local communities and wildlife. In practice this is achieved by braking the turbines at high speed, reducing energy outputs and efficiency. For both aircraft wings and turbine blades, the sharp trailing-edge is a well-understood and unavoidable source of noise, scattering vortical, hydrodynamic disturbances within the boundary-layer into far-field, acoustic, noise.

Inspired by nature, for example the silent flight of owls, modification of the flow within the boundary-layer near the trailing-edge, either through passive or active devices, appears to offer methods of reducing far-field noise. The precise mechanisms are not completely understood, and this work focuses on the effect of varying boundary-layer parameters near the trailing-edge on the resulting far-field noise. Alternative methods of noise reduction include the addition of linings, for example via arrays of Helmholtz resonators. The junctions at the leading- and trailing-edges of such linings can again be a source of far-field noise, through a similar mechanism to that of a trailing-edge.

This scattering is analysed within a simplified mathematical framework through an application of Rapid Distortion Theory, considering linearised perturbations to a transversely sheared background flow. Within this framework, the development of disturbances within a boundary-layer are investigated, both hydrodynamic and acoustic, over a variety of mixed boundary conditions. The inclusion of background shear requires numerical solution of differential equations, which are paired with complex variable techniques such as the Wiener-Hopf method, constructed for the solution of boundary-value problems with discontinuous boundary conditions. The possibility of exact solutions using this technique allows asymptotic methods to be used to directly evaluate far-field noise.

Table of contents

1	Introduction	1
1.1	Trailing-edge noise: generation and control	1
1.1.1	Airframe noise	1
1.1.2	Trailing-edge noise control	2
1.1.3	Vortex sound models	4
1.1.4	Rapid Distortion Theory	6
1.1.5	Scattering	8
1.1.6	Acoustic linings	10
1.2	Thesis structure	11
2	Mathematical formulation of Rapid Distortion Theory	17
2.1	Basic concepts	17
2.1.1	Equations of fluid dynamics	17
2.1.2	Mathematical conventions	20
2.2	A wave equation for pressure	25
2.2.1	Assumptions	26
2.2.2	Compressible Rayleigh's equation	27
2.3	The adjoint problem for general continuous background profile	30
2.4	Streamwise-homogeneous boundary conditions	33
3	Long-wavelength disturbances to piecewise-linear background flow	37
3.1	Introduction	37
3.2	Rapid Distortion Theory in the long-wavelength limit	39
3.2.1	Outer region	40
3.2.2	Inner region	41
3.2.3	Alternative derivation of the equation in the inner region	42
3.2.4	Linear shear	43
3.3	Analytic solutions in the long-wavelength limit	45

3.3.1	Matching at shear junctions	48
3.3.2	Streamfunction for generic N -piece profile	49
3.4	A point source in sheared flow	53
3.4.1	Fixed mass or momentum source: Setup	54
3.4.2	Auxiliary functions and the general solution for arbitrary (linear) boundary conditions	56
3.4.3	Preliminaries: towards an analytic solution	58
3.4.4	Explicit choice of piecewise linear background profiles	60
3.5	Fixed mass or momentum source: Hard-wall	62
3.5.1	The dispersion function	63
3.5.2	Fourier inversion	65
3.5.3	Branch cut contribution: Matching to radiating acoustic outer solution	67
3.5.4	Modal solutions	72
3.5.5	Variation of internal shear	74
3.6	Lined walls: pressure-release and impedance conditions	78
3.6.1	Quantity of pressure-release modes	80
3.6.2	Stability of pressure-release modes	83
3.6.3	Impedance modes	86
3.6.4	Far-field noise	89
3.7	Fixed mass or momentum source: Wake	91
3.7.1	Simplification in the symmetric case	93
3.8	Discussion and conclusions	96
4	Disturbances to continuously sheared flow above a homogeneous boundary	99
4.1	Introduction	99
4.2	Solving the adjoint compressible Rayleigh equation	101
4.2.1	Preliminaries	102
4.2.2	Analytic solution: Uniform flow	104
4.2.3	Numerical solution: Integration across boundary-layer	105
4.2.4	Numerical solution: Integration across "complex" boundary-layer .	109
4.2.5	Asymptotic solution: High frequency acoustics	114
4.3	A point mass source in continuous shear	118
4.3.1	Far-field noise: Steepest descent	120
4.4	Hard-wall boundaries	125
4.4.1	Integrated near-field solutions	127
4.4.2	Far-field sound: outside shear layer	127
4.4.3	Far-field sound: downstream of source	136

4.5	Pressure-release and impedance boundaries	138
4.5.1	Pressure-release conditions	139
4.5.2	General impedance boundary condition	142
4.6	Wake solutions	146
4.6.1	Auxiliary functions	146
4.6.2	Complete inversion	150
4.6.3	Far-field noise	151
4.7	Discussion and conclusions	157
5	Scattering from a junction	159
5.1	Introduction	159
5.2	The generic scattering problem	161
5.2.1	Half-range Fourier transforms and the Wiener-Hopf method	162
5.2.2	Explicit computation of splitfunctions	165
5.2.3	Generalised half-planes	169
5.2.4	Numerical computation of splitfunctions	170
5.2.5	Multiplicative factorisation: Winding numbers, continuity of log and curved branch cuts	170
5.2.6	Linking small x_1 and large k_1 behaviour	172
5.3	Slipping sheared flow: Hard-soft transition	173
5.3.1	Problem setup and incident field	173
5.3.2	The Wiener-Hopf kernel and factorisation	175
5.3.3	Numerical inversion	180
5.3.4	Far-field noise	182
5.4	Non-slipping sheared flow: Hard-soft transition	190
5.4.1	Far-field kernel	190
5.4.2	Numerical inversion	191
5.4.3	Behaviour of scattered solution near the junction	196
5.4.4	Far-field noise	197
5.4.5	The consistency of the no-slip limit	197
5.4.6	The incompressible (long-wavelength) limit	197
5.5	Transition between two different lined surfaces	200
5.5.1	Soft to hard transition	200
5.5.2	Impedance to impedance transition	200
5.6	Restabilisation of unstable modes	203
5.6.1	Restabilisation of an unstable mode	205
5.6.2	Finite unstable lining	206

5.7 Discussion and conclusions	210
6 Scattering from a sharp trailing-edge	215
6.1 Introduction	215
6.2 Scattering from a generic trailing-edge	217
6.2.1 Scattering from a generic, harmonic, incident field	217
6.2.2 The Green's function: incident vortex sheet	221
6.2.3 Simplification in the symmetric case	223
6.2.4 Kernel far-field behaviour and factorisation	223
6.2.5 Near- and far-field inversion for $g^{(s)}$	226
6.3 Distributed boundary-layer vorticity	231
6.3.1 Numerical solutions	233
6.4 Analysis of noise-reduction hypotheses	236
6.4.1 Modification of the transfer function by shear layer	237
6.4.2 Reduction of wall pressure by vorticity displacement	238
6.4.3 Wall-pressure and far-field noise prediction from a physically motivated boundary-layer	242
6.5 Conclusions and discussion	245
7 Conclusions	247
7.1 Summary and discussion	247
7.1.1 Implementation of quasi-numerical methods	247
7.1.2 Development of the understanding of scattering problems	248
7.1.3 Explaining noise control devices	249
7.2 Future work	251
References	253
Appendix A Appendices to Chapter 3	263
A.1 The existence N hard-wall modes	263
A.2 Numerical complex methods implementation	264
A.2.1 Integration	264
A.2.2 Pole/zero finding	265
Appendix B Appendix to Chapter 4	269
B.1 Numerical solution: Frobenius methods	269
B.1.1 Computation of Taylor/Laurent coefficients	271
B.1.2 Construction of ODE solutions, and range of validity	272

Chapter 1

Introduction

1.1 Trailing-edge noise: generation and control

1.1.1 Airframe noise

Understanding of the propagation and generation of small pressure perturbations in air or water, perceived by the human ear as sound, is fundamental in controlling its impact on day-to-day life. Noise generation has been studied within a mathematical framework since Lighthill's 1952 theory of aerodynamic sound [69, 70], which concerns itself with the generation of acoustic noise from a region of turbulent flow. The resulting sound waves propagate at a well-understood speed of sound (which depends on the medium), however the generation of these waves is driven by chaotic breakdown of instabilities in viscous shear flow.

As anybody who lives near an airport can attest, aircraft are noisy. A large proportion of this noise is airframe noise: the noise of an aircraft in flight not due to the engine and other propulsive devices [32]. Over the past few decades, certification requirements (particularly with regards noise near airports) have gradually tightened to the point where the required noise reductions cannot be achieved through reduction of engine noise alone. A large component of airframe noise is related to wing flaps and landing gear, however there is a large contribution from the sharp trailing-edge of the aerofoil. This trailing-edge is a well understood and unavoidable source of noise. Vortical disturbances within a turbulent boundary layer interact with the sharp trailing-edge of an aerofoil, with the resulting broadband scattered pressure fluctuations propagating to the far-field as sound. The sound intensity of this noise source scales with velocity as $U^3 Ma^2$ independently of the behaviour of the unsteady flow [34], with $Ma = U/c_0$ the flow Mach number. This should be compared to the classical result of sound intensity of turbulence with no

hard boundaries within the flow, scaling as $U^3 Ma^5$ [70]. Similar trailing-edge generated noise arises in other contexts, in particular wind turbines. As with aircraft, there are restrictions on the noise output of wind turbines so as to reduce their impacts on local communities and wildlife [67]. In practice this is achieved by braking the turbines at high speed, reducing energy outputs and efficiency.

1.1.2 Trailing-edge noise control

The sharp trailing-edge is necessary aerodynamically for lift, and hence controlling this noise is difficult. With this in mind, a variety of noise-control devices have been proposed, either through modification of the aerofoil geometry or by controlling the behaviour of the turbulent flow near the trailing-edge. These two different broad forms of noise control arise from fundamentally different mechanisms, illustrated by considering Amiet's theory of trailing-edge noise [5, 6], which links the spectrum of far-field sound (denoted here $S_{pp}(x_1, x_2, 0, \omega)$ for observer location (x_1, x_2) at frequency ω) with the surface pressure fluctuations, $S_{pp}(\omega)$. There is the simple relationship [41]

$$S_{pp}(x_1, x_2, 0, \omega) \approx b \left(\frac{\omega c x_2}{4\pi c_\infty r_e^2} \right)^2 l_p(\omega) S_{pp}(0, \omega) |\mathcal{L}^2|. \quad (1.1.1)$$

The leading coefficients relate to aerofoil size (chordlength c and spanlength b), acoustic parameters (frequency ω and speed of sound c_∞) and observer location (observer distance r_e , minorly modified by the presence of background flow), and thus do not change with the addition of simple noise control devices. The remaining terms are the surface pressure fluctuations, encapsulated in S_{pp} , the spanwise correlation lengthscale l_p , and Amiet's transfer function \mathcal{L} . This function depends on the geometry of the trailing-edge itself, and can be computed exactly for a flat aerofoil.

Inspiration for a variety of trailing-edge noise control devices arises from the silent flight of owls [49, 71, 37]. Uniquely amongst birds of prey, large owls rely on the almost complete elimination of self-noise so as to both hear and not be heard by their prey. Alongside their reduced speed of flight (ranging from just 2.5 ms^{-1} to 10 ms^{-1} [78]), it is possible to isolate the three primary biological features that give rise to this noise reduction: a comb of hooks on the leading-edge of the wing; an elastic fringe of feathers at the trailing-edge; and a soft downy coating on both the upper and lower surfaces of the wing. The leading edge comb does not appear to have a direct impact on noise control, suggested to act as a vortex sheet generator ensuring the flow over the wing remains laminar and attached [51, 68]. Conversely, the effect of the trailing-edge fringe is to vastly

reduce the noise of the owl [71], though this alone cannot explain the entirety of the noise reduction. This fringe has been modelled mathematically by Jaworski and Peake [63], as a porous and elastic trailing-edge using the Wiener-Hopf technique, suggesting the noise scales like $U^3 Ma^3$ as opposed to $U^3 Ma^2$ for a hard edge, particularly at medium and higher frequencies (in this case above approximately 1.6 kHz, which corresponds to an acoustic wavelength comparable to the observed minimal wing chord of silent owls – smaller owls which don't rely on being silent do not have the previous discussed wing features).

A variety of trailing-edge control devices mimicking this behaviour have previously been proposed and implemented. The use of serrated trailing-edges (both sawtooth and sinusoidal) for noise reduction has been studied (with success) experimentally [65, 74] and mathematically [57, 72], and indeed has been applied to wind turbines in the form of Siemens' DinoTail [100]. With regards Amiet's formula (1.1.1), these primarily lead to modification of the transfer function \mathcal{L} , as with porous and elastic trailing-edge modifications (for example [99]), though the exact mechanism behind this varies.

Recent work by Clark et al. [28, 26, 25, 24] led to the development of finlets, streamwise-oriented fence-like objects near, or upstream of, the trailing-edge, deriving inspiration from fibres on the upper surface of the wing of a silent owl. Numerical and experimental investigations of similar objects show a reduction in far-field noise resulting from trailing-edge scattering [3, 4, 15]. Active noise control measures have also been proposed, typically blowing or suction near the trailing-edge or into the wake, both constantly and periodically [118, 36, 106]. These methods have the advantage of a far greater degree of control, and thus applicability to a wider range of flow conditions. Common to both blowing and the finlet or fence-like devices is the reduction in surface pressure fluctuations S_{pp} , identified in (1.1.1) as the critical measurable quantity that is transferred to the far-field. Further, the “cutting” effect of the fence-like structure is hypothesised to reduce the spanwise correlation lengthscales l_p . There are detailed measurements of boundary-layer profile both for finlets and for near-edge blowing, both showing boundary-layer distortion and a separation of the turbulent boundary-layer behind the device. Typically, hot-wire measurements of the boundary-layer profile are used to measure the mean streamwise flow velocity, and the root mean square of velocity perturbations, sometimes at a variety of streamwise locations both upstream, above, and downstream of the noise control devices [106]. Further, recent large eddy simulations [16] support both the argument of a reduction in spanwise lengthscales through “chopping” of turbulent eddies, and a reduction in surface pressure fluctuations through movement of eddies away from the hard surface. Further numerical work, again supporting the argument of noise reduction through

deflection of turbulence, includes some limited, two-dimensional RANS simulations [98], though the two-dimensional setup limits the applicability of this investigation.

Whilst these devices broadly seem successful in the reduction of far-field noise, it is worth noting a pair of caveats. Firstly, any noise control device must not have a large effect on the aerodynamic characteristics of the aerofoil. For the finlets/fence case, careful analysis of the lift and drag (compared to a clean aerofoil) at a variety of angles of attack was investigated [26], showing no change in the lift characteristics except very close to stall at high angle of attack, and a mild increase in drag (consistent with regarding the applied finlets as a rough surface). This is not always measured, for example more complicated configurations [4] of streamwise orientated structures doesn't include measurement of lift and drag, which may limit practical application.

Secondly, under certain configurations the noise control devices themselves may become a source of sound. This is most noticeable for very closely-spaced finlets at low frequencies, for example the low-frequency peak seen in figure 15 of Clark et al. [26] for finlet spacing of 1 mm. Instead of acting as a sharp trailing-edge, the aerofoil (with finlet modifications) begins to act as a bluff body, with the resulting vortex shedding from the trailing-edge a new source of noise. This imposes a practical limit on how much finlets can be utilised to reduce noise, with otherwise noise reduction being enhanced by closer-spaced finlets. Quantification and explanation of the precise noise reduction mechanisms are still required.

1.1.3 Vortex sound models

As noted above, trailing-edge noise fundamentally arises from the interaction between vorticity within the boundary-layer with the sharp trailing-edge. This can be quantified in a simple mathematical framework through the theory of vortex sound, which considers primarily the motion of a point vortex as it passes a (potentially thick) trailing-edge, following on from the work of Crighton [30]. Crighton considered a line vortex passing a semi-infinite flat plate, moving under the self-induced motion due to the presence of the plate. In this case, in the absence of background flow, the trajectory of the vortex can be exactly computed. The Green's function due to a point vortical source near a half-plane can be computed and, in the acoustic far-field, the amplitude of the resulting pressure fluctuations can be computed as the vortex moves, which is purely a function of vortex location at retarded time (the time modified by the time it takes the resulting sound wave to reach the observer). This theory can be extended to more complicated geometries (see [58] and [41, §7] for a detailed overview), in particular to a thick trailing-edge [54]. Provided a conformal map can be determined which maps the thick trailing-edge to the

flat trailing-edge, it is possible to write down an approximation to the far-field Green's function (under the assumption that the trailing-edge is *acoustically compact*, that is that the acoustic wavelength is much larger than the thickness of the aerofoil, more appropriate at lower frequencies).

Focusing on the flat half-plane (and noting there are analogous results for thicker half-planes) we have the first-order far-field Green's function [55]

$$G(\mathbf{x}, \mathbf{y}, t - \tau) \approx \frac{\phi^*(\mathbf{x})\phi^*(\mathbf{y})}{\pi|\mathbf{x}|} \delta((t - \tau) - |\mathbf{x}|/c_0). \quad (1.1.2)$$

This relates the signal seen at location $\mathbf{x} = (x_1, x_2)$ due to a disturbance at $\mathbf{y} = (y_1, y_2)$, essentially a wave propagating at speed of sound c_0 commencing at the vortex location at time $t = \tau$. The solution is driven by the potential $\phi^*(\mathbf{x}) = \sqrt{r} \sin(\theta/2)$, with $x_1 = r \cos(\theta)$, $x_2 = r \sin(\theta)$. Tailoring for a thick edge requires simply substituting out $\phi^*(\mathbf{y})$ in favour of a solution of Laplace's equation satisfying no penetration on the new boundaries, that asymptotically looks like ϕ^* , which is relatively straightforward if conformal maps can be determined. Importantly, the strength of a vortex is related strongly to the distance $|\mathbf{y}|$ of the source from the trailing-edge.

This is not the complete picture, as strictly this quantity needs to be integrated against the driving hydrodynamic quantity $\rho_0^{-1} \nabla \cdot (\rho \mathbf{u} \times \boldsymbol{\omega})$, where \mathbf{u} is the flow field and $\boldsymbol{\omega} = \nabla \times \mathbf{u}$ the derived vorticity field. This therefore scales with the background velocity at the location of the vortex (assuming the flow is otherwise irrotational and thus vorticity is concentrated at this point). The divergence ensures it is the deviation of the path from free-stream advection that drives far-field vortex noise, and as such a relationship between the source location (for example, the point of closest approach to the trailing-edge tip) and the resulting noise can be derived (alternatively, one can consider various norms of the noise due to a single vortex during its passage [81]). Broadly speaking, the further the source is from the sharp trailing-edge the quieter it is [81].

Recalling the detailed measurements of turbulence displacement mentioned previously, qualitative models of this behaviour have been explained, through development of the above vortex sound models to include quasi-porous objects attached to an aerofoil [25, 40], which suggest a reduction in surface pressure fluctuations and thus far-field sound due to a movement of vorticity from the trailing-edge, which is comparable to experimental observations [3, 106, 4]. That these models provide a simple mechanism for noise reduction, albeit qualitatively, suggests this mechanism is worth investigating further in a more comprehensive mathematical framework.

The vortex sound model framework is limited. Full use of the tools of conformal maps requires limitation to two dimensions, as does useful implementation of any vortex shedding at the trailing-edge (for example by releasing a vortex at each timestep [54] or using the Brown and Michael formulation [23, 53]). This limits use in investigating the fundamentally three-dimensional behaviour of finlets. Further, vortex sound models typically neglect underlying viscous considerations, important in thin regions near surfaces. Given experimental measurements show not only a broad movement in location of turbulence but also a stronger variation in boundary-layer shear, inclusion of some viscous effects, if only in the imposition of background rotational flow, appears necessary.

1.1.4 Rapid Distortion Theory

Rapid distortion theory (RDT) has its roots in the study of the development of turbulence by Batchelor and Proudman [13]. At the fundamental level, it concerns the distortion of turbulence as it passes through a region of large-scale straining motions [60]. This assumption of rapid convection allows linearisation of the governing vorticity equation around some mean flow, consistent with Taylor's hypothesis, that in a frame moving with the mean flow the turbulence will be nearly frozen [108]. This hypothesis cannot hold if nonlinear terms (for example Reynolds stresses) and viscous terms (leading to dissipation of eddies) are important, though arises naturally from linearisation of the Euler equations (in which viscosity is treated as negligible, at least with regards the perturbations). RDT was applied in an aeroacoustic sense in 1978 by Goldstein [42], considering perturbations to some background irrotational flow. This is broadly equivalent to the vortex sound analysis above, in the limit that vortex self-propulsion (due to the flow generated by the perturbation vorticity itself) can be neglected.

In the absence of background vorticity, perturbation entropy and vorticity are convected with the mean flow [47]. The perturbation flow can be decomposed as $\mathbf{u}' = \nabla\phi + \mathbf{u}_R$, where the rotational perturbation is solely within \mathbf{u}_R . In the absence of background rotation, linearisation of the background flow results in decoupled equations for ϕ (satisfying a convected wave equation) and for \mathbf{u}_R (convected with the mean flow), and we can thus describe ϕ as the usual acoustic velocity potential. Only this latter term carries with it a pressure perturbation: the vortical and entropic solutions are silent. We can, however, define \mathbf{u}_R as the gust solution, generalising the vortical solution in the vortex sound model above.

For *sheared* flow, the background flow is not irrotational. Such flows could arise due to a jet or a non-negligible boundary-layer near an object. Fundamentally, this leads to a coupling between vortical and acoustic components of the velocity perturbation.

However, the idea of a gust can be generalised in the case of transversely sheared flow, as identified by Goldstein et al. in the late 1970s [42, 44] and recently extended [46, 48]. In the case of a parallel background flow, it is possible to identify two quantities that are convected with the background flow, which in turn drive the development of physical variables. Most importantly, the pressure perturbation is driven by a single convected quantity, which can be identified as a generalisation of the perturbation vorticity. The details of this can be found in §2.

That perturbation vorticity is convected in sheared flow is the classical result of Orr [80], from investigations into the stability of simply sheared Couette flow. If the background shear is constant, then perturbation vorticity is exactly convected, which in turn drives the fluid motion through the solution of the Poisson equation. This setup, whilst fundamentally concerned with incompressible (and as such non-acoustic) motions, can be utilised in the compressible case as an inner problem, provided the boundary-layer thickness is negligible on the lengthscale of acoustic fluctuations. This is typically true provided frequencies are suitably low and the background flow is slow compared to the speed of sound. Even for higher frequencies, the linear shear approximation removes some of the underlying mathematical difficulties, based around the singularity of the governing differential equation when the wavenumber of a disturbance corresponds to the convective wavenumber due to the background flow. This linear shear approximation removes this difficulty, though similar problems may arise in more complicated geometries [22].

Even this simple setup, which in the incompressible limit permits analytical solutions, can highlight interesting phenomena. While a mass source placed in uniform flow cannot generate any vortical (rotational) perturbations, through the interaction with background shear a trailing vortical sheet can be generated [92]. This recent result is extended in this work by considering only a finite region of shear (considered previously by, for example, Schuster [96]), which allows precise matching to an acoustic solution beyond the boundary-layer, and by considering a more refined piecewise-linear approximation to the background flow. This naturally requires discontinuity in background shear, which generates atypical behaviour and shall be investigated in detail.

This model is useful in the context of noise control devices, particularly finlet-like structures. These devices are small compared to the boundary-layer thickness, for example Afshari et al. [4] considered devices with heights around 0.16δ , where δ is the boundary-layer thickness. With regards the mean flow, this leads to a substantial increase in near-wall shear. Similar models of fibre canopies have been considered [27], considering the attenuation of instability waves by the localised shear layer around the fibres. With the

mean flow profile an input to the model, it is straightforward to investigate these effects in a RDT framework.

A second benefit of the model is control of the gust solution. As the previous vortex models have shown, vorticity deflection can have a large impact on the scattered noise, and this model gives a handle on vorticity deflection (through the convected quantity generalising vorticity) within an explicit boundary-layer context. Given repeated measurements of noise control devices show a general movement of eddies away from scattering surfaces, it is worth quantifying the effect this might have on scattered noise in the far-field. Indeed, for lower frequencies, with acoustic wavelengths much larger than boundary-layer thicknesses, we expect minimal effect from the boundary-layer structure, which is on a scale essentially unseen by the acoustic disturbance. However, regarding vorticity as the source of noise, the location and strength of this hydrodynamic source itself, strongly dependent on boundary-layer structure, is expected to have a great impact on perceived noise, through the scattering process.

It is worth comparing the discussion here with Amiet's formula above, (1.1.1). That formulation is derived by considering the scattering of some harmonic "gust" of the form

$$\exp(i\omega(t - x_1/U_c)), \quad (1.1.3)$$

that is, a wave moving at some convection velocity U_c which is less than the free-stream velocity, beyond the boundary-layer. The scattering of such a gust can be computed exactly in terms of exponential integrals, using either Schwarzschild's solution [97] (a Green's function for half-plane scattering) or more directly through application of the Wiener-Hopf technique [79], discussed below. This gives rise to the transfer function \mathcal{L} . As well as being somewhat agnostic to the exact structure of the forcing term (since the main experimental input is the wall pressure, again modified by the source structure), it requires measurement or input of the convection velocity U_c . Conversely, with the RDT formulation, the convection velocity is an intrinsic character of the vorticity distribution, being the background velocity at the location of the vorticity.

1.1.5 Scattering

The solution to the classical Sommerfeld scattering problem, of an (electromagnetic) wave scattered by a half-plane, dates back to 1896 [104], giving rise to the well-known diffraction pattern from a sharp edge. Solutions can also be derived via Schwarzschild's method [97], which constructs a Green's function for the half-plane problem (and so, given surface forcing, can compute the far-field radiated noise). Both these solutions, however, are

solely for Helmholtz equation (the time-harmonic wave equation), with reasonably simple imposed boundary conditions.

The Wiener-Hopf technique was developed as a way of solving a class of singular integral equations in 1931 [117]. It was noted by a variety of authors in the 1940s that the method could be applied to (acoustic or electromagnetic) diffraction problems, and we consider primarily the formulation constructed by Jones in 1950 [64], which works directly in the Fourier transformed space rather than direct and consistent consideration of integral equations, and is the approach taken by Noble in the classical reference book [79]. We essentially extend the range of problems that can be solved by the Fourier transform (and other transforms) with discontinuous boundary data, by considering the complex analyticity of the partial transform of the data. As well as providing an elegant analytic solution to the simple diffraction problems (and more complicated, similar problems), it is useful even for more complicated problems. In particular, the method offers a great degree of control at discontinuities of boundary conditions. Numerical computation of scattering problems is difficult near sharp corners, in particular the application of the unsteady Kutta condition [31] (the insistence that perturbations are minimally singular at the trailing-edge of an aerofoil), due to the presence of (singular) eigensolutions radiating from the tip. Analytic application of the Kutta condition allows the correct eigensolution to be chosen, which is vital for correct understanding of the far-field noise [8].

Much acoustic consideration of scattering problems using the Wiener-Hopf technique focusing on leading- and trailing-edges, typically considering perturbations to uniform flow, or to first-order (irrotational) corrections due to camber, angle of attack or aerofoil thickness [75, 76, 9]. However, the method is applicable to sheared flow and to scattering from discontinuities along a continuous boundary, for example at the start or end of a lined section of wing. Consideration of background rotational flow typically leads to governing equations that are not analytically tractable, except in certain limits, but the complex analytic methods permitted by the Wiener-Hopf technique transfer over even if numerical computation of functions is required. The junction scattering problem (between a hard-wall and a soft-wall, and vice versa) has been considered previously [93, 101] in an analytically tractable limit, which does however pose difficulties in computation of the scattered solution. By considering the numerical analogue of this problem, in the suitable limit of speed of sound tending towards infinity, it is possible to reevaluate the results suggested by this analytic analysis.

1.1.6 Acoustic linings

This work will discuss the evolution of perturbations above a lined surface. Acoustic linings, typically acoustic damping materials made up of an array of Helmholtz resonators, are used throughout aircraft to reduce noise, most notably within the turbofan aeroengine (the most important source of take-off noise), and could be considered a model of the soft upper side of the wing of an owl [38]. A variety of complexity in liner models can be considered, for example the nonlinear models of Innes and Crighton in 1989 [62] and more recently of Singh and Rienstra [102]. A typical simple model of a linear posits a relationship between the pressure and the velocity on a surface, linked by some complex impedance Z which depends on the frequency ω of the disturbance. We consider a locally reacting liner, which relates pressure and velocity perturbations at a surface via some linear relationship $p' = Z v'$, where v' is the wall-normal velocity perturbation [59], and Z contains terms relating to the adsorption and reactance of the liner. This should be suitably modified in the presence of background flow and shear [61, 77] (see (2.4.4)).

Much study has been done of this problem in acoustic ducts (as opposed to disturbances above flat surfaces in this work). Typically, in a duct with a hard boundary, acoustic disturbances can be characterised by a complete set of modal disturbances. These propagate either upstream or downstream from some source, and are either cut-off (decaying exponentially away from the source) or cut-on (neutrally stable propagating down the duct). These can broadly be associated with the acoustic branch cut in the problem considered here, which replaces a line of modal solutions with a branch cut in complex wavenumber space. For a lined duct, these modes are all attenuated, but can still broadly be associated as either upstream or downstream propagating, and as generalisations of cut-on or cut-off [82].

Importantly, however, a new collection of modes appears in considering disturbances to background flow above a lined wall. These *surface modes* remain confined to a very thin region near the wall, and were identified by Rienstra [86, 87]. The number of such modes differs based on the presence or not of background shear and of the exact flow configurations, and they can be quite difficult to find [88]. For disturbances to uniform flow, up to four such modes could be found, which rises to six when background shear is included [111, 110]. The potential instability of such modes causes problems, as identified by Rienstra and Darau [91] and by Brambley (and Peake) [18, 19], of the Myers boundary condition being fundamentally ill-posed in the limit of the boundary-layer thickness tending towards zero, and as such some finite region of inviscid boundary-layer must be included in the analysis, motivating the work of Rienstra, Darau and Brambley [92] in considering hydrodynamic disturbances to simple linear shear, which allows exact com-

putation of the surface mode behaviour in sheared flow, and a corresponding numerical analysis [22] considering critical-layer effects. The modal scattering problem has been considered in ducts [85, 89]. Whilst surface modes are fundamentally hydrodynamic, and do not themselves generate far-field noise, the scattering of excited surface modes, for example at the trailing-edge of a section of lining could be a source. Inclusion of realistic shear within a boundary-layer further allows another look at scattering from a lined wall, considered previously in a limited case by Rienstra and Singh [93, 101].

1.2 Thesis structure

This work gradually builds up a picture of the gust solution in transversely sheared flow, before computing the scattering of such a solution firstly from the junction between two liners before focusing on the trailing-edge scattering problem. The goal of this thesis is to understand the fundamental mechanisms behind control of the boundary-layer in reduction of far-field noise, be it from point disturbance or scattering from boundary discontinuities.

We consider the Rapid Distortion Theory approximations outlined above. The differential equations governing infinitesimal pressure perturbations and a generalised acoustic potential are derived in the following chapter, §2. Beginning from the fundamental equations governing the evolution of a general, compressible fluids, linearisation around a base fluid, under a number of simplifying assumptions, allows for the construction of solvable differential equations. To facilitate further discussion, some mathematical conventions are introduced, in particular discussion of *causality* in acoustic problems, the insistence that disturbances are not incident from infinity. This, as with most of the work throughout this thesis, requires understanding of complex variable techniques.

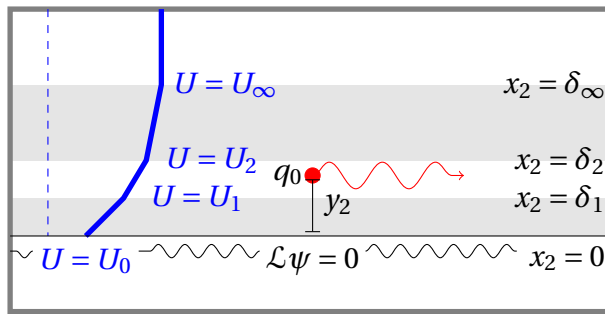


Fig. 1.2.1 The setup for Chapter 3: a point source disturbance to piecewise-linear flow (in the incompressible limit)

Chapter 3: Long-wavelength disturbances to piecewise-linear background flow. The governing differential equation, whilst linear, does not permit closed-form analytic solutions, except in certain limits. Motivated by the classical work of Orr [80], and more recent work by Schuster [96] and Rienstra et al. [92], §3 considers a linearly sheared boundary-layer. In the limit of long acoustic wavelength, the incompressible limit of this equation can be considered the inner problem of a more general acoustic disturbance. Further, upon Fourier transformation it results in an ordinary differential equation that can be solved analytically in terms of simple functions. This property transfers over to piecewise-linear background profiles. When the background shear is discontinuous (but the background velocity is continuous) then perturbation pressure and wall-normal velocity must be continuous, else the discontinuity acts as either a source of momentum or of mass, respectively. This condition can be applied in the long wavelength limit, and analytic solutions persist.

Specifically, the problem (as considered by Rienstra et al. [92]) of a point mass source in this extended setup is considered. Despite the possibility of analytic solutions to the streamwise Fourier transformed problem, due to the complexity of the resulting solutions the inverse Fourier transform cannot practically be done analytically. However, it is possible to implement rapidly convergent inversion numerically, and using similar methods attain the far-field behaviour of the solution, which can be matched with a radiating acoustic solution beyond the boundary layer. This problem is considered not just above a hard-wall, but also above a variety of lined surfaces, which gives rise to surface modes as identified by Rienstra, Brambley and others [85, 21, 20], as well as to additional nearly-stable modes which can be associated with the discontinuities in shear.

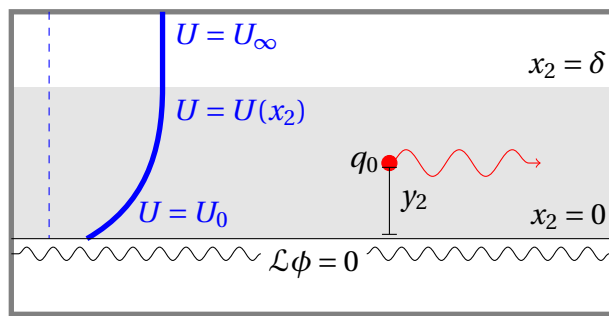


Fig. 1.2.2 The setup for Chapter 4: a point source disturbance to continuously sheared flow

Chapter 4: Disturbances to continuously sheared flow above a homogeneous boundary. The preceding chapter has established the existence of analytic solutions in cer-

tain limits, but is quite limited in its scope. This chapter extends consideration to *any* continuous background profile, through numerical solution of the governing (Fourier-transformed) ordinary differential equation. Whilst this requires additional numerical work in solving the differential equation, the use of complex methods reduces the numerical complexity quite substantially, by ensuring all integrals (particularly Fourier inversions) decay rapidly and thus the differential equation need only be solved for a comparatively small values of the wavenumber k_1 .

Numerical difficulties arise from the regular singular point of the differential equation when $k_1 = \omega/U(x_2)$, which gives rise to the critical-layer. This appears in the dispersion function as a branch cut along the real axis for $k_1 \in (\omega/U(x_2 \rightarrow \infty), \omega/U(0))$, where $U(x_2)$ is the background velocity profile, assumed increasing in x_2 . This branch cut causes difficulties, particularly when attempting to evaluate functions near this critical-layer, and methods are introduced to move it in the complex plane, for example by integrating through a complex extension of real space. By way of illustrating the success of these integration routines, the point mass source problem is again considered in this more developed framework. Further, in this case direct evaluation of the far-field radiation is possible via the method of steepest descent. The dependence of this acoustic radiation on imposed boundary condition is investigated, with the reappearance of surface modes identified and associated with the preceding incompressible case.

This chapter is constructed so as to understand the upstream gust solution, which will be useful for scattering problems (converting this gust solution to an acoustically radiating solution), as well as illustrating the success of quasi-numerical routines, coupled with complex analysis, for grid-invariant analysis of the mathematical problem.

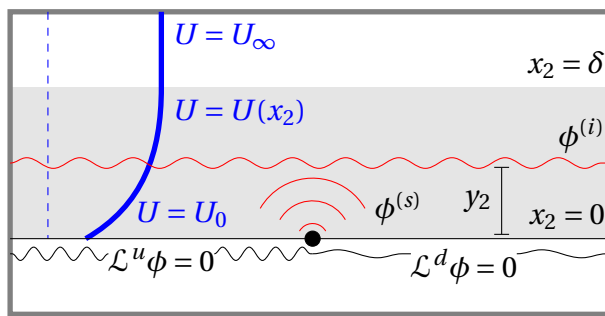


Fig. 1.2.3 The setup for Chapter 5: scattering off an abrupt change in surface boundary condition

Chapter 5: Scattering from a junction. The generic problem of scattering from a discontinuity in boundary condition is solved via the construction of a scalar Weiner-Hopf

equation. This is solved via appeal to known complex analyticity of transformed boundary conditions, coupled with some knowledge of the behaviour of the scattered solution near the junction itself, typically by minimising any singularities at this point. This complex analytic technique gives solutions that are accurately known, at least in terms of integrals, and can readily be computed numerically.

By considering the scattering of perturbations to a realistically sheared boundary layer as it passes over the leading- or trailing-junction of a lined surface, it is possible to quantify the far-field noise due to this scattering alone. This is extended to considering scattering by a section of lining of finite length. If surface modes are excited at the first junction, the scattering and restabilisation of these modes at the end of the lining can be a very strong source of sound, even without direct acoustic coupling between the two junctions.

Previous work [101] has considered the hard-soft and soft-hard junction scattering problem in the incompressible limit, with a constant shear, infinite thickness boundary-layer, which was then matched to an outer solution. This problem is reanalysed here, considering the incompressible case as instead the limit at the speed of sound, $c_0 \rightarrow \infty$, in the compressible framework. This numerical approach allows precise evaluation of the strengths of the previous work, highlighting difficulties due to the loss of a strip of analyticity in the incompressible limit, and the resulting difficulties this poses for the Wiener-Hopf technique. Inclusion of a shear layer further allows precise evaluation of scattering when the background profile is forced to be non-slipping, which has previously created issues [20].

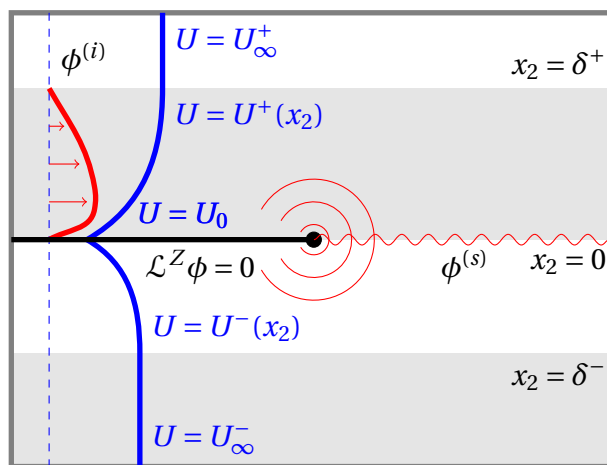


Fig. 1.2.4 The setup for Chapter 6: a convected vortical disturbance scattering off a (potentially lined) sharp trailing-edge

Chapter 6: Trailing-edge scattering. The final substantial chapter focuses on the problem of scattering from a trailing-edge, which can be linked to the problems considered in §5 if the background flow profile is symmetric, though this model allows relaxation of this assumption. Further, it is reasonably straightforward to permit consideration of scattering from a lined trailing-edge, which is also done, and may generate upstream-propagating surface modes as well as modes propagating in the wake. Again, far-field evaluation allows rapid determination of the dominant acoustic contribution through the steepest descent method. The basic layout of this chapter is shown in figure 1.2.4.

The previous chapter considered a convected vortex sheet, which bore similarities to a perturbation vortex sheet. This term is carefully understood, and more general convected generalised vortical disturbances within the boundary-layer are considered, in particular how they scatter off the trailing-edge. The linearity of this model makes this a straightforward extension of the previous work, in particular the scattering problem extends straightforwardly to more complicated incident disturbances. With the vortex sheet more carefully understood, it is possible to directly analyse the effect on the *amplitude* of the sound, as well as directivity, of variations in background shear and the upstream location of the perturbation vortex sheet. We are therefore in a position to directly analyse the noise control devices mentioned previously, particularly focusing on the experimental measurements of background mean flow and of turbulence intensity within the boundary-layer. This provides compelling evidence of the importance of turbulence location on wall-pressure and, in turn, on far-field noise.

Chapter 2

Mathematical formulation of Rapid Distortion Theory

Consideration of linearised perturbations to transversely sheared background flow are common to all the problems considered in this work, based on the earlier work of Goldstein and others [42, 44, 46]. The derivation of the fundamental equations governing these perturbations are discussed here, along with some mathematical conventions and techniques used throughout this work.

2.1 Basic concepts

2.1.1 Equations of fluid dynamics

In the continuum approximation, a fluid is characterised by its flow field $\mathbf{u}(\mathbf{x}, t)$ and a variety of other physical quantities, for example the pressure $p(\mathbf{x}, t)$ and density $\rho(\mathbf{x}, t)$, which are functions of spatial position \mathbf{x} and time t . A general fluid obeys the equations of conservation of mass and momentum, which in differential form can be written

$$\frac{D\rho}{Dt} = -\rho \nabla \cdot \mathbf{u}, \quad (2.1.1a)$$

$$\frac{D\mathbf{u}}{Dt} = -\nabla p + \mathbf{f} + \nabla \cdot \boldsymbol{\sigma}, \quad (2.1.1b)$$

where we have introduced the material derivative

$$\frac{D}{Dt} = \frac{\partial}{\partial t} + \mathbf{u} \cdot \nabla, \quad (2.1.2)$$

which governs the rate of change of a quantity moving with the fluid. In (2.1.1b), \mathbf{f} is some body force acting on the fluid (for example gravity), and $\boldsymbol{\sigma}$ is the deviatoric stress tensor, representing frictional forces between fluid elements.

For a *Newtonian* fluid, which includes air and water to a reasonable approximation, the deviatoric stress tensor can be directly related to the rate of strain tensor $e_{ij} = \partial u_i / \partial x_j$, with $\boldsymbol{\sigma} = \mu(\mathbf{e} + \mathbf{e}^T)$, where the proportionality constant μ defines the *dynamic viscosity*, and in this case $\nabla \cdot \boldsymbol{\sigma}$ is simply $\mu \nabla^2 \mathbf{u}$.

Consider a fluid with a reference density ρ (for example, the density of the fluid when stationary or moving at a constant velocity). Suppose this fluid is moving at a speed U over some lengthscale L . We can then define the dimensionless Reynolds number, Re , as

$$Re = \frac{\rho U L}{\mu} \quad (2.1.3)$$

which governs the balance between inertia and viscosity [12, 41]. For fluids with high Re this suggests we can ignore the viscous terms. However, this is not a valid assumption near the boundaries of the domain, which can be noted either by spotting that the reference lengthscale, L , becomes small, or that the second derivative $\nabla^2 \mathbf{u}$ could become very large here. For the bulk fluid, away from the boundaries, it seems reasonably to broadly ignore viscosity, though at times it may be reintroduced as appropriate. To quantify the Reynolds number of interest, consider the flight of an owl. Large owls typically have a wing chord-length of up to 400 mm (see for example Table 1 in [63], collated from other works). The mean flight speed of a barn owl is of the order 5 ms^{-1} [78, 38, 37]), which, with kinematic viscosity of air, $\nu = \mu / \rho$, of the order $\nu \approx 1 \times 10^{-5} \text{ m}^2 \text{s}^{-1}$ gives a Reynolds number of the order 1×10^5 . Of course, if much finer lengthscales are looked at, for example the spacing of fibres on the surface of the wing, much smaller Reynolds numbers are attained.

The equations governing motion of a compressible fluid are not closed, unlike their incompressible counterparts, with another equation required to link pressure and density. Under the assumption that acoustics are a *adiabatic* thermodynamic process not involving any exchange of heat or dissipation, it is possible to write an energy equation in terms of the entropy s . Any thermodynamic variable can be written in terms of the other two, and so it follows that for a perfect gas

$$ds = c_V \frac{dp}{p} - c_p \frac{d\rho}{\rho}, \quad (2.1.4)$$

where c_V and c_p are the specific heats for constant volume and pressure respectively. In the case that entropy is everywhere constant, so that $ds = 0$, this can be rewritten as

$$\frac{p}{\rho^\gamma} = \text{const.} \quad (2.1.5)$$

In this equation γ is the ratio of specific heat capacities, $\gamma = c_p/c_V$. This is the *homentropic* assumption, and is slightly stronger than what is needed. We consider the more general specification of an *isentropic* fluid: the entropy of a moving fluid element does not change, and as such

$$\frac{Ds}{Dt} = 0. \quad (2.1.6)$$

Use of the differential form for ds immediately gives a relationship between the material derivatives of p and ρ , as [41]

$$\frac{Dp}{Dt} = \frac{\gamma p}{\rho} \frac{D\rho}{Dt}, \quad (2.1.7)$$

where $\gamma p/\rho = (\partial p/\partial \rho)_s$ in the isentropic case. This corresponds to the (square of) the usual definition of the speed of sound, as

$$c^2 = \left. \frac{\partial p}{\partial \rho} \right|_s, \quad (2.1.8)$$

with subscript s denoting the derivative at fixed entropy.

That the quantity c is indeed the speed of acoustic waves is most easily seen by considering small perturbations to quiescent flow of constant density ρ_0 (and thus speed of sound c_0), neglecting quantities quadratic in perturbation variables and any external forces. The governing equations reduce to

$$\frac{\partial \rho'}{\partial t} = -\rho_0 \nabla \cdot \mathbf{u}', \quad (2.1.9)$$

$$\rho_0 \frac{\partial \mathbf{u}'}{\partial t} = -\nabla p', \quad (2.1.10)$$

$$\frac{\partial p}{\partial t} = c_0^2 \frac{\partial \rho}{\partial t}. \quad (2.1.11)$$

Elimination of density perturbations through use of the third equation into the first gives

$$\frac{\partial p'}{\partial t} = -\rho_0 c_0^2 \nabla \cdot \mathbf{u}'. \quad (2.1.12)$$

Taking the time derivative of this equation and the divergence of the equation for velocity perturbations allows elimination of the cross term, $\rho_0 \partial/\partial t(\nabla \cdot \mathbf{u}')$, common to both equa-

tions and results in a single second-order differential equation for pressure perturbations:

$$\frac{\partial^2 p'}{\partial t^2} - c_0^2 \nabla^2 p' = 0. \quad (2.1.13)$$

This is clearly a wave equation, with the wavespeed given, as expected, by the speed of sound c_0 . This derivation, for a more complicated base flow, is revisited in the next section.

The above derivation supposed the speed of sound and the background density were constant. This is broadly true if the Mach number is low, where we define the Mach number Ma as

$$Ma = \frac{U}{c_0}, \quad (2.1.14)$$

for some reference speed of the fluid U and speed of sound c_0 . This assumption of constant background density can be quantified somewhat, for example if we have a homentropic flow with averaged flow speed upstream U_∞ (with corresponding density ρ_∞), then the relationship with the local density ρ_0 can be written [41]

$$\left(\frac{\rho_0}{\rho_\infty}\right)^{\gamma-1} = 1 + \frac{(\gamma-1)}{c_\infty^2}(U_\infty^2 - U^2), \quad (2.1.15)$$

and a low Mach number assumption allows the second term to be neglected. If we do not make this assumption there may be some variation in background density ρ_0 and thus background speed of sound c_0 , and we keep this option in mind in later derivations, though where $Ma^2 \ll 1$ we can reasonably take ρ_0 and c_0 constant in space.

2.1.2 Mathematical conventions

A few mathematical conventions will be used in this and following chapters, mostly to simplify notation. This section gives a brief overview of the important points, most notably the sign convention used for Fourier transformation.

Fourier transforms. Fourier transforms, both spatial and temporal, are used throughout this chapter and the following. Where it is unambiguous, subscripts are used to define the transform variable. For example, given a function $f(\mathbf{x}, t)$ we have

$$f_0(\mathbf{x}, \omega) = \int_{-\infty}^{\infty} f(\mathbf{x}, t) e^{-i\omega t} dt \quad (2.1.16)$$

(or, if necessary, $\int_{-T}^T dt$ as $T \rightarrow \infty$) and

$$f_1(k_1, \mathbf{x}_T, t) = \int_{-\infty}^{\infty} f(\mathbf{x}, t) e^{+ik_1 x_1} dx_1. \quad (2.1.17)$$

with \mathbf{x}_T being the components of \mathbf{x} other than x_1 . We define wall-normal and spanwise Fourier transforms analogously to the streamwise case, with complex wavenumbers k_2 and k_3 respectively, denoted by subscript \cdot_2 and \cdot_3 .

The inversion of these is given by

$$f(\mathbf{x}, t) = \frac{1}{2\pi} \int_{-\infty}^{\infty} f_0(\mathbf{x}, \omega) e^{i\omega t} d\omega \quad (2.1.18)$$

$$f(\mathbf{x}, t) = \frac{1}{2\pi} \int_{-\infty}^{\infty} f_1(k_1, x_2, t) e^{-ik_1 x_1} dk_1 \quad (2.1.19)$$

These transformations stack to form multivariate transformations, if required. They can also be applied to differential operators, normally through the transformations $\partial/\partial t \mapsto i\omega$ and $\partial/\partial x_j \mapsto -ik_j$.

Causality: Briggs-Bers and the radiation condition. Suppose we are considering the problem of a point source near a boundary, with the domain extending to infinity both upstream and downstream in the x_1 direction (an *open* shear flow) and to $x_2 \rightarrow \infty$. If the source is switched on at a given time, for example $t = 0$ without loss of generality, then it is reasonable to insist that there is no disturbance before the source is switched on. Further, we insist that, spatially, no waves propagate *inwards* from infinity: all disturbances are created at the source. Whilst these conditions are easy to understand physically, care must be taken to implement them in Fourier space.

We first deal with the temporal causality condition, that there is no disturbance before the source is turned on. Consider, for a generic linear partial differential operator \mathcal{D} in one spatial dimension, the equation governing some disturbance ϕ with some source $S(t, x_1)$:

$$\mathcal{D}\left(\frac{\partial}{\partial t}, \frac{\partial}{\partial x_1}\right) \phi(t, x_1) = S(t, x_1) \quad (2.1.20)$$

with $S \equiv 0$ for $t < 0$. We impose the same condition on ϕ , that $\phi \equiv 0$ for $t < 0$. We apply the double Fourier transform as outlined above, with

$$\phi_{01}(\omega, k_1) = \int_{-\infty}^{\infty} \int_{-\infty}^{\infty} \phi(t, x_1) \exp(-i(\omega t - k_1 x_1)) dt dx_1 \quad (2.1.21)$$

which simply reduces (2.1.20) to

$$\mathcal{D}_{01}(\omega, k_1)\phi_{01}(\omega, k_1) = S_{01}(\omega, k_1), \quad (2.1.22)$$

an algebraic equation. The dispersion function \mathcal{D}_{01} is obtained simply by substituting $\partial/\partial t = i\omega$ and $\partial/\partial x_1 = -ik_1$ into the expression for \mathcal{D} . This is trivial to solve in Fourier space, as

$$\phi_{01} = \frac{S_{01}}{\mathcal{D}_{01}} \quad (2.1.23)$$

We now invert the temporal Fourier transform. Inverting along the real axis, as per (2.1.19), might give contributions for $t < 0$, which conflicts with the temporal causality assumption. We can choose the inversion contour, denoted L_ω , to lie beneath all singularities of S_{01}/\mathcal{D}_{01} , with

$$\phi_1(t, k_1) = \frac{1}{2\pi} \int_{L_\omega} \frac{S_{01}(\omega, k_1)}{\mathcal{D}_{01}(\omega, k_1)} \exp(i\omega t) d\omega \quad (2.1.24)$$

If L_ω lies beneath all roots of the dispersion relation, \mathcal{D}_{01} then we can close the $= 0$ integration contour, for $t < 0$, in the lower-half ω plane (LH ω P). Since the integrand is free of singularities, this is identically zero. The contribution from the closure contour in the lower half plane decays, as the real part of $i\omega t$ is negative. This is precisely analogous to inversion of the Laplace transform, where the inverse contour is taken to the right of all singularities in the s -plane: essentially the Laplace transformation and the causal Fourier transformation equivalent with $s \mapsto i\omega$.

Depending on what we want to do, there are two things we can now do. The majority of the discussion in this work focuses on a *harmonic* disturbance. That is, the solution oscillates in time at a single, real, frequency ω . This is slightly at odds with the above, where a complete temporal solution was considered. In particular, a harmonic solution proportional to $\exp(i\omega t)$ is non-causal, however we do want to use temporal causality arguments. We can do this by taking the imaginary part of ω to be sufficiently large and negative, and then relax it back to the real axis. This is analogous to continuing the process that returned ϕ_1 above, and carefully considering the spatial inversion contour, which shall be done by way of illustration.

Suppose that there is a single temporal mode for which $\mathcal{D}_{01}(\omega, k_1) = 0$, given by $\omega(k_1)$. Since L_ω lies beneath this singularity by construction, we can close in the upper half-plane

and apply the residue theorem to give, for positive time,

$$\phi_1(t, k_1) = -\frac{i S_{01}(\omega(k_1), k_1)}{\frac{\partial \mathcal{D}_{01}}{\partial \omega}(\omega(k_1), k_1)} \exp(-i\omega(k_1)t) \quad (2.1.25)$$

Unlike the temporal inversion contour, there is no need for the spatial inversion contour F_{k_1} to be anything other than the real axis: indeed, this is assumed for the existence of spatial Fourier transforms (namely, decays as $|x| \rightarrow \infty$), as opposed to the causal assumptions on the temporal transform. Thus, the precise solution ϕ can be obtained by computing the standard spatial inversion of the above, noting that the singularities, in the k_1 plane, of the integrand of (2.1.24) will not cross F_{k_1} as ω varies: solutions $k_1(\omega)$ satisfying $\mathcal{D}_{01}(\omega, k_1(\omega))$ are confined to loci in the upper- or lower-half k_1 plane as ω varies.

This observation allows relaxation of the L_ω contour to the real axis, provided the F_{k_1} contour is suitably deformed so as to maintain the observation above. This is not always possible, for example if two poles, on either side of the F_{k_1} contour for large negative $\text{Im}(\omega)$, come together for some $\text{Im}(\omega)$ which is still non-zero, thereby forcing the F_{k_1} contour between this pair of “pinched” contours. This leads to absolute instability, and is beyond the scope of this work.

For the purposes of this work, we care only about identifying solutions which propagate upstream and those that propagate downstream, analogously to the above. For negative imaginary part of ω , it is possible to unambiguously identify poles of Fourier transformed quantities with either the upper- or lower-half k_1 plane, corresponding respectively to upstream and downstream-propagating modes upon inversion. This requires further that no branch cuts cross the real k_1 axis, which for example determines the direction of the branch cuts of $\gamma = \sqrt{k_1^2 - \omega^2/c_0^2}$ (or similar) later (see (4.2.12)), with branch points connected each other through complex infinity. The Briggs-Bers procedure, as we understand it, then requires that these modal solutions, and any branch cut contributions, remain in the same generalised “half-plane”, with the complex plane bisected by $F(k_1)$, as the imaginary part of ω is relaxed to zero. This can lead to unstable modal solutions growing downstream, for example, for real ω . This is demonstrated for pressure-release modes in §3.6. Essentially the condition that quantities are integrable (and thus we can compute Fourier transforms) is replaced by a condition that nothing propagates inwards from upstream or downstream infinity, even if it means the outward-radiating solution is infinite there (and thus doesn’t have a classical Fourier transform). This is demonstrated schematically in figure 2.1.1.

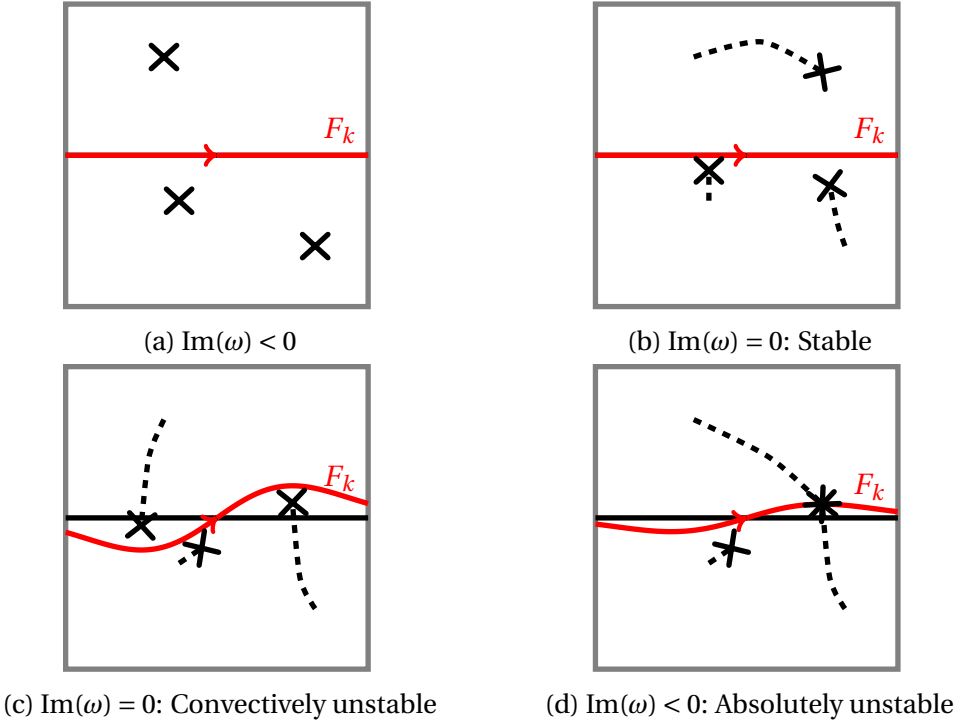


Fig. 2.1.1 The construction of causal solutions through the Briggs-Bers procedure. For $\text{Im}(\omega)$ sufficiently negative, there is no ambiguity in the half-plane of inversion singularities, with all Fourier transforms converging, and no propagation from positive infinity. As $\text{Im}(\omega)$ is relaxed to zero, three things are possible. Firstly, the singularities remain in the same half plane, and we have a stable, causal solution with no work. If the singularities change half-plane, then the inversion contour F_k must be deformed to maintain causality, and thus there are linearly unstable solutions. This is convective instability, with instabilities convected out of the domain. The final case, not directly considered in this work, is where two poles, initially in different half-planes, pinch together and prevent further contour deformation, whilst $\text{Im}(\omega)$ is still negative. This is absolute instability.

The above primarily concerns itself with the streamwise direction, that nothing is incident from $x_1 \rightarrow \pm\infty$. We must add a further radiation condition that waves are outgoing at infinity in all directions. For harmonic waves, with timelike dependence $e^{i\omega t}$, this is simply the condition that solutions have wavelike dependence

$$p' \sim \exp(i(\omega t - \mathbf{k} \cdot \mathbf{x})) \quad (2.1.26)$$

as $\mathbf{x} \rightarrow \infty$, which can be written more precisely, for an n -dimensional solution to Helmholtz equation, as

$$\lim_{|\mathbf{x}| \rightarrow \infty} \mathbf{x}^{n-1} 2(\nabla + ik_0) p' = 0 \quad (2.1.27)$$

with $k_0 = \omega/c_0$ the Helmholtz number [105]. This is a condition of no energy coming from infinity. It is important to check this condition is satisfied, with careful choice of sign depending on the choice of Fourier transformation conventions. Typically, for the work in this and later chapters, we utilise the condition that streamwise transformed, harmonic solutions look like $e^{-\gamma x_2}$ as $x_2 \rightarrow \infty$, where γ has positive real part.

Plotting complex functions. Functions of a complex variable, $w = f(z) = f(x + iy)$, are ubiquitous throughout this work. There are a variety of methods of visualising complex analytic functions. Whilst sometimes the real and imaginary parts of a map will be plotted separately, which is sometimes useful (for example in determining contours on which the imaginary part of a function is constant), typically the most useful plot is a plot of the complex phase [113, 103], where the hue of the plot is associated with the complex argument. This can be generalised to associate, for example, the brightness of the plot with the magnitude of the complex function. Since both hue and argument are periodic, such plots clearly show up singularities and branch cuts in the complex plane, and will be used throughout this work without comment. An example of this plot showing branch cuts can be seen later in figure 4.2.1, for the acoustic exponent $\gamma(k_1)$, which has two finite branch points (joined through infinity).

2.2 A wave equation for pressure

The introduction saw a quick derivation of the wave equation for small, acoustic pressure perturbations to a quiescent flow. This derivation is now extended to linearised perturbations to a prescribed parallel flow, resulting in a more complicated equation governing pressure fluctuations. In particular, we focus on a boundary-layer flow, where there is a uniform flow sufficiently far away from the boundary along $x_2 = 0$ (x_2 being

the wall-normal coordinate), in the streamwise (x_1) direction. Within the boundary-layer itself, for $0 < x_2 < \delta$, the background flow may be sheared.

This can be generalised to a wake or a jet, where there is a finite region, $\delta^- < x_2 < \delta^+$, for which the background shear $U'(x_2)$ is non-zero, with the background flow otherwise being constant beyond this region. The derivation of the equations assumes nothing more than the background flow is sheared, so it is applicable to sheared flow in a duct, for example, once further geometrical factors are included, which gives rise to the Pridmore-Brown equations [82]. Application of this Rapid Distortion Theory argument (the basis for neglection of nonlinear terms and effects of viscosity: convection drives perturbations through the domain on a much more rapid timescale than that of the effect of viscosity and nonlinearity) to boundary-layer and jet flow has been considered in detail by Goldstein and others [42, 44, 46, 48], and it is this work that forms the basis of this derivation.

2.2.1 Assumptions

As suggested above, we make a variety of initial assumptions. The Reynolds number is assumed large, allowing viscosity to be neglected in the momentum equation. While this assumption cannot be true near boundaries (where the length scales of interest are small), we assume that we are always far enough away from surfaces that viscous effects on perturbation quantities can be neglected¹. We make the further assumption that any flow we are considering is isentropic, allowing closure of the system of governing equations written in the following form

$$\frac{D\rho}{Dt} + \rho \nabla \cdot \mathbf{u} = 0, \quad (2.2.1a)$$

$$\rho \frac{D\mathbf{u}}{Dt} + \nabla p = 0, \quad (2.2.1b)$$

$$\frac{Ds}{Dt} = 0. \quad (2.2.1c)$$

If we consider the entropy as a function of density and pressure, $s = s(\rho, p)$ then the energy equation (2.2.1c) can be rewritten, linking pressure and density via the speed of sound

$$\frac{Dp}{Dt} = c^2 \frac{D\rho}{Dt}. \quad (2.2.2)$$

¹This assumption must be relaxed when scattering problems are considered, with the unsteady Kutta condition taking into account the effect of viscosity near sharp junctions, as seen in later chapters.

This in turn allows combination of the mass (2.2.1a) and energy equations (2.2.1c) into a single equation

$$\frac{Dp}{Dt} + c^2 \rho \nabla \cdot \mathbf{u} = 0. \quad (2.2.3)$$

As above, making the slightly stronger assumption that the fluid we're considering is an ideal gas, for example air, then pressure and density can be related to the speed of sound via

$$c^2 = \frac{\gamma p}{\rho}, \quad (2.2.4)$$

where γ is the adiabatic index (for air, around 1.4 [116]). This allows replacement of $c^2 \rho$ by γp if appropriate.

We now consider small, compressible disturbances to some prescribed, steady background flow. We assume that this background flow, \mathbf{u}_0 , is rectilinear and does not develop as it moves downstream, and as such is independent of the coordinate x_1 which we define as the *streamwise* coordinate. The remaining spatial coordinates shall be called the transverse coordinates, $\mathbf{x}_T = (x_2, x_3)$. Typically we shall consider x_2 to be a wall-normal coordinate and x_3 a spanwise coordinate, with respect to a horizontal aerofoil, though for the present the general case is considered. With these assumptions the base flow $\mathbf{u}_0 = U(\mathbf{x}_T)\mathbf{e}_1$ for some scalar U . For this and later chapters, we assume U is constant outside some boundary-layer ($x_2 > \delta^+ > 0$, $x_2 < \delta^- < 0$), though this does not effect the derivation of the governing equations.

2.2.2 Compressible Rayleigh's equation

Denoting perturbation quantities with a prime, the total velocity is written as $\mathbf{u}(\mathbf{x}, t) = \mathbf{u}_0(\mathbf{x}_T) + \mathbf{u}'(\mathbf{x}, t)$. Similarly, the total pressure is decomposed as $p(\mathbf{x}, t) = p_0(\mathbf{x}_T) + p'(\mathbf{x}, t)$ and density $\rho(\mathbf{x}, t) = \rho_0(\mathbf{x}_T) + \rho'(\mathbf{x}, t)$, with mean quantities \cdot_0 depending only on transverse position \mathbf{x}_T and, like \mathbf{u}_0 , assumed known. The stronger assumption of parallel, transversely sheared background flow indicates, from (2.2.1b), that the background pressure p_0 is temporally and spatially constant. We also define the convective derivative with respect to the base flow

$$\frac{D_0}{Dt} = \frac{\partial}{\partial t} + \mathbf{u}_0 \cdot \nabla = \frac{\partial}{\partial t} + U \frac{\partial}{\partial x_1}. \quad (2.2.5)$$

The governing equations, linearised around the parallel base flow $\mathbf{u}_0 = U(\mathbf{x}_T)\mathbf{e}_1$ (i.e. neglecting quantities quadratic or smaller in primed quantities) are

$$\frac{D_0 p'}{Dt} + c_0^2 \rho_0 \nabla \cdot \mathbf{u}' = 0, \quad (2.2.6a)$$

$$\rho_0 \frac{D_0 \mathbf{u}'}{Dt} + \rho_0 \mathbf{u}'_T \cdot \nabla_T U \mathbf{e}_1 + \nabla p' = 0, \quad (2.2.6b)$$

with $\mathbf{u}'_T = (0, u'_2, u'_3)$ (so that $\mathbf{u}' = u'_1 \mathbf{e}_1 + \mathbf{u}'_T$) and $\nabla_T = (0, \partial/\partial x_2, \partial/\partial x_3)$ the transverse components of the perturbation velocity field and gradient operator respectively. The first equation requires the assumption that we have an ideal gas, and so $c_0^2 \rho_0$ can be regarded as constant. Combining these linearised governing equations through

$$\frac{D_0}{Dt} \left[\frac{D_0}{Dt} (2.2.6a) - \nabla \cdot (c_0^2 (2.2.6b)) \right] + 2c_0^2 \frac{\partial}{\partial x_1} (2.2.6b) \cdot \mathbf{e}_1 \quad (2.2.7)$$

gives (the compressible) Rayleigh's equation

$$\left(\frac{D_0}{Dt} \left[\frac{D_0^2}{Dt^2} - \nabla \cdot (c_0^2 \nabla) \right] + 2c_0^2 \frac{\partial U}{\partial x_j} \frac{\partial^2}{\partial x_1 \partial x_j} \right) p' = 0. \quad (2.2.8)$$

This reduces to (a convected derivative of) the usual (convected) wave equation in regions with constant background flow, with the shear-dependent term $\partial U / \partial x_j$ vanishing.

Depending on the context, this might also be referred to as the Pridmore-Brown equation [82], which is typically used for this equation in a cylindrical duct (and often after Fourier expansion in the azimuthal direction, and Fourier transformation in the streamwise direction, i.e. the resulting r -dependent ODE). This does not change the equation above, but it differs from the Cartesian case primarily through the introduction of factors of $1/r$ in derivatives. In other contexts, particularly in the extension of Lighthill's acoustic analogy (thereby an exact rearrangement of the Euler equations, and with source terms on the right-hand side), this is referred to as Lilley's equation [45]. With the operator referred to in the literature as both the Pridmore-Brown and Rayleigh operators, for precision we term the operator in Cartesian geometry as the compressible Rayleigh operator throughout this work.

Inclusion of mass and momentum sources. With this setup, it is straightforward to include mass and momentum sources by including non-zero terms on the right-hand side of the governing equations of motion. With mass and momentum sources added to the

right-hand side of (2.2.1), we have

$$\frac{D\rho}{Dt} + \rho \nabla \cdot \mathbf{u} = q(\mathbf{x}, t), \quad (2.2.9a)$$

$$\rho \frac{D\mathbf{u}}{Dt} + \nabla p = \mathbf{f}(\mathbf{x}, t), \quad (2.2.9b)$$

$$\frac{Ds}{Dt} = 0, \quad (2.2.9c)$$

where q and \mathbf{f} are mass and momentum (force) sources respectively, per unit volume. We suppose these sources are the same order of magnitude as infinitesimal perturbations, which would allow them to be added instead to the right-hand side of the linearised equations, (2.2.6). By combining the governing equations, analogously to (2.2.7), we obtain Rayleigh's equation with source terms:

$$\left(\frac{D_0}{Dt} \left[\frac{D_0^2}{Dt^2} - \nabla \cdot (c_0^2 \nabla) \right] + 2c_0^2 \frac{\partial U}{\partial x_j} \frac{\partial^2}{\partial x_1 \partial x_j} \right) p' = \frac{D_0}{Dt} \left[\frac{D_0}{Dt} (c_0^2 q) - \nabla \cdot (c_0^2 \mathbf{f}) \right] + 2c_0^2 \frac{\partial f_1}{\partial x_1}. \quad (2.2.10)$$

The spatial and temporal form of these sources can be chosen to match the problem, as required.

Conditions at discontinuities of U and its derivatives. We need not assume U or its derivatives are continuous, though relaxing this assumption requires care on conditions applied to perturbation quantities at these points. The underlying physical assumptions are of continuity of particle displacement and no net force acting across such a junction (an assumption that also holds across a wake). We suppose there is such a discontinuity at $x_2 = \chi_2$ and define the jump across χ_2 for some function f as

$$[f]_{\chi_2} = f(\chi_2^+) - f(\chi_2^-), \quad (2.2.11)$$

with the limit $f(\chi_2^\pm)$ defined as $\lim_{x_2 \rightarrow \chi_2} f(x_2)$ from $x_2 \gtrless \chi_2$ respectively. With this notation, we have

$$[p']_{\chi_2} = 0, \quad (2.2.12)$$

$$v'(\chi_2^\pm) = \frac{D_0^\pm \eta}{Dt}(x_1, x_3, t) \quad (2.2.13)$$

with D_0^\pm / Dt the mean-flow material derivative for $x_2 \gtrless \chi_2$, and particle displacement η continuous across χ_2 . It is straightforward to eliminate η if it is, for example, harmonic

in its variables. In the special case of continuous U (but discontinuous $\partial U / \partial x_2$) then we simply have

$$[v']_{\chi_2} = 0 \quad (2.2.14)$$

In later chapters, we assume the background flow U is everywhere continuous, even if the derivative is not. We therefore need only impose conditions of continuity of v' and p' at discontinuities of $\partial U / \partial x_2$.

2.3 The adjoint problem for general continuous background profile

Typically for acoustic problems it might be possible to construct an acoustic potential, ϕ , from which it is possible to derive representations of pressure and velocity fluctuations. In the simplest case of perturbations to a quiescent fluid, these are given simply by

$$\mathbf{u}' = \nabla \phi, \quad p' = -\rho_0 \frac{\partial \phi}{\partial t}, \quad (2.3.1)$$

with the acoustic potential satisfying the usual wave equation. This naturally extends to *uniform* background flow by replacement of time derivatives with convective derivatives, and we can derive a partial differential equation for ϕ from which all physical variables can be extracted.

Following Goldstein [44], this can be generalised to include shear. For reasons that become clear in the derivation, we suggest a generalised acoustic velocity potential ϕ such that

$$p' = -\frac{D_0^3 \phi}{Dt^3}. \quad (2.3.2)$$

The form of this potential is unusual. Typically in a uniform flow problem we would have acoustic potential with $\mathbf{u} = \nabla \phi$, and so $p' = -\rho_0 D_0 \phi / Dt$. The additional derivatives in the newly introduced potential are required to put the resulting equation into the correct form, though this means we cannot compute all components of velocity directly from this potential. The transverse components of the linearised momentum equation, (2.2.6b), is

$$\rho_0 \frac{D_0 \mathbf{u}'_T}{Dt} + \nabla_T p' = 0 \quad (2.3.3)$$

with, as before, \mathbf{u}'_T the transverse components of the perturbation velocity field. Substituting the ansatz for pressure then gives

$$\frac{D_0}{Dt}(\rho_0 \mathbf{u}'_T) = \frac{D_0^3}{Dt^3}(\nabla_T \phi) + \frac{D_0^2}{Dt^2} \left(3\nabla_T U \frac{\partial \phi}{\partial x_1} \right). \quad (2.3.4)$$

This has been constructed to ensure all terms are a convected derivative, and thus can be integrated up, giving an explicit equation for \mathbf{u}'_T (in terms of some unknown convected quantity \mathbf{C}_T):

$$\mathbf{u}'_T = \frac{1}{\rho_0} \left[\frac{D_0^2}{Dt^2}(\nabla_T \phi) + \frac{D_0}{Dt} \left(3\nabla_T U \frac{\partial \phi}{\partial x_1} \right) + \mathbf{C}_T \right]. \quad (2.3.5)$$

We can then substitute this expression into the (more complicated) streamwise component of the linearised momentum equation, (2.2.6b)

$$\rho_0 \frac{D_0 u'_1}{Dt} + \rho_0 \mathbf{u}'_T \cdot \nabla_T U + \frac{\partial p'}{\partial x_1} = 0. \quad (2.3.6)$$

Substitution then gives

$$\frac{D_0}{Dt}(\rho_0 u'_1) + \frac{D_0^2}{Dt^2}(\nabla_T U \cdot \nabla_T \phi) + \frac{D_0}{Dt} \left(3|\nabla_T U|^2 \frac{\partial \phi}{\partial x_1} \right) + \nabla_T U \cdot \mathbf{C}_T = \frac{D_0^3}{Dt^3} \frac{\partial \phi}{\partial x_1}. \quad (2.3.7)$$

We would, as before, have an exact convective derivative if the earlier convected quantity, \mathbf{C}_T , was such that $\mathbf{C}_T \cdot \nabla_T U = 0$. We can ensure this by exploiting a degree of freedom in ϕ : by choosing $\phi \mapsto \phi + F$, with $D_0^2 F / Dt^2 = 0$, the pressure is unchanged and the expression for transverse velocity is changed by some convected quantity, which we can absorb into C_T . By suitably choosing F , it is possible to eliminate the component of \mathbf{C}_T in the sheared direction, as required. Upon doing this, we have

$$u'_1 = \frac{1}{\rho_0} \left[-\frac{D_0}{Dt}(\nabla_T U \cdot \nabla_T \phi) - \left(3|\nabla_T U|^2 \frac{\partial \phi}{\partial x_1} \right) + \frac{D_0^2}{Dt^2} \frac{\partial \phi}{\partial x_1} + C_1 \right]. \quad (2.3.8)$$

Again, we have an unknown convected quantity C_1 , and again we have a degree of freedom remaining, as $\phi \mapsto \phi + G$, with $D_0 G / Dt = 0$, still returns the same pressure field, which allows for control of C_1 .

We can derive a differential equation for ϕ by substitution into the linearised mass-energy equation, (2.2.6a). Ideally, this equation will be independent of \mathbf{C} , for which we require $\nabla \cdot (\mathbf{C}/\rho_0) = 0$. We have two degrees of freedom for choosing the three components

of \mathbf{C} , and thus it can be written in terms of a single, scalar convected quantity θ (subject to the twin conditions $\nabla_T U \cdot \mathbf{C}_T = 0$ and $\nabla \cdot \mathbf{C}/\rho_0 = 0$). These conditions hold if

$$\mathbf{C} = \rho_0 \nabla U \times \nabla \theta \quad (2.3.9)$$

where $\theta = \theta(t - x_1/U(\mathbf{x}_T), \mathbf{x}_T)$ is some undetermined convected quantity, and returns Goldstein's result [44, 46, 48].

The resulting differential equation for ϕ is then

$$\frac{D_0}{Dt} \left[\frac{D_0^3}{Dt^3} - \frac{\partial}{\partial x_i} \left(c_0^2 \left(\frac{\partial}{\partial x_i} \frac{D_0}{Dt} + 2 \frac{\partial U}{\partial x_i} \frac{\partial}{\partial x_1} \right) \right) \right] \phi = 0. \quad (2.3.10)$$

Since this arises directly from the mass-energy equation it is straightforward to include mass sources on the right-hand side, by inserting the term $c_0^2 q(\mathbf{x}, t)$.

We define the operator

$$\mathcal{D}_R^\dagger = \frac{D_0^3}{Dt^3} - \frac{\partial}{\partial x_i} \left(c_0^2 \left(\frac{\partial}{\partial x_i} \frac{D_0}{Dt} + 2 \frac{\partial U}{\partial x_i} \frac{\partial}{\partial x_1} \right) \right), \quad (2.3.11)$$

where the notation \dagger is used to show that this is the adjoint of the Rayleigh operator applied to the pressure, namely

$$\mathcal{D}_R = \left(\frac{D_0}{Dt} \left[\frac{D_0^2}{Dt^2} - \nabla \cdot (c_0^2 \nabla) \right] + 2c_0^2 \frac{\partial U}{\partial x_j} \frac{\partial^2}{\partial x_1 \partial x_j} \right), \quad (2.3.12)$$

as per (2.2.8), in the sense that, for two well-behaved functions u and v ,

$$\int_V d^3x \int dt (u \mathcal{D}_R v - v \mathcal{D}_R^\dagger u) = \text{boundary terms}, \quad (2.3.13)$$

which can be easily verified [107].

It is straightforward to integrate the equation

$$\frac{D_0}{Dt} \mathcal{D}_R^\dagger \phi = 0 \quad (2.3.14)$$

up once, to give

$$\mathcal{D}_R^\dagger \phi = F(t - x_1/U(\mathbf{x}_T), \mathbf{x}_T), \quad (2.3.15)$$

where F is some arbitrary convected quantity. This can, as suggested by the piecewise-linear discussion below, be considered a generalisation of the perturbation vorticity $\omega' = \nabla \times \mathbf{u}'$, including the effects of boundary-layer shear and of variations in the background speed of sound, as well as direct compressibility effects. It is possible to construct conservation laws to suggest the form of this quantity [48], or incorporate source terms to drive this forcing, as done later in this work in sections 3.4 and 4. For example, a point mass source in shear generates a trailing vortex sheet.

We can also consider the (generalised) vortex sheet solution, where this convected quantity is confined to an infinitesimal region around a single streamline of the background flow. If we assume the temporal Fourier transform of (2.3.15) exists, akin to assuming the decay of all transients, then we have

$$\mathcal{D}_{R0}^\dagger \phi_0 = e^{-i\omega x_1/U(\mathbf{x}_T)} F_0(\mathbf{x}_T), \quad (2.3.16)$$

from which solutions can be constructed by using a Green's function satisfying

$$\mathcal{D}_{R0}^\dagger G_{R0}^\dagger = e^{-i\omega x_1/U(\mathbf{y}_T)} \delta(\mathbf{x}_T - \mathbf{y}_T), \quad (2.3.17)$$

which is exactly the generalisation of a vortex sheet, up to some leading constants which depend on the background flow. This naturally occurs in the wake a point source, and will be used later.

Noting that \mathcal{D}_R and \mathcal{D}_R^\dagger are adjoint allows use the direct Green's function \mathcal{G} , which satisfies

$$\mathcal{D}_{R0} G_{R0}(\mathbf{x}; \mathbf{y}) = \delta(\mathbf{x} - \mathbf{y}). \quad (2.3.18)$$

This can be used to more generally compute the generalised velocity potential ϕ via use of (2.3.13), as done by Goldstein et al. [46, 48], but this approach is not directly considered in this work.

2.4 Streamwise-homogeneous boundary conditions

The following two chapters are concerned with perturbations above some streamwise-homogeneous boundary at $x_2 = 0$, from $-\infty < x_1 < \infty$ and, if a third dimension is considered, $-\infty < x_3 < \infty$. The resulting perturbation quantity is therefore defined on $x_2 > 0$. The related problem of a wake (perturbations to a background flow defined on $-\infty < x_2 < \infty$) is also discussed, and in this case the perturbation quantity is defined on all x_2 .

Causality. These problems involve a source being placed in the fluid, and the resulting perturbations being investigated. It is important, therefore, to impose that all disturbances are due to this source and have not come from outside the domain, for example waves coming in from infinity, for which we refer to the introductory section §2.1. We impose the Briggs-Bers stability criterion, by first considering large negative imaginary part of ω to determine the direction of propagation of solutions.

Hard-wall and pressure release conditions. The simplest boundary condition is a hard-wall boundary condition, where the fluid does not penetrate the wall, and is equivalent to saying that the wall-normal velocity perturbation vanishes, i.e.

$$v'(x_2 = 0) = 0 \quad (2.4.1)$$

We can also, similarly, consider pressure-release walls (which cannot support any pressure) which instead simply have

$$p'(x_2 = 0) = 0 \quad (2.4.2)$$

Lined wall. We can generalise by considering an impedance lining with both the hard-wall and pressure release solutions a special case. Acoustic linings, used to reduce noise, are typically modelled as a linear relationship between the wall-pressure and normal velocity at the wall, with

$$Z(\omega) = \frac{p'}{\mathbf{u}' \cdot \mathbf{n}} \quad (2.4.3)$$

for harmonic disturbances proportional to $\exp(i\omega t)$. This must, however, be modified if there is a slipping background flow, leading to the Ingard-Myers boundary condition [61, 77], which considers fluid particle displacement as opposed to normal velocity, and gives

$$i\omega Z(\omega) \mathbf{u}' \cdot \mathbf{n} = (i\omega + \mathbf{u}_0 \cdot \nabla - (\mathbf{n} \cdot \nabla \mathbf{u}_0) \cdot \mathbf{n}) p'. \quad (2.4.4)$$

For a straight wall, the final term is identically 0. Importantly, this gives a straightforward linear relationship between v' ($= \mathbf{u}' \cdot \mathbf{n}$) and p' , which allows application of the usual Fourier transform-based methods. The limit of large $|Z|$ is exactly the hard-wall limit, and the limit of vanishing Z the pressure-release limit (a wall that does not support force).

Wake. Finally, the case of a background flow field $U(x_2)$ defined for all $x_2 \in (-\infty, \infty)$ will be considered. While we assume this is everywhere continuous, we do not assume the same condition holds on derivatives (for example, it is reasonable to suppose $U'(x_2)$ is discontinuous at $x_2 = 0$, which could for example represent a developed wake behind a plate,

on which the flow is smoothed out over some inner viscous lengthscale). Thus, as suggested for junctions in §2.2.2, we impose continuity of velocity and pressure perturbations across $x_2 = 0$. Causality here dictates waves only propagate outwards for both $x_2 \rightarrow \pm\infty$, and it is this new condition at $x_2 \rightarrow -\infty$ that fulfills the same role as the boundary in the earlier examples.

If $U(x_2) = U^*(-x_2)$ for $x_2 < 0$, then under the transformation $x_2 \mapsto -x_2$ the differential equation governing perturbations is unchanged, save for U being replaced by U^* . This means that solutions on $x_2 < 0$ can be computed as solutions on $x_2 > 0$, without changing any routines or methods, save substitution of the flow field. In particular this means solutions with specified boundary conditions are identical under $x_2 \mapsto -x_2$ if the flow profile is symmetric, $U(x_2) = U(-x_2)$, which simplifies analysis.

Chapter 3

Long-wavelength disturbances to piecewise-linear background flow

By considering small perturbations to some known background shear flow, the hydrodynamic and acoustic behaviour of a point source, be it of mass, momentum or vorticity, is considered as the perturbation evolves downstream. In this chapter, the simplified case of long-wavelength disturbances to a piecewise-linearly sheared background flow is considered, above a range of (streamwise-homogeneous) boundaries. This model is developed and its strengths and limitations are discussed.

3.1 Introduction

The interaction of vortical motion within a turbulent boundary-layer with a sharp edge of an aerofoil generates waves with acoustic wavelengths which radiate to the far-field as noise. A sharp edge, or a discontinuity in the boundary condition on the surface of the aerofoil, provides a strong mechanism to convert the hydrodynamic boundary-layer turbulence into far-field noise, stronger than the normal quadrupole noise due to free turbulence [34]. In practice, an incident turbulent wave, confined to a boundary-layer, is modelled by a *gust*: a wavelike solution with particular frequency and wavenumber propagating at a speed below the uniform free-stream velocity. The scattering of this wave, from a sharp trailing-edge or other mixed boundary boundary conditions, can then be solved using the Wiener-Hopf method.

This and the following chapter, §4, are focused on the understanding of the vortical gust solution, in preparation for later scattering problems. The gust, confined to the boundary-layer, critically depends on the shear inherent in the underlying flow. Infinitesi-

mal disturbances to sheared flow is a classical problem stretching back to Lord Rayleigh [84]. Orr [80] considered hydrodynamic disturbances to Couette flow in a pipe, that is uniformly transversely sheared parallel flow, and the development of disturbances downstream. Noting inviscid two dimensional disturbances to linearly sheared background flow $U(x_2)$ satisfy

$$\left(\frac{\partial}{\partial t} + U(x_2) \frac{\partial}{\partial x_1} \right) \omega' = 0, \quad (3.1.1)$$

with ω' the perturbation vorticity, such that $\nabla \times \mathbf{u}' = \omega' \mathbf{e}_3$, the solution is driven by vortical solutions propagating with the mean velocity (i.e. dependent on time and streamwise direction x_1 only in the combination $t - x_1/U(x_2)$).

This simple setup can be used for considering acoustic problems and more complicated background flow, through a long-wavelength approximation and consideration of piecewise linear background shear. The long acoustic wavelength limit of the equations derived by Goldstein [42] reproduce Orr's equation in a thin region near boundaries, which can in turn be matched to a radiating acoustic solution. As far as the acoustic motion is concerned the boundary is *compact* and can therefore in a sense be ignored, in that a sound wave propagating through an acoustically thin shear layer wouldn't be modified by the shear. However, both the gust setup and more careful treatment within this chapter have sources *within* the boundary-layer, which therefore require an understanding of the underlying acoustic behaviour within the boundary-layer itself.

Modelling a background flow as a continuous profile built from linear pieces has multiple benefits. It results in analytically tractable solutions. Further, as noted by various authors, (for example Heaton and Peake [50]), the presence of background vorticity modifies the acoustic problem, primarily through the need to consider a *critical layer*, with the governing differential equations having a regular singular point when the streamwise wavenumber $k_1 = \omega/U(y_2)$, for some y_2 within the boundary-layer. The resulting branch cut in the (complex) dispersion function $D(k_1, \omega)$ might give rise to disturbances that grow or decay only algebraically downstream. This problem is avoided solely in the case that $U'' = 0$ above a flat plate (as opposed to, for example, within a cylindrical geometry), almost exactly returning to the case considered by Orr. By considering a piecewise-linear profile, with $U'' = 0$ everywhere except discrete points, the critical-layer is again of little concern and the problem can be solved, to some extent, algebraically. This is the setup used by Rienstra, Darau and Brambley [92] (hereafter RDB), who consider a point mass source in infinite linear shear above a wall.

This chapter extends the results of RDB to a piecewise linear profile matched to uniform flow outside some boundary layer, and considers it as the inner problem to some

more general acoustic problem, through asymptotically matching to an acoustic solution in uniform flow above this hypothetical boundary layer, using standard techniques [52]. This allows consideration of approximating more complicated background profiles without removing all the mathematical niceties of this construction. Further, by considering uniform flow outside some boundary-layer of finite thickness, issues of far-field convergence in two dimensions, due to a perceived "infinite" far-field background flow, do not occur. The following chapter will generalise these results to more complicated profiles, and assess the suitability of this approximation.

Inclusion of realistic shear within a boundary-layer also allows another look at perturbations above a lined wall [85, 89]. By considering a non-negligible boundary-layer of reasonably arbitrary thickness this chapter allows analyses the imposition of an impedance condition for slipping and non-slipping flow, avoiding some of the pitfalls of typical uniform flow models, as previously done for a duct [22].

This chapter begins by simplifying the governing Rapid Distortion Theory equations from the preceding chapter, §2. The problem of a point source above a surface with streamwise-homogeneous boundary conditions is then considered, limited not only to a hard-wall but more general boundary conditions (for example a lined wall) as well. Finally, the evolution of disturbances in a wake is considered. These are primarily setting up later chapters, via careful construction of the boundary-layer "gust" solution. Later we will look at the scattering induced by a change from one boundary condition to another, for which a complete understanding of boundary-layer solutions is useful. Further, this chapter provides a straightforward model for boundary-layer noise, with limited numerical complexity.

3.2 Rapid Distortion Theory in the long-wavelength limit

Motivated by RDB [92], we first consider the limit of long acoustic wavelength, for which analytic progress can be made. For a harmonic solution proportional $\exp(i\omega t)$, we can define an acoustic wavenumber

$$k_0 = \frac{\omega}{c_0}. \quad (3.2.1)$$

The wavelength of acoustic waves (which propagate with speed given by speed of sound c_0) is related to k_0 as $\lambda_a = 2\pi/k_0$, and so k_0^{-1} is a measure of the acoustic lengthscale. This gives two lengthscales of interest for the problem, if the geometry of interest does not have any lengthscales (such as the streamwise homogeneous case considered in this chapter, or with semi-infinite streamwise boundary conditions considered in later scattering problems),

namely the boundary-layer thickness δ , outside which the background flow is uniform, and the acoustic lengthscale k_0^{-1} . This is physically appropriate for a large range of frequencies and geometries. For $k_0\delta \ll 1$, we require

$$\omega \ll \frac{c_0}{\delta}. \quad (3.2.2)$$

If δ is on the order of centimetres, this approximation is valid provided $\omega \ll 10^4 \text{ s}^{-1}$, which covers a broad range of reasonably low, audible, frequencies.

We consider then the limit $k_0\delta \rightarrow 0$, which can be done in two ways: firstly by scaling distances on the acoustic lengthscale k_0^{-1} , giving rise to an outer solution that doesn't see the boundary-layer at all, save in the imposition of boundary conditions; and secondly by scaling distances on the boundary-layer lengthscale δ . The latter scaling (under certain conditions on the Mach number) removes the majority of acoustic effects, and under further assumptions allows analytic solution to the governing equations. The acoustics of the problem then arise through matching to an appropriate outer solution.

3.2.1 Outer region

We firstly scale lengths with the reciprocal of (the real part of¹) the acoustic wavenumber k_0 . We suppose that the timescale of evolution is ω^{-1} for some frequency ω , and use this and the speed of sound at infinity with $c_0(x_2) \rightarrow c_\infty$ as $x_2 \rightarrow \infty$, to define an acoustic wavenumber $k_0 = \omega/c_\infty$ and scale physical variables accordingly:

$$T_a = \omega t \quad (3.2.3a)$$

$$X_{ai} = k_0 x_i \quad (3.2.3b)$$

$$M_a = \frac{U}{c_\infty} \quad (3.2.3c)$$

$$c_a = \frac{c_0}{c_\infty} \quad (3.2.3d)$$

which rescale Rayleigh's equation (2.2.8) as

$$\left(\frac{D_a}{DT_a} \left[\frac{D_a^2}{DT_a^2} - \nabla_a \cdot (c_a^2 \nabla_a) \right] + 2c_a^2 \frac{\partial M_a}{\partial X_{aj}} \frac{\partial^2}{\partial X_{a1} \partial X_{aj}} \right) p' = 0 \quad (3.2.4)$$

¹As outlined in the Briggs-Bers process in §2.1.2, we take the mathematical limit $\text{Im}(\omega) \rightarrow 0^-$ to understand causality, so ω and k_0 might be complex. This does not occur physically in the final solution, so for scaling purposes we consider only the real part of ω and of k_0 .

where $D_a / DT_a = \partial / \partial T_a + M \partial / \partial X_{a1}$ and $\nabla_{ai} = \partial / \partial X_{ai}$. The form of the equations is unchanged. However, if we impose that U is uniform outside some boundary-layer confined to $x_2 \in (0, \delta)$, then

$$\frac{\partial M_a}{\partial X_{aj}} = 0 \quad (3.2.5)$$

for $X_{a2} > \delta k_0 \rightarrow 0$, i.e. almost everywhere in \mathbf{X}_a space, save for a thin region near $X_{2a} = 0$. Thus, Rayleigh's equation in the outer region is simply the convected wave equation

$$\left[\frac{D_a^2}{DT_a^2} - \nabla_a^2 \right] p' = 0. \quad (3.2.6)$$

The superfluous convective derivative has been removed either by arguing there are no sources within the outer region (where the flow is not turbulent) or by returning to the original governing equations of momentum and mass-energy and noting the original differentiation step is not required to remove the shear when there is no shear. We make the further assumption that $c_a = 1$ is constant outside the boundary-layer.

As suggested by the above, we cannot directly apply boundary conditions at $X_{a2} = 0$, since the shear need not be negligible there. Further, we expect acoustic sources to occur within the boundary layer, which are not encapsulated by this limiting process.

3.2.2 Inner region

To deal with the near-wall region, we can scale with boundary-layer thickness δ as a lengthscale, defining instead

$$T_b = \omega t \quad (3.2.7a)$$

$$X_{bi} = \frac{x_i}{\delta} \quad (3.2.7b)$$

$$U_b = \frac{U}{\delta \omega} \quad (3.2.7c)$$

$$c_b = \frac{c_0}{c_\infty} \quad (3.2.7d)$$

and Rayleigh's equation scales to

$$\left(\frac{D_b}{DT_b} \left[\epsilon^2 \frac{D_b^2}{DT_b^2} - \nabla_b \cdot (c_b^2 \nabla_b) \right] + 2c_b^2 \frac{\partial U_b}{\partial X_{bj}} \frac{\partial^2}{\partial X_{b1} \partial X_{bj}} \right) p' = 0 \quad (3.2.8)$$

with $\epsilon = \omega\delta/c_\infty = k_0\delta$, and the limiting process assumes that this is small. We can eliminate the convective derivative in the square brackets provided the convection itself is not strong, that the flow Mach number, $M_b = U_b/c_\infty$ is small for some representative U_b (e.g. at the edge of the boundary-layer). Explicitly, if $M_b^2 \ll 1$ we have the incompressible form of Rayleigh's equation:

$$\left(\frac{D_b}{DT_b} [\nabla_b^2] - 2 \frac{\partial U_b}{\partial X_{bj}} \frac{\partial^2}{\partial X_{b1} \partial X_{bj}} \right) p' = 0, \quad (3.2.9)$$

where we have made the further assumption that the speed of sound and the background density ρ_0 are constant within the boundary-layer, which is consistent with the assumption of reasonably small M_b (as discussed in §2.1). We can thus define the linear differential operator \mathcal{D}_i , the incompressible Rayleigh operator

$$\mathcal{D}_i = \frac{D_0}{Dt} [\nabla^2] - 2 \frac{\partial U}{\partial x_j} \frac{\partial^2}{\partial x_1 \partial x_j}. \quad (3.2.10)$$

3.2.3 Alternative derivation of the equation in the inner region

This equation can be attained directly from the governing equations in the “limit” $c_0 \rightarrow \infty$, wherein the mass-energy equation reduces to

$$\nabla \cdot \mathbf{u} = 0. \quad (3.2.11)$$

This is the expected expression for conservation of mass in an incompressible fluid. Importantly this solenoidal property allows the velocity field \mathbf{u} to be written as the curl of a vector potential, and if the disturbance is two dimensional (and doesn't depend on x_3) then this potential has a single component $\psi' \mathbf{e}_3$, with the streamfunction defined as usual with

$$u' = \frac{\partial \psi'}{\partial x_2}, \quad (3.2.12a)$$

$$v' = -\frac{\partial \psi'}{\partial x_1}, \quad (3.2.12b)$$

so that $\mathbf{u}' = \nabla \times (\psi' \mathbf{e}_3)$. By instead eliminating pressure from the governing equations, it is straightforward to get an equation governing the evolution of ψ' . The pressure is most easily eliminated by taking the curl of the momentum equation (2.2.1b) to give the

vorticity equation (with density assumed constant throughout the fluid)

$$\frac{D\omega}{Dt} - \boldsymbol{\omega} \cdot \nabla \mathbf{u} = 0 \quad (3.2.13)$$

The first term governs the change in vorticity $\boldsymbol{\omega} = \nabla \times \mathbf{u}$ as it is advected with the flow, deforming purely through stretching by the fluid, encapsulated in the second term. Linearised around a steady base flow \mathbf{u}_0 , with $\boldsymbol{\omega}_0 = \nabla \times \mathbf{u}_0$, this equation becomes

$$\frac{D_0}{Dt} \boldsymbol{\omega}' + \mathbf{u}' \cdot \nabla \boldsymbol{\omega}_0 = \boldsymbol{\omega}_0 \cdot \nabla \mathbf{u}' + \boldsymbol{\omega}' \cdot \nabla \mathbf{u}_0 \quad (3.2.14)$$

with primes denoting perturbations around the mean flow as usual. We make the same assumption as before, that $\mathbf{u}_0 = U(x_2, x_3)\mathbf{e}_1$, and make the further assumption that the perturbation is entirely two dimensional (so that \mathbf{u}' is a function of x_1 and x_2 alone, and has no x_3 component, an assumption made purely to simplify the problem) which gives $\boldsymbol{\omega}' = \omega' \mathbf{e}_3$. The third component of the vorticity equation (3.2.14) is then

$$\frac{D_0 \omega'}{Dt} - u'_2 \frac{\partial^2 U}{\partial x_2^2} = 0. \quad (3.2.15)$$

The assumptions on the two-dimensional nature of the perturbation allow use of the streamfunction discussed above, for which we have

$$\frac{D_0}{Dt} [\nabla^2 \psi'] - U''(x_2) \frac{\partial \psi'}{\partial x_1} = 0, \quad (3.2.16)$$

if we make the final simplification that U is a function of wall-normal coordinate x_2 alone, though this isn't strictly necessary. This is the usual form of Rayleigh's stability equation. The resulting differential operator acting on ψ , $\bar{\mathcal{D}}_i$, is given by

$$\bar{\mathcal{D}}_i = \frac{D_0}{Dt} [\nabla^2] - U'' \frac{\partial}{\partial x_1}. \quad (3.2.17)$$

3.2.4 Linear shear

Most numerical difficulty in solving (2.2.8) arises from the singular nature of the ordinary differential equation resulting from a spatial and temporal Fourier transform at points with $\omega - U(x_2)k_1 = 0$, when there is a regular singular point of the differential equation for almost all choices of U . However, this difficulty disappears uniquely in the case that $U'' = 0$. This can most obviously be seen (in the case c_0 large) from the equation for the streamfunction, (3.2.16), where the second term vanishes and we are simply left with an

equation stating that the perturbation vorticity, $-\nabla^2\psi'$, is convected with the mean flow. Thus in this limit we need only solve

$$\nabla^2\psi = -\omega_0(t - x_1/U(x_2), x_2) \quad (3.2.18)$$

for some imposed upstream vorticity field ω_0 .

We can generalise to slightly more complicated background profiles than ones simply satisfying $U''(x_2) = 0$, instead considering piecewise-linear U . Not only does this allow matching with a uniform velocity field at infinity, it allows approximation of more complicated velocity fields by a more mathematically-tractable case. A continuous N -piece profile is given by

$$U(x_2) = U_j + \frac{U_{j+1} - U_j}{\delta_{j+1} - \delta_j} (x_2 - \delta_j) \quad x_2 \in [\delta_j, \delta_{j+1}] \quad (3.2.19)$$

with j ranging from 0 to N , and both $\delta_{j+1} > \delta_j$ and $U_{j+1} > U_j$ (the latter ensuring the background profile is monotonic, though is not essential), see figure 3.3.2 later. We identify $I_j = [\delta_j, \delta_{j+1}]$ and $\sigma_j = (U_{j+1} - U_j)/(\delta_{j+1} - \delta_j)$ the shear in I_j . To ensure the flow is uniform as $x_2 \rightarrow \infty$, we let $\delta_{N+1} = \infty$ and set $\sigma_N = 0$. Finally, we note the convention of using subscript ∞ in place of subscript N where appropriate. This results in a profile with N segments with non-zero shear, matched to an outer uniform region for $x_2 > \delta_\infty$, which can be associated with the δ previously scaled with.

Matching at shear junctions. As suggested above, the localised regions where $U'' \neq 0$, caused by discontinuities in shear, need to be treated with caution. We can either treat this mathematically, with U'' written as a sum of δ -functions and careful integration over them, or by appealing to the underlying physics: both outcomes are the same [33]. As outlined in §2.2.2 we impose continuity of vertical velocity v' and pressure p' across these junctions, essentially stating they are a source of neither momentum or mass respectively. If we define two operators

$$\mathcal{V}^{x_2} = -\frac{\partial}{\partial x_1} \quad (3.2.20a)$$

$$\mathcal{P}_x^{x_2} = \left(\frac{\partial}{\partial t} + U(x_2) \frac{\partial}{\partial x_1} \right) \frac{\partial}{\partial x_2} - U'(x_2) \frac{\partial}{\partial x_1}, \quad (3.2.20b)$$

which when applied to ψ' generated v' and $-(\rho_0^{-1})\partial p/\partial x_1$ respectively. With these operators, and using the streamwise homogeneity of the junction to transfer continuity of p' to

continuity of its streamwise derivative, we can write the conditions at the junctions using the notation in (2.2.11), namely

$$[\mathcal{V}_0^{x_2} \psi']_{\delta_j} = [\mathcal{P}_x^{x_2} \psi']_{\delta_j} = 0. \quad (3.2.21)$$

In the next section, we will transform in both time and the streamwise direction, after which we obtain velocity and pressure operators (this time without the streamwise derivative)

$$\mathcal{V}_{01}^{x_2} = ik_1, \quad (3.2.22a)$$

$$\mathcal{P}_{x01}^{x_2} = \frac{1}{ik_1} \left(C(x_2) \frac{d}{dx_2} - C'(x_2) \right), \quad (3.2.22b)$$

with $C = i(\omega - UK_1)$ the transformed convective operator. The pressure operator is singular for $k_1 = 0$. This is a result of the x_1 -derivative in the definition, which leads to the choice of an arbitrary x_1 -independent constant.

3.3 Analytic solutions in the long-wavelength limit

Exact solutions are permitted in the case of long wavelength and constant shear, where the complete adjoint compressible Rayleigh equation reduces to

$$\frac{d^2\phi}{dx_2^2} + \left[\frac{4C'}{C} \right] \frac{d\phi}{dx_2} - (k_1^2 + k_3^2) \phi = 0, \quad (3.3.1)$$

with $C' = -ik_1 U'$ constant in x_2 and C a simple linear function. This is extended by considering *piecewise* linear shear, matching across discontinuities of U' as outlined above. The resulting solutions can still be written down in terms of elementary functions, though their representation is less simple.

Whilst (3.3.1) doesn't obviously look like it has elementary solutions, we can use the alternative formulation from §3.2 to derive them straightforwardly. A two-dimensional solution has streamfunction satisfying (under streamwise transformation)

$$\left(\frac{d^2}{dx_2^2} - k_1^2 \right) \psi_{01} = 0, \quad (3.3.2)$$

which is equivalent to (3.3.1), and has trivial solutions

$$\psi_{\pm} = \exp(\pm |k_1| x_2), \quad (3.3.3)$$

from which the pressure can be derived as

$$p'_{\pm} \propto [\pm |k_1| C - C'] \exp(\pm |k_1| x_2). \quad (3.3.4)$$

This directly arises from the streamwise component of the momentum equation,

$$\frac{dp'}{dx_1} = -\rho_0 \left[\frac{D_0}{Dt} \frac{\partial \psi}{\partial x_2} - U' \frac{\partial \psi}{\partial x_1} \right]. \quad (3.3.5)$$

Since ϕ is, in this construction, given by $-p'/C^3$, we suppose a generalised solution to (3.3.1)

$$\phi_{\pm} \propto \left(\pm \frac{\kappa}{C^2} - \frac{C'}{C^3} \right) \exp(\pm \kappa x_2) \quad (3.3.6)$$

where $\kappa^2 = k_1^2 + k_3^2$, and the square roots again taken to avoid the real axis. This requires slightly more care, particularly when $k_3 = 0$, than with γ later (see (4.2.12)), with the branch cuts shown schematically in figure 3.3.1 as $k_3 \rightarrow 0$.

It is the long-wavelength limit of γ as $c_0 \rightarrow \infty$. It is straightforward to show the posited ϕ satisfy the differential equation. It is also straightforward to show that the derived pressure, $p' = -(\pm \kappa C - C') \exp(\pm \kappa x_2)$ satisfies (3.2.9), as we would expect. We thus have, for some scaling constant $A(k_1, k_3)$, in a region of constant shear, two solutions for ϕ with derived physical quantities

$$\phi_{\pm} = A \left(\pm \frac{\kappa}{C^2} - \frac{C'}{C^3} \right) \exp(\pm \kappa x_2), \quad (3.3.7a)$$

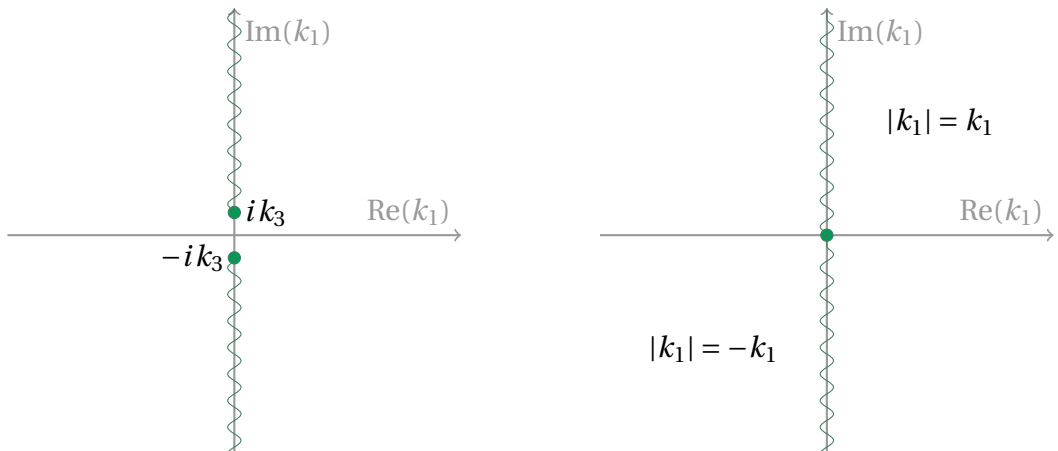
$$p_{\pm} = A (\mp \kappa C + C') \exp(\pm \kappa x_2), \quad (3.3.7b)$$

$$\rho_0 v_{\pm} = A \kappa^2 \exp(\pm \kappa x_2), \quad (3.3.7c)$$

$$\rho_0 u_{\pm} = A \left(i k_1 \left(\mp \kappa + \frac{C'}{C} \right) + \frac{\kappa^2 C'}{i k_1 C} \right) \exp(\pm \kappa x_2), \quad (3.3.7d)$$

$$\rho_0 w_{\pm} = A \left(i k_3 \left(\mp \kappa + \frac{C'}{C} \right) \right) \exp(\pm \kappa x_2). \quad (3.3.7e)$$

The simple forms for the vertical velocity component is as would be expected from the streamfunction representation, with some three-dimensional effects in the other com-



(a) Schematic of branch cut locations of $\sqrt{k_1^2 + k_3^2}$, for non-zero k_3 (assumed positive without loss of generality).

(b) The branch cuts defining $|k_1|$, separating the complex plane into two.

Fig. 3.3.1 Definition of $\kappa = \sqrt{k_1^2 + k_3^2}$ requires specification of the branch cuts associated with branch points (in the k_1 -plane) at $\pm ik_3$, alongside choosing the branch $\kappa = k_1$ along the positive real axis. As with γ later (4.2.12), these are chosen to avoid the real k_1 -axis for non-zero k_3 . When k_3 is zero, this choice of branch cuts is retained, and so $\kappa = \pm k_1$ for $\text{Re}(k_1) \gtrless 0$. This poses difficulties when considering contours passing between the branch points.

ponents from allowing spanwise variation. If the disturbance is purely two-dimensional ($w' = 0$, and no dependence on x_3), we then have a streamfunction

$$\psi_{\pm} = \exp(\pm \kappa x_2), \quad (3.3.7f)$$

arising if we choose $A = ik_1\rho_0/\kappa^2 = -\rho_0/(ik_1)$, and it will often be this quantity used in place of ϕ , as it arises more naturally and has a simpler form.

3.3.1 Matching at shear junctions

Suppose that U' is discontinuous across $x_2 = \chi_2$, for some χ_2 , so that $U = U_0 + \sigma_1(x_2 - \chi_2)$ for $x_2 > \chi_2$ (up to some upper value, that we are not interested in), and $U = U_0 + \sigma_2(x_2 - \chi_2)$ for $x_2 < \chi_2$. Suppose further that we are looking for a specific solution to (the now incompressible) Rayleigh's equation, with

$$\phi = \begin{cases} A_1 e^{-\kappa \chi_2} \phi_+ + B_1 e^{\kappa \chi_2} \phi_- & x_2 > \chi_2 \\ A_2 e^{-\kappa \chi_2} \phi_+ + B_2 e^{\kappa \chi_2} \phi_- & x_2 < \chi_2 \end{cases}, \quad (3.3.8)$$

and we would like to be able to determine A_2 and B_2 in terms of A_1 and B_1 , or *vice versa*.

Since the flow profile has been chosen to be continuous, all we require is imposition of continuity of vertical velocity and of pressure. We identify $C_{1,2} = i(\omega - U_0 k_1)$ (both identical) and $C'_{1,2} = -i\sigma_{1,2}k_1$ (discontinuous) and then the continuity conditions, respectively of v' and p' , become

$$A_1 + B_1 = A_2 + B_2 \quad (3.3.9a)$$

$$(\kappa C_1 - C'_1)A_1 + (-\kappa C_1 - C'_1)B_1 = (\kappa C_2 - C'_2)A_2 + (-\kappa C_2 - C'_2)B_2. \quad (3.3.9b)$$

We can write this in matrix form as $\mathbf{M}_1 \mathbf{A}_1 = \mathbf{M}_2 \mathbf{A}_2$ with $\mathbf{A}_j = (A_j, B_j)$ and the matrices (and their inverses) given by

$$\mathbf{M}_j = \begin{pmatrix} 1 & 1 \\ \kappa C_j - C'_j & -\kappa C_j - C'_j \end{pmatrix}, \quad \mathbf{M}_j^{-1} = \frac{1}{2\kappa C_j} \begin{pmatrix} \kappa C_j + C'_j & 1 \\ \kappa C_j - C'_j & -1 \end{pmatrix}. \quad (3.3.10)$$

With $C_1 = C_2 \equiv C_0$, the product $\mathbf{S}_1 = \mathbf{M}_1^{-1} \mathbf{M}_2$ can be written in terms of a single quantity, Δ , defined as

$$\Delta = \frac{C'_1 - C'_2}{2\kappa C_0} = \frac{k_1(\sigma_2 - \sigma_1)}{2\kappa(\omega - U_0 k_1)} \quad (3.3.11)$$

with

$$\mathbf{S}_1 = \mathbf{M}_1^{-1} \mathbf{M}_2 = \begin{pmatrix} 1 + \Delta & \Delta \\ -\Delta & 1 - \Delta \end{pmatrix}. \quad (3.3.12)$$

A similar expression is obtained for $\mathbf{S}_2 = M_2^{-1} M_1$ via $\Delta \mapsto -\Delta$. With these, we have

$$\mathbf{A}_1 = \mathbf{S}_1 \mathbf{A}_2, \quad (3.3.13a)$$

$$\mathbf{A}_2 = \mathbf{S}_2 \mathbf{A}_1. \quad (3.3.13b)$$

From this we can construct analytic solutions for reasonably complicated, piecewise-linear, background profiles.

3.3.2 Streamfunction for generic N -piece profile

Recall §3.2.4, where defined a generic, piecewise linear, background profile for $x_2 \geq 0$ as

$$U(x_2) = U_j + \sigma_j x_2 \quad (3.3.14)$$

for $x_2 \in I_j = [\delta_j, \delta_{j+1})$, and $I_N = [\delta_N, \infty)$. Here, $(\delta_0, \delta_1, \dots, \delta_N)$ and (U_0, U_1, \dots, U_N) are prescribed parameters, with $\delta_j > \delta_{j-1}$ for all j . This setup is shown in figure 3.3.2, extended to include negative j (which does little to the mathematics, but allows for more general behaviour to be considered). The shear in each layer, σ_j , is chosen to ensure continuity, with

$$\sigma_j = \frac{U_{j+1} - U_j}{\delta_{j+1} - \delta_j} \quad (3.3.15)$$

for $j = 0, 1, \dots, N-1$, with $\sigma_N = 0$. We therefore have a piecewise linear profile with $U(\delta_j) = U_j$ and uniform background flow for $x_2 > \delta_N \equiv \delta_\infty$, where $U(x_2) = U_N \equiv U_\infty$. This can easily be used to approximate more complicated profiles with line segments, though the validity of this approximation is tested in this chapter.

For such a generic profile, we have solutions of the form

$$\psi(x_2) = A_j \psi_+(x_2) + B_j \psi_-(x_2) \quad x_2 \in I_j \quad (3.3.16)$$

with only one pair of A_j and B_j to be prescribed, with the rest derived via the matching formulae above.

We consider three solutions: the decaying solution, the solution with vanishing wall-normal perturbation velocity on $x_2 = 0$, and the solution with vanishing perturbation pressure on $x_2 = 0$. The former requires (with a choice of normalisation) $A_N = 0, B_N = 1$,

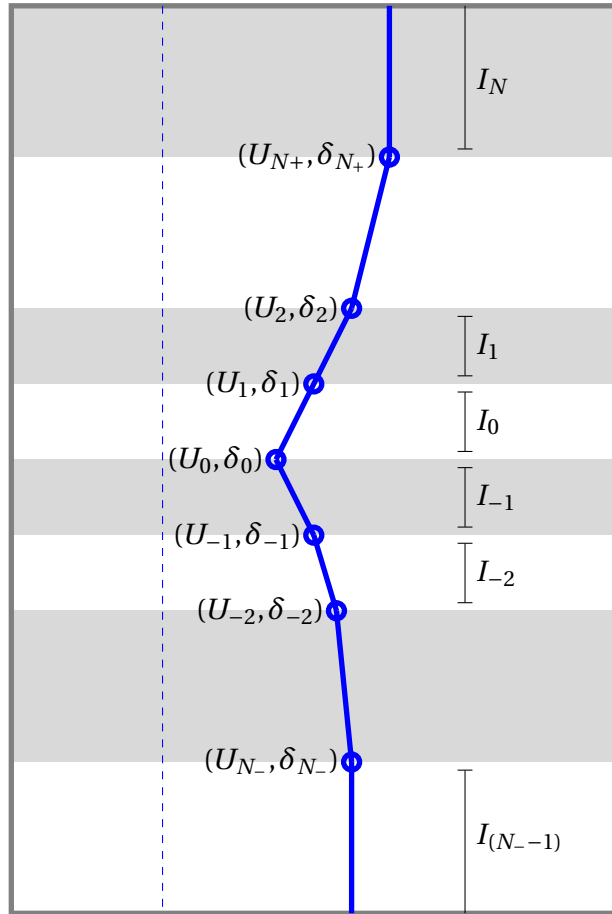


Fig. 3.3.2 A generic piecewise linear profile, with interval I_j and points (U_j, δ_j) as described in the text. In this case, the trivial extension to negative j is included, which will be important for construction of wake solutions later.

and will be denoted ψ_d . The latter two shall be denoted ψ_h (hard-wall) and ψ_p (pressure-release) respectively and we have

$$\psi_h: \quad A_0 = \frac{1}{2\kappa} \quad ; \quad B_0 = -\frac{1}{2\kappa} \quad (3.3.17a)$$

$$\psi_p: \quad A_0 = -\frac{C_0}{2C'_0} - \frac{1}{2\kappa} \quad ; \quad B_0 = -\frac{C_0}{2C'_0} + \frac{1}{2\kappa} \quad (3.3.17b)$$

with $C_0 = i(\omega - U_0 k_1)$ and $C'_0 = -ik_1\sigma_0$. Normalisation has been chosen so that $\psi'_h(x_2 = 0) = 0$ and $\psi_p(x_2 = 0) = -C_0/C'_0$, for reasons explained in later sections.

In some simple cases, it is possible to write down analytic expressions for the complete functions, though for N even reasonably large it only makes sense to compute the coefficients numerically, as the expressions for the case $N = 2$ suggest.

Single piece profile: $N = 1$. This case is completely prescribed by slip velocity U_0 and free-stream velocity U_∞ , with $\delta_0 = 0$ without loss of generality and boundary-layer thickness $\delta_1 = \delta_\infty$, and studied in detail by [96]. For ψ_d , we have

$$A_0 = -\Delta_1 e^{-2\kappa\delta_\infty}, \quad (3.3.18a)$$

$$B_0 = (1 + \Delta_1). \quad (3.3.18b)$$

For ψ_h we have

$$A_1 = \frac{1}{2\kappa} \left(1 + \Delta_1 - \Delta_1 e^{-2\kappa\delta_\infty} \right), \quad (3.3.19a)$$

$$B_1 = \frac{1}{2\kappa} \left(\Delta_1 - 1 - \Delta_1 e^{2\kappa\delta_\infty} \right). \quad (3.3.19b)$$

Finally, for ψ_p we have

$$A_1 = -\frac{1}{2\kappa} \left(1 + \Delta_1 - \Delta_1 e^{-2\kappa\delta_\infty} \right) - \frac{C_0}{2C'_0} \left(1 + \Delta_1 + \Delta_1 e^{-2\kappa\delta_\infty} \right), \quad (3.3.20a)$$

$$B_1 = -\frac{1}{2\kappa} \left(\Delta_1 - 1 - \Delta_1 e^{2\kappa\delta_\infty} \right) - \frac{C_0}{2C'_0} \left(1 - \Delta_1 - \Delta_1 e^{2\kappa\delta_\infty} \right). \quad (3.3.20b)$$

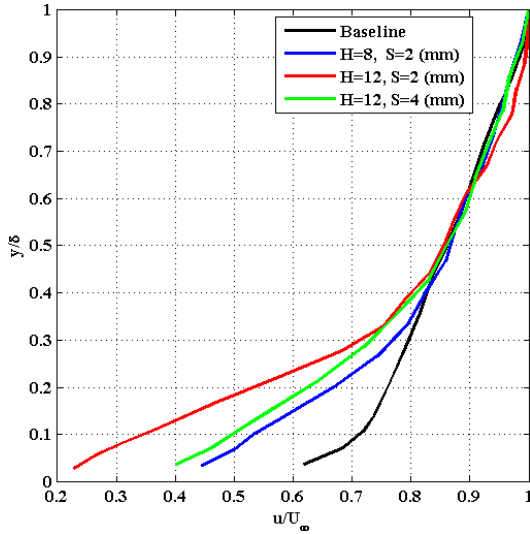
with, in all cases, Δ_1 defined analogously to Δ in the jump conditions derivation, evaluated at $x_2 = \delta_1$, namely

$$\Delta_1 = \frac{C'_1 - C'_0}{2\kappa C_1} = \frac{k_1 \sigma_0}{2\kappa(\omega - U_1 k_1)} \quad (3.3.21)$$

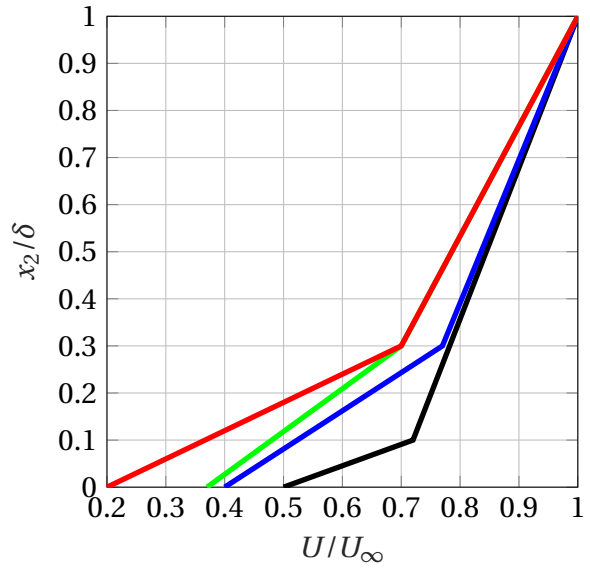
since there is no shear for $x_2 > \delta_1$. This is singular when $k_1 = \omega/U(\delta_1)$, which corresponds to wavelike solutions moving at the free-stream velocity.

Infinite boundary-layer. If we take δ_∞ to infinity, but fix the shear σ_0 , then the decaying solution naturally reduces to $\exp(-\kappa x_2)$ for all x_2 . This gives direct rise to the infinite boundary-layer analysis previously considered by Rienstra and others [92, 93, 90, 101].

Two-piece profile: $N = 2$. It is possible to provide a reasonable approximation to physical boundary-layers, including the effect of a viscous near-wall sublayer in the background profile, via construction of a two-piece background profile. This is demonstrated by comparison with the passive noise control experiments of Afshari et al. [3] in figure 3.3.3.



(a) Figure taken from work of Afshari et al. [3], demonstrating the experimentally observed effect on background flow due to fence-like objects near the trailing edge of an aerofoil.



(b) Demonstration of approximation of the above background profiles as a piecewise linear profile.

Fig. 3.3.3 Boundary-layer data, experimentally measured, suggests a clear division into three regions: the outer, free-stream profile (with constant velocity), an inner layer and a viscous sublayer, with the background flow approximately linear in each. This holds even with some surface treatment, in this case comparing with finlet (or related fence-like structure) measurements.

With $(U_0, U_1, U_2 = U_\infty)$ and $(\delta_0 = 0, \delta_1, \delta_2 = \delta_\infty)$ prescribed, we can do an exactly analogous derivation to the preceding 1-piece section. Note that this does not require monotonicity in the background profile, that is U_j need not be greater or less than U_{j-1} . This allows treatment of inflectional profiles, which will be unstable for some range of frequencies [33]. With A_∞ and B_∞ for the decaying profile unchanged, as are A_0 and B_0 for the hard wall and pressure-release solutions, we can determine the coefficients in the

other regions. For ψ_d , we have

$$A_1 = -\Delta_2 e^{-2\kappa\delta_2}, \quad (3.3.22a)$$

$$B_1 = (1 + \Delta_2), \quad (3.3.22b)$$

$$A_0 = -\Delta_2(1 - \Delta_1)e^{-2\kappa\delta_2} - \Delta_1(1 + \Delta_2)e^{-2\kappa\delta_1}, \quad (3.3.22c)$$

$$B_0 = -\Delta_1\Delta_2 e^{2\kappa(\delta_1 - \delta_2)} + (1 + \Delta_1)(1 + \Delta_2). \quad (3.3.22d)$$

For ψ_h we have

$$2\kappa A_1 = 1 + \Delta_1 - \Delta_1 e^{-2\kappa\delta_1}, \quad (3.3.23a)$$

$$2\kappa B_1 = -(1 - \Delta_1) - \Delta_1 e^{2\kappa\delta_1}, \quad (3.3.23b)$$

$$2\kappa A_2 = (1 + \Delta_1)(1 + \Delta_2) - \Delta_1(1 + \Delta_2)e^{-2\kappa\delta_1} - (1 - \Delta_1)\Delta_2 e^{-2\kappa\delta_2} - \Delta_1\Delta_2 e^{-2\kappa(\delta_2 - \delta_1)}, \quad (3.3.23c)$$

$$2\kappa B_2 = -(1 - \Delta_1)(1 - \Delta_2) - \Delta_1(1 - \Delta_2)e^{2\kappa\delta_1} - (1 + \Delta_1)\Delta_2 e^{2\kappa\delta_2} + \Delta_2\Delta_1 e^{2\kappa(\delta_2 - \delta_1)}. \quad (3.3.23d)$$

The expression for ψ_p is omitted for brevity, but it can be similarly computed. As can be seen, finding analytic expressions for these coefficients rapidly increases in difficulty with the number of pieces involved, though all involve products of Δ_j , $(1 \pm \Delta_j)$ and exponentials of the form $\exp(\pm\kappa\delta_j)$ and, other than scaling factors, no other terms.

3.4 A point source in sheared flow

Now we have determined a variety of ways of solving the long-wavelength limit of the Rayleigh equation, we focus on using these solutions in a specific case: that of a point source at some location in sheared flow, with a disturbance evolving downstream, above some streamwise-homogeneous boundary. We begin by considering the long-wavelength problem allowing treatment of the disturbance within the boundary-layer as incompressible, matched to a compressible (acoustic) outer solution in the free-stream. This section primarily focuses on the *inner* problem: two-dimensional disturbances to piecewise-linear background flow with the governing equations set out in §3.2, slightly extended to take into account a variety of upstream sources, either of mass or momentum at a fixed location in the flow, or more generally a vortex sheet evolving from a fixed location. The next chapter §4 will extend this analysis to the more general case of compressible disturbances to continuously sheared background flow.

3.4.1 Fixed mass or momentum source: Setup

Following RDB [92], we first consider the disturbances produced by a mass or momentum source at some fixed location in the flow. This is done most readily by returning to the (alternative) derivation of the governing equation for the streamfunction in the inner region (see §3.2) and introducing source terms on the right-hand side of the mass and momentum equations, namely

$$\rho \nabla \cdot \mathbf{u} = q, \quad (3.4.1a)$$

$$\rho \frac{D\mathbf{u}}{Dt} + \nabla p = \mathbf{f}. \quad (3.4.1b)$$

The mass source q and momentum source \mathbf{f} are potentially functions of time and space (both per unit volume). If $\rho = \rho(p)$ alone, as we expect under the earlier assumption of an isotropic fluid, then $\nabla p \times \nabla \rho = 0$. Then, upon taking the curl of the momentum equation (3.4.1b) and substituting in (3.4.1a), gives the vorticity equation with source terms:

$$\frac{D\boldsymbol{\omega}}{Dt} - \boldsymbol{\omega} \cdot \nabla \mathbf{u} = \nabla \times \left(\frac{\mathbf{f}}{\rho} \right) - \boldsymbol{\omega} \frac{q}{\rho}. \quad (3.4.2)$$

Linearisation of a two-dimensional disturbance to parallel base flow $U(x_2)\mathbf{e}_1$, as before, gives

$$\frac{D_0\omega'}{Dt} - u'_2 U''(x_2) = \frac{\partial}{\partial x_1} \left(\frac{f_2}{\rho} \right) - \frac{\partial}{\partial x_2} \left(\frac{f_1}{\rho} \right) + \frac{U'q}{\rho} \quad (3.4.3)$$

where we have assumed the mass and momentum source are the same order of magnitude as the perturbation. For an N -piece piecewise linear flow, $U'' = 0$ (or, more generally, $U'' = \sum_{j=1}^N \delta(x_2 - x_{2j})$, with junctions at x_{2j}) and so almost everywhere

$$\frac{D_0}{Dt} \nabla^2 \psi' = F(t, \mathbf{x}) \quad (3.4.4)$$

with $F(t, \mathbf{x}) = -U'q/\rho - (\nabla \times \mathbf{f}/\rho)_3$. We consider a time-harmonic mass source², of strength q_0 , concentrated at fixed location $(0, y_2)$, so that

$$\left(i\omega + U \frac{\partial}{\partial x_1} \right) \nabla^2 \psi'_0 = - \frac{U'(y_2)q_0}{\rho(y_2)} \delta(x_1) \delta(x_2 - y_2) \quad (3.4.5)$$

²Subscript 0 here denoting the (implicit) temporal Fourier transformation

which integrates to give

$$\nabla^2 \psi'_0 = -\frac{U'(y_2)q_0}{U(y_2)\rho(y_2)} \delta(x_2 - y_2) H(x_1) \exp(-i\kappa_1(y_2)x_1). \quad (3.4.6)$$

The vorticity is confined to a line along $x_2 = y_2$, beginning at $x_1 = 0$. The integration has been done so that the perturbation vorticity vanishes upstream of the source, so that the disturbance entirely consists of terms radiating away from the source.

This is the first appearance of the convection wavenumber

$$\kappa_1(y_2) = \frac{\omega}{U(y_2)}. \quad (3.4.7)$$

This is the streamwise wavenumber of a vortical disturbance propagating at the background flow speed, $U_c = U(y_2)$, which is lower than the free-stream velocity U_∞ for a monotonic boundary-layer type background flow. If the background flow is instead a jet near a wall, this convection velocity (related to the jet velocity) will exceed the free-stream velocity.

If ω is complex (with non-zero imaginary part), the argument of κ_1 is the same as the argument of ω . This allows streamwise Fourier transformation of both sides of (3.4.6) provided $\text{Im}(\omega) < 0$, an assumption that can later be relaxed to consistently define the Fourier transformation of the Heaviside function. Streamwise transformation of (3.4.6), under this assumption on ω , then gives

$$\left(\frac{d^2}{dx_2^2} - k_1^2 \right) \psi_{01} = -\frac{U'(y_2)q_0}{U(y_2)\rho(y_2)} \delta(x_2 - y_2) \frac{1}{i(k_1 - \kappa_1)}. \quad (3.4.8)$$

We couple this equation with jump conditions at shear junctions, which upon Fourier transformation are continuity of

$$\mathcal{V}_{01}^{x_2} \psi_{01} = i k_1 \psi_{01}(x_2), \quad (3.4.9a)$$

$$\mathcal{P}_x^{x_2} \psi_{01} = C(x_2) \psi'_{01}(x_2) - C'(x_2) \psi_{01}(x_2). \quad (3.4.9b)$$

The coupling of the transformed Laplacian and these jump conditions is exactly equivalent to choosing solutions derived in the previous section, §3.3, where construction of the streamfunction solution, with matching across boundaries, has been carefully performed.

The radiation condition translates to $\psi_{01} \rightarrow 0$ as $x_2 \rightarrow \infty$. If a wake is being considered, we also require $\psi_{01} \rightarrow 0$ as $x_2 \rightarrow -\infty$. Finally, we impose boundary conditions on $x_2 = 0$.

Generalising across hard-wall, pressure-release and impedance boundary conditions, we suppose the streamwise-temporal transformation of the boundary condition can be written in terms of some linear operator $\mathcal{L}_{01}(\omega, k_1)$, with ψ_{01} satisfying

$$\mathcal{L}_{01}\psi_{01} = 0 \quad (3.4.10)$$

on $x_2 = 0$, the wake case requiring separate consideration. Since ψ''_{01} is known in terms of ψ_{01} and ψ'_{01} , without loss of generality this condition is

$$\ell_1(\omega, k_1)\psi'_{01} + \ell_2(\omega, k_1)\psi_{01} = 0 \quad (3.4.11)$$

for some ℓ_j ($j = 1, 2$).

For the cases of interest, we choose the operators (with a degree of normalisation) as shown in table 3.1. The normalisation is chosen (fixing $\ell_2 = 1$) so that the limits of $Z \rightarrow 0$ and $Z \rightarrow \infty$ reproduce the pressure-release and hard-wall operators, respectively. Care must be taken with the seemingly free division through by k_1 , particularly at $k_1 = 0$, where ℓ_1 has a pole in both the pressure-release and impedance cases (corresponding to some choice of integration constant in the solution).

Boundary condition	Operator	ℓ_1	ℓ_2
No-penetration	\mathcal{V}	0	1
Pressure-release	\mathcal{P}	$-\frac{C}{C'}$	1
Impedance	\mathcal{L}^Z	$\frac{C^2}{i\omega Z k_1^2 - C'C}$	1

Table 3.1 Boundary conditions operators being considered, with normalisation. \mathcal{L}^Z is the formulation of the Myers boundary condition in this framework.

3.4.2 Auxiliary functions and the general solution for arbitrary (linear) boundary conditions

As per §3.3, the solution space of the differential equation

$$\left(\frac{d^2}{dx_2^2} - k_1^2 \right) \psi_{01} = 0, \quad (3.4.12)$$

coupled with the relevant jump conditions, is spanned by any two linearly-independent solutions which can be found analytically. For solution of the problem of interest, we

choose two specific solutions: the decaying solution and the solution that satisfies the boundary conditions of interest on $x_2 = 0$. Explicitly, we normalise the decaying solution ψ_d such that

$$\psi_d(x_2) = \exp(-|\kappa_1|x_2) \quad x_2 > \delta_\infty, \quad (3.4.13)$$

and we choose the wall solution ψ_ℓ satisfying

$$\mathcal{L}_{01}\psi_\ell = 0 \quad x_2 = 0. \quad (3.4.14)$$

There still remains a single degree of freedom in normalising this function, which will be exploited later. Methods for explicitly writing down these auxiliary functions were found in §3.3, utilising the fact that it is straightforward to solve (3.4.12) analytically, with difficulty arising only from the matching conditions.

In terms of these functions, the solution to (3.4.8) is

$$\psi_{01}(x_2) = -\frac{U'(y_2)q_0}{U(y_2)\rho(y_2)} \frac{1}{i(k_1 - \kappa_1)} \frac{1}{W(y_2)} \times \begin{cases} \psi_d(x_2)\psi_\ell(y_2) & x_2 > y_2 \\ \psi_\ell(x_2)\psi_d(y_2) & x_2 < y_2 \end{cases}. \quad (3.4.15)$$

The Wronskian $W = \psi'_d\psi_\ell - \psi'_\ell\psi_d$ ensures the jump in derivative across $x_2 = y_2$ is as expected (due to the δ function). Further, W is independent of its x_2 (due to the lack of first x_2 -derivative in (3.4.12)) and can thus be evaluated at any point. Evaluating at $x_2 = 0$, where we recall $\ell_1\psi'_\ell + \ell_2\psi_\ell = 0$, we have

$$W(0) = \frac{\psi_\ell}{\ell_1} (\ell_1\psi'_d + \ell_2\psi_d) = \frac{\psi_\ell}{\ell_1} \mathcal{L}_{01}\psi_d, \quad (3.4.16)$$

with all functions evaluated at $x_2 = 0$. There is a degree of freedom with ψ_ℓ , and thus we choose $\psi_\ell(0) = \ell_1$. We now define the dispersion function for this boundary condition, $D_\ell(\omega, k_1)$, to be precisely the remaining part:

$$D_\ell = \mathcal{L}_{01}\psi_d(x_2 = 0). \quad (3.4.17)$$

Zeros of this function correspond to solutions to the differential equation that satisfy the boundary conditions at both ∞ and at 0 . Whilst these generally don't exist, or are trivial, for uniform flow, the presence of the boundary layer enriches the behaviour of the

dispersion function. The solution for ψ_0 is then

$$\psi_0(x_1, x_2) = -\frac{1}{2\pi i} \frac{U'(y_2) q_0}{U(y_2) \rho(y_2)} \int_{F_1} \frac{\psi_{\geq}(x_2; k_1) \psi_{\leq}(y_2; k_1)}{D_\ell(k_1)} \frac{e^{-ik_1 x_1}}{(k_1 - \kappa_1)} dk_1. \quad (3.4.18)$$

The notation ψ_{\geq} is used to make the above expression more compact, with $\psi_{\geq}(x_2; k_1) = \psi_d(x_2; k_1)$ for $x_2 > y_2$ and $\psi_\ell(x_2; k_1)$ for $x_2 < y_2$, with the converse applying for ψ_{\leq} .

The inversion contour F_1 is the real axis provided $\text{Im}(\omega)$ is suitably negative, so that spatial causality is correctly captured. As ω is relaxed to the real axis, the contour must be deformed so that all upstream poles (zeros of either D_ℓ or $k_1 - \kappa_1$) lie beneath the integration contour, as discussed in §2.1.

By considering explicit boundary conditions in the following sections, it will be demonstrated how the inversion contour can be deformed to reduce numerical complexity, with propagating solutions separated from components of the solution that decay away from the source. Further, the inversion above assumes suitable behaviour of the integrand which may not always hold, particularly at $k_1 = 0$. This typically relates to the specification of an arbitrary constant, which must be consistently dealt with. This is discussed in the sections on pressure-release and impedance solutions in §3.6.

Unlike the infinite shear case considered in RDB [92], the inversion integration is typically not analytically tractable, at least if an analytic solution that is practical to manipulate is looked for. With this in mind, methods of numerical evaluation of complex integrals are discussed in appendix §A.2.1. Further, the related problem of finding poles and zeros of complex functions numerically, and thereby the wavenumbers of modal solutions, is discussed in appendix §A.2.2.

3.4.3 Preliminaries: towards an analytic solution

As we shall see, the long-wavelength, quasi-incompressible formulation runs into difficulties when $k_1 = 0$, where the integrand may well be singular. We shall explicitly demonstrate this via computation of the integrand of (3.4.15) in the case of a constant-shear boundary-layer with finite thickness δ . In particular, we focus on the case with the source within the boundary-layer ($y_2 < \delta$) and compute the solution outside the boundary-layer $x_2 > \delta$. We are then interested in determination of the kernel of the Fourier inversion in (3.4.18), I_ℓ , defined as

$$I_\ell = \frac{\psi_d(x_2; k_1) \psi_\ell(y_2; k_1)}{D_\ell(k_1)(k_1 - \kappa_1)}. \quad (3.4.19)$$

In turn we will find the inverse Fourier transform of this quantity. By construction, $\phi_d = \exp(-\kappa x_2)$, with $\kappa = |k_1|$. We consider two cases: hard-wall and pressure release, and

indicate an important difference. For the hard-wall case, we have (from §3.3, rewritten)

$$\psi_h(y_2) = \frac{\sinh(\kappa y_2)}{\kappa}, \quad (3.4.20)$$

$$D_h = A_0 + B_0 = (1 + \Delta) - \Delta e^{-2\kappa\delta_1}, \quad (3.4.21)$$

with $\Delta = -k_1\sigma_0/(\omega - U_1 k_1)$. The hard-wall integrand is then

$$I_h = \frac{e^{-\kappa x_2} \sinh(\kappa y_2)(\omega - U_1 k_1)}{\kappa(k_1 - \kappa_1)((\omega - U_1 k_1) + k_1\sigma_0 - k_1\sigma_0 e^{-2\kappa\delta_1})}. \quad (3.4.22)$$

Similarly, for the pressure-release problem (so that $p' = 0$ on $x_2 = 0$) we have

$$\psi_p(y_2) = -\frac{\sinh(\kappa y_2)}{\kappa} - \frac{C_0 \cosh(\kappa y_2)}{C'_0}, \quad (3.4.23)$$

$$D_p = (A_0 + B_0) + \kappa\ell_1(A_0 - B_0) = \left((1 + \Delta) - \Delta e^{-2\kappa\delta_1} \right) + \frac{\kappa C_0}{C'_0} \left((1 + \Delta) + \Delta e^{-2\kappa\delta_1} \right). \quad (3.4.24)$$

again allowing explicit expression of the inversion kernel

$$I_p = \frac{-e^{-\kappa x_2}(\omega - U_1 k_1) \left[C'_0 \sinh(\kappa y_2) + \kappa \cosh(\kappa y_2) \right]}{\kappa(k_1 - \kappa_1) \left[C'_0 ((\omega - U_1 k_1) + k_1\sigma_0(1 - e^{-2\kappa\delta_1})) + \kappa C_0 ((\omega - U_1 k_1) + k_1\sigma_0(1 + e^{-2\kappa\delta_1})) \right]}. \quad (3.4.25)$$

D_p is non-singular, albeit discontinuous, at $k_1 = 0$. An issue arises, however, in ψ_p . When $k_1 \rightarrow 0$, the second term of (3.4.24) behaves as $1/k_1$, since $C'_0 = -i\sigma_0 k_1$ and $\cosh(\kappa y_2) \rightarrow 1$. With this singularity trapped between the two branch points of κ , the inversion contour must pass through this point and as such there seems to be no way of inverse Fourier transforming this quantity. This can be dealt with by looking at the transformation of the Heaviside function, as per RDB [92].

We can take a slightly different approach here. This singularity essentially corresponds to the choice of an arbitrary constant, and should also appear in the hard-wall solution, too, as in neither case does the imposition of either a pressure-release or zero-velocity boundary condition determine what, arbitrary, value of streamfunction ψ can be added to the solution. That it vanishes in the hard-wall case follows from the imposition of vanishing streamfunction, rather than vanishing vertical velocity, on the wall $x_2 = 0$. This fixes this choice of constant by imposing that $\psi \rightarrow 0$ downstream. With the boundary no longer a (perturbation) streamline in the pressure-release case, we cannot make this assumption, and we cannot impose a value of ψ on $x_2 = 0$ *a priori*. However, it is worth noting that *physical* quantities – the vertical velocity and pressure – arising from application

of the velocity and pressure operators \mathcal{V}_{01}^0 and \mathcal{P}_{01}^0 remove the singularity at $k_1 = 0$ when applied to ψ_p . This is not purely fortune: the boundary conditions and causality impose vanishing pressure in the far-field and far upstream, as well as along the wall $x_2 = 0$, enough to remove any ambiguity (analogously to the streamfunction in the hard-wall case). With this subtle observation, we expect we cannot compute ψ_{0p} , though the resulting physical quantities v'_{0p} and p'_{0p} are well-defined.

This appears to be the limit of analytical progress, and any further inversions will require numerical integration. It is worth noting that the solution of RDB [92], with disturbances to infinitely sheared flow, naturally arises as we send $\delta \rightarrow \infty$, a setup that permits analytic solutions in terms of the exponential integral.

3.4.4 Explicit choice of piecewise linear background profiles

Whilst the results in §3.4.1 are general, it is useful to demonstrate the analysis on a specific choice of piecewise-linear background profiles. We consider a pair of piecewise-linear background profiles defined above the wall, and a profile valid for all $x_2 \in (-\infty, \infty)$ which will be used to investigate the effect of asymmetry on the wake. The flow fields are given by the expression (3.3.14): essentially a series of straight-line segments such that $U(\delta_j) = U_j$ with j running from 0 to N . The outer segment corresponding to $j = N$ corresponds to uniform flow beyond the region of shear, and the corresponding location δ_N and (constant) flow speed U_N will be denoted, consistent with earlier derivations, as δ_∞ and U_∞ , the boundary-layer thickness and free-stream velocity respectively, to emphasise this fact.

I. Variation of wall-shear With motivation from the effect of the boundary-layer by both active and passive noise control devices, a two-piece linear profile is investigated. The symmetric case is initially considered, with flow chosen so that $U_1 = 0.8$ and $\delta_1 = 0.2$, matching to a uniform flow with $U_\infty = 1$ at $\delta_\infty = 1$. We allow U_0 , the slip-velocity directly above the plate, to vary (see figure 3.4.1a). Variation of the slip velocity also modifies the shear $\sigma_0 = (U_1 - U_0)/\delta_1$. The effect of variation of this internal shear is investigated. This could provide a model for physically realistic boundary-layers [4], see figure 3.3.3.

II. Approximation of parabolic profile We have an arbitrary choice of N , which allows close approximation to profiles with $U'' \neq 0$. We demonstrate this by approximating the parabolic, slipping, profile

$$U(x_2) = 1 - (1 - U_0)(x_2 - 1)^2 \quad (3.4.26)$$

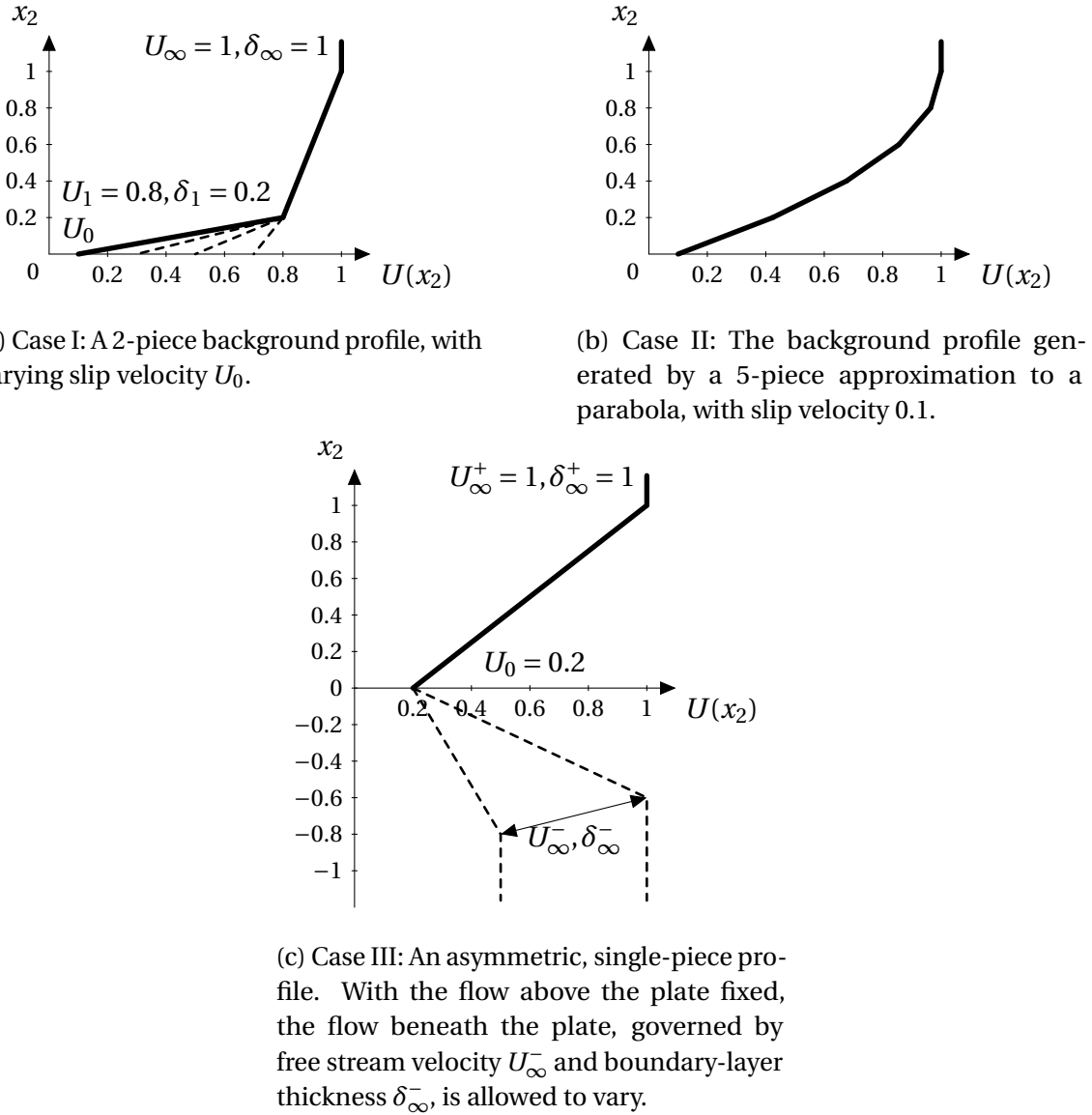


Fig. 3.4.1 The three background profiles considered throughout §3.

for $x_2 < 1$. This has slip velocity $U(0) = U_0$, by construction. By letting $\delta_j = j/N$ and $U_j = U(\delta_j)$, we obtain a N -piece approximation to this profile, in terms of linear pieces. Increasing N leads to richer behaviour of the dispersion functions, which makes certain facets of noise generation clearer. Here, we shall primarily consider the case $N = 5$, fixing $U_0 = 0.1$, as shown in figure 3.4.1b.

III. Wake asymmetry This model allows consideration of an asymmetric profile. With this in mind, we consider a pair of single-piece profiles, above and below $x_2 = 0$. This gives three parameters that can be varied – the slip velocity U_0 (which is assumed the same above and below the plate, as continuity across the wake is required), as well as the boundary-layer thickness below the plate, δ^- , and the free-stream velocity below the plate U_∞^- . For precision, we fix $U_0 = 0.2$ and allow the other two parameters to vary, shown in figure 3.4.1c.

3.5 Fixed mass or momentum source: Hard-wall

The hard-wall case is the most straightforward to consider, with fewer issues of stability to worry about. As well as physically being the most important case, considering for example a point source above the surface of a rigid aerofoil, it allows illustration of the numerical methods which will be used in the more complicated lined cases in the next section, §3.6. The hard-wall case arises from setting $\mathcal{L}_{01}^h = \mathcal{V}_{01}^0$, so that $\ell_1 = 0$ and $\ell_2 = ik_1$. However, we can simplify further by instead letting

$$\mathcal{L}_{01}^h \psi = \psi \quad (3.5.1)$$

so that $\ell_2 = 1$. This has been alluded to in both §3.3 and in §3.4.1, and is equivalent to, instead of insisting that $v' = 0$ on $x_2 = 0$, that $x_2 = 0$ corresponds to the streamline $\psi = 0$. This fixes a choice of arbitrary constant in ψ , however it is valid as there is nothing stopping the imposition that $\psi \rightarrow 0$ as $x_1 \rightarrow -\infty$, since there is no perturbation far upstream. This choice eliminates difficulties that arise at $k_1 = 0$. With this, we have ψ_h the auxiliary function that vanishes on $x_2 = 0$, with $\psi'_h(x_2 = 0) = 1$ replicating the normalisation that lead to (3.4.17). We label the corresponding dispersion function $D_\ell \rightarrow D_h$, explicitly

$$D_h(\omega, k_1) = \psi_d(0; \omega, k_1) \quad (3.5.2)$$

3.5.1 The dispersion function

The inversion integral (3.4.18) depends on the behaviour of (the reciprocal of) D_h , and thus a thorough understanding of this function, in the complex k_1 -plane, is required. For the 5-piece case II above, the behaviour of D_h is plotted in the complex plane in Figure 3.5.1. As can be seen, there is a branch cut along the imaginary axis (a discontinuity of phase, i.e. colour), which comes immediately from the $|k_1|$ permeating the derivation of ϕ_d , though the branch point at the origin is in a sense “weak”, with $D_h(0, \omega)$ well-defined and non-zero. More interestingly are the poles and zeros of D_h (correspondingly the zeros and poles of its reciprocal).

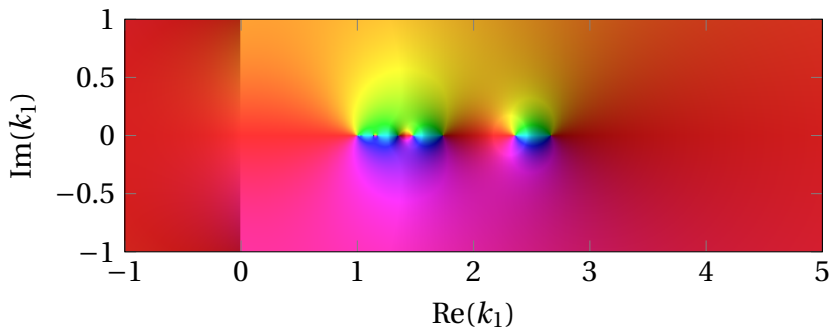


Fig. 3.5.1 A phase plot of the hard-wall dispersion function for a 5-piece parabolic approximation (type 2) with $U_0 = 0.1$ and $\omega = 1$. Colour represents complex argument, showing a sequence of alternating poles and zeros along the real axis. Brighter colours indicate larger magnitude, and as such can be used to distinguish the poles and zeros.

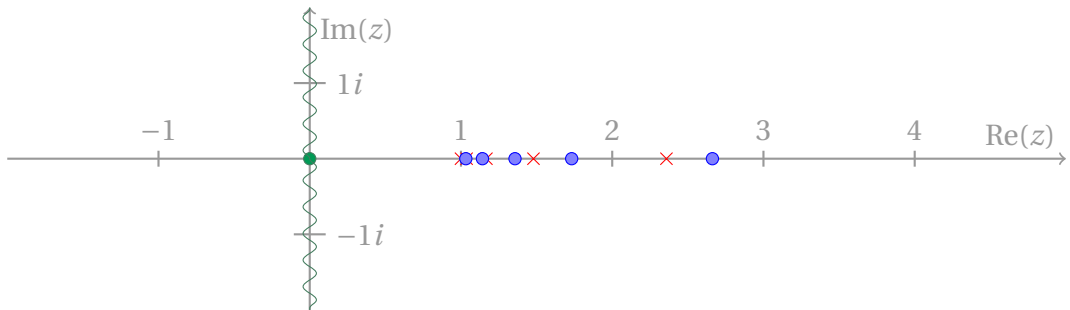


Fig. 3.5.2 Schematic representation of the zeros (o) and poles (x) of the hard-wall dispersion function $D_h(k_1, 1)$, with the branch cut along the imaginary axis shown, in case II with $N = 5$. There are N poles and N zeros, and they alternate, which consistently holds provided the jump in shear is always negative (equivalent to $U'' \leq 0$).

D_h has N poles at $k_1 = \omega/U_j$, for $j = 1, \dots, N$. This is because the continuity conditions applied to the velocity and to the pressure are inconsistent at $x_2 = \delta_j$ for these k_1 , requiring

both ϕ and $U'\phi$ to be continuous. It is practical and straightforward to remove these poles by defining a *reduced* dispersion function

$$\bar{D}_h(k_1, \omega) = R(k_1, \omega) D_h(k_1, \omega) \quad (3.5.3)$$

with

$$R(k_1, \omega) = \prod_{j=1}^N \left(k_1 - \omega/U_j \right). \quad (3.5.4)$$

The resulting dispersion function is analytic everywhere in the complex plane, away from the branch cuts along the imaginary axis.

For small k_1 , the jump conditions simply reduce to continuity of ϕ and ϕ' , with the condition of continuity of pressure being asymptotically unaffected by the jump in shear and as such the decaying solution reduces to $\exp(-\kappa x_2)$ as in the uniform case, and $D_h(k_1) \rightarrow 0$ as $k_1 \rightarrow 0$.

A similar argument can be made for large k_1 . With all solutions the summation of terms like $\exp(\pm |k_1| x_2)$, the $+$ -term dominates for large k_1 and therefore the derivative $\psi' \sim |k_1| \psi$, which indicates ψ' and ψ must be continuous as above. This can be determined alternatively by directly considering the analytic expressions for $A_0 + B_0$ as $k_1 \rightarrow \infty$. Due to the exponential decay of most terms in the matching formulae, we have

$$D_h \sim B_0 \sim (1 + \Delta_1)(1 + \Delta_2)\dots(1 + \Delta_N) \quad (3.5.5)$$

and all Δ decay (as $1/k_1$) in the limit $k_1 \rightarrow \infty$. The above approximation is very good for a large range of k_1 , due to the exponential decay of all other terms as k_1 increases.

Finally, and most interestingly, there are zeros of D_h , roots of the dispersion relation $D_h = 0$. These contribute to the downstream Fourier inversion of the mass source, and thus a complete understanding of them is desirable. Typically there are as many of these zeros as poles, a claim discussed in the appendix, §A.1. These correspond to disturbances convected with the flow. Provided the flow profile is concave, that is the shear in each layer decreases with x_2 , these are real for real ω and are thus neutrally stable, essentially an application of Rayleigh's stability criterion, that a non-inflecting, parallel incompressible flow is stable [33]. The poles and zeros for case II (a parabolic approximation), with $U_0 = 0.1$ and $N = 5$, are shown schematically Figure 3.5.2.

3.5.2 Fourier inversion

Whilst analytic expressions for all terms in (3.4.18) can be determined, inversion of the Fourier transform evades closed-form evaluation in anything but the most simple cases. In practice, it is done numerically. We recall that the Fourier transforms are defined only for ω with negative imaginary part, so that transforms of, for example, the Heaviside function exist. However, if we relax $\text{Im}(\omega) \rightarrow 0$ and deform the Fourier inversion contour so that there is no large change to the behaviour of the solution, we have an integral solution that is valid even for real ω , displayed in Figure 3.5.3.

To invert, we deform the inversion contour onto the branch cuts, or more generally into the upper and lower half planes for x_1 respectively less than or greater than 0, shown schematically in figure 3.5.4. This allows the integral to be decomposed into a rapidly spatially decaying integral and a sum of residual contributions from poles, which correspond to roots of the dispersion relation (and of the Cauchy-type kernel). Recall (3.4.18), defining $Q(y_2) = q_0 U'(y_2)/(U(y_2)\rho(y_2))$. For the hard-wall case we have

$$\psi_0(x_1, x_2) = -\frac{Q(y_2)}{2\pi i} \int_{F_1} \Psi(k_1) e^{-ik_1 x_1} dk_1, \quad (3.5.6)$$

where the Fourier transformed function $\Psi(k_1) = \psi_{01}(k_1)$ is

$$\Psi(k_1) = \frac{\psi_{\gtrless}(x_2; k_1) \psi_{\lessgtr}(y_2; k_1)}{D_h(k_1)} \frac{1}{(k_1 - \kappa_1)}, \quad (3.5.7)$$

for $x_2 \gtrless y_2$, with $\psi_> = \psi_d$ and $\psi_< = \psi_h$. Deforming F_1 off the real axis, onto branch-cut contours $C_{U,L}$ in the upper- and lower-half complex planes (as per figure 3.5.4), respectively, allows this to be written as

$$\psi_0(x_1, x_2) = -\frac{Q}{2\pi i} \int_{C_U} \Psi(k_1) e^{-ik_1 x_1} dk_1 \quad (3.5.8)$$

for $x_1 < 0$, for which there are no pole contributions (for $U > 0$). For $x_1 > 0$, we have

$$\psi_0(x_1, x_2) = -\frac{Q}{2\pi i} \int_{C_L} \Psi(k_1) e^{-ik_1 x_1} dk_1 + Q \left[\sum_{j=1}^N \text{Res}_{\Psi}(k_{1j}) e^{-ik_{1j} x_1} + \text{Res}_{\Psi}(\kappa_1) e^{-i\kappa_1 x_1} \right]. \quad (3.5.9)$$

The residue of f at a (simple³) pole a defined in the usual way as $\text{Res}_f(a) = \lim_{z \rightarrow a} (z - a)f(z)$. The zeros of the dispersion relation k_{1j} give rise to a selection of neutrally stable

³Poles of the integrand, or zeros of the dispersion relationship, are assumed to be simple. This will be true unless the parameter are chosen such that two poles are coincident, which occurs at the boundaries of stability.

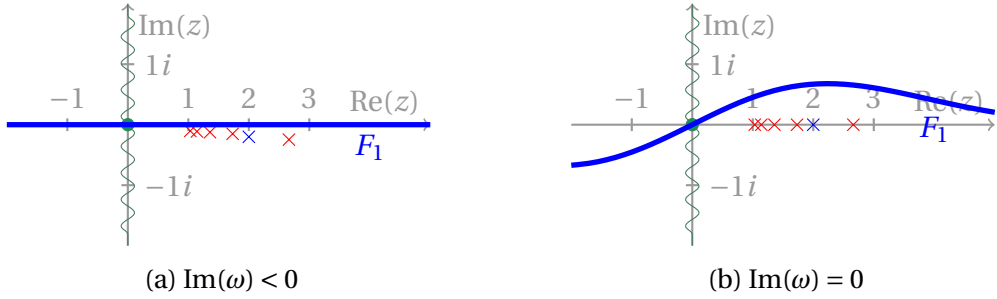


Fig. 3.5.3 Deformation of the Fourier inversion contour F_1 as $\text{Im}(\omega) \rightarrow 0$. Explicit data taken from profile II with $U_0 = 0.1$ and $N = 5$. The modes (both convected, red, and vortex shedding, blue) move onto the real axis and the contour is deformed so that they remain on the same side of the contour.

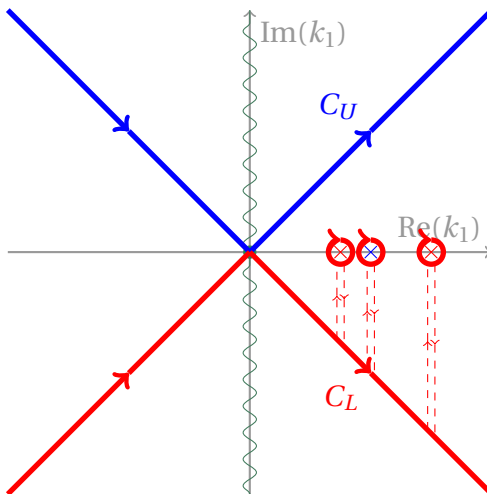


Fig. 3.5.4 Deformation to $C_{U,L}$ contours in the upper- and lower-half k_1 plane respectively, with pole contributions (here schematically shown as a pair of modal solutions, red, and the single trailing vorticity solution, blue) picked up when deforming into the lower-half plane. Deformation onto C_U occurs for negative x_1 , and onto C_L for positive x_1 (typically, for $U > 0$, the only time residual contributions are picked up). The angle of these contours can be chosen so that the integrand decays exponentially along them, without oscillating, as shall be seen when computing far-field sound in figure 3.5.7, with these “branch-cut” contours dominating the integral and leading to radiated sound.

spatially-harmonic modes, provided $\text{Im}(k_1) = 0$ (which they do if U is concave). The Residue at the Cauchy-type mode, with $k_1 = \kappa_1$, can be written down as

$$\text{Res}_\Psi(\kappa_1) = \frac{\psi_{\gtrless}(x_2; \kappa_1)\psi_{\lessgtr}(y_2; \kappa_1)}{D_h(\kappa_1)} \quad (3.5.10)$$

and is the direct response to the vortex sheet trailing behind the point source. The modal solutions at $k_1 = k_{1j}$ arise through the interaction of this solution and the boundaries, and we define the j th convective mode to be

$$M_j(x_1, x_2) = \text{Res}_\Psi(k_{1j})e^{-ik_{1j}x_1} \quad (3.5.11)$$

Numerical computation of the branch cut component, coupled with the residual modal contributions, gives a solution continuous across $x_1 = 0$, as shown in figure 3.5.5 for a 5-piece parabolic profile as per case II (exactly the case in figure 3.4.1b). A clear vortex sheet downstream of the source at $(0, 0.3)$ is visible, with the contribution of convective modes becoming more apparent downstream. The behaviour of these modes, and their dependence on the flow parameters, is discussed below.

3.5.3 Branch cut contribution: Matching to radiating acoustic outer solution

As shown in figure 3.5.6, the branch cut contributions (from C_U and C_L) decay away from the source location. It is possible to quantify this decay by considering the large $|x|$ behaviour of the integral, and in turn match this to a radiating acoustic solution outside the boundary layer. Outside the boundary layer $\psi_d = \exp(-|k_1|x_2)$ by construction, and hence the branch cut integral (which shall be denoted by ψ_{BC}) becomes

$$\psi_{BC} = -\frac{Q}{2\pi i} \int_{C_{U,L}} \frac{\psi_h(y_2; k_1)}{D_h(k_1)(k_1 - \kappa_1)} \exp(-|k_1|x_2 - ik_1 x_1) dk_1. \quad (3.5.12)$$

We deform to the steepest descent contour (trivial in this case) for which the imaginary part of the exponent is constant. Introducing $z = x_1 + ix_2$, we integrate along rays from the k_1 origin as shown in figure 3.5.7, making an angle of $\arg(z) - \pi/2$ to the real axis. We define the kernel of the integral

$$I(k_1) = -\frac{Q}{2\pi i} \frac{\psi_h(y_2; k_1)}{D_h(k_1)(k_1 - \kappa_1)}. \quad (3.5.13)$$

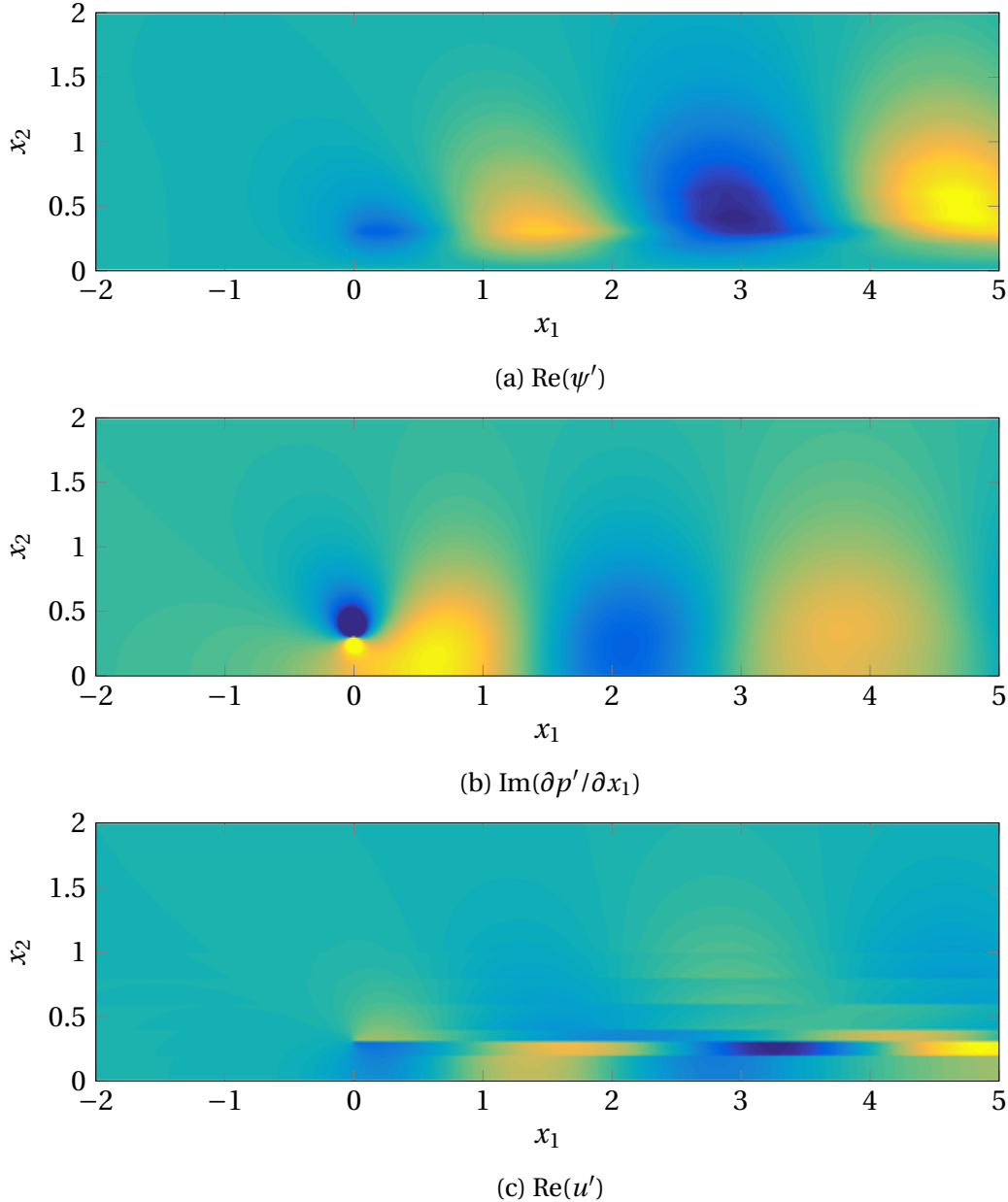


Fig. 3.5.5 For a 5-piece approximation to a parabolic background profile (with slip velocity 0.1), the behaviour of long-wavelength disturbances to a harmonic point source, with $\omega = 1$, at $x_2 = 0.3$, above a hard-wall, is shown. All lengths and speeds normalised on free-stream velocity and boundary-layer thickness. Each plot shows the strength of the hydrodynamic quantity listed at $t = 0$. The streamwise perturbation displays discontinuities at discontinuities of background shear, which naturally arises with no viscosity to smooth out perturbations across a background vortex sheet.

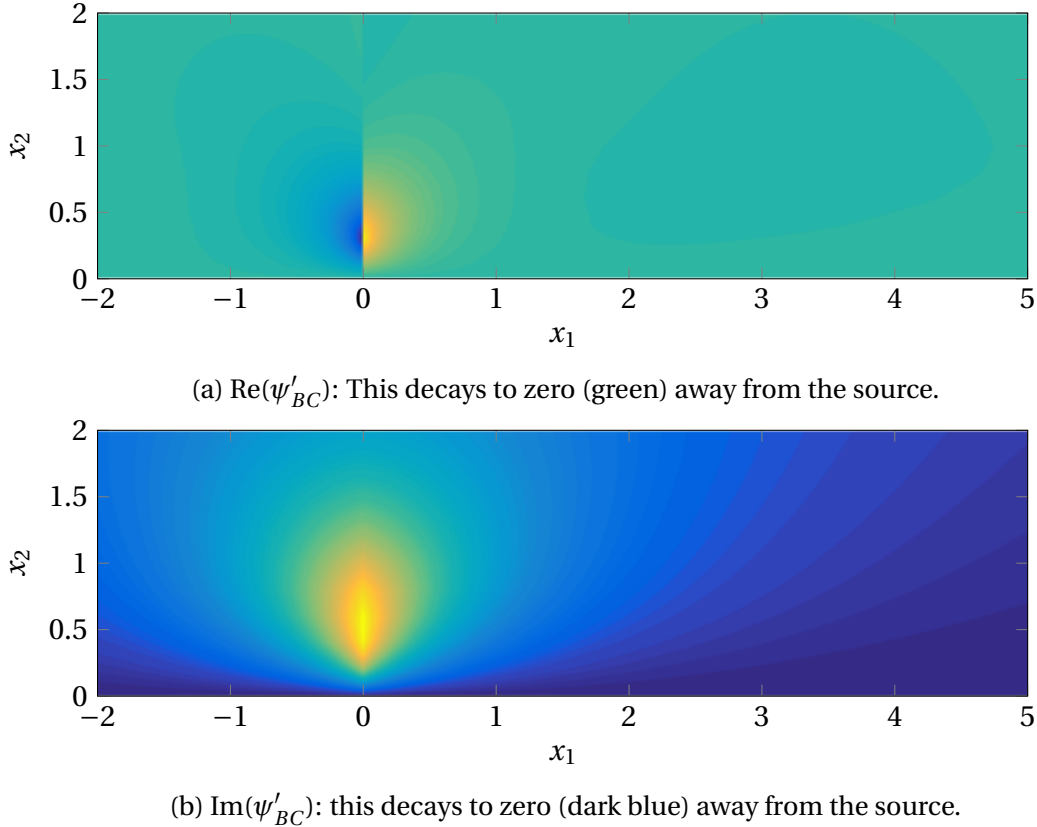


Fig. 3.5.6 The contribution to the solution, as per figure 3.5.6, from the branch cut integral alone (that is, upon removal of the convected poles), with real and imaginary parts evaluated at $t = 0$. The colour schemes on the plots differ, since the imaginary part is always positive, and both decay to zero away from the source (at $(0, 0.3)$).

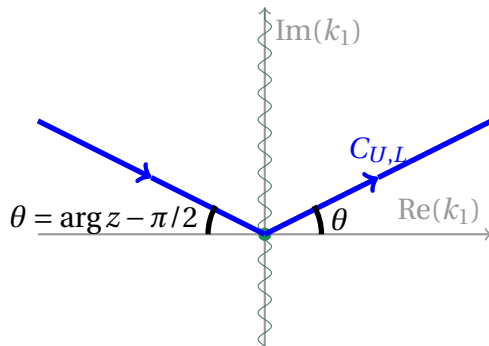


Fig. 3.5.7 Exact far-field integration contours $C_{U,L}$ for observer location $x_1 = r \cos(\theta)$, $x_2 = r \sin(\theta)$

This differs from the earlier I_h by the removal of the $\psi_d(x_2) = e^{-|k_1|x_2}$ term. With the substitution $s = ik_1 z$ in the left-half k_1 plane (running from ∞ to 0) and $s = ik_1 z^*$ in the right-half k_1 -plane, the integral reduces to

$$\psi_{BC} = \int_0^\infty \left[\frac{1}{iz^*} I\left(\frac{s}{iz^*}\right) - \frac{1}{iz} I\left(\frac{s}{iz}\right) \right] e^{-s} ds. \quad (3.5.14)$$

This is of the form required for application of Watson's lemma [112] i.e. noting that this exponentially decaying integral is dominated by the behaviour near $s = 0$ in the limit of large z (with the argument of I tending to 0). It is possible to directly evaluate $I(k_1 = 0)$, since the auxiliary functions ψ_h and ψ_d reduce to simple hyperbolic functions and exponentials, respectively. With the chosen normalisation, we have

$$I(0) = \frac{Q}{2\pi i} \frac{y_2}{\kappa_1} \quad (3.5.15)$$

with I continuous at the origin, despite the branch cuts along the imaginary axis. Hence

$$\psi_{BC} \sim \frac{Q}{2\pi i} \frac{y_2}{\kappa_1} \left(\frac{1}{iz^*} - \frac{1}{iz} \right) \int_0^\infty e^{-s} ds = \frac{Q}{\pi i} \frac{y_2}{\kappa_1} \frac{x_2}{x_1^2 + x_2^2}. \quad (3.5.16)$$

The corresponding free stream pressure is then (neglecting terms which decay more rapidly in $|\mathbf{x}|$)

$$p'_{\text{inner}} \sim q_0 y_2 U'(y_2) \frac{x_1}{\pi(x_1^2 + x_2^2)}. \quad (3.5.17)$$

The pressure depends purely on the shear at the location of the disturbance, and the distance of this disturbance from the wall. Beyond this local shear, there is no dependence on the structure of the boundary-layer itself. Further, we see that a free-stream disturbance ($U' = 0$) is silent: vorticity and therefore far-field acoustics are generated as an interaction of the source with background shear.

This solution of the *inner* problem, confined to the boundary-layer, can be matched to a radiating solution of the *outer* problem, with lengths scaled by acoustic wavelengths k_0^{-1} , as per §3.2.1, where the boundary-layer appears thin. The (time-harmonic) outer pressure perturbation p'_{outer} satisfies, in outer coordinates, Helmholtz's equation

$$(\nabla^2 + k_0^2) [p'_0 \exp(ik_0 M_\infty x_1)] = 0 \quad (3.5.18)$$

taking into account the background convection through the exponential term, under the assumption that M_∞^2 , the free-stream Mach number, is suitably small (but allowing first order corrections). This can be compared to the Prandtl-Glauert transformation [39] for

more general subsonic flows. The acoustic wavenumber is $k_0 = \omega/c_0$, as before. To match with the source term, we require a solution radiating from the origin $x_1 = x_2 = 0$, or $r = 0$ in cylindrical coordinates (r, θ, x_3) , corresponding to the location of the source in outer coordinates (with $y_2 \mapsto 0$). We have the condition that $\partial p'_0 / \partial x_2 = 0$ on $x_2 = 0$, equivalent to $\partial p'_0 / \partial \theta = 0$ on $\theta = 0, \pi$. Finally, we impose a condition of outward radiating waves, which requires $p'_0 \propto r^{-1/2} \exp(-ik_0 r)$ for r large, up to some scaling (with no terms proportional to $\exp(+ik_0 r)$).

The generic solution to Helmholtz equation $(\nabla^2 + k_0^2)\phi = 0$, in two-dimensional polar coordinates (so that $x_3 = 0$) can be found using separation of variables [114] and is

$$\phi(r, \theta) = \sum_{n=0}^{\infty} (A_n J_n(k_0 r) + B_n Y_n(k_0 r)) (C_n \cos(n\theta) + D_n \sin(n\theta)). \quad (3.5.19)$$

Here J_n and Y_n are Bessel functions of the first and second kinds, respectively. The introduction of the Hankel function of the second kind⁴ given by

$$H_n^{(2)} = J_n - i Y_n \quad (3.5.20)$$

allows the general radiating solution to be written down as

$$\phi(r, \theta) = \sum_{n=0}^{\infty} (C_n \cos(n\theta) + D_n \sin(n\theta)) H_n^{(2)}(k_0 r). \quad (3.5.21)$$

Asymptotically [2], $H_n^{(2)}(z) \sim \sqrt{2/\pi z} \exp(-iz - i(n\pi/2 + \pi/4))$ and so we have the correct complex exponential at infinity for outgoing waves.

To match with an inner solution like $\cos(\theta)$, for the hard-wall problem we take $C_1 = C$ and all other constants to be zero. This gives outer pressure solution

$$p'(r, \theta, t) = C \exp(i\omega t - ik_0 M_\infty r \cos \theta) H_1^{(2)}(k_0 r) \cos(\theta) \quad (3.5.22)$$

with the unknown scaling C derived from matching to the inner solution. We match by considering r small in the outer coordinates. For r small, we have

$$H_1^{(2)}(k_0 r) \sim -i Y_1(k_0 r) \sim \frac{2i}{\pi k_0 r} \quad (3.5.23)$$

and we have precisely the same functional dependence on r and θ for the outer and inner solutions p' . It is important to note that r is a different variable in each case. If we define

⁴This choice, as opposed to the first kind $H_n^{(1)} = J_n + i Y_n$, corresponds to the choice of the sign of the frequency, and ensures waves are outgoing, not incoming.

$r = r_o$ for the outer solution and $r = r_i$ for the inner, they are related via $r_i/\delta = r_o k_0$, with δ some measure of the boundary-layer thickness. With this, the proportionality constant is then

$$C = \frac{q_0 y_2 U'(y_2)}{2i\delta} \quad (3.5.24)$$

with the shear, $U'(y_2)$, considered as a function of the inner coordinate.

3.5.4 Modal solutions

In addition to this branch cut contribution, we have modal solutions, defined in (3.5.11) as

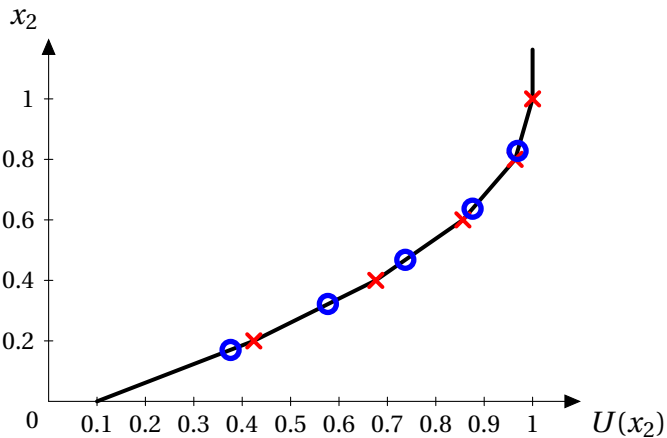
$$M_j(x_1, x_2) = \text{Res}_\Psi(k_{1j}) e^{-ik_{1j}x_1} \quad (3.5.25)$$

with k_{1j} the roots of the dispersion relation $D_h = 0$. For an N -piece profile, it can be argued that there are N such solutions, see an outline argument in the appendix, §A.1.

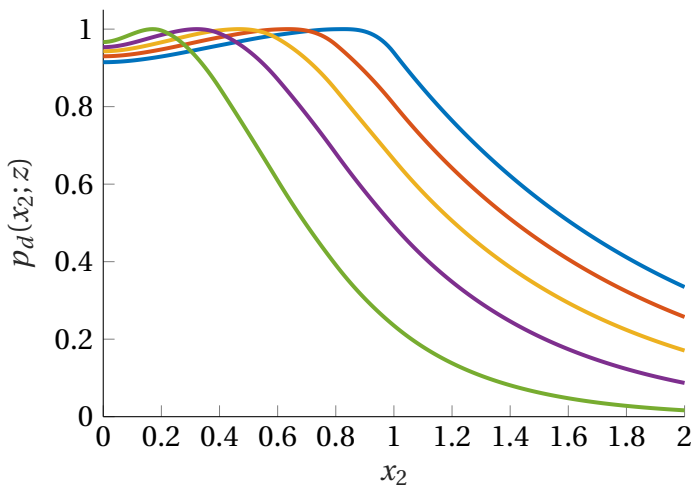
If the background profile is stable, these solutions are neutrally stable, they neither grow nor decay downstream, and the k_{1j} are real. This is the case if the background profile is concave, with the shear increasing closer to the wall, via a standard application of Rayleigh's stability criterion [33], though this condition is not necessary for stability (at a given frequency). For real k_{1j} , these solutions convect at a speed $U_{cj} = \omega/k_{1j}$, which lies between the slip velocity U_0 and the free-stream velocity U_∞ . Further, we can assign a physical location to these convecting modes, by noting that (assuming U is monotonic⁵) then we can invert the function $U(x_2)$ to give $y_{2j} = U^{-1}(\omega/k_{1j})$. For the approximate-parabolic slipping case, the physical locations of these modes, and their corresponding convective velocity, is shown in figure 3.5.8a, and their corresponding shapes in figure 3.5.8b.

Unlike the branch cut contribution, these solutions cannot be matched to an external acoustic field. They propagate in the streamwise direction with phase velocity $U_c < U_\infty$, proportional to $\exp(i(\omega(t - x_1/U_c)))$, a form of solution not satisfying Helmholtz's equation. This does not cause a conflict: these solutions decay exponentially away from the wall and we would not expect them to radiate acoustically. Despite these solutions not appearing in the outer solution, however, they are critical in the computation of any scattering problem, providing explicit, naturally occurring examples of gust solutions, with streamwise propagating solutions, each moving at convection velocity $U_c < U_\infty$. These resemble that typically used as the incident field in scattering problems.

⁵This is also practical for non-monotonic profiles provided that for there is a unique x_2 for each U_{cj} , which permits inflection, and even non-monotonicity for some frequencies



(a) The physical location of zeros (blue circles) and poles (red crosses) of the hard-wall dispersion relation $D_h(k_1, \omega)$ obtained as $y_2 = U^{-1}(\omega/k_1)$. As can be seen, each linear piece supports a mode (when the profile is monotonic).



(b) The corresponding mode shapes. Here, the perturbation pressure shape is plotted throughout the boundary layer, normalised to be 1 at the maximum. The peaks of the modes roughly correspond to the velocity of the modes, as per the previous plot. Modes with physical location much closer to the boundary-layer thickness ($\delta = 1$) have an impact further beyond the boundary-layer. Further, pressure is broadly constant between the physical mode location and the wall (on which $\partial p'/\partial x_2 = 0$).

Fig. 3.5.8 For the parabolic profile (II), approximated by a 5-piece linear profile, the physical locations within the boundary-layer, and shapes of the 5 convected modes are shown for $\omega = 1$.

3.5.5 Variation of internal shear

Consider the two-piece profile, case I, with slip velocity U_0 allowed to vary but otherwise the profile is held fixed. This leads to a thin region of variable background shear for $x_2 \in (0, \delta_1 = 0.2)$, with a broad region of low shear outside this region. This is an ideal setup to investigate the effect of *shear shielding*, whereby an internal shear layer may reduce wall pressure or scattered noise, or alternatively a thin region of shear may be a large source of noise. A mass source only generates vortical disturbances when the background shear is non-zero, and hence inclusion of a mass source in the outer region ($x_2 \in (\delta_1, \delta_2 = 1)$) provides a consistent generator of vorticity (with the shear constant in this region, independent of U_0).

Indeed, it can be seen that the far-field acoustic response to a mass source is unchanged, with the acoustic response a function of the *local* background shear and source location (and strength) only, as per (3.5.24). This might suggest that varying internal shear has little effect on the trailing vorticity and excited convected modes. This is not the case, however, as demonstrated in figure 3.5.9. The case with $U_0 = 0.75$ is treated as a base case, this corresponding to the internal shear $\sigma_0 = (U_1 - U_0)/(\delta_1)$ being the same as the external shear, $\sigma_1 = (U_\infty - U_1)/(\delta_\infty - \delta_1)$, i.e. an essentially a single-piece profile. As the internal shear is increased, a shorter-wavelength mode becomes visible, gradually increasing in strength. This mode has the shortest wavelength (and is strongest) in the non-slip case $U_0 = 0$ (figure 3.5.9d), with the "outer mode" that dominates in the single-piece plot (figure 3.5.9a) essentially invisible. Further we note the disturbance at the source itself, $y_2 = 0.5$, are identical between the plots: the source is not varying in strength.

For the two-piece case we have two convected modes, roots of the dispersion relation

$$\begin{aligned} 0 &= D_h(\omega, k_1) \\ &= 1 + \Delta_1 \left(1 - e^{-2\kappa\delta_1} \right) + \Delta_2 \left(1 - e^{-2\kappa\delta_2} \right) + \Delta_1 \Delta_2 \left(1 - e^{-2\kappa\delta_2} - e^{-2\kappa\delta_1} - e^{-2\kappa(\delta_2 - \delta_1)} \right) \end{aligned} \quad (3.5.26)$$

when we hold ω fixed. The zeros are real for all ω provided $U_0 \leq 0.75$, which follows from Rayleigh's criterion (the profile is non-inflecting, $U_0 = 0.75$ corresponding to exactly the case where shear is continuous at $x_2 = \delta_1$). In this range, there is an "outer" mode with $k_1^{(o)} \in (\omega/U_\infty, \omega/U_1)$ and an "inner" mode with $k_1^{(i)} \in (\omega/U_1, \omega/U_0)$, both of which can be mapped to a physical location via inversion of $k_1 = \omega/U(x_2)$, which is unambiguous for a monotonic profile, and remains unambiguous for a slightly inflecting profile, in this case $U_0 \in (0.75, 0.825)$ (a range which depends on frequency ω). The behaviour of these modes is shown as U_0 is varied (for frequency $\omega = 1$ fixed) in figure 3.5.10, showing the coalescence of the modes at some critical value of $U_0 > 0.75$. After this point, the modes

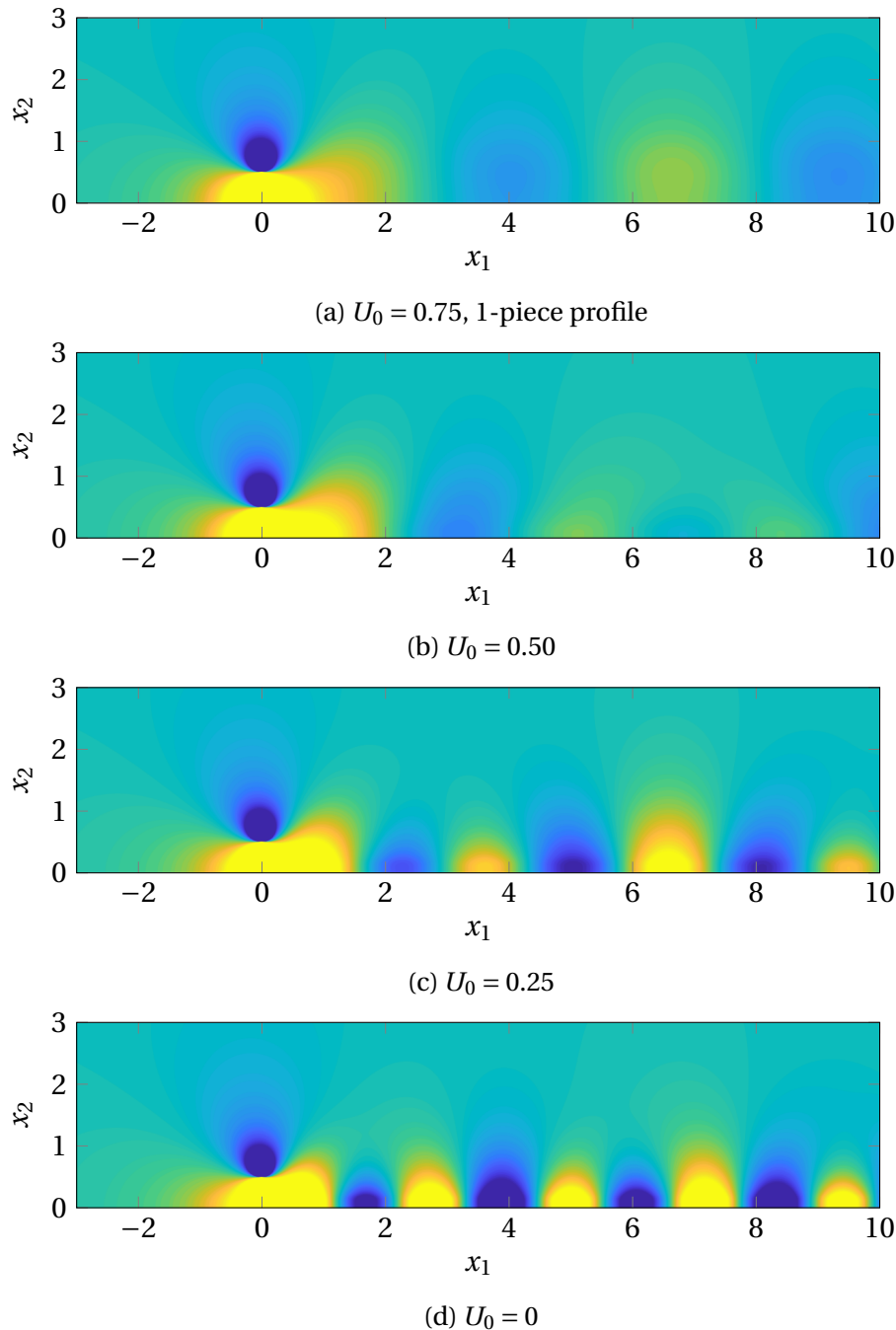


Fig. 3.5.9 Pressure disturbances above a hard-wall as discussed in the text, at fixed frequency $\omega = 1$. All plots have the same strength source and are displayed with the same colour range. The first plot, figure 3.5.9a, shows the case with no inner shear layer, with the inner shear increasing in magnitude through the plots.

become complex conjugates of each other, and lose stability. $U_0 = 0.75$ corresponds to a single-piece profile, and we see the location of the inner mode is exactly $x_2 = 0.2$, with $k_1^{(i)} = \omega/U_1 = 1.2$ for $U_0 = 0.75$. D_h has a pole at $k_1 = \omega/U_1$ for all U_0 , which cancels out this zero for $U_0 = 0.75$, resulting in the expected single observed zero of the single-piece profile.

It is also worth getting a handle on the shape of these modes, as done (again in the case $\omega = 1$) in figure 3.5.11. The two families of modes have similar shapes, exponentially decaying beyond the shear layer they correspond to, and remaining broadly constant across their shear-layer. We note the hard-wall condition translates to $\partial p'/\partial x_2 = 0$, which clearly holds in all these cases. All the plots are normalised to behave as $\exp(-|k_1|x_2)$ outside the boundary-layer, which allows noting the gradual increase in strength of the inner mode with inner shear. The mode decays rapidly across the boundary-layer, for $x_2 > \delta_1 = 0.2$. Conversely, the outer mode shape is broadly unchanged with varying inner shear, being as it is driven by the outer shear layer. In both cases, the peak of the modal disturbance roughly corresponds to the “physical location” of the disturbance as per figure 3.5.10b, which lends weight to this earlier designation.

The full inversion plots figure 3.5.9 show that the inner mode gradually dominates as U_0 is decreased (and internal shear increased). We can get a handle on the strength of the excitation of each mode by revisiting the modal contribution M_j from (3.5.11). Without loss of generality focusing on the wall pressure (which, as the mode shape profiles have suggested, is broadly the same as the perturbation pressure across each shear layer), we quantify the strength of modal solutions via

$$\text{Res}_{\mathcal{P}\Psi}(k_{1j}) \propto \frac{p_d(0; k_{1j})\psi_h(y_2; k_{1j})}{D'_h(k_{1j})} \frac{1}{k_{1j} - \kappa_1} \quad (3.5.27)$$

with all other terms dependent only on source location and background shear. For $k_1 = k_1^{(o,i)}$, ϕ_d and ϕ_h are proportional to each other, since these modal solutions satisfy both the hard-wall and decaying boundary conditions. This contribution is plotted, for fixed values of y_2 , in figure 3.5.12. Three values of y_2 are shown: firstly $y_2 = 0.5$ and $y_2 = 0.8$, respectively above and below the physical location of the outer mode. Both plots show the same broad trend: when the inner shear is equal to the outer shear, i.e. $U_0 = 0.75$, only the outer mode is excited (shown in blue). This is expected as the inner mode does not exist for this single-piece profile. As U_0 decreases, the inner mode is gradually excited more and more, whilst the excitation of the outer mode reduces. They cross over at some internal shear, and for high internal shears the inner mode dominates. There are, however, intermediate ranges of shear in which the *total* wall pressure is less than it would be if the

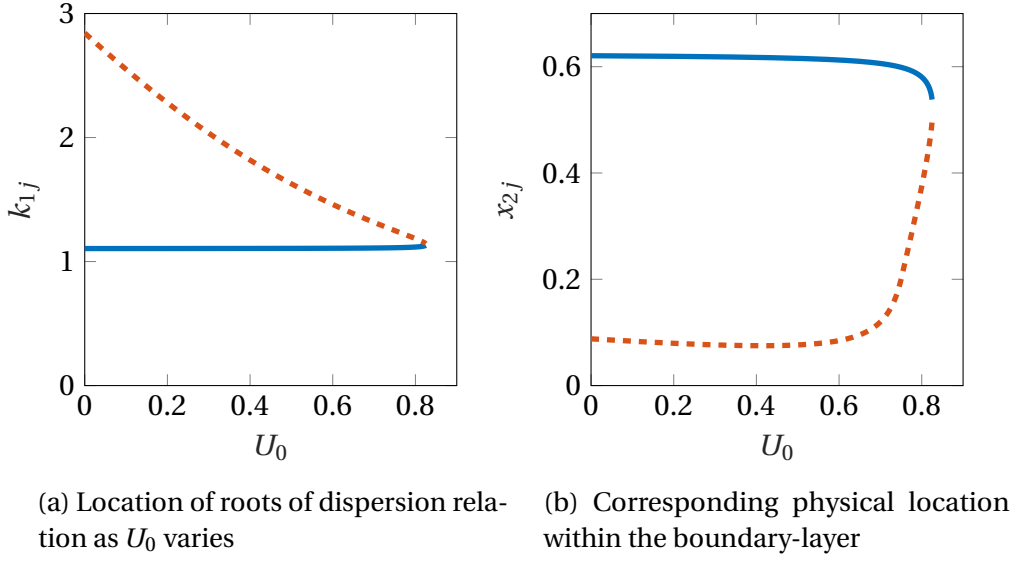


Fig. 3.5.10 For $\omega = 1$, the locations (both in wavenumber and physical space) of the convected modes in the complex plane. They coalesce when $U_0 \approx 0.825$ and become complex (and the profile becomes unstable). Both the outer mode (blue) and the internal mode (orange, dashed) remain at a broadly fixed location unless the internal shear is comparable to the external shear ($U_0 \gtrsim 0.7$). For inflecting profiles ($U_0 \geq 0.75$), both modes are physically located on the outer shear region ($x_2 > \delta_1 = 0.2$).

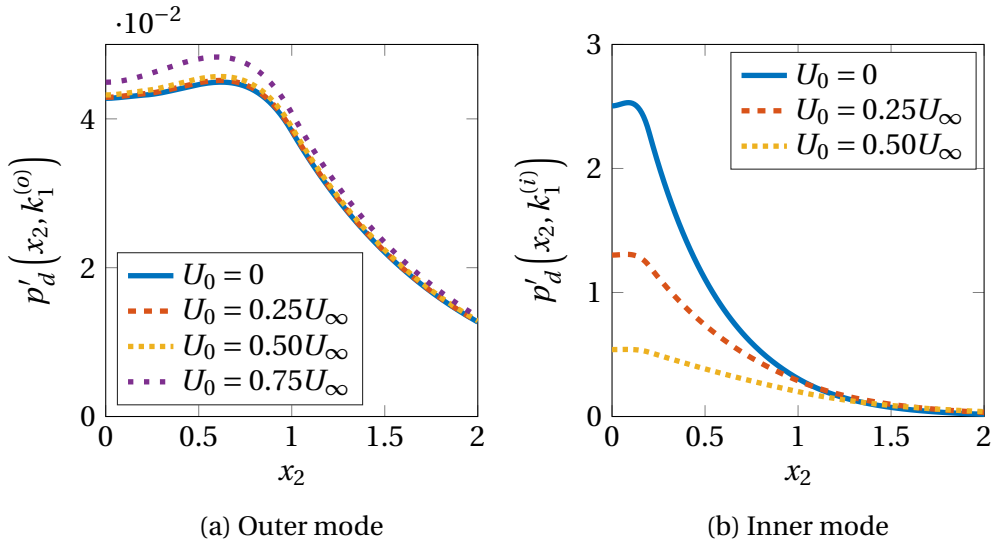


Fig. 3.5.11 Shape of the pressure modes as U_0 varies, with $\omega = 1$. The outer mode (corresponding to smaller $k_1 \in (\omega/U_\infty, \omega/U_0)$) is far less affected by variations in internal shear, which is unsurprising, especially given the previous plot figure 3.5.10 showing the limited effect on location of this mode as shear varies.

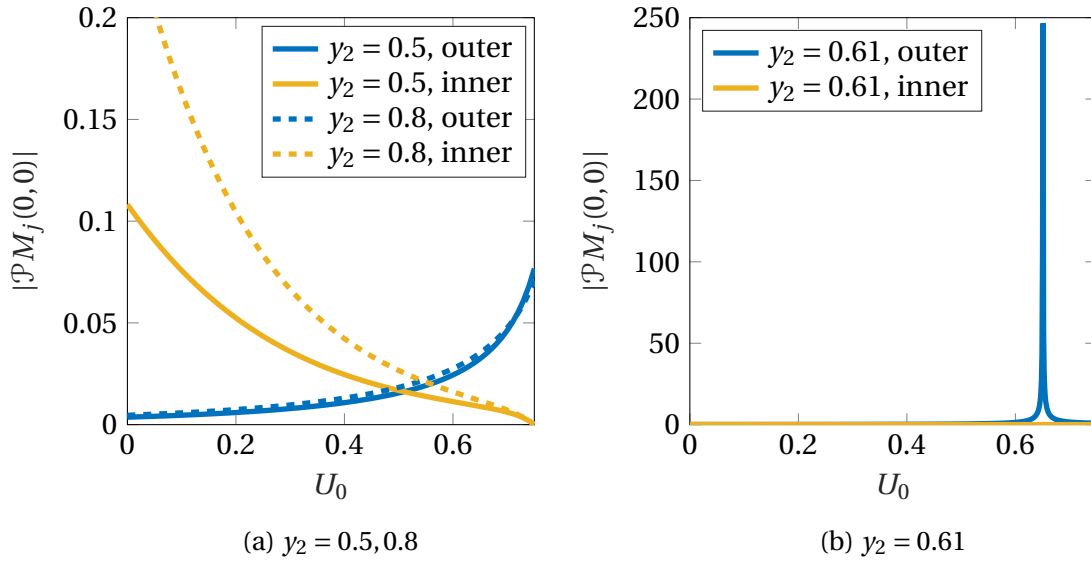


Fig. 3.5.12 Wall pressure of modal contributions from a fixed source, as the inner shear is varied (through variation of U_0). In all cases, $\omega = 1$. Broadly there is a transfer from the outer mode to the inner mode as the shear is increased (U_0 decreased) though the singular case when the outer mode location $k_1^{(o)}$ passes through κ_1 (the forcing location) is shown in figure 3.5.12b, with the outer mode crossing $x_2 = 0.61$ seen in figure 3.5.10b.

internal shear layer were not there, here with $U_0 \approx 0.5$ and so $\sigma_0 \approx 1.5$. Finally, the case $y_2 = 0.61$ is shown in figure 3.5.12b. This corresponds to $k_1^{(o)} \approx \kappa_1 = \omega/U(y_2)$. Whilst $k_1^{(o)}$ varies only slightly with U_0 , in this case it passes across κ_1 , where the mode excitation is singular. Varying the inner shear moves the excited mode location further from the forcing location, and thus, in this singular case, greatly reduces noise for all $U_0 < 0.6$, though the singular nature of this case is worth reemphasising.

We have seen that increasing internal shear can draw energy away from an outer, large-scale mode, though at the expense of exciting an inner mode. Provided these are suitably balanced, there is some argument for a shear-shielding effect, that an inner shear layer can reduce wall-pressure. If this disturbance is incident on some scattering junction, the resultant far-field noise (driven by wall pressure) could be reduced, though this is a careful optimisation that depends on the frequency of interest.

3.6 Lined walls: pressure-release and impedance conditions

The numerical method changes little for the pressure-release solution, where we instead impose $p' = 0$ on $x_2 = 0$. This generalises neatly to considering a more general impedance

solution with impedance Z relating the wall-normal velocity and pressure on the wall, via

$$i\omega Z v'_{o1} = Cp'_{o1} \quad (3.6.1)$$

encapsulated in the operator \mathcal{L}_{01}^Z . The pressure-release solution is obtained in the limit $Z \rightarrow 0$ and the hard-wall solution as $Z \rightarrow \infty$, and as such both can be regarded as specific cases of a more general solution.

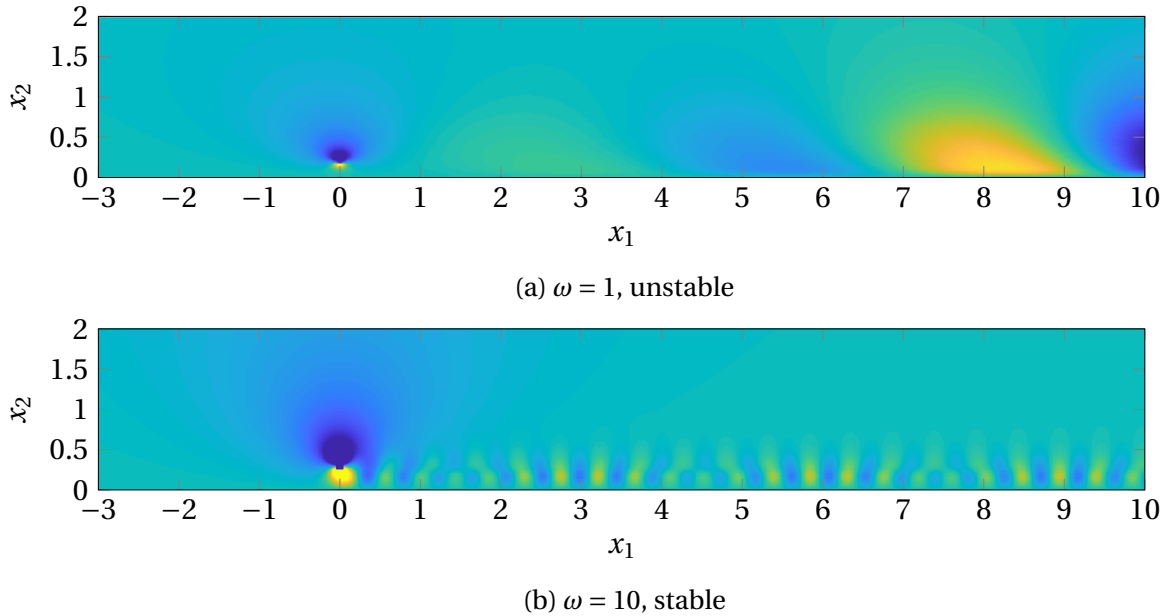


Fig. 3.6.1 Pressure disturbances above a pressure-release wall for three-piece profile (I), with $U_0 = 0.2$. There is a point mass source at, $(0, 0.3)$ with all lengths scaled by boundary-layer thickness and all speeds by the free-stream velocity. For lower frequencies this setup is unstable, whereas stability is regained for higher frequencies.

Figure 3.6.1 show two solutions obtained in the pressure-release case, highlighting some important caveats to the generalisation of the hard-wall solution. Firstly, there may or may not be *unstable* modes. Unlike the hard-wall case, where it is possible to derive conditions such that all modes are neutrally stable for all frequencies, there is typically a band of frequencies for which unstable modes, with complex wavenumbers, exist. Further, the number of modes is no longer fixed, which can be demonstrated in the simplest case of infinite shear.

The final caveat is that an expression for the streamfunction ψ itself cannot be easily determined, due to the choice of an arbitrary constant which is affected by the presence of a mass source. Nevertheless, the derived quantities of pressure and of velocity can still be determined through the integral formulation, both removing the singularities present at

$k_1 = 0$. Since these physical quantities, rather than the streamfunction itself, are important in practice, this does not pose difficulties.

3.6.1 Quantity of pressure-release modes

Typically there appear to be $N + 1$ roots of the pressure-release dispersion function. This is not always the case, however, particularly in the singular case $\omega \approx \sigma_0$, the wall-shear.

Consider first the 1-piece dispersion function for pressure-release boundary conditions (3.4.24), namely

$$D_p = \left((1 + \Delta) - \Delta e^{-2\kappa\delta} \right) + \frac{\kappa C_0}{C'_0} \left((1 + \Delta) + \Delta e^{-2\kappa\delta} \right). \quad (3.6.2)$$

In the limit $\delta \rightarrow \infty$, this reduces simply to

$$D_p = 1 + \frac{\kappa C_0}{C'_0} = 1 - \frac{|k_1|(\omega - U_0 k_1)}{k_1 \sigma_0}. \quad (3.6.3)$$

The number of zeros of this relation, corresponding to convected modes, depends on the relative magnitude of ω and σ_0 (the shear). If $\omega > \sigma_0$, there is a single zero at $k_1 = U_0^{-1}(\omega - \sigma_0)$ whereas if $\omega < -\sigma_0$, there is a zero at $k_1 = U_0^{-1}(\omega + \sigma_0)$. In the intermediate region, $-\sigma_0 < \omega < \sigma_0$, there are no zeros. In a sense there are always two zeros, but one of them (and possibly both) lie on the alternative Riemann sheet, due to the branch cuts of κ . It is worth noting that all zeros move to infinity in the limit $U_0 \rightarrow 0$, which causes difficulties in consideration of the non-slipping case.

The difference in numbers of zeros for $\omega \gtrless \sigma$ does not generalise to a finite boundary-layer, as shall be seen below (for example figure 3.6.3 which looks at the simplest case of a single shear layer). Whereas the infinite shear case either has one or no zeros, there are always at least two zeros in the case of a single shear layer, which might rise to more in certain situations, in particular when frequency and shear are of comparable size. The disappearance of the shear mode is, however, an artefact of the infinite shear approximation.

A stability analysis is done for the 5-piece profile (profile II) in the next section, and 6 zeros are found with pressure-release boundary conditions (for $\omega\delta/U_\infty = 1$). This seems completely expected, based on the hard-wall case (where an N -piece profile has N zeros), with the extra zero arising from the zero that exists in the uniform flow case (due to the slightly more complicated boundary operator). This is not, however, necessarily the case. If we return to the 1-piece dispersion relation, and scale all lengths and speeds by δ and U_∞ respectively (so that the shear is $(1 - U_0)$), then D_p as a function of k_1 has only two

parameters, ω and U_0 , explicitly

$$D_p(k_1; \omega, U_0) = \left(1 - \frac{\text{sgn}(k_1)(\omega - U_0 k_1)}{1 - U_0}\right) \left(1 + \frac{(1 - U_0) \text{sgn}(k_1)}{2(\omega - k_1)}\right) - \left(1 + \frac{\text{sgn}(k_1)(\omega - U_0 k_1)}{1 - U_0}\right) \frac{(1 - U_0) \text{sgn}(k_1)}{2(\omega - k_1)} e^{-2|k_1|}. \quad (3.6.4)$$

We focus on the right-half plane, with $\text{Re}(k_1) > 0$ (so that $\text{sgn}(k_1) = k_1/|k_1| = 1$), and assume $U_0 > 0$. This function is plotted in figure 3.6.2, for the non-slipping case $U_0 = 0$, with frequency $\omega = 1.1$. We saw in the infinite shear case that $\omega \gtrless 1$ gives rise to two different behaviours, and by including a finite boundary-layer we are in a position to investigate this. For $\omega \approx 1$, as in the figure, more zeros are apparent. In the limit $\omega - 1 \equiv \epsilon \ll 1$ we have approximate dispersion relation (in the $\text{RH}k_1\text{P}$)

$$D_p \approx -\epsilon \left(1 + \frac{1}{2(1 - k_1)}\right) - e^{-2k_1}(1 - k_1). \quad (3.6.5)$$

The reduced dispersion relation $\bar{D}_p = (1 - k_1)D_p$ then has zeros satisfying

$$e^{-2k_1} + \epsilon \left(\frac{3}{2} - k_1\right) = 0 \quad (3.6.6)$$

which permits exact solutions in terms of the Lambert-W function (or product log function), namely

$$k_1 \approx \frac{3}{2} + \frac{1}{2} W_n \left(\frac{2}{\epsilon e^3}\right) \quad (3.6.7)$$

with W_n the inverse of $z = W_n e^{W_n}$, choosing the n th branch. This function is available in most common programming languages, and thus this approximation can easily be checked. Based on the earlier assumption, only the solutions with $\text{Re}(k_1) > 0$ are valid as zeros of the exact dispersion relation, and thus the number of zeros varies as ϵ decreases.

We can get a bound for the number of zeros with positive real part by looking at the asymptotic behaviour of W_n as n is increased. Following Corless et al. [29], for n large we have

$$W_n(z) \approx \log(z) + 2\pi i n - \log(\log(z) + 2\pi i n) \quad (3.6.8)$$

which means the approximate location of the zeros, for n large, are

$$k_1 \approx \frac{1}{2} \left(\log(2/\epsilon) + 2\pi i n - \log[\log(2/\epsilon) - 3 + 2\pi i n] \right). \quad (3.6.9)$$

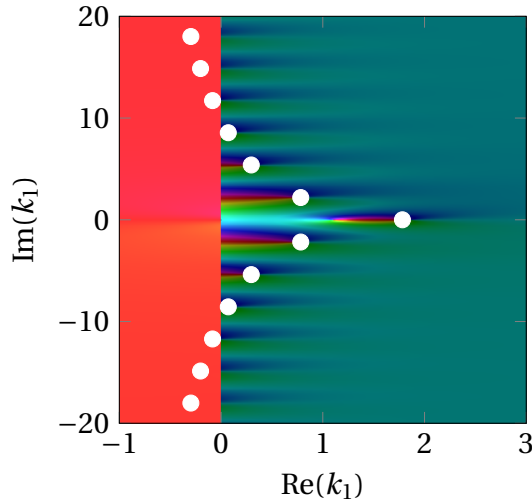


Fig. 3.6.2 The dispersion function, D_p , for a non-slipping profile with $\omega = 1.1$, and background shear $\sigma = 1$. With $U_0 = 0$, the non-slipping one-piece profile only has a single, non-dimensional, parameter ω . For $\omega \approx 1$, a number of new zeros appear in the dispersion function. Here, we have $\omega = 1.1$, with 7 visible zeros (and one pole) shown in the phase plot, the points around which the colour takes all values. As $\omega \rightarrow 1$, the zeros on the other Riemann sheet move through the branch cut along the imaginary axis and onto the visible complex k_1 -plane. The white circles display the approximate location of these zeros as predicted by (3.6.7).

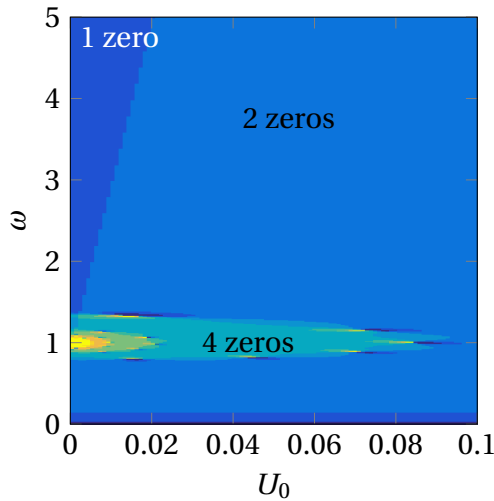


Fig. 3.6.3 The approximate number of zeros of \bar{D}_p in the k_1 -plane, with $U_\infty = \delta = 1$, for a one-piece profile, with U_0 and ω the only free parameters. The number of zeros in the box $\text{Re}(k_1) \in (0.001, 200)$ and $\text{Im}(k_1) \in (-50, 50)$ is computed by integrating around this box, as per §A.2.2. The truncated range of integration leads to the region in the top-left of the plot with a single zero: in reality there are two zeros, but the second has $\text{Re}(k_1) > 200$. There is a region around $U_0 = 0$, $\omega = 1$, where the number of zeros grows, and is unbounded at this critical point.

These have positive real part (for real ϵ) if

$$1 < \frac{(2/\epsilon)^2}{(\log(2/\epsilon) - 3)^2 + (2\pi n^2)}. \quad (3.6.10)$$

Therefore we have an upper bound on n (with the number of zeros $2n$ by symmetry in the imaginary part) as

$$|n| \leq \frac{\sqrt{(2/\epsilon)^2 - (\log(2/\epsilon) - 3)^2}}{2\pi}. \quad (3.6.11)$$

This works well: for $\epsilon = 0.1$, as in the earlier plot, this predicts 7 zeros, exactly as we saw in figure 3.6.2, and the number of zeros is essentially linear in $1/\epsilon$. As the shear and the frequency approach each other, suitably scaled, a series of hitherto unseen modes become visible. A similar analysis could be done for non-zero U_0 , explaining the numerically computed figure 3.6.3 showing a substantial increase in the number of modal pressure solutions in the region around $\omega = \sigma = (1 - U_0) = 1$.

3.6.2 Stability of pressure-release modes

D_p has the property that $D_p(k_1^*)^* = D_p(k_1)$ for real ω (or, equivalently, $D_p(k_1)$ is real for real k_1). This can clearly be seen in the expression for the one-piece case above, with Δ , κ and C_0/C'_0 all obeying this property. It generalises nicely, with general dispersion function

$$D_\ell = (A_0 + B_0) - \ell_1 \kappa (A_0 - B_0) \quad (3.6.12)$$

it suffices that A_0 , B_0 and ℓ_1 satisfy the property, and we have already established that $\ell_1 = -C_0/C'_0$ does. From the matching formulae, if k_1 is real then Δ_j is real, and as such all coefficients A_j and B_j satisfy the condition if A_∞ and B_∞ do, which is trivially the case for the decaying solution. This observation does not necessarily stretch to general D_ℓ^Z , where ℓ_1 may not satisfy this condition (if Z is non-real, as it usually is in practice). This condition indicates that if $D_p(z) = 0$ for non-real z , then $D_p(z^*) = 0$ also, and so any unstable modes are paired with stable modes.

With all speeds scaled by the free-stream velocity U_∞ and all lengths by the boundary-layer thickness δ , so that we have $\omega \rightarrow \omega\delta/U_\infty$ dimensionless, the simple profile of a 5-piece approximation to a slipping parabolic profile (case II) is unstable for $\omega = 1$, with 4 real zeros of D_p and a pair of complex conjugate zeros. We can use the Briggs-Bers method (§2.1.2) to demonstrate that this instability propagates downstream, and thus grows away from the source, as done in figure 3.6.4. For $\text{Im}(\omega)$ sufficiently negative, all zeros lie beneath the real k_1 axis. As ω is relaxed to the real axis, the unstable mode moves

across the real axis, and is thus convectively unstable. However, it poses no problems in deformation of the Fourier inversion contour from the real axis, to account for this mode being in some generalised lower half k_1 plane. That this mode propagates downstream is unsurprising: the real part of the wavenumber lies on the critical-layer, corresponding to solutions convected with the mean flow, and naturally we would expect this solution to be convected downstream with the (positive) mean flow. Where the mean flow is negative (for example if moving in the frame with a convected source, with negative background velocity between the source and the wall), it is very possible that upstream propagating disturbances might exist and Briggs-Bers should be used carefully.

This analysis can be performed using the zero-finding methods outlined in the appendix, §A.2.2. Iterating over some array of frequencies, $\{\omega_j\}$, a guess for the location of zeros for case ω_{j+1} is provided by the computed location for ω_j . Provided $\omega_{j+1} - \omega_j$ is sufficiently small, the displacement in the location of the root is small enough that the previous location is a good estimate for the new location, and thus Newton-Raphson efficiently determines the location of the new zero. The most difficult case is the initial case, where all zeros must be located with no information. For the plot in figure 3.6.4, the case of real ω was computed first, and then the imaginary part was gradually made more negative.

We have previously noted that the same background flow might be unstable at some frequencies and yet stable at other frequencies. As the magnitude of the frequency changes, the movement of modes can be observed. At some critical frequency, two (neutrally stable) zeros in the k_1 -plane will meet, and with further variation in frequency become a complex conjugate pair. The alternative process may happen at some higher frequency still, with the two conjugate modes coming together and restabilising. Numerically, this proceeds analogously to the above, with instead of small variation of $\text{Im}(\omega)$, $\text{Re}(\omega)$ is varied instead, with zeros found using a Newton-Raphson method with initial guess given by the preceding solution. This is demonstrated for the simple two-piece case in figure 3.6.5, with the two modes unstable for lower frequencies stabilising at higher frequencies. As a caveat to the numerical procedure outlined above: there is a critical frequency at which two modes are coincident (corresponding to the boundary of stability). After this point, the preceding value of mode location has two identical values, and thus this routine fails to find the final mode. To get around this, figure 3.6.5 was computed in both directions (from $\omega = 0.5$ and from $\omega = 8$) and matched in the middle.

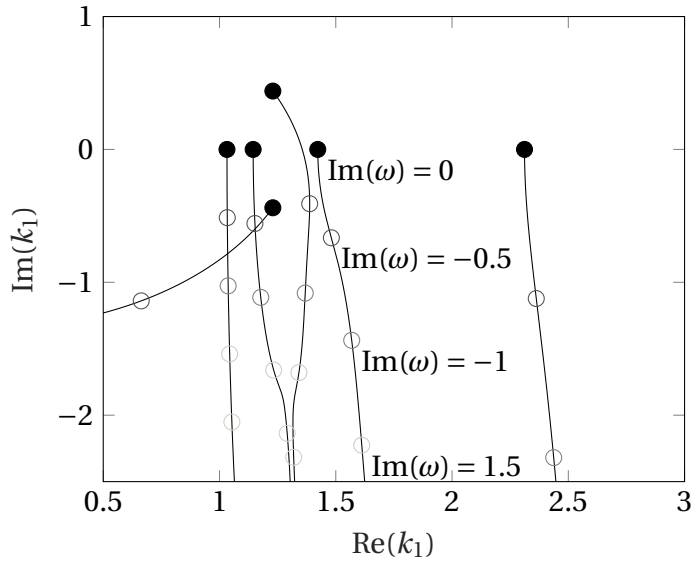


Fig. 3.6.4 For a five-piece profile approximating a parabola, with slip velocity $U_0 = 0.1$ (speeds scaled by U_∞ and lengths by δ), there are five pressure modes for $\omega = 1 - i\epsilon$. Here, they are tracked as ϵ is decreased to zero. For ϵ large, all zeros of D_p (and hence modal solutions) lie in the lower half-plane, and are thus all downstream-propagating modes. The unstable mode, with $k_1 \approx 1.3 + 0.5i$ when $\omega = 1$ is real, is downstream propagating, and thus any inversion contours must pass *above* this zero (or pole, when considering the reciprocal) in the complex plane.

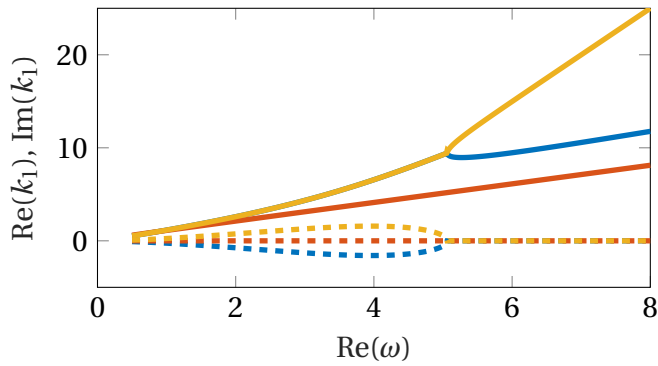


Fig. 3.6.5 Location of the three zeros of D_p for the two-piece profile, with $U = (0.2, 0.8, 1)$ and $\delta = (0, 0.2, 1)$. The solid line is the real part, and the dashed the respective imaginary part, with modes stable when the imaginary part vanishes (or is negative). The frequency is varied, with the modes all stable for frequencies greater than some critical frequency (slightly more than 5). The "outer" mode, with the smallest magnitude of wavenumber and a physical location corresponding to $x_2 > 0.2$ is at all times stable.

3.6.3 Impedance modes

Having separately analysed the case of a wall with no penetration of the fluid through it, and of a wall which cannot support any pressure, we now consider the case where the perturbation pressure and velocity are linked by some linear relationship, quantified in this case by an impedance Z , with boundary conditions as posed in table 3.1. The introduction of this Z does little to change the behaviour of the method of solution, with decomposition into branch cut contributions (and thus far-field noise) and finding propagating modal solutions combining to give a complete solution.

The biggest change from the pressure-release case is that, unless Z is purely imaginary, the dispersion relationship D_Z no longer satisfies the symmetry property $D_Z(k_1^*) = D_Z^*(k_1)$, or equivalently that the relationship is real for real k_1 . Therefore the resulting modes do not pair themselves up into complex conjugate pairs, and further none of them are exactly neutrally stable (all lie off the real axis).

When locating zeros, the first step is typically to eliminate poles of the dispersion function, which are mostly analytically known (arising directly from the singularities in the matching formulae for the piecewise linear case, and thus at $k_1 = \omega/U_j$). In the hard-wall case, a *reduced* dispersion function was defined by multiplying the dispersion function D_h by the product $R(k_1, \omega) = \prod_{j=1}^N (k_1 - \omega/U_j)$, resulting in a function without poles in the k_1 -plane, with the only singularities being the branch point at zero and thus the resulting branch cuts dividing the k_1 -plane into right and left halves. This reduction allowed the use of numerical schemes to find zeros of D_h . A similar reduction can be used in the impedance case. However, an extra pole arises from the definition of ℓ_1^Z , namely the pole arising when the denominator of ℓ_1^Z vanishes, at the roots of

$$i\omega Z k_{1Zp}^2 - \sigma_0 k_{1Zp}(\omega - U_0 k_1) = 0. \quad (3.6.13)$$

The shear at the wall, σ_0 , and the flow speed at the wall, U_0 , both appear as parameters. The trivial root at $k_{1Zp} = 0$ can be ignored (though as we have seen, this does affect the inversion, with care needed at 0), and thus we have an additional pole at

$$k_{1Zp} = \frac{\sigma_0 \omega}{\sigma_0 U_0 + i\omega Z} = \frac{\omega/U_0}{1 + i\omega Z/(U_0 \sigma_0)}. \quad (3.6.14)$$

The reduced impedance dispersion function is then

$$\bar{D}_Z(k_1; \omega) = R(k_1; \omega)(k_1 - k_{1Zp}(\omega))D_Z(k_1; \omega). \quad (3.6.15)$$

This is now analytic in both the right and left-half planes away from the branch point at $k_1 = 0$, and thus amenable to numerical zero-finding methods. This additional pole gives rise to the possibility of an additional zero, giving an estimate of $N + 2$ zeros, for a generic case (away from the singular behaviour seen if $\omega \sim \sigma$ in the pressure-release case): the N zeros for the pole from each shear layer, the additional one from the pole at $k_1 = 0$ (seen in the pressure-release case similarly) and the new zero corresponding to this new pole, k_{1Zp} . The dynamics of the resulting modes, as Z changes, are interesting: when $Z = 0$ one of the modes lies at ω/U_0 and is exactly cancels the additional pole computed above, so doesn't appear for vanishing Z , and thus we reduce to the number of poles seen in the pressure-release case. Conversely, as $|Z|$ gets large we would expect a reduction to exactly N modes, and thus two of the zeros must disappear. The only mathematically consistent ways of this occurring is for them to go through the branch cuts, and thus off the visible k_1 -plane, though their contribution might still be seen through the branch-cut integrals; or for them to go to infinity.

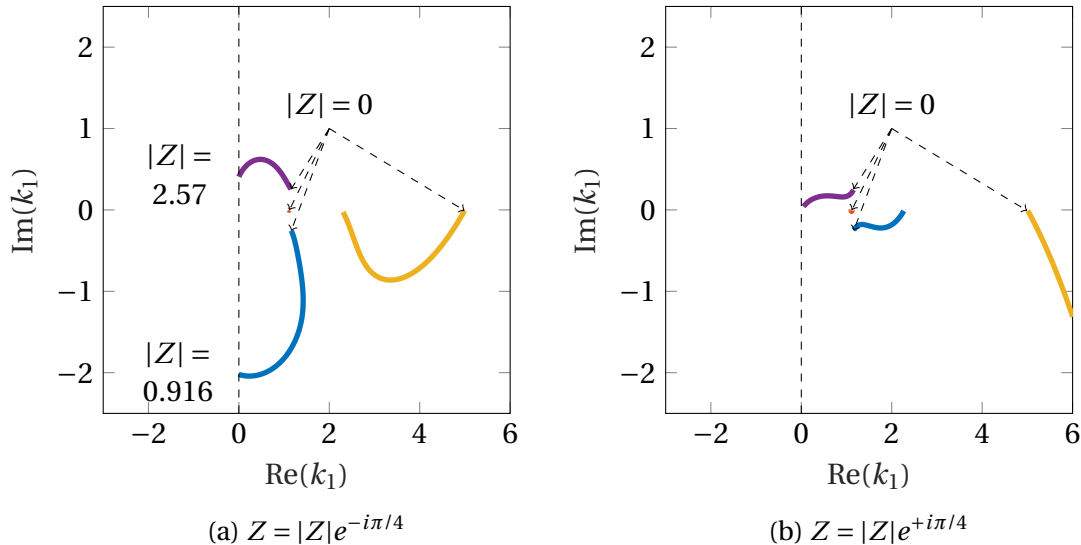


Fig. 3.6.6 For simple two-piece profile ($U = (0.2, 0.8, 1)$; $\delta = (0, 0.2, 1)$, $\omega = 1$), the 4 boundary-layer modes are tracked as the amplitude of the impedance is varied, with $Z = 0$ indicated for all modes.

The boundary-layer modes of a simple two-piece profile are considered in figure 3.6.6, as the magnitude of Z varies (with complex argument $\pm\pi/4$). The pressure-release case is attained at $Z = 0$. The "outer" mode $k_1 \sim 1.11$ varies little in Z , and is therefore hard to pick out on this figure. In both cases the hard-wall modes are found as $Z \rightarrow \infty$, though they do not correspond to the same pressure-release modes: in the case $\text{Im}(Z) < 0$, two modes (the unstable pressure modes) move behind the branch cut at some finite $|Z|$ and

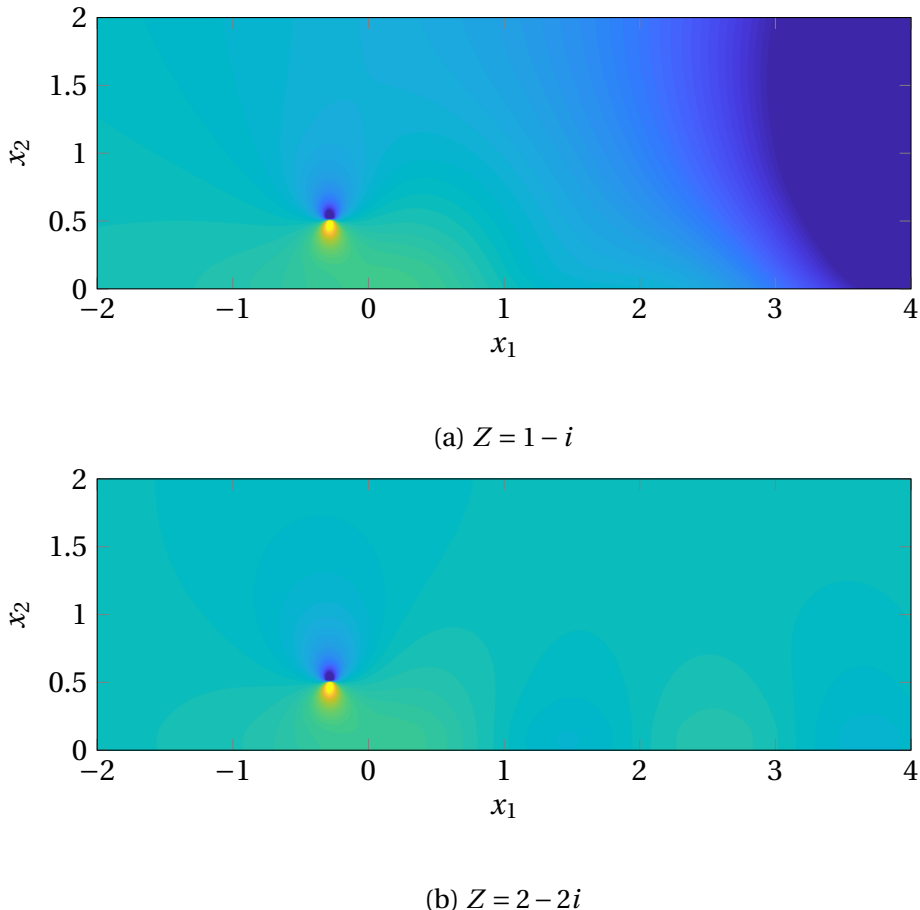


Fig. 3.6.7 For the same flow profile and frequency as figure 3.6.6, the complete pressure perturbation, above a lined wall with impedance Z , is calculated. With colour scales the same between plots, the clear difference between the unstable case in (a) and the stable case in (b) can be seen, with the exponentially growing mode (in (a)) on the other sheet of the complex plane for larger Z , and thus not present in the final solution.

leave the two stable modes for the hard-wall boundary condition. Conversely, in the case $\text{Im}(Z) > 0$, one unstable mode moves to $k_1 = 0$ (and thus cancels out the pole there), but is unstable for all finite $|Z|$. One mode, the “inner” stable mode, moves to ∞ in the LH k_1 P, and the final hard-wall mode is actually the stable pressure-release mode.

Following an identical decomposition as before, with a branch cut integral (decaying exponentially) and contributions from the modes discussed, the complete perturbation field can be computed, for example the pressure perturbation shown in figure 3.6.7 for the two-piece profile, with two different impedances. The latter impedance is such that the unstable mode is behind the branch cut, as per figure 3.6.6a, and thus does not contribute to the solution, and thus the solution is stable provided $|Z|$ is suitably large.

3.6.4 Far-field noise

When computing the far-field noise due to a mass source above a hard boundary, we could directly write down an expression for far-field streamfunction, ψ . However, as we have seen, the integral expression for the Fourier inversion for ψ has a pole at 0, which causes difficulties. We can, however, compute expressions for the far-field velocity components due to the inner solution, which can in turn be matched to an outer solution.

We work with the generic boundary condition, on $x_2 = 0$, with $\mathcal{L}\psi = \ell_1\psi' + \ell_2\psi = 0$. We have the integral expression for v'_0 , the wall-normal velocity perturbation, outside the boundary layer (so $x_2 > \delta$)

$$v' = \frac{Q(y_2)}{2\pi i} \int_{F_1} \frac{ik_1\phi_\ell(y_2; k_1)}{D_\ell(k_1)} \frac{e^{-|k_1|x_2 - ik_1x_1}}{k_1 - \kappa_1} dk_1 \quad (3.6.16)$$

with Q defined as for (3.5.6). By Watson's lemma, this is dominated near $k_1 = 0$, where we need evaluate both ϕ_ℓ and $D_\ell = \mathcal{L}\phi_d$. In this limit the shear jump becomes unimportant, and we thus have

$$\phi_\ell \sim A_0 e^{|k_1|x_2} + B_0 e^{-|k_1|x_2} \quad (3.6.17)$$

as $k_1 \rightarrow 0$, (for all x_2) where

$$A_0 = -\frac{\ell_2}{2|k_1|} + \frac{\ell_1}{2} \quad (3.6.18a)$$

$$B_0 = +\frac{\ell_2}{2|k_1|} + \frac{\ell_1}{2} \quad (3.6.18b)$$

and $D_\ell \rightarrow -|k_1|\ell_1 + \ell_2$ as $k_1 \rightarrow 0$. Both of these results are completely generic, regardless of the exact form of the boundary condition imposed. If we consider some region of the complex k_1 -plane near the origin, we then have

$$v' \sim -\frac{Q}{2\pi i \kappa_1} \int_{F_{1c}} \frac{ik_1(\ell_1 - \ell_2 y_2)}{\ell_2 - |k_1|\ell_1} e^{-|k_1|x_2 - ik_1x_1} dk_1 \quad (3.6.19)$$

where we have reduced the exponentials in the auxiliary function for small k_1 . Introducing complex observer location $z = x_1 + ix_2$, we integrate along the rays parameterised by $s = ik_1 z^*$ for $\text{Re}(k_1) > 0$ and $s = ik_1 z$ for $\text{Re}(k_1) < 0$, exactly as in figure 3.5.7. We then have

$$v' \sim -\frac{Q}{2\pi i \kappa_1} \int_0^\infty I\left(\frac{s}{iz^*}\right) e^{-s} \frac{ds}{iz^*} + \frac{Q}{2\pi i \kappa_1} \int_0^\infty I\left(\frac{s}{iz}\right) e^{-s} \frac{ds}{iz} \quad (3.6.20)$$

with

$$I(k_1) = \frac{ik_1(\ell_1 - \ell_2 y_2)}{\ell_2 - |k_1|\ell_1} \quad (3.6.21)$$

For both the pressure and impedance boundary conditions, we have $\ell_2 = 1$ and $\ell_1 \sim \frac{C}{C'} \sim \frac{\omega}{k_1 \sigma}$ as $k_1 \rightarrow 0$. It is this singularity of ℓ_1 at $k_1 = 0$ that leads to the resulting singularity of the integrand when computing ψ , for example. With this, we have

$$I = \frac{ik_1 \alpha}{1 - \alpha \operatorname{sgn}(k_1)} \quad (3.6.22)$$

for k_1 small, where $\alpha = \omega/\sigma$ is the ratio between the frequency and the background shear at the wall. Importantly, this is finite (albeit discontinuous) at $k_1 = 0$, for $\alpha \neq \pm 1$. The far-field contribution is then

$$v' \sim \frac{Q}{2\pi\kappa_1} \left[\frac{\alpha}{\alpha - 1} \frac{1}{z^*} - \frac{\alpha}{\alpha + 1} \frac{1}{z} \right] \quad (3.6.23)$$

for $x_2 \gg \delta$. We focus firstly on the latter term, noting that $1/z$ corresponds could correspond to an irrotational velocity potential $W = \phi + i\psi = \log(z)$. This in turn can be matched to an irrotational far-field flow $\phi \propto H_0^{(2)}(k_0 r)$, which is an expected solution of Helmholtz equation, and critically it does not depend on the angle with respect to the source, θ . It is exactly the solution due to a mass source in shear flow with no boundary, and the alternate term, containing $1/z^*$, is exactly the image source required to satisfy the boundary condition on $x_2 = 0$: again radiating like $H_0^{(2)}(k_0 r)$. We thus suppose we have a far-field acoustic potential ϕ , so that $\mathbf{u} = \nabla\phi$ and $p' = \rho_0 D\phi/Dt$. ϕ satisfies the convected Helmholtz equation, and as such we have (assuming limited angular dependence due to the form of the inner solution)

$$\phi = e^{-ik_0 M_\infty r \cos(\theta)} A H_0^{(2)}(k_0 r) \quad (3.6.24)$$

which satisfies the convected Helmholtz equation (for $U_\infty \ll 1$), as noted in §3.5.3 and equation (3.5.18). As $r \rightarrow 0$,

$$H_0^{(2)}(k_0 r) \sim \frac{2i}{\pi} \log(k_0 r/2). \quad (3.6.25)$$

Matching both terms of the inner solution to this (assuming their contribution is the same, or for example letting $x_2 \mapsto -x_2$ to properly deal with the z^* term), we have

$$\frac{2i}{\pi} A = \frac{Q}{2\pi\kappa_1} \left[\frac{\alpha}{\alpha - 1} - \frac{\alpha}{\alpha + 1} \right]. \quad (3.6.26)$$

and so

$$A = \frac{Q}{2i\kappa_1} \frac{\alpha}{\alpha^2 - 1} \quad (3.6.27)$$

From this, we can deduce we have an outgoing cylindrical pressure wave, with p approximately given by $i\omega\phi$. There are two contributions: the contribution from the source itself, and the contribution from the reflection off the wall. Since the reflected solution does not correspond to the original solution, due to the distortion by the boundary-layer shear, they are not cancelled out exactly and the radiated sound consists of the summation of two cylindrical waves (in phase through the long-wavelength assumption). Compare this with the hard-wall, where the choice of boundary conditions ensured a cancellation of original and image sources, and a dipole in the far-field.

It is worth stress-testing this result, especially due to the non-routine methods of dealing with the z^* term. If there is no shear, and no flow, we have $\alpha \rightarrow 0$ and $A \rightarrow 0$. This does not correspond to no far-field noise due to the source, just that the monopole-type source vanishes. There will still be the dipole source. Essentially, when the flow is uniform, the original source (above the wall) and the image source (below the wall) exactly cancel each other out in the far-field. When ω is small, A is non-zero since κ_1 as well as α is proportional to ω .

Finally, we note that this is singular when $|\alpha| = 1$, and large for $|\alpha| \approx 1$. It is worth comparing this result to the earlier analysis of the single-piece shear, when the limit $\alpha \rightarrow 1$ gave rise to a countable infinity of otherwise unseen modal solutions.

3.7 Fixed mass or momentum source: Wake

As a final boundary condition, we consider the case with no surface at $x_2 = 0$, with instead the domain stretching to $x_2 \rightarrow -\infty$. Before we insisted on solely outgoing waves as $x_2 \rightarrow \infty$, leading to the imposition of decay like $\exp(-|k_1|x_2)$ in streamwise Fourier space. This time, we similarly impose decay as $x_2 \rightarrow -\infty$, and thus behaviour like $\exp(|k_1|x_2)$, as $x_2 \rightarrow -\infty$, in Fourier space, which motivates the construction of the second auxiliary function, controlling behaviour beneath the vortex sheet at $x_2 = y_2$, as being the solution that exponentially decays as $x_2 \rightarrow -\infty$.

For concreteness, we consider the flow profile illustrated in figure 3.3.2 (in turn explaining the extended domain of that figure) and define two auxiliary functions $\psi_{1,2}$ to be the solution to the governing equations $((d^2/dx_2^2 - k_1^2)\psi = 0$, with associated jump

conditions at δ_j) such that

$$\psi_1(x_2) = \exp(-|k_1|x_2) \quad x_2 > \delta_{N_+} \equiv \delta_\infty \quad (3.7.1a)$$

$$\psi_2(x_2) = \exp(|k_1|x_2) \quad x_2 < \delta_{N_-} \equiv \delta_{-\infty} \quad (3.7.1b)$$

That is, $\psi_1 = \psi_d$ is the decaying solution from before. If we defined an reversed flow profile via $U_j^- = U_{-j}$ and $\delta_j^- = \delta_{-j}$, then $\psi_2(x_2) = \psi_d^{U^-}(-x_2)$, with the decaying solution arising from the reversed profile. For a *symmetric* profile, defined here as one with $U_j = U_{-j}$ and $\delta_j = \delta_{-j}$, then $\psi_2(x_2) = \psi_1(-x_2)$, which somewhat simplifies the analysis.

The general solution to the point mass source is unchanged, under the choice of the new auxiliary functions, with

$$\psi_{01}(x_2) = -\frac{U'(y_2)q_0}{U(y_2)\rho(y_2)} \frac{1}{i(k_1 - \kappa_1)} \frac{1}{W(y_2)} \times \begin{cases} \psi_1(x_2; k_1)\psi_2(y_2; k_1) & x_2 > y_2, \\ \psi_2(x_2; k_1)\psi_1(y_2; k_1) & x_2 < y_2, \end{cases} \quad (3.7.2)$$

exactly as in (3.4.15). Whilst the Wronskian, as a function of y_2 , is easy to define as

$$W(y_2) = \psi'_1(y_2)\psi_2(y_2) - \psi'_2(y_2)\psi_1(y_2), \quad (3.7.3)$$

we would like a y_2 -independent expression, namely $W(0)$. Since, typically, we have chosen $x_2 = 0$ to correspond to δ_0 , care is required here with the values of ψ'_1 and ψ'_2 discontinuous over δ_0 . Further, to really exploit the generalisation of ϕ_d to generate ϕ_2 , we would like to evaluate ϕ_2 below the wake, at $x_2 = 0^-$. Using the jump condition, we have

$$W(0^+) = \psi'_1(0^+)\psi_2(0^-) - \psi'_1(0^+)\psi_2(0^-) + \Delta_0\psi_1(0^+)\psi_2(0^-). \quad (3.7.4)$$

As before, the jump across the shear junction at δ_0 , this time corresponding to the wake, is controlled by

$$\Delta_0 = \frac{i k_1 (\sigma(0^+) - \sigma(0^-))}{i(\omega - U_0 k_1)}. \quad (3.7.5)$$

We compare this to a dispersion function, created directly from imposition of pressure and velocity across the wake, as

$$D_w(\omega, k_1) = \mathcal{P}_{01}^{0^+}\psi_1\mathcal{V}_{01}^{0^-}\psi_2 - \mathcal{P}_{01}^{0^-}\psi_2\mathcal{V}_{01}^{0^+}\psi_1 \quad (3.7.6)$$

with zeros of this function directly corresponding to solutions of the governing equation which decay as $|x_2| \rightarrow \infty$ in both directions. As hoped, and analogously with the earlier

work, this corresponds to the Wronskian with

$$D_w = i(\omega - k_1 U_0) W, \quad (3.7.7)$$

and we therefore have exactly the solution of the form required. Fourier inversion can then proceed as before: modal solutions from zeros of the dispersion function are combined with integration around the $|k_1|$ branch cut to determine a complete, causal solution.

3.7.1 Simplification in the symmetric case

As noted above, ψ_1 and ψ_2 are closely linked when the background profile is symmetric, with $\psi_1(0^+) = \psi_2(0^-)$ and $\psi'_1(0^+) = -\psi'_2(0^-)$, with the dispersion function in the symmetric case therefore reducing to

$$D_w = 2\mathcal{V}_{01}^{0^+} \psi_d \mathcal{P}_{01}^{0^+} \psi_d = 2D_h \cdot D_p, \quad (3.7.8)$$

with ψ_d simply the decaying solution as when there was a boundary at $x_2 = 0$ (so corresponding to ψ_1).

We have a natural separation into hard-wall and pressure-release solutions, which is unsurprising, by considering constructing modal solutions. Suppose we have a hard-wall modal solution $\psi_{mh}(x_2; k_{1mh})$, with $\psi_{mh} \rightarrow 0$ as $x_2 \rightarrow \infty$ and $v_{mh} = 0$ on $x_2 = 0$. Then the streamfunction given by

$$\psi = \begin{cases} \psi_{mh}(x_2; k_{1mh}) & x_2 > 0, \\ -\psi_{mh}(-x_2; k_{1mh}) & x_2 < 0, \end{cases} \quad (3.7.9)$$

satisfies decay in both directions $|x_2| \rightarrow \infty$, as well as continuity of wall-normal velocity and pressure across $x_2 = 0$. The former is trivial, as $v' = 0$ here, the latter follows from the antisymmetry of the pressure operator across $x_2 = 0$ (when the background profile is symmetric, so that $C'(0^+) = -C'(0^-)$). That is, hard-wall modal solutions are also symmetric wake modal solutions. The same result holds with pressure-release solutions, the only difference being replacement of the leading $-$ sign for $x_2 < 0$ by a $+$: essentially the pressure-release and hard-wall modal solutions correspond to antisymmetric and symmetric wake solutions respectively (when the background flow is symmetric).

This observation gives a handle on the expected number of modal solutions in the symmetric case, with $N_w = N_p + N_h$ (where N_j are the number of zeros of D_j). For simple profiles (away from the singular limit $\sigma \approx \omega$), this suggests we would expect $(N+1) + N = 2N+1$ zeros, where N is the number of piecewise linear pieces of the background profile

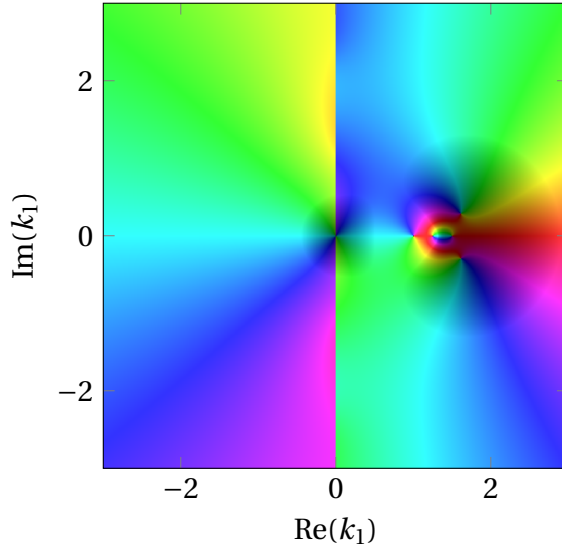


Fig. 3.7.1 Dispersion function $D_w(k_1)$ for $U = (0.8, 0.2, 1), \delta = (-1, 0, 1)$, an example of profile III introduced earlier, with frequency $\omega = 1$. This is the complete, rather than reduced, dispersion function, so two poles, due to the jumps in shear, are visible as the brightest points on the plot. There are a pair of complex conjugate zeros and a single real zero, essentially generalising the pair of complex conjugate zeros for an unstable pressure-release wall and the stable zero for a hard-wall.

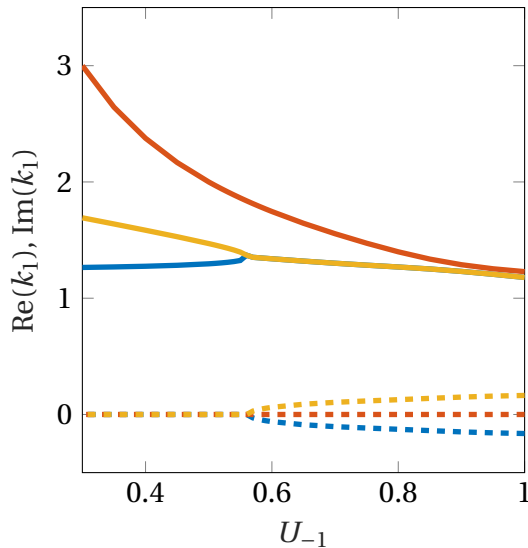


Fig. 3.7.2 The effect of asymmetry on the stability of the modes is investigated, by considering $\delta = (-1, 0, 1)$ fixed and allowing $U = (U_{-1}, 0.5, 1)$ to vary. We fix $\omega = 1$, and profiles stable with this frequency need not be stable to other frequencies. The real (solid) and imaginary (dashed) parts of the three modes are shown, as U_{-1} varies: all three modes are stable for suitably low free stream velocities below the “wake”.

(limited to $x_2 > 0$). This number extends to asymmetric profiles, though if there is a large difference between the flow above and below the wake these modes could disappear behind the branch cut along the real axis.

An example of the dispersion function for an asymmetric profile can be seen in figure 3.7.1, with a conjugate pair of stable/unstable modes and a single neutrally stable mode (as well as the two poles at ω/U_∞^\pm , the brightest colours on the image), bearing many similarities to the pressure-release dispersion function as before. The stability of these modes as the free-stream velocity below the plate, denoted U_{-1} , is varied is considered in figure 3.7.2, for a slightly different profile. For the lower velocity suitably small, so the profile is monotonic ($U_{-1} \leq 0.5$), or nearly so, all the modes are stable for the chosen frequency.

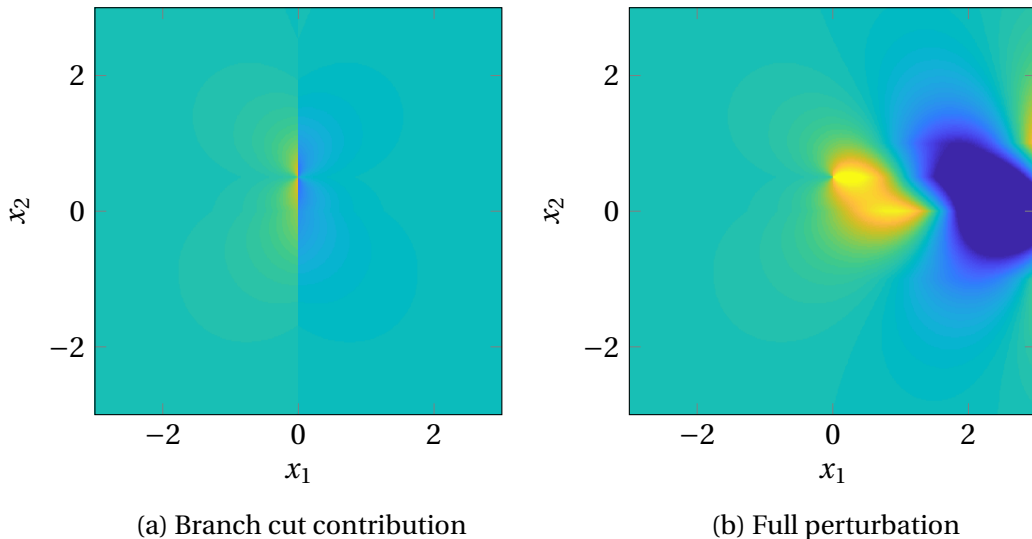


Fig. 3.7.3 The vertical velocity disturbance to an asymmetric wake due to a point source, at $y_2 = 0.5\delta_1$, with profile as in figure 3.7.1. Whilst the colours are capped in the second image, due to the rapid growth of the exponentially unstable mode (and so that the two figures have the same scale), a clear growth along the wake itself, excited by the trailing vortex sheet behind the source, can be seen, and quickly dominates the solution.

The observation that modes can be decoupled into pressure-release and hard wall, in the symmetric case, also indicates the earlier Briggs-Bers analysis for unstable pressure modes still holds, and thus they are typically convected downstream (provided the background flow profile remains positive), and thus the typical contour deformation seen earlier is still useful, and can straightforwardly be applied to this geometry without modification (save to include negative x_2). For a simple profile with limited asymmetry, the resulting velocity perturbation is plotted in figure 3.7.3, with the contribution from

the branch cuts (either in the UHP for negative x_1 or the LHP for positive x_1) synthesised without the modal excitation.

3.8 Discussion and conclusions

Previous work has shown that consideration of a constant-shear boundary-layer gives rise to analytically tractable solutions to the equations governing long-wavelength perturbations, which can be matched to a radiating acoustic solution in the far-field. This chapter has extended that work to more complicated boundary-layers, comprised of intervals of constant shear, with careful matching conditions across the interfaces where the background shear is discontinuous. This model lends itself to consideration of a point mass source which, in agreement with a similar problem studied by Rienstra et al. [92], generates a vortical and an acoustic disturbance in the presence of background shear.

This previous work noted a modal solution due to the presence of linear shear, a term similarly found by Brambley et al. [22] in considering a similar problem in a curved duct, though in the latter case work was required to separate this mode from the critical-layer due to the curvature of the duct. This chapter has developed this theory, demonstrating the presence of this modal solution is a natural consequence of a jump in background shear. By increasing the number of junctions across which the background shear jumps, there is a corresponding increase in the number of modal solutions. This should partially serve as a warning with using broken-line profiles as approximations to profiles with continuously varying shear, as the next chapter will investigate, with this modal solutions not necessarily appearing in the latter case.

As noted in the introduction, the existence of surface modes, stable and unstable, above a lined wall was identified by Rienstra and others in uniform flow [86, 87], and later for sheared flow [111]. This work reproduces these results with surface modes naturally dropping out of the analysis for lined walls, which in turn can be matched back to pressure-release modes for $Z = 0$. The “outer” modes, corresponding to convective velocities further away from the walls, are little changed by the introduction of a lined wall, maintaining a similar location and structure to the hard-wall case, though the introduction of lining can have a much greater effect on the “inner” modes. Further, we established that it is not possible to cleanly identify pressure-release or hard-wall modes with impedance modes as Z varies, since different modes disappear (either through a branch cut or to infinity) depending on the argument of Z .

The quasi-numerical model developed in this chapter offers a rapid tool for computing near field scattering from a mass source, though it is limited only to long-wavelength dis-

turbances, and rapidly loses numerical efficiency as the number of pieces, N , is increased. That said, it is possible to use the results to calculate far-field noise directly, since analytic expressions for Fourier transformed quantities exist. Whilst this work only considers the first-order far-field contribution, via a limited application of Watson's lemma, expansion of the Fourier inversion integrand near $k_1 = 0$ in a series would allow a complete asymptotic expansion of the far-field sound as a sum of Hankel-type solutions to Helmholtz equation.

Two caveats must be mentioned, both considering the pressure-release (or impedance) case when the background shear σ and the frequency ω are comparable. Two points jump out: firstly that we cannot use the methods developed in this chapter to compute the far-field sound, with seemingly infinite acoustic response developing. The second issue is the emergence of “branch cut” modes, which are otherwise hidden on another Riemann sheet of the complex plane. As has been demonstrated, an infinity of such modes occur as $\omega \rightarrow \sigma$, and their effect is not completely understood. These two issues suggest this limit should be investigated more closely, in particular understanding the physical mechanism that leads to this singular behaviour.

The central aim of this chapter was to understand gust-like, rotational solutions to Rayleigh's equation in an analytically tractable limit. Through the identification of preferentially excited modal solutions, we obtain a family of solutions convecting at a speed beneath the free-stream velocity, regardless of the boundary condition being considered. Given typical scattering models consider a gust-type harmonic solution convecting at some prescribed convection velocity, beneath the free-stream velocity, we have a natural theoretical determination of potential convection velocities, dependent on the physical “location” of the modal solution within the boundary-layer.

The next chapter will develop a more comprehensive method for solving a similar problem, which loses the analytic nicety of this method but is more generally applicable, and allows revisiting of some potentially problematic results presented in this chapter, for example the radiation above a pressure-release or impedance lining.

Chapter 4

Disturbances to continuously sheared flow above a homogeneous boundary

The results of the previous chapter, §3, are extended to include an arbitrary continuous background profile, allowing for variation of background density (or equivalently background speed of sound), inclusion of three-dimensional effects and direct inclusion of compressibility in the perturbations. This allows analysis and development of the gust solutions identified in the previous chapter, by focusing again on the acoustic disturbance scattered from a point mass source.

4.1 Introduction

Whilst allowing for analytic solutions, the simplification of the Rayleigh equation in the previous chapter neglects many of the physical effects contained within the full equation, in particular the opportunity to directly consider compressible solutions. Relaxing these assumptions requires numerical solution of the time-harmonic, streamwise transformed Rayleigh equation, or its adjoint. Here, we focus on the adjoint equation as it gives rise to a similar convected quantity as Orr's equation (3.1.1), generalising the perturbation vorticity, and therefore allows direct treatment of the wake of a point mass source.

Numerical solution of the (adjoint) compressible Rayleigh equation throws up new difficulties that the previous formulation avoided with the need to carefully treat the critical-layer [73, 22, 50]. For fixed streamwise wavenumber k_1 , there is a regular singular point of the differential equation wherever $k_1 = \omega/U(x_2)$. We primarily consider monotonic boundary-layers, with $U(0)$ and $U(\delta) = U_\infty$ at the edge of the boundary-layer (where δ could be infinite). The differential equation then has a regular singular point

at $x_2 = U^{-1}(\omega/k_1)$ if $k_1 \in (\omega/U_\infty, \omega/U_0)$ (or $k_1 \in (\omega/U_0, \omega/U_\infty)$ if the profile is decreasing in x_2). A standard quantity of interest is the (hard-wall) dispersion function, $D_h = \nabla\phi_d$, which is the wall-normal velocity at the wall of the solution which decays as $x_2 \rightarrow \infty$. This can be computed by matching to ϕ_d at either the edge of the boundary-layer, or as $x_2 = \infty$, using the fact that was can solve the governing differential equation in uniform flow. As noted in the previous chapter, zeros of this dispersion function correspond to modal solutions of the differential equation.

This dispersion function has a branch cut, in the streamwise wavenumber plane, along $k_1 \in (\omega/U_\infty, \omega/U_0)$, driven by the singular point. This can cause numerical difficulties when evaluation near this critical-layer is required (for example when computing Fourier inversion) or when the behaviour of functions on the critical-layer itself is of interest (for example if there is a pole on the critical-layer). Previous work [22] has suggested a Frobenius series-based approach, which allows for very precise solutions near the regular singular point itself, where the solution is in some sense “known”, which can be matched to integrated solutions either side of the critical point. The Frobenius series naturally gives rise to a logarithmic term at this point, and theoretically the choice of the branch cut of the logarithm allows some control of the location of the critical-layer. Whilst this is practical when the background profile is linear, since there is only a single singular point, it becomes more difficult for profiles that, if extended beyond the boundary-layer, would be non-monotonic. An alternative method is outlined here, which instead integrates the differential equation through the complex extension of physical coordinate x_2 . This allows deformation of the branch cut as required, though it still connects the points ω/U_∞ and ω/U_0 . It also reduces the number of numerical points required, since evaluation of the ODE solution near the critical-layer requires a very small step size to reduce error caused by proximity to the singular point. The methods of these solutions are outlined in §4.2, and the resulting strengths and weaknesses are analysed. This also allows evaluation of the strength of the piecewise-linear methods, in the preceding chapter, as approximations to more complicated profiles.

With this done, the point source problem is reintroduced, including direct evaluation of the far-field sound through the method of steepest descent. This problem is primarily considered as an introduction to the methods of Fourier inversion used in later chapters, as well as to motivate the construction of gust solutions for scattering problems, permitting rapid computation of the scattered solution in the near-field. The use of complex analytic procedures, where appropriate, results in a solution that is independent of the grid being evaluated on, which allows variation of output resolution with computational time directly scaling with the number of evaluation points. When considering disturbances above

lined or pressure-release walls, the surface modes identified in the previous chapter reemerge, and can indeed be associated with the hydrodynamic surface modes found previously (with only minor effects from compressibility). The careful deformation of Fourier inversion contours allows correct understanding of the propagation and growth of these resulting surface modes, dealt with in §4.5. Finally, in §4.6, the previously outlined methods are extended to consider disturbances above a wake, which requires extension of the background flow field to be defined for all x_2 .

4.2 Solving the adjoint compressible Rayleigh equation

The name conventionally given to the governing equation varies depending on context. In a cylindrical duct, the streamwise and azimuthally Fourier transformed/expanded form of the pressure equation, (2.2.8), is typically referred to as the Pridmore-Brown equation [82]. In this section, we consider the temporal, streamwise and spanwise transformed version of the *adjoint* equation (2.3.10) in a boundary-layer, resulting in a second order ordinary differential equation (ODE) in the wall-normal coordinate x_2 . Whilst this bears many similarities to the Pridmore-Brown equation, the rectilinear geometry (and thus removal of terms like $1/r$) means we are, in practice, merely solving the compressible analogue of the incompressible Rayleigh stability equation. In regions of uniform flow (and the long-wavelength limit with uniform shear as seen in the previous chapter), this can be solved analytically, and the solutions are developed below. High-frequency asymptotic solutions are also readily attainable via the WKBJ method [1]. Both are then compared to numerical methods of solving the equations, chosen to be efficient in variation of the streamwise wavenumber k_1 : both brute-force Runge-Kutta integration across the boundary-layer, and a Frobenius expansion-based method to properly understand the behaviour of the equation near the critical point, when $\omega = U(x_2)k_1$.

Methods for solution of both the direct and adjoint Rayleigh equation are essentially analogous; in the Fourier transformed case reducing both to second-order differential equations, linear in wall-normal coordinate x_2 , and the resulting modal solutions are the same. This section focuses on the solution to the adjoint equation, as it is useful for the work related to a point source disturbance later in the chapter, with a convected disturbance trailing the source easily picked up through the adjoint formulation. However, in later chapters solution of the direct equation may be preferable (thereby directly obtaining solutions for pressure, p , as function of transformation parameters $\{\omega, k_1, k_3\}$), in particular when the forcing term is streamwise homogeneous (such as far downstream

from a source), and the methods outlined in this section must be suitably modified for the equation $\mathcal{D}_{R013} p_{013} = 0$, which is a straightforward redefinition of ODE coefficients.

4.2.1 Preliminaries

We assume the background flow U and the density ρ_0 (and thus the speed of sound c_0) depend only on the wall-normal coordinate x_2 . The general, transformed equation that we are finding the solution to is

$$\mathcal{D}_{R013}^\dagger \phi_{013} = 0. \quad (4.2.1)$$

The untransformed adjoint Rayleigh operator can be written

$$\begin{aligned} \mathcal{D}_R^\dagger &= D_0^3 - c_0^2 (\partial_1^2 + \partial_3^2) D_0 - \partial_2 (c_0^2 (\partial_2 D_0 + 2U' \partial_1)) \\ &= \left[D_0^3 - c_0^2 (\partial_1^2 + \partial_3^2) D_0 - (3U'(c_0^2)' + 3U''c_0^2) \partial_1 \right] - \left[(c_0^2)' D_0 + 4c_0^2 U' \partial_1 \right] \partial_2 - \left[c_0^2 D_0 \right] \partial_2^2 \end{aligned} \quad (4.2.2)$$

using $D_0 = D_0 / Dt$ and $\partial_i = \partial / \partial x_i$ to simplify notation. The extraction of the wall-normal derivatives ∂_2 allows the triply-transformed Rayleigh operator to be written as

$$\mathcal{D}_{R013}^\dagger = \left[C^3 + c_0^2 C (k_1^2 + k_3^2) - (3C'(c_0^2)' + 3C''c_0^2) \right] - \left[(c_0^2)' C + 4c_0^2 C' \right] \partial_2 - \left[c_0^2 C \right] \partial_2^2, \quad (4.2.3)$$

with, as in §3.2, $C = i(\omega - U(x_2)k_1)$ the transformed convective operator, and thus $C' = -iU'k_1$. Division through by $-c_0^2 C$ and rewriting the derivatives as total derivatives (since everything is now a function of x_2 alone) gives the ODE

$$\frac{d^2\phi}{dx_2^2} + \left[\frac{(c_0^2)'}{c_0^2} + \frac{4C'}{C} \right] \frac{d\phi}{dx_2} + \left[\frac{3(C'c_0^2)'}{c_0^2 C} - (k_1^2 + k_3^2) - \frac{C^2}{c_0^2} \right] \phi = 0. \quad (4.2.4)$$

If the background speed of sound is constant, this reduces further to

$$\frac{d^2\phi}{dx_2^2} + \left[\frac{4C'}{C} \right] \frac{d\phi}{dx_2} + \left[\frac{3C''}{C} - (k_1^2 + k_3^2) - \frac{C^2}{c_0^2} \right] \phi = 0. \quad (4.2.5)$$

A useful fact that will be often used is that the Wronskian can be easily written down. If we have two linearly independent solutions to (4.2.4), ϕ_1 and ϕ_2 then the Wronskian $W = \phi_1 \phi_2' - \phi_2 \phi_1'$ satisfies the differential equation

$$\frac{dW}{dx_2} = - \left[\frac{(c_0^2)'}{c_0^2} + \frac{4C'}{C} \right] W \quad (4.2.6)$$

with the term in square brackets exactly the leading coefficient of ϕ' in the differential equation. Noting it is exactly the derivative of $\log(c_0^2 C^4)$ allows solution of (4.2.6) as

$$W(x_2) = \frac{W_0}{c_0^2 C^4} \quad (4.2.7)$$

with W_0 some constant that can be evaluated at a single location.

From ϕ , we can evaluate wall-normal velocity v' and pressure p' , upon Fourier transformation, as

$$p_{013} = -C^3 \phi_{013}, \quad (4.2.8a)$$

$$v_{013} = -\frac{1}{\rho_0 C} \frac{d}{dx_2} (C^3 \phi_{013}). \quad (4.2.8b)$$

Auxiliary functions

The solution to the ODE is defined by any pair of linearly independent solutions (that is, for which the derived Wronskian does not vanish), as any solution can be constructed from a linear combination of them. However, for comparison between methods, and for the later mathematical analysis, it is useful to focus on a well-defined pair of auxiliary functions. For this purpose, we define ϕ_d and ϕ_h as the decaying and hard-wall solutions respectively, with decaying solution

$$\phi_d(x_2) \sim \exp(-\gamma(k_1, k_3; U_\infty)x_2) \quad x_2 \rightarrow \infty \quad (4.2.9)$$

that is, the decaying solution in uniform flow (see definition of γ in (4.2.12) below), given $U(x_2) \rightarrow U_\infty$ as $x_2 \rightarrow \infty$. The hard-wall solution is chosen so that the derived velocity $v_h = 0$ on $x_2 = 0$. This leaves freedom to normalise ϕ , and thus p_h is arbitrarily chosen to be unity on $x_2 = 0$. Mathematically

$$p_h(0) = 1, \quad (4.2.10a)$$

$$v_h(0) = 0. \quad (4.2.10b)$$

This is the solution above a hard-wall, with no particle displacement through $x_2 = 0$. In later analysis other auxiliary functions, tailored to different boundary conditions, will also be considered, though they can always be written as a linear combination of ϕ_d and ϕ_h .

4.2.2 Analytic solution: Uniform flow

The case of uniform flow is straightforward, and identical to the usual analysis. If C' and $(c_0^2)'$ both vanish, then the ODE is simply

$$\phi'' - \gamma^2(k_1, k_3; U)\phi = 0 \quad (4.2.11)$$

where we define the recurring function γ via

$$\gamma^2 = \left(k_1^2 + k_3^2 \right) - \frac{(\omega - U k_1)^2}{c_0^2} \quad (4.2.12)$$

with the square roots taken so that the branch cuts at the two branch points (in the k_1 -plane) avoid the real axis when the imaginary part of ω is negative (and the relaxation of this when ω is real, as shown in figure 4.2.1) with the branch chosen by the condition that, if k_1 , k_3 and k_0 are all real and $k_1^2 + k_3^2 > k_0^2$, then $\gamma(k_1)$ is the positive square root. With this choice, ϕ has the solutions

$$\phi_{\pm} = \exp(\pm \gamma x_2). \quad (4.2.13)$$

The choice of branch cuts ensures that ϕ_- decays as $x_2 \rightarrow \infty$, and represents outgoing waves, which will be very useful in later analysis. We further note the $\phi_d \rightarrow \phi_-$ by definition (4.2.9), as $x_2 \rightarrow \infty$.

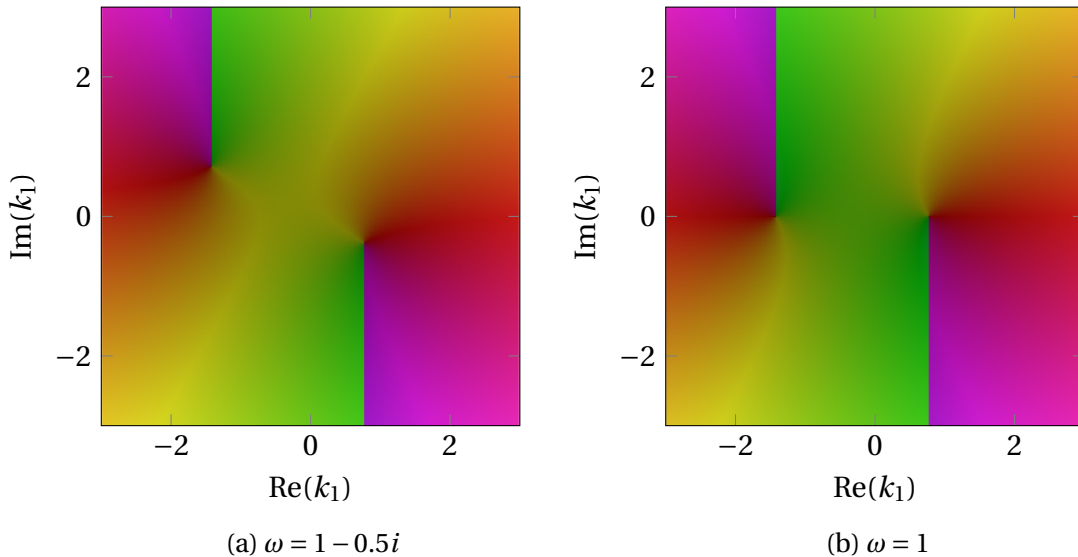


Fig. 4.2.1 Phase plots of γ as ω is relaxed to the real axis. We have $U = 0.3$ and $c_0 = 1$ in both plots. The branch cuts (discontinuities of colour) are chosen to avoid the real axis in the first case, and this is preserved as ω is made real.

4.2.3 Numerical solution: Integration across boundary-layer

For fixed parameters and wavenumbers, it is relatively routine to find the numerical solution to (4.2.4). Imposition of a condition either at infinity (in the decaying case, or if considering perturbations to a wake) or at zero (in the hard-wall case, or other cases with similarly prescribed boundary conditions) and recasting the differential equation into the form

$$\frac{d\Phi}{dx_2} = \mathbf{F}(x_2, \Phi(x_2); \omega, k_1, k_3) \quad (4.2.14)$$

allows implementation of routine Runge-Kutta or similar methods.

The simplest approach is to take $\Phi_1 = \phi$ and $\Phi_2 = \phi'$, which gives simply

$$F_1 = \Phi_2 \quad (4.2.15a)$$

$$F_2 = -q\Phi_1 - p\Phi_2 \quad (4.2.15b)$$

with p and q , functions of x_2 , derived from the governing equation as in (4.2.22) (and not to be confused with pressure fluctuations). In terms of $\Phi = (\Phi_1, \Phi_2)$, the derived physical quantites are

$$p_{013} = -C^3\Phi_1 \quad (4.2.16a)$$

$$v_{013} = -3c_0^2 C' C \Phi_1 - c_0^2 C^2 \Phi_2 \quad (4.2.16b)$$

which can be used to set hard-wall and pressure-release boundary conditions in terms of Φ . If we have U constant outside some region $0 < x_2 < \delta$, then the decaying and hard-wall boundary conditions are, respectively

$$(\Phi_1)_d(\delta) = \exp(-\gamma_\infty \delta) \quad (\Phi_2)_d(\delta) = \left(-\gamma_\infty - \frac{3C'_\infty}{C_\infty} \exp(-\gamma_\infty \delta) \right), \quad (4.2.17)$$

$$(\Phi_1)_h(0) = -\frac{1}{C_0^3} \quad (\Phi_2)_h(0) = \frac{3C'_0}{C_0^4}. \quad (4.2.18)$$

Subscript ∞ implies evaluation at $x_2 = \delta$ and subscript 0 at $x_2 = 0$. Note: this imposes a choice of branch cut on ϕ_d , driven by the behaviour at infinity, through γ_∞ . This, as the asymptotic consideration above, leads to some interesting behaviour as the branch points of γ change as x_2 varies.

For *fixed* k_1 , it is straightforward to use inbuilt integration routines to compute the differential equation solution, for example Matlab's `ode45`, which uses a variable-step mixed RK4/RK5 routine. Varying k_1 can be done by a simple loop over values of k_1 which

require evaluation. This, however, is a slow process, with Matlab being ill-equipped to rapidly evaluate loops. For this purpose, a fixed-step RK4 algorithm, evaluated for vector-input k_1 , was constructed, allowing for evaluation at a large amount of wavenumbers simultaneously. This is useful for both plotting and understanding of dispersion functions (which involve fine complex grids) and for computing Fourier inversions (which require evaluation for many k_1 along the integration contour). The fixed-step criterion is then required to ensure we have the same x_2 grid for each value of k_1 . This causes accuracy issues when terms get large, particularly near the critical layer (see below). The implementation is a standard fourth-order Runge-Kutta scheme (see [115] for example), although use of other integration routines (for example Adams-Bashford based methods, which require a fixed step size in all situations) could also be used.

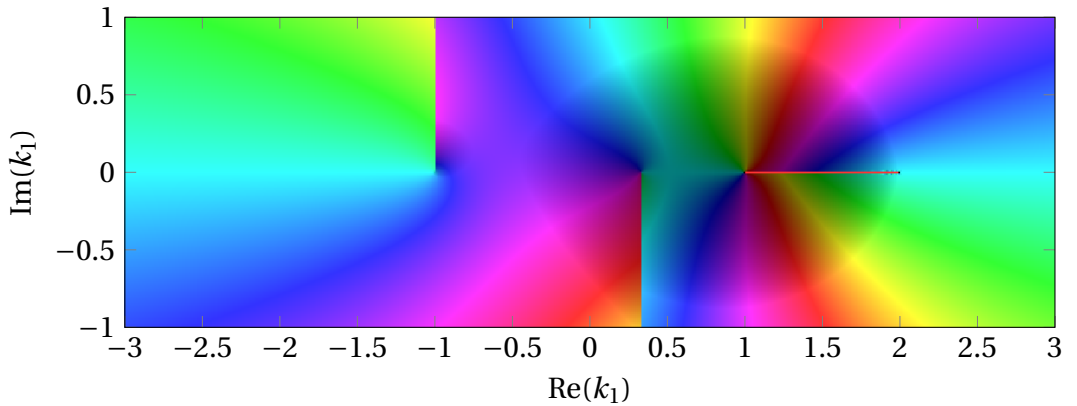
Accuracy of the routine is highly dependent on step size, for which the number of steps N shall be used as a proxy (with step size $\delta x_2 = \delta/N$), and it is worth quantifying the error inherent in this method. We shall do this by analysing the convergence of the hard-wall dispersion function, D_h , defined as

$$D_h(\omega, k_1, k_3) = v_d(0; \omega, k_1, k_3) \quad (4.2.19)$$

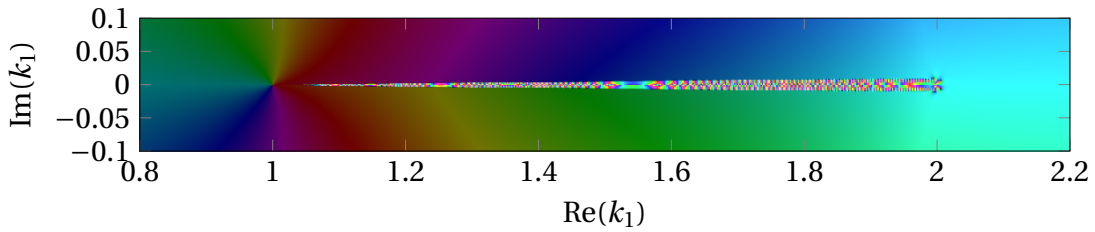
which will be ubiquitous in later analysis. This dispersion function, computed numerically using the above scheme, is shown for a specific boundary-layer configuration in figure 4.2.2 with $N = 1000$, with the second image figure 4.2.2b highlighting errors in the numerical method near the critical layer, the line along which $k_1 = \omega/U(x_2)$ for some x_2 within the boundary-layer.

Given the somewhat *ad hoc* identification of numerical error in the above, essentially through lack of continuity of the dispersion function in k_1 , it is useful to understand how this error behaves as N is increased, which is expected to increase accuracy. This is analysed in a specific case in figure 4.2.3, with the expected N^{-5} dependence that the fourth-order Runge-Kutta algorithm as implemented should obtain. Very close to the critical-layer, for example the point $1.5 + 0.01i$, machine error is reached before an interval of N on which the decay is algebraic, providing a hard-limit on how close to the critical-layer we can evaluate D_h , independently of N .

Comparison of analytic, incompressible solution and integrated numerical solution with finite speed of sound. Given we have an analytic, or at least quasi-analytic, solution for the dispersion function as per the preceding section, it is worth comparing this to the integrated solution obtained when the speed of sound is finite, and how the two solutions converge as the speed of sound is increased. For a linear profile, the *exact*



(a) Dispersion function, capturing the interesting regions near the acoustic branch points and the critical layer.



(b) Magnification of the critical layer from above, showing numerical discrepancies (oscillations near the branch cut).

Fig. 4.2.2 Hard-wall dispersion function for a parabolic boundary-layer, chosen to have continuous shear at $x_2 = \delta = 1$, with $U(\delta) = 1$ and $U(0) = 0.5$, with constant speed of sound $c_0 = 2$ and frequency $\omega = 1$. The branch cuts are clearly visible as discontinuities of phase (colour) and the critical-layer, to the right-hand side of the first image, is zoomed in on in the second. These are computed with a Runge-Kutta routine, with $N = 1000$.

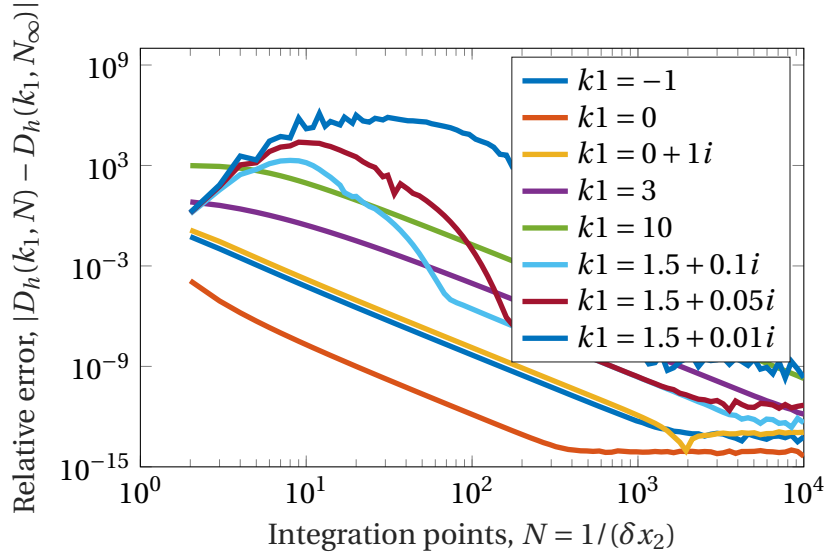


Fig. 4.2.3 The convergence of the numerical routine, computing D_h at arbitrary values of k_1 , as number of integration points, N , is increased. This is compared to evaluation at $N = N_\infty = 10^5$, where the total error of the routine is dominated by machine error, and the computed solution merely fluctuates around some constant value. A simple parabolic profile with $U_0 = 0.5$ and $U_\infty = 1$, with $c_0 = 2$ constant, is used, for frequency $\omega = 1$, though this result is general. The slope is -5 when the above plot is linear, as would be expected for a fourth-order Runge-Kutta algorithm, for all values of k_1 chosen until machine error dominates, after which the error is broadly constant. The only difference is points near the critical-layer, here with $k_1 = 1.5 + i\epsilon$ for various ϵ , where N must be sufficiently high for the error to decay, with the required N increasing as ϵ decreases, and if ϵ is sufficiently small there is a bound on accuracy.

incompressible solution for the dispersion function, $D_{h,\text{incompressible}}$ is compared to the numerically computed solution as $c_0 \rightarrow \infty$ in figure 4.2.4a. As would be expected, there is quite clear divergence for small speeds of sound (and correspondingly large Mach numbers) but as the speed of sound decreases we obtain rapid convergence to the analytic solution, except in an increasingly small region near $k_1 = 0$ (where discrepancy would be most expected, given the inconsistency on the interval between the acoustic branch cuts, $k_1 \approx \pm\omega/c_0$, as $\gamma \rightarrow |k_1|$).

We can do similar analysis for non-linear background profiles, approximated as a combination of piecewise-linear shear pieces in the incompressible case. Again, as c_0 increases the agreement between the two solutions increases, as shown in figure 4.2.4b, *except* along the critical-layer, in this case the interval in the complex k_1 plane between 5 and 10. It is worth noting this plot was computed with k_1 given a slight imaginary part near the critical-layer so as to avoid the numerical problems previously seen. The oscillatory discrepancy is then due to the difference between a branch cut (in the numerical case) and a series of zeros and poles (in the analytic case), and it is expected that the two methods cannot agree in this region. However, the agreement between the two methods increases as the number of piecewise linear pieces, N , is increased (N here is not to be confused with the number of integration points in the numerical calculation). Figure 4.2.5 demonstrates this, by computing the maximal difference between the solutions along the critical layer (that is, the maximal difference of the ratio of the computed dispersion functions from unity). As N increases this error decreases (though very slowly), and the sequence of zeros and poles more closely resembles the branch cut it is approximating. That these are fundamentally different things must be borne in mind when doing calculations with the linear-shear approximation: the reduction of the critical-layer branch cut to a series of poles and zeros misses out some of the fundamental mathematics associated with the branch cut, even though the two solutions appear to behave similarly as $N \rightarrow \infty$.

4.2.4 Numerical solution: Integration across "complex" boundary-layer

For fixed k_1 , the critical points of the differential equation, at $x_2 = U^{-1}(\omega/k_1)$, cause numerical problems if they lie on or near the real axis, when we attempt to determine ϕ_{01} on $x_2 \in (0, \delta)$. While routines based on the method of Frobenius, for example, can alleviate this problem in simple cases (see appendix §B.1), there is a desire to use numerical integration methods that are exact near $k_1 \in (\omega/U_\infty, \omega/U_0)$, values of k_1 such that a critical point lies within the (real) boundary-layer. This can be done via the introduction of a complex coordinate z , with $z = x_2$ on the real axis, and instead of integration of the differential equation along the real contour with x_2 running from δ to 0 (or the other way

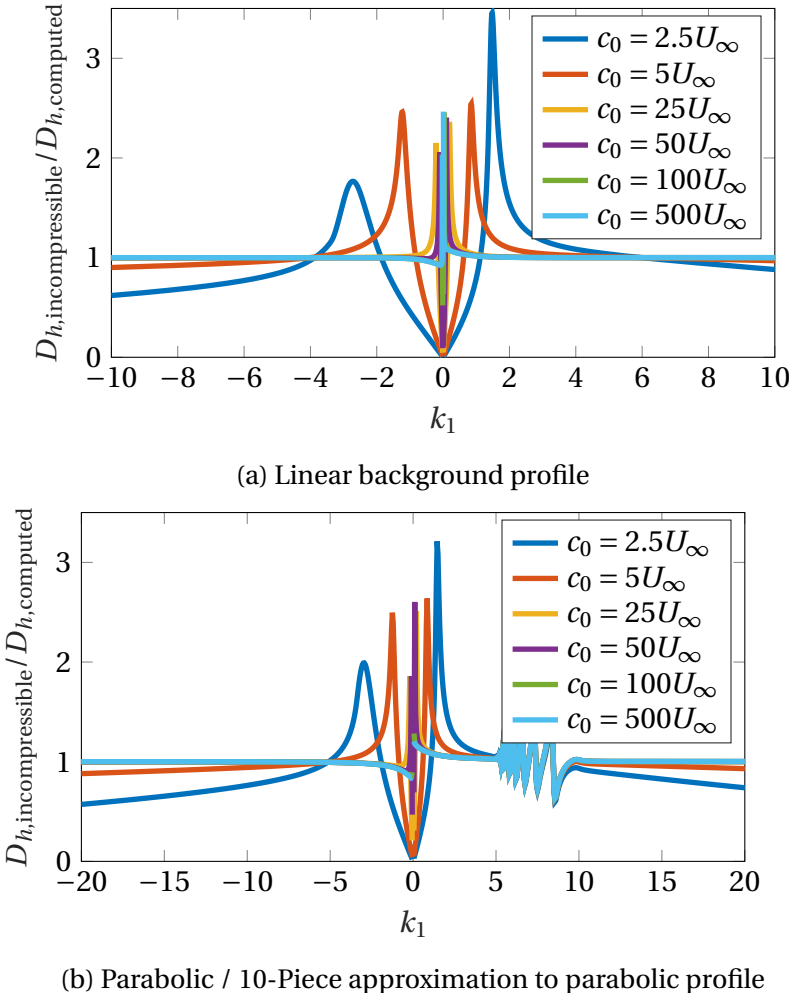


Fig. 4.2.4 For profiles with $U_0 = 0.1$ and $U_\infty = 0.2$, the ratio of the computed dispersion function with finite c_0 , with the analytic incompressible dispersion function is displayed. For the second case, a parabolic profile, the background profile is approximated by N linear pieces in the incompressible case. For large c_0 , both solutions are equivalent except near $k_1 = 0$ and along the critical-layer in the second case. It is worth noting the discrepancy along the critical-layer is broadly independent of c_0 .

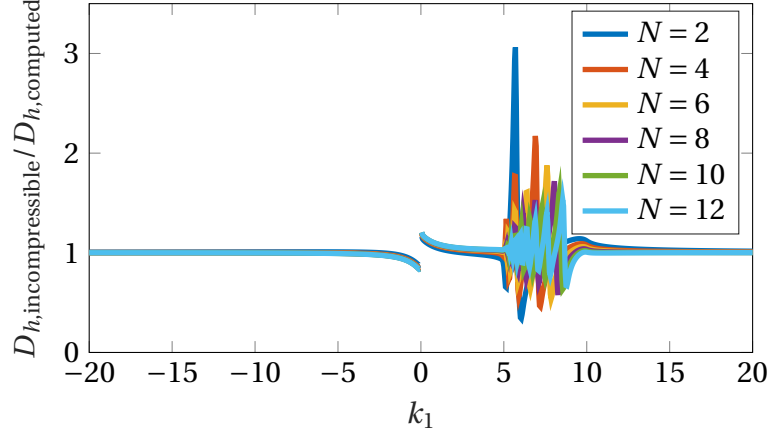
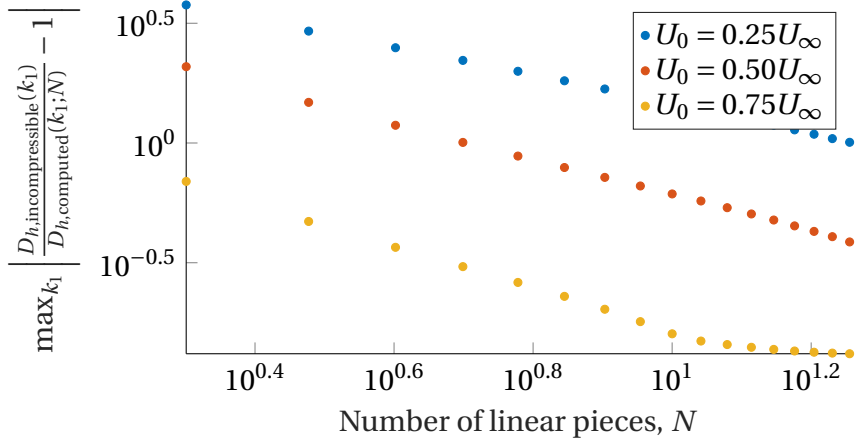
(a) An N -piece approximation to a parabola with continuous shear at the free-stream(b) The maximal value of the discrepancy of the two functions. The slope is around -0.75 in the three cases considered.

Fig. 4.2.5 As per the previous figure, figure 4.2.4, the analytic and numeric solutions differ on the critical-layer. This figure shows the increase in accuracy as the number of linear pieces, N , is increased. The first figure shows that, away from the critical-layer, only a small value of N is required for very close accuracy (here, $c_0 = 500U_\infty$ and so the numerical solution is very close to incompressible). The peak of the discrepancy is used as an estimate of the error, which is plotted in the lower figure for three different parabolic flow profiles (by varying the slip velocity). The accuracy increases with N , but slowly, and the error is still large (and non-negligible) for large N . This suggests care is required when approximating a background profile with non-constant shear by a sequence of line segments, as the critical-layer effects can never be entirely obtained: in particular the replacement of a branch cut by a sequence of poles and zeros leads to non-decaying modes, whereas (as we shall see) the contribution from the critical-layer typically decays downstream.

around), instead run z from δ to 0 via a suitably chosen contour in the *complex* plane. This requires $U(z)$ to be a complex analytic function of its argument, which is trivially the case with simple polynomial profiles as previously discussed, as well as more complicated profiles such as a tanh profile, or a suitably computed Blasius profile.

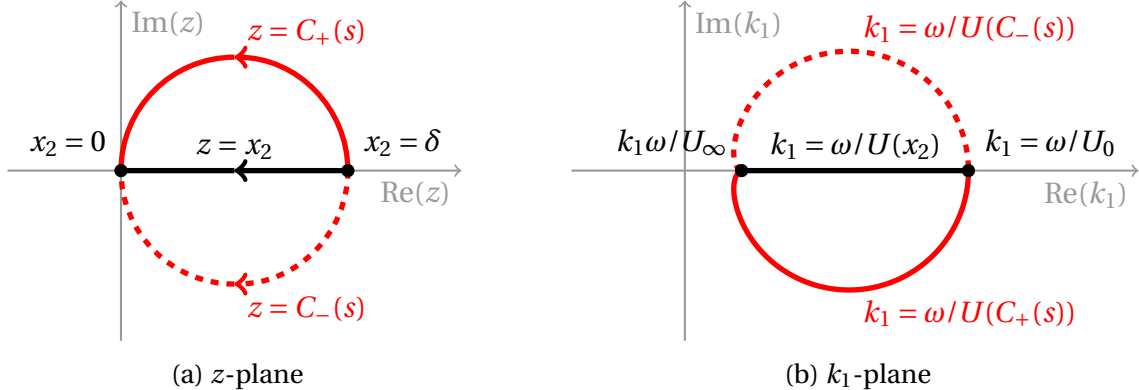


Fig. 4.2.6 Integrating along the semicircular contours in the complex extension of physical x_2 -space, shown in figure 4.2.6a, deform the critical layer to the line $\omega/U(C_{\pm}(s))$, which is away from the real k_1 -axis except at the end points. This example is shown for slipping parabolic profile, with $U_0 = 0.2U_\infty$.

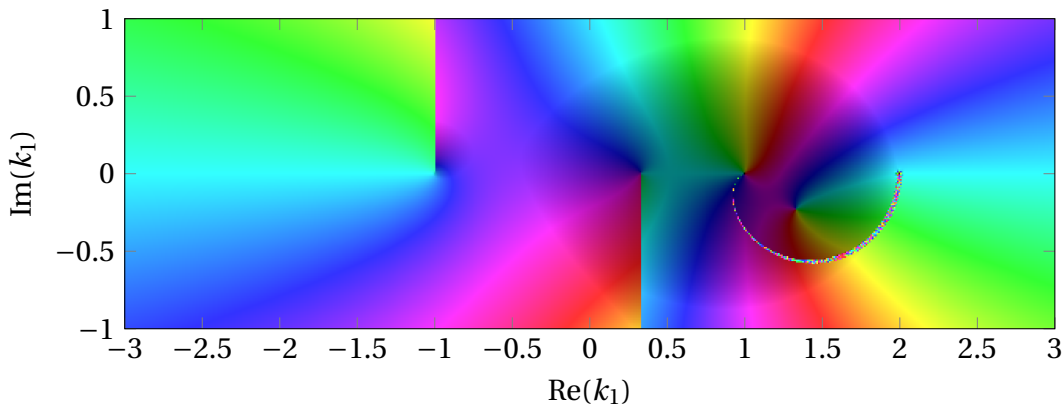


Fig. 4.2.7 Dispersion function, with the same setup as figure 4.2.2, of a slipping parabolic profile, as per (4.3.10). The integration is performed via C_+ , a semicircular contour in the UHzP, with z the analytic extension of real wall-normal coordinate x_2 . The critical-layer contour, previously on the complex line $k_1 \in (\omega/U_\infty, \omega/U_0)$ (i.e. from 1 to 2) has been deformed by the choice of integration contour to the LH k_1 P.

We illustrate this idea by considering the contour parameterised by s :

$$z = C_{\pm}(s) = \frac{\delta}{2} \left(1 + e^{\pm i\pi s} \right) \quad (4.2.20)$$

which describes a semicircle in the complex plane from $z = \delta$ to $z = 0$, with \pm denoting the contour transversed in the upper- or lower-half z plane respectively (U/LHzP). These are sketched in figure 4.2.6a. In general, along a contour parameterised by $z = C(s)$, (4.2.14) simply transforms to

$$\frac{d\Phi}{ds} = \frac{dC}{ds} \mathbf{F}(C(s), \Phi(C(s)); \omega, k_1, k_3) \quad (4.2.21)$$

reducing exactly to the form considered before, and thus amenable to the usual methods of Runge-Kutta integration. Critically, however, numerical problems from the singularity of the differential equation are encountered when $C(s) \approx U^{-1}(\omega/k_1)$. For the semicircular contour shown above, this no longer occurs for real k_1 , unless k_1 lies near ω/U_0 or ω/U_∞ , where the contour is approximately real again. This leads to, for example, a deformation of the critical-layer branch cut in the dispersion function to the curve $\omega/U(C_\pm(s))$, as shown schematically in figure 4.2.6b, and in figure 4.2.7 for the parabolic profile considered in the previous sections. Away from the end points, we can precisely evaluate the function of interest on the critical-layer, in this case directly above it. Similarly, deforming the Runge-Kutta integration contour into the LHzP allows direct evaluation on the lower side of the critical-layer, which has been deformed into the UH k_1 P.

This extension of previous numerical methods allows precise evaluation of functions near "physical" branch cuts, thereby greatly reducing computational time, as shall be seen in §4, as well as drawing out singularities hidden on this branch cut due to the physical setup (for example, hydrodynamic forcing terms leading to poles of Fourier transforms on this cut). Further, the behaviour on the alternative "sheet", hidden by the branch cut, is made more apparent. For example, the root of the dispersion relation on alternative branch of the branch cut, with $k_1 \approx 1.33 - 0.23i$, could shed light upon the behaviour of branch-cut solutions.

The direction of branch cut deformation is determined by which side of the branch cut we wish to evaluate. The majority of the work in this chapter, and later chapters, concerns Fourier inversion with causality considerations. For this purpose, the imaginary part of ω is relaxed to zero from negative values. Since the critical layer is the straight line in the complex plane between ω/U_∞ and ω/U_0 (or $\omega/U(x_2)$ if evaluating functions within the boundary layer), the critical layer lies along a ray with the same argument as ω . If U is positive, then the critical layer has the same imaginary sign as ω and thus lies in the LHzP for ω with negative imaginary part. Thus, most integrations require evaluation *above* the critical layer, and thus contours in the UH k_1 P will typically be used. If evaluating the jump across the branch cut, as will be required for isolating the critical layer contribution, the

cut can be deformed into the LH $k_1 P$ when evaluating at $k_1 + i0$ in the UH $k_1 P$, and vice versa. This allows very precise evaluation either side of the branch cut, with comparatively little numerical expense.

4.2.5 Asymptotic solution: High frequency acoustics

For high frequency, short-wavelength disturbances, a routine application of the WKBJ method allows determination of the asymptotic behavior of the solution, with arbitrary boundary-layer and density profiles. This allows verification of the numerical methods for higher frequencies, allows understanding of the large k_1 behaviour of the dispersion function (important in the scattering later) and provides a simple framework for analytic progress. The WKBJ process assumes the wall-normal wavelength is much shorter than the boundary-layer thickness (and thus, in some sense, the solution is determined by the local background flow speed as opposed local background shear).

We begin by working (4.2.4) into canonical form, a step that isn't necessary but simplifies the analysis. We write the ODE as

$$\frac{d^2\phi}{dx_2^2} + p(x_2) \frac{d\phi}{dx_2} + q(x_2)\phi = 0 \quad (4.2.22)$$

with $p(x_2) = \log(c_0^2 C^4)'$ and $q(x_2) = 3(C' c_0^2)'/(c_0^2 C) - \gamma(k_1, k_3; U(x_2))^2$, as determined above. We remove the first derivative term by posing $\phi = A\Phi$, with $A(x_2)$ to be determined. If

$$\frac{1}{A} \frac{dA}{dx_2} = -\frac{p}{2} \quad (4.2.23)$$

then the equation for Φ is of the form

$$\frac{d^2\Phi}{dx_2^2} + Q(x_2)\Phi = 0 \quad (4.2.24)$$

with

$$Q(x_2) = \frac{A''}{A} - \frac{p^2}{2} + q. \quad (4.2.25)$$

Since the integral of p is known (returning the Wronskian), we can integrate the equation for A to obtain

$$A(x_2) = \frac{1}{c_0 C^2}. \quad (4.2.26)$$

At the moment this is simply a direct reformulation of the ODE for ϕ , and nothing has actually been done. It is now that we suppose the frequency, ω , is in some sense large. We

first note that the dominant wavenumbers of interest scale broadly with ω , so if ω is large then so is k_1 (and possibly k_3). We use k_1 to define a small lengthscale $\epsilon = k_1^{-1}$. Defining $O(1)$ quantities

$$\Omega = \epsilon\omega \quad (4.2.27a)$$

$$K_i = \epsilon k_i \quad (4.2.27b)$$

$$\Gamma = \epsilon\gamma = \sqrt{K_1^2 + K_3^2 - (\Omega - U(x_2)K_1)^2/c_0(x_2)^2} \quad (4.2.27c)$$

then we can rewrite Q , grouping terms by powers of ϵ ,

$$Q(x_2) = \frac{-\Gamma^2(K_1, K_3; U(x_2))}{\epsilon^2} + O(\epsilon^0). \quad (4.2.28)$$

The local effects of mean flow (encapsulated in the acoustic exponent Γ) dominate the local effects of shear (contained within $-p^2/2$ and A''/A in (4.2.25)). Positing a solution to (4.2.24) of the form

$$\Phi = \exp\left(\epsilon^{-1} \sum_{n=0}^{\infty} \epsilon^n S_n(x_2)\right) \quad (4.2.29)$$

allows equating of functions at each order in ϵ , by putting this into the ODE (4.2.24)¹. The first order equations are

$$S_0'^2 = \Gamma^2 \quad (4.2.30a)$$

$$2S_0' S_1' + S_0'' = 0 \quad (4.2.30b)$$

with no $O(\epsilon^{-1})$ contribution from $Q(x_2)$ in the second equation, and primes denoting x_2 derivatives. This is exactly the method and solution in Bender and Orszag [14], with these equations respectively the eikonal and transport equations. We can solve to give

$$S_0 = \pm \int^{x_2} \Gamma(K_1, K_3, U(x_2)) dx_2, \quad (4.2.31a)$$

$$S_1 = \log\left(\pm \Gamma^{-1/2}\right), \quad (4.2.31b)$$

giving a pair of solutions, asymptotically correct to $O(1)$ in ϵ :

$$\phi_{\pm} \sim \frac{1}{\gamma^{1/2} c_0 C^2} \exp\left(\pm \int \gamma(x_2) dx_2\right). \quad (4.2.32)$$

¹There is no *a priori* reason to expand in ϵ itself, rather than some function of ϵ (for example $\epsilon^{1/2}$), other than knowledge of the final solution.

Explicit dependence on the somewhat fabricated ϵ has been dropped, though it should be understood this is only strictly valid for high frequencies or wavenumbers. This solution trivially becomes the uniform flow solution when U is constant, as expected. The pressure and wall-normal velocity perturbation fields can be derived as

$$v_{\pm} \sim -C^2 \phi' \sim \mp \frac{\gamma^{1/2}}{c_0} \exp\left(\pm \int \gamma(x_2) dx_2\right), \quad (4.2.33a)$$

$$p_{\pm} \sim -C^3 \phi \sim -\frac{C}{\gamma^{1/2} c_0} \exp\left(\pm \int \gamma(x_2) dx_2\right), \quad (4.2.33b)$$

Both are continuous over discontinuities of U' , since γ is continuous (if not differentiable).

It remains to validate this solution, which we can do via a comparison with the preceding numerical solution. In particular, we wish to show that these solutions are asymptotically equivalent to the exact solution as $k_1 \rightarrow \infty$, even for moderate ω , a property which will be important in the scattering analysis in later chapters. As before, we use the hard-wall dispersion function as validation, for which we require

$$\phi_d \sim \frac{\gamma^{1/2}(\delta) c_0(\delta) C(\delta)^2}{\gamma^{1/2}(x_2) c_0(x_2) C(x_2)^2} \exp\left(\int_{x_2}^{\delta} \gamma(s) ds - \gamma(\delta)\delta\right) \quad (4.2.34)$$

with the scaling constants chosen to ensure $\phi_d \sim \exp(-\gamma x_2)$ for $x_2 > \delta$. The dispersion function is then asymptotically

$$D_h \sim \frac{\gamma^{1/2}(\delta) \gamma^{1/2}(0) c_0(\delta) C(\delta)^2}{c_0(0)} \exp\left(\int_0^{\delta} \gamma(s) ds - \gamma(\delta)\delta\right). \quad (4.2.35)$$

For very simple profiles it is possible to do the integral

$$I = \int_0^{\delta} \sqrt{k_1^2 + k_3^2 - c_0^{-2}(s)(\omega^2 - k_1 U(s))^2} ds \quad (4.2.36)$$

exactly in terms of elementary functions, and it is straightforward to compute for more complicated profiles numerically.

By way of validation, the asymptotic dispersion function is compared to the computed dispersion function, with very small step size, along the real k_1 axis in figure 4.2.8. This comparison could be done across any ray in the complex k_1 -plane with similar results. As the log-plot, figure 4.2.8b shows, the difference between the computed and precise solutions decays like k_1^{-1} , as would be expected from the asymptotic analysis. This validation allows numerical computations to be replaced by the comparatively trivial WKBJ

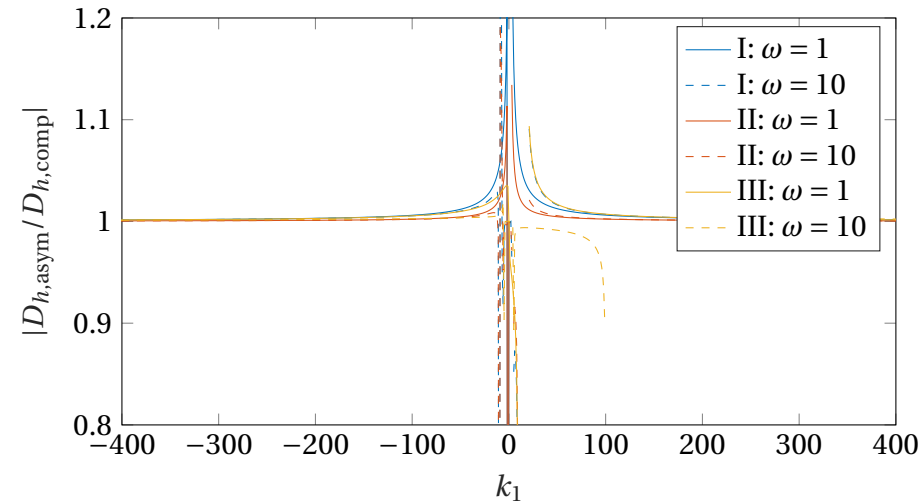
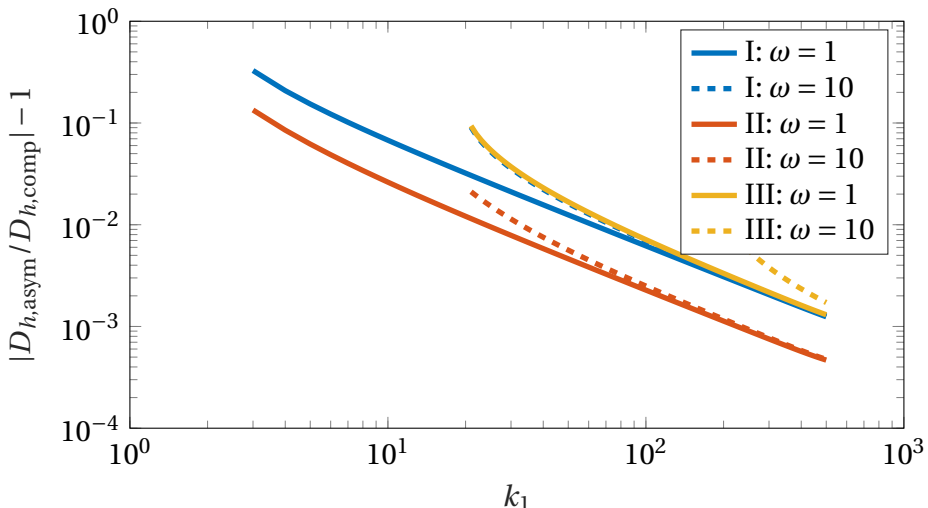
(a) Ratio along the real k_1 axis.(b) log-plot of the difference from unity of this ratio, for k_1 positive.
In all cases the slope tends to -1 .

Fig. 4.2.8 Along the real axis, the ratio of computed and asymptotic hard-wall dispersion functions is computed for three cases. In all cases we have free-stream speed of sound $c_0 = 2$, and ω varies as given, with all lengths scaled by δ . I and III are parabolic profiles as per (4.3.10), with continuous shear at δ , with $U_\infty = 1, 0.1$ and $U_0 = 0.5, 0.05$ respectively, i.e. equivalent but different speeds relative to the background speed of sound, and giving free-stream Mach numbers of 0.25 and 0.025 respectively. Case II is a linear profile, as per (4.3.9), with the same slip and free-stream velocities as case I (and a discontinuity in shear at δ). In all cases the asymptotic form of the solution agrees with the high-accuracy ($N = 10000$) integrated solution for large k_1 , provided k_1 lies far from the critical-layer. The difference decays as k_1^{-1} as the asymptotic analysis would suggest, as per the second figure.

solution for large k_1 , which will be critical when the scattering problem is considered in later chapters.

4.3 A point mass source in continuous shear

The work of §3, specifically from sections 3.4.1 onwards, is generalised to more arbitrary background profile $U(x_2)$. Other than the supposition that the profile is continuous, this can be prescribed as desired, though we expect instability for inflecting profiles. Again, we consider the setup of a harmonic mass source in shear flow, generating a vortical disturbance in its wake, and consider both the downstream development of disturbances and the far-field acoustics from the source. The generic setup is shown in figure 4.3.1, which will be revisited and the relevant lengthscales discussed in section 4.4.2.

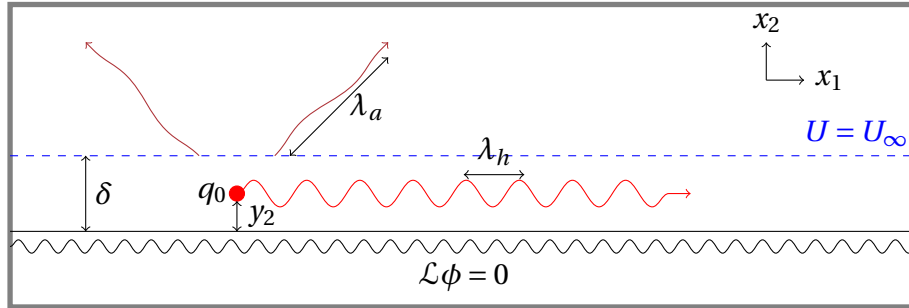


Fig. 4.3.1 Schematic of the setup of this section, highlighting the four lengthscales of interest: the boundary-layer thickness δ , source location y_2 , and the two scattered lengthscales, corresponding to hydrodynamic motion in the boundary-layer (λ_h) and acoustic disturbances propagating to the far-field (λ_a).

This generalisation, allowing finite speed of sound and (somewhat) arbitrary wavelengths and thus including the effects of incompressibility, gives rise to the existence of a critical-layer. Whilst this can be dealt with and removed via the inclusion of viscosity, we focus on the inviscid case and thus the effects of the critical-layer must be studied directly.

Recall (2.3.10), governing the evolution of a generalised velocity potential for acoustic disturbances. With a mass source $q(\mathbf{x}, t)$, we have

$$\frac{D_0}{Dt} \left(\mathcal{D}_R^\dagger \phi \right) = c_0^2 q \quad (4.3.1)$$

with the adjoint Rayleigh operator given by

$$\mathcal{D}_R^\dagger = \frac{D_0^3}{Dt^3} - \frac{\partial}{\partial x_i} \left(c_0^2 \left(\frac{\partial}{\partial x_i} \frac{D_0}{Dt} + 2 \frac{\partial U}{\partial x_i} \frac{\partial}{\partial x_1} \right) \right). \quad (4.3.2)$$

If we again consider a point mass source, $q = q_0 e^{i\omega t} \delta(x_1) \delta(x_2 - y_2)$, we obtain, exactly analogously to (3.4.6), a partial differential equation for ϕ :

$$\mathcal{D}_R^\dagger \phi = \frac{c_0(y_2)^2 q_0}{U(y_2)} \delta(x_2 - y_2) H(x_1) \exp(-i\kappa_1(y_2)x_1). \quad (4.3.3)$$

In the long-wavelength, constant shear case, the perturbation vorticity was confined to a streamline starting at the source. This solution extends this to a more generalised vortical quantity, confined again to a streamline, which drives the evolution of the perturbation quantities. For streamwise homogenous boundary condition on $x_2 = 0$, $\mathcal{L}\phi = 0$ for some linear operator \mathcal{L} which doesn't depend on x_1 or x_3 , we can solve using Fourier transforms as before to give

$$\phi_{013} = \frac{c_0(y_2)^2 q_0}{U(y_2)} \frac{1}{i(k_1 - \kappa_1)} \frac{1}{W(y_2)} \begin{cases} \phi_d(x_2)\phi_\ell(y_2) & x_2 > y_2 \\ \phi_\ell(x_2)\phi_d(x_2) & x_2 < y_2 \end{cases} \quad (4.3.4)$$

with $\phi_d \sim \exp(-\gamma_\infty(k_1, k_3)x_2)$ as $x_2 \rightarrow \infty$, and $\mathcal{L}_{013}\phi_\ell = 0$ on $x_2 = 0$, with both auxiliary functions satisfying the ODE

$$\mathcal{D}_{R013}^\dagger \phi_{013} = 0 \quad (4.3.5)$$

with solution as discussed in §4.2. As yet, other than the constants in front q_0 , this is unchanged from §3.4.1. The difference in the constants follows from the consideration of a different potential, ϕ here as opposed to ψ previously. As noted in (4.2.7), the Wronskian is not constant in this case. Provided the inner solution ϕ_ℓ is scaled analogously to the previous section, so that $W(x_2 = 0) = D_\ell(\omega, k_1, k_3)$, the dispersion function given by $\mathcal{L}_{013}\phi_d(x_2 = 0)$, then

$$W(y_2) = \frac{c_0(0)^2 C(0)^4}{c_0(y_2)^2 C(y_2)^4} D_\ell \quad (4.3.6)$$

with $C(x_2) = i(\omega - U(x_2)k_1)$ as usual. If the boundary condition is written $\ell_1\phi'_\ell + \ell_2\phi_\ell = 0$, this setup requires

$$\phi_\ell(0) = \ell_1, \quad (4.3.7a)$$

$$\phi'_\ell(0) = -\ell_2. \quad (4.3.7b)$$

Both sides of this implicitly depend on k_1 (and the other parameters). If a different normalisation is chosen, this must be included in the Wronskian (and so it cancels out).

We can therefore write down the time-harmonic solution

$$\phi_{03} = \frac{1}{2\pi i} \frac{c_0(y_2)^4 q_0}{c_0(0)^2} \int_{F_1} \frac{C(y_2; k_1)^4 \phi_{\gtrless}(x_2; k_1) \phi_{\leqslant}(y_2; k_1)}{C(0; k_1)^4 D_\ell(k_1)} \frac{e^{-ik_1 x_1}}{k_1 - \kappa_1} dk_1. \quad (4.3.8)$$

The conventions in the previous section is maintained, with $\phi_{\gtrless}(x_2)$ given by $\phi_d(x_2)$ for $x_2 > y_2$ and ϕ_ℓ for $x_2 < y_2$. The Fourier inversion contour is deformed off the real k_1 axis so as to preserve causality as the imaginary part of ω is relaxed to zero. Deformation of this contour to a semicircle at infinity will pick up not only contributions from any poles, and from the acoustic branch cuts, but also from the hydrodynamic branch cut of the critical layer. As before, it is sensible to consider this with an explicit choice of boundary condition, which we shall do in the following section.

Typically from here on, we will consider straightforward polynomial background boundary-layer profiles, with linear profile given by (for $x_2 < \delta$)

$$U(x_2) = U_0 + (U_\infty - U_0) \frac{x_2}{\delta} \quad (4.3.9)$$

and parabolic profile, with continuous shear at the edge of the boundary-layer, given by

$$U(x_2) = U_\infty - (U_\infty - U_0) \left(1 - \frac{x_2}{\delta}\right)^2. \quad (4.3.10)$$

In both cases, the slip velocity $U_0 = U(0)$ and the boundary-layer is matched to a constant profile $U = U_\infty$ for $x_2 > \delta$. In this work the speed of sound is typically a constant, with $c_0 > U_\infty > U_0$, though the model allows variation of background speed of sound (through variations in background density), a simplification justified in the derivation §2 for low Mach-number flows. If not explicit, lengths will be scaled by boundary-layer thickness δ and speeds by the free-stream velocity U_∞ , equivalently setting $\delta = U_\infty = 1$.

4.3.1 Far-field noise: Steepest descent

For $x_2 > \delta$, outside the boundary-layer, or as $x_2 \rightarrow \infty$ if we take the boundary-layer to be infinitely thick, we recall we defined $\phi_d \sim \exp(-\gamma_\infty x_2)$, thereby putting the inversion integral into the form

$$\phi_{03} = \int_{F_1} I_\ell(k_1) \exp(-ik_1 x_1 - \gamma_\infty x_2) dk_1 \quad (4.3.11)$$

with I_ℓ depending on the boundary-conditions and various physical parameters. For the point mass source, we have

$$I_\ell = \frac{1}{2\pi i} \frac{c_0(y_2)^4 q_0}{c_0(0)^2} \frac{C(y_2; k_1)^4}{C(0; k_1)^4} \frac{\phi_\ell(y_2; k_1)}{D_\ell(k_1)} \frac{1}{k_1 - \kappa_1(y_2)} \quad (4.3.12)$$

and derivatives can be computed via $\partial/\partial x_1 = -ik_1$ and (outwith the boundary layer) $\partial/\partial x_2 = -\gamma_\infty$.

Along the real axis, or near the real axis, this integral is oscillatory, driven by the Fourier inversion factor $e^{-ik_1 x_1}$. The ideal contour to integrate along is the *steepest descent* contour, on which the exponent has constant imaginary part, and thereby the integral is (essentially) non-oscillatory. For $r = |\mathbf{x}| \gg \delta$, the rapid decay of this exponent, along a suitably chosen contour, allows asymptotic approximation of the integral from a single saddle point contribution.

Suppose we are at an observation point (x_1, x_2) such that $x_1 = R \cos(\Theta)$ and $\beta x_2 = R \sin(\Theta)$, where we introduce

$$\beta = \sqrt{1 - M_\infty^2} \quad (4.3.13)$$

with the far-field Mach number $M_\infty = U_\infty(\delta)/c_0(\delta)$ (or a similarly defined limit at infinity), and we introduce the acoustic wavenumber $k_0 = \omega/c_0(\delta)$ similarly, with the length of acoustic waves, in the free-stream, given by its reciprocal. The reason for the introduction of β is to reduce the following calculation, and can be considered a Doppler-shift effect. The integral outside the boundary-layer then looks like

$$\phi_{03} = \int_{F_1} I_\ell(k_1) \exp(-R f(k_1; \Theta)) dk_1 \quad (4.3.14)$$

where we define the exponent

$$f(k_1; \Theta) = ik_1 \cos(\Theta) + \beta^{-1} \gamma_\infty(k_1) \sin(\Theta) \quad (4.3.15)$$

where $\gamma_\infty^2 = k_1^2 + k_3^2 - (k_0 - k_1 M_\infty)^2$. If we now introduce new wavenumbers

$$K_1 = k_1 + \frac{M_\infty k_0}{\beta^2} \quad (4.3.16a)$$

$$K_0^2 = \frac{k_0^2}{\beta^4} - \frac{k_3^2}{\beta^2} \quad (4.3.16b)$$

and rearrange, we obtain

$$f = -\frac{iM_\infty k_0}{\beta^2} \cos(\Theta) + iK_1 \cos(\Theta) + \sqrt{K_1^2 - K_0^2} \sin(\Theta) \quad (4.3.17)$$

The first term is constant and doesn't effect the computation of the steepest descent contour, and so we focus on

$$F(K_1; \Theta) = iK_1 \cos(\Theta) + \sqrt{K_1^2 - K_0^2} \sin(\Theta) \quad (4.3.18)$$

which is identical to the zero-velocity, spanwise invariant case if $k_1 = K_1$ and $K_0 = k_0$, essentially we have corrected for mean flow (and cross-flow variations), which can be compared to the Prandtl-Glauert transformation [39]. In this case we could have $K_0^2 < 0$ due to the presence of k_3 terms, which must be treated carefully.

The error, due to oscillations, is minimised if a contour is chosen that passes through a saddle point of this exponent [52]. The best contour to choose is the one on which the imaginary part of F is constant, which can be determined parametrically for given Θ . First noting saddle points are located at zeros of F' , with

$$F' = i \cos(\Theta) + \frac{K_1}{\sqrt{K_1^2 - K_0^2}} \sin(\Theta) \quad (4.3.19)$$

which has a single zero when $K_1 = K_{1s} = K_0 \cos(\Theta)$ (with care being required with the sign of this solution, which results from the choice of branch cuts of γ and the imaginary part of ω), and as such we want the contour passing through this point with $\text{Im}(F(K_1)) = \text{Im}(F(K_{1s})) = K_0$. This is most cleanly done via the substitution $K_1 = K_0 \cosh(u) = K_0 \cosh(u_r + iu_i)$, which gives

$$\text{Im}(F) = K_0 \cosh(u_r) [\cos(\Theta) \cos(u_i) + \sin(\Theta) \sin(u_i)] = \cosh(u_r) \cos(\theta - u_i) = K_0 \quad (4.3.20)$$

Choosing to parameterise by $t = -\tanh(u_r)$ we can write down the steepest descent contour, as a function of t , via

$$K_{1SD}(t; \Theta) = K_0 \left[\left(\cos(\Theta) + \frac{t}{\sqrt{1-t^2}} \sin(\Theta) \right) + i \left(-\frac{t^2}{\sqrt{1-t^2}} \cos(\Theta) + t \sin(\Theta) \right) \right] \quad (4.3.21)$$

with t running from -1 to 1 , and K_{1SD} tending towards complex infinity in two different directions at either endpoint. This parameterisation has the advantage that it a *finite* integral in t , and thus a useful substitution for numerical integration, as well as removing

ambiguity about the square root. The change of variables gives

$$dk_1 = dK_1 = \left[\frac{1}{(1-t^2)^{3/2}} \sin(\Theta) + i \left(\frac{t(t^2-2)}{(1-t^2)^{3/2}} \cos(\Theta) + \sin(\Theta) \right) \right] dt \quad (4.3.22)$$

which is singular as $t \rightarrow \pm 1$, though the exponential decay of the integrand makes this unimportant. The saddle point is now located at $t = 0$ where $dk_1 = k_0(1+i)\sin(\Theta)dt$.

This contour is useful to integrate along even when R is not large, for example just outside the boundary-layer, and we further make the assumption it is a reasonable integration contour for $x_2 < \delta$, as the exponential behaviour isn't greatly changed. For $Rk_0 \gg 1$, we can determine the first-order asymptotic behaviour of the contour integral via Laplace's method, with the saddle point dominating. This might not be the first-order contribution to the entire integral, with contributions from the deformation to the steepest descent contour to be expected, particularly from poles at roots of the relevant dispersion relation.

The steepest descent integral is of the form

$$J = \int_{-1}^1 I(t) e^{-RG(t)} dt \quad (4.3.23)$$

with $G(t) = F(K_{1SD}(t)) - F(K_{1SD}(0))$ a real function of t , and $I(t)$ complex and well-behaved along the contour (with integrable singularities at the end points that we will for now ignore). $G(t)$ is minimal when $t = 0$, and the vicinity of this global minimum dominates the integral for R large (which can be made explicit via, for example, Watson's lemma [112], compare §4.4.2). Near $t = 0$, $G(t) \approx K_0 t^2$, the simplicity of this expression again supporting the choice of definition of t . Locally we consider the integral

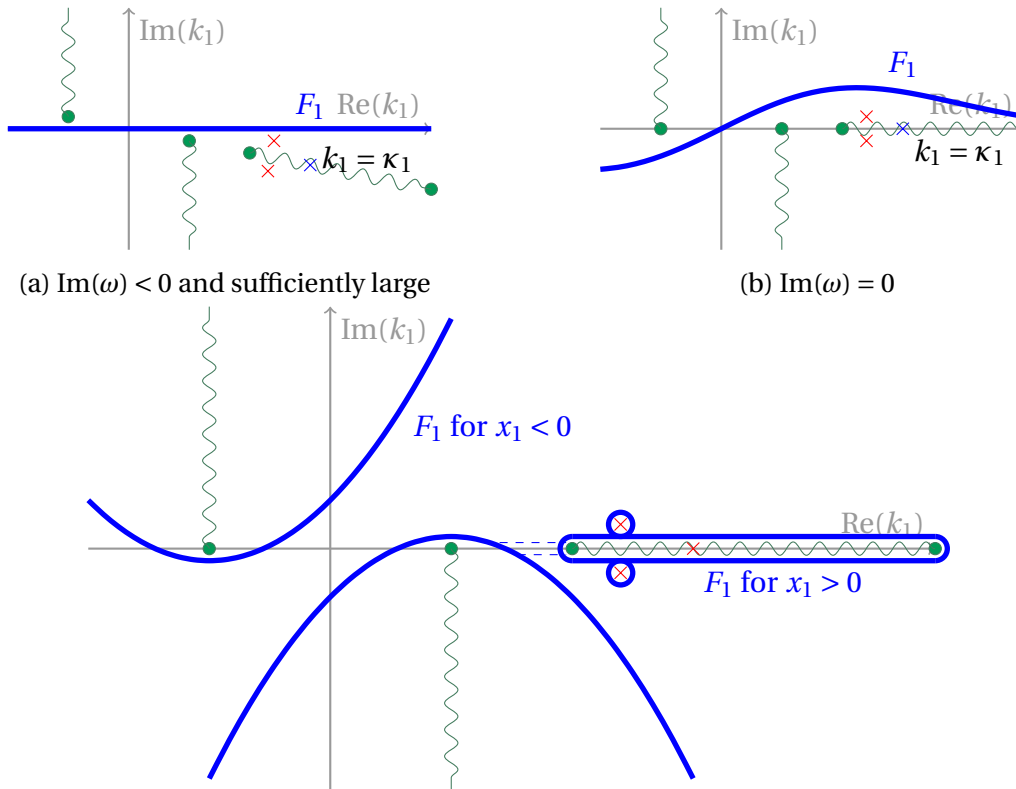
$$J_\epsilon = \int_{-\epsilon}^\epsilon I(t) e^{-RK_0 t^2} dt \sim \int_{-\sqrt{RK_0}\epsilon}^{\sqrt{RK_0}\epsilon} \frac{I(0)}{\sqrt{RK_0}} e^{-u^2} du \sim I(0) \sqrt{\frac{\pi}{RK_0}} \quad (4.3.24)$$

with ϵ small but finite, in the limit $RK_0 \rightarrow \infty$. This contribution is a cylindrical wave, driven by the value of I at the saddle point.

In terms of the earlier $I_\ell(k_1)$ (equation (4.3.12)) and the physical parameters, this contribution is (recalling the various extra factors, including the change of variable contribution)

$$I_\ell \left(\frac{(k_0^2 - \beta^2 k_3^2)^{1/2}}{\beta^2} \frac{x_1}{(x_1^2 + \beta^2 x_2^2)^{1/2}} \right) \frac{x_2 (2i\pi)^{1/2} (k_0^2 - \beta^2 k_3^2)^{1/4}}{(x_1^2 + \beta^2 x_2^2)^{3/4}} \exp \left[\frac{i x_1}{\beta^2} \left(M_\infty k_0 - (k_0^2 - \beta^2 k_3^2)^{1/2} \right) \right] \quad (4.3.25)$$

Deformation to the steepest descent contours and the critical-layer contribution. A typical, general, form of the integral and inversion contour, with ω relaxed to the real axis, is shown in figure 4.3.2, as well as a pair of typical steepest descent contours for $x_1 \gtrless 0$, with the saddle point at the location the contour crosses the real axis between the two acoustic branch cuts. To deform onto these contours, one must pick up contributions from all poles of the integrand and from the branch cut due to the critical-layer, which in turn has the forcing pole at $k_1 = \kappa_1$ on it. The steepest descent contour asymptotes to $K_0(\pm \sin(\Theta) - i \cos(\Theta))$ as $t \rightarrow \pm 1$, which are either both in the UH $k_1 P$ if $\cos(\Theta) < 0$ or both in the LH $k_1 P$ if $\cos(\Theta) > 0$, i.e. $x_1 \gtrless 0$ respectively, as we would expect.



(c) Contour deformation for Fourier Inversion schematically showing the steepest descent contour, a critical layer integral and residues at remaining poles.

Fig. 4.3.2 Complex plane deformation of the inversion contour as the imaginary part of ω is relaxed to 0, with the streamwise inversion contour deformed to preserve causality. To compute the integral, deformation to a steepest descent contour reduces numerical difficulty, at the expense of careful evaluation of poles and the critical-layer contribution.

4.4 Hard-wall boundaries

With any singularities of the dispersion function, and thus the integrand, confined to the real k_1 axis, the case of a point source above a hard-wall boundary is easiest to deal with, with no additional modal contributions aside from those contained within the critical layer integral. We impose the boundary condition that $\mathcal{V}_{013}^0 \phi_{013} = 0$, explicitly corresponding to $\ell_1 = -C^2$, $\ell_2 = -3CC'$, both evaluated at $x_2 = 0$, which corresponds to imposing the perturbations having no wall-normal velocity at the wall, and thus there is no fluid penetration through the surface.

The dispersion function for this problem is shown in figures 4.4.1, for both a linear and parabolic background profile, as computed using the standard techniques from §4.2, and hence leading to numerical discrepancies near the critical layer (in this case, with $U_0 = 0.3$ and $U_\infty = 1$, and unit frequency $\omega = 1$, the interval $k_1 \in (1, 3.33)$ on the real axis). However, it can be seen that the critical layer in the linear case is removable (in that the argument of D_h does not jump across it), which is not true in the parabolic case. This leads to fundamental differences in the computed solution: as in the piecewise linear case, the linear case gives rise to propagating modes, whereas the parabolic case gives rise to an algebraically decaying contribution.

Also shown in figures 4.4.1 are the integration contours to be used to evaluate this inversion. Two things are worth noting here: whilst the "branch cut" contours $C_{U,P}$, extending into the U/LH k_1 P and centred around the branch points of γ_∞ , resemble the Steepest Descent contours, they need not be exactly the same. This reduces the need for the contours to depend on x_1 and x_2 , the physical coordinates, and vastly speeds up computation time, though the steepest descent contour (and resulting saddle point contribution) are useful for evaluating the far-field contribution from this integral, and fewer points are needed for convergence if the contour goes through or near the saddle point. Secondly, the critical-layer contribution is evaluated explicitly via an integral around the branch cut. This is done due to the presence of poles on the branch cut itself: if they did not exist, or utilisation of a principal valued integral was worthwhile, the critical layer integral could be reduced to a single integral along the contour (with arbitrary precision attained by deforming the physical integration path in the real plane so that the critical layer moves away from the contour of integration). This is done to evaluate the downstream behaviour of this contribution later.

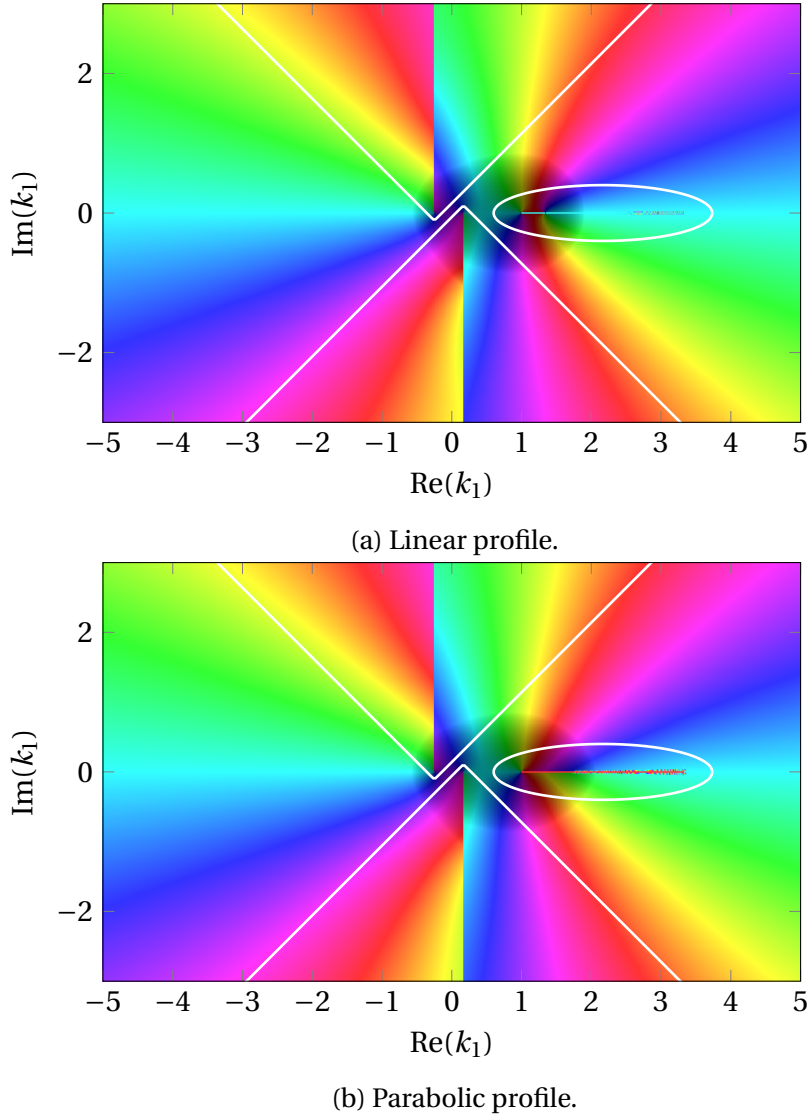


Fig. 4.4.1 Hard-wall dispersion functions for both a linear and a parabolic background flow. U_∞ and δ are fixed at 1, with $U_0 = 0.3$ in both cases and $c_0 = 5$ constant. The parabolic profile is such that shear is continuous at $x_2 = \delta$. Also shown are the numerically implemented integration contours for this case: the steepest descent contours are here approximated by hyperbolae centred on the branch points, with any remaining contributions coming from the critical layer (or, in the linear case, the poles along where the critical layer would be).

4.4.1 Integrated near-field solutions

With the contour deformation suggested earlier (no non-convected poles to worry about, lying away from the critical layer), it is quick to numerically integrate the inversion formula. An example of this is shown in figures 4.4.2 and 4.4.3, respectively for a linear and parabolic profile, both with the same slip velocity $U_0 = 0.3$ and free-stream velocity $U_\infty = 1$, and both at a reasonably high free-stream Mach number of 0.2. The solution can be decomposed into the two parts indicated by the contour sketch in figure 4.3.2. It is focusing on the critical layer contribution that the biggest difference between the two profiles is noted: the critical-layer contribution decays downstream in the parabolic case (the exact decay analysed in §4.4.3) and yet persists in the linear case.

The latter is easy to demonstrate as neutrally stable, arising from a pole (a zero of D_h) on the critical layer itself, and thus giving rise to a convected wavelike solution proportional to $\exp(i\omega t - ik_{1c}x_1)$ with $k_{1c} \in (\omega/U_\infty, \omega/U_0)$, moving at a speed lower than the free-stream velocity. This modal solution is exactly analogous to the modal solutions from the piecewise linear approximation we saw earlier, and arises solely due to the jump in background shear at the edge of the boundary-layer, $x_2 = \delta = 1$.

Whilst full numerical inversion is required to compute the solution near the source, it is possible to get a good understanding of the solution far from the source, both far away from the boundary and downstream within the boundary, by approximating the two integrals separately.

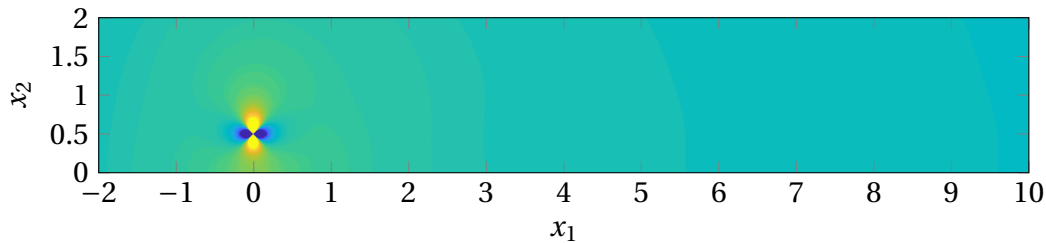
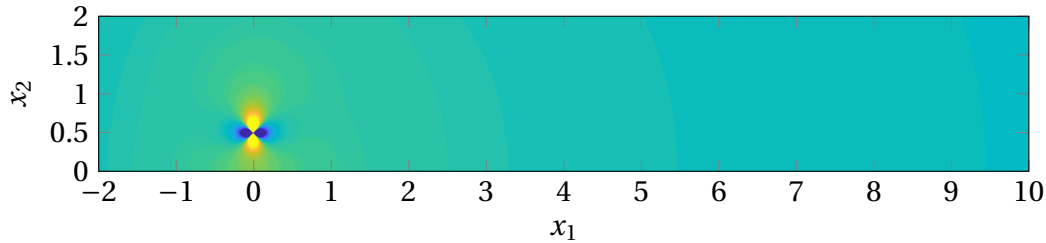
4.4.2 Far-field sound: outside shear layer

Outwith the shear layer, we can use the steepest descent formulation described above in §4.3.1. In particular, we can compute the first-order behaviour of the radiating solution for $x_2 \gg \delta$, with evaluation on at the saddle point (a function of observer angle θ) required, since the critical-layer solution, and any propagating modes, decay exponentially in x_2 . In particular, we can focus on the directivity of the solution, contained within

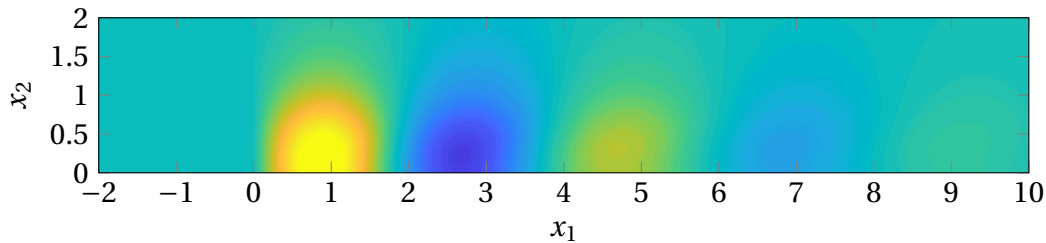
$$I_{FF}(\theta) = \sin(\Theta(\theta))\phi_h(y_2; k_s(\theta))K(k_s(\theta)). \quad (4.4.1)$$

K contains the remaining k_1 -dependent part of the integrand, namely

$$K(k_1) = \frac{C(y_2; k_1)^4}{C(0; k_1)^4} \frac{1}{D_h(k_1)(k_1 - \kappa_1(y_2))} \quad (4.4.2)$$

(a) Full scattered pressure field, at $t = 0$.

(b) ‘Steepest descent’, radiating acoustic contribution



(c) Critical-layer contribution only, with colour scaled by a factor of 100.

Fig. 4.4.2 The scattered pressure field, decomposed into the various integral contributions, for perturbations (from a mass source at $y_2 = 0.5$) to a parabolic background flow (4.3.10), $U_0 = 0.3$, $U_\infty = 1$, $c_0 = 5$ constant, and frequency $\omega = 1$. Due to the much reduced strength of the critical layer contribution (and thus the similarity of the first two images) its strength has been magnified in the third figure.

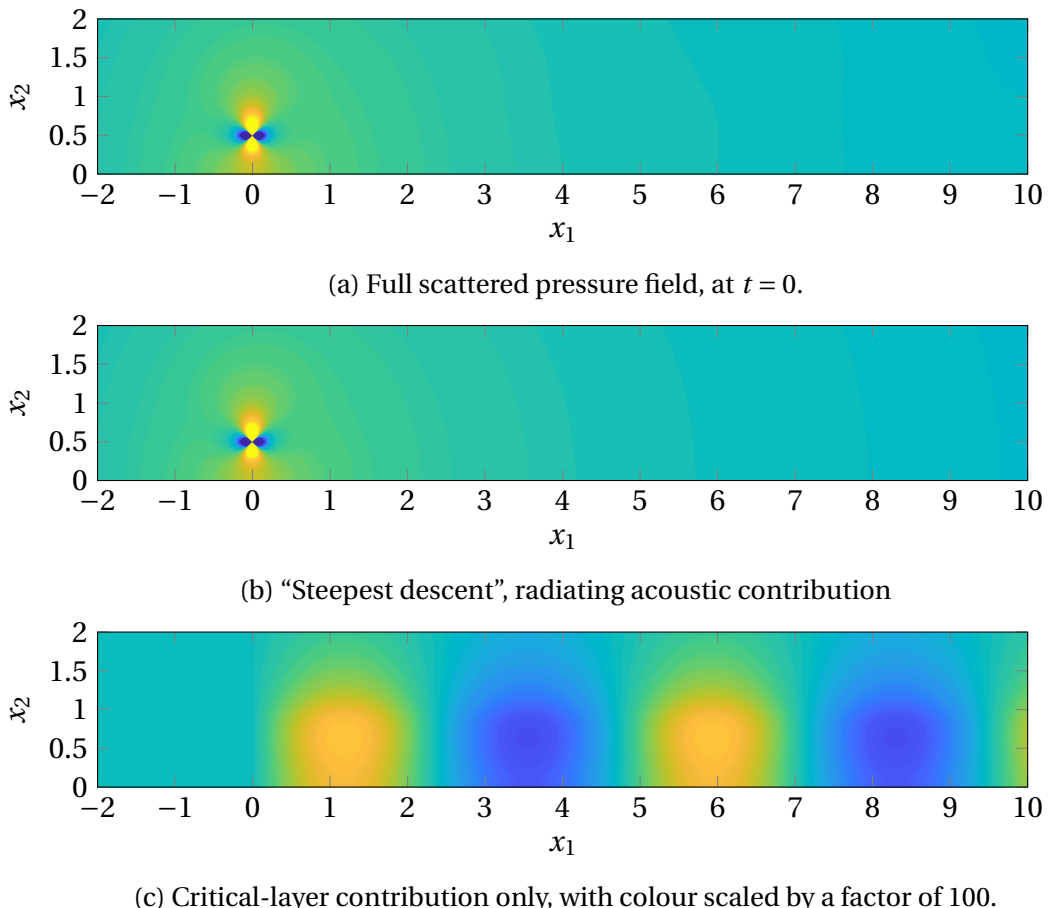


Fig. 4.4.3 The scattered pressure field, decomposed into the various integral contributions, for perturbations (from a mass source at $y_2 = 0.5$) to a linear background flow (4.3.9), $U_0 = 0.3$, $U_\infty = 1$, $c_0 = 5$ constant, and frequency $\omega = 1$. The major difference between this image and the former is that the critical layer does not decay downstream.

and need only be evaluated at the saddle point $k_s = K_0 \cos(\Theta) - k_0 M / (1 - M^2)$, with K_0 and Θ the Doppler-shifted wavenumber and observer angle respectively. Since this function requires evaluation at a single value of k_1 for each observer location only, it is very quick to evaluate and provides a useful tool for investigation of the effect of varying parameters. We also introduce the far-field pressure directivity and far-field wall-normal velocity directivity, respectively \mathcal{P}_{IFF} and \mathcal{V}_{IFF} .

It is worth at this point being precise about the lengthscales of interest, as shown in figure 4.3.1 at the start of the previous section. There are four lengthscales to be considered, and therefore three that can be varied independently, after scaling all lengths by boundary-layer thickness δ . The source location, y_2/δ , is typically $O(1)$, though might be smaller if we have a source very close to the wall (where the physical basis of these approximations is less likely to hold). We then have two frequency-driven lengthscales. Firstly, the *hydrodynamic wavelength*:

$$\lambda_h = \frac{2\pi}{\kappa_1} = \frac{2\pi U(y_2)}{\omega}. \quad (4.4.3)$$

Alternative such lengthscales arise with different convected wavenumbers, but all scale as U_∞/ω . This is the wavelength of convected disturbances in the boundary-layer. Secondly, we have the *acoustic wavelength*:

$$\lambda_a = \frac{2\pi}{k_0} = \frac{2\pi c_0}{\omega} \quad (4.4.4)$$

which is larger than the hydrodynamic wavelength, and for low Mach numbers considerably so. This is the wavelength of acoustic disturbances, and if the boundary-layer is compact with regards this lengthscale, $\delta \ll \lambda_a$, we expect the acoustic response to depend little on the structure of the boundary-layer.

The saddle point contribution is fundamentally acoustic, and thus has wavelength of the order of the acoustic wavelength λ_a , with the saddle point lying between the two acoustic branch cuts and therefore having streamwise wavenumber smaller than k_0 . There are thus two fundamentally distinct cases of directivity: when the acoustic wavelength is larger than the boundary-layer thickness, $\lambda_a \gtrsim \delta$, and when the acoustic wavelength is smaller (or of comparable size) to the boundary-layer thickness $\lambda_a \lesssim \delta$. For reasonably low free-stream Mach numbers, the former case reduces to the locally incompressible case seen before, with the only effect of the shear to change the strength of the source, and the resulting acoustic pressure disturbance is simply a radiating monopole, without

dependence of directivity on θ . The accompanying wall-normal velocity fluctuations therefore have a $\sin(\theta)$ -like dipole directivity.

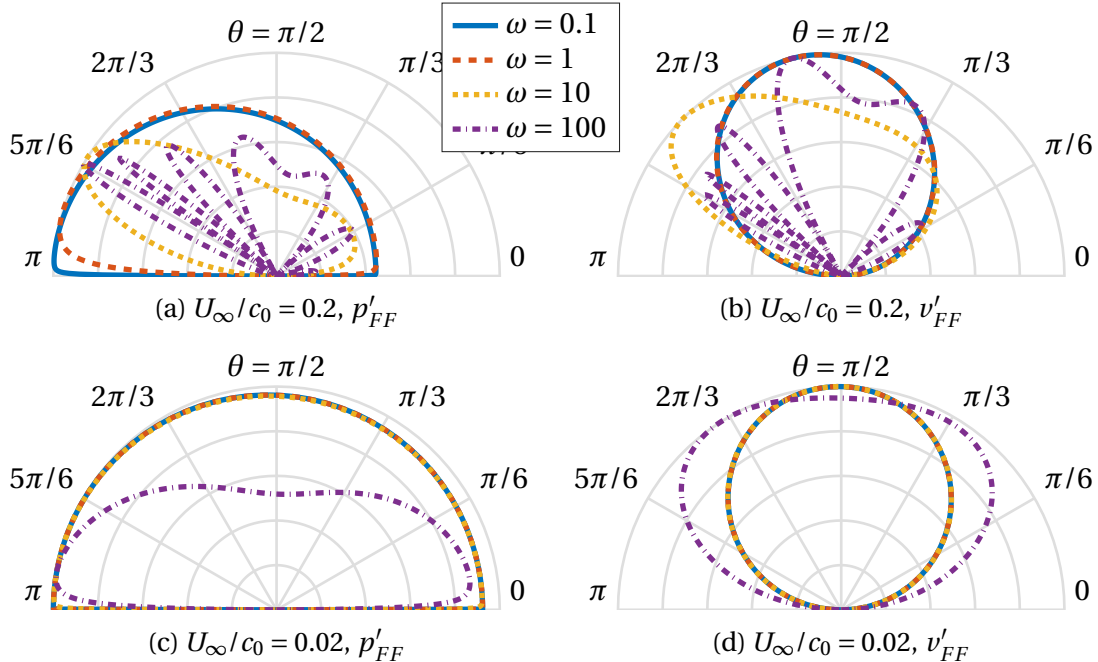


Fig. 4.4.4 The directivity $|\mathcal{P}I_{FF}(\theta)|$ or $|\mathcal{V}I_{FF}(\theta)|$ of the acoustic pressure field generated by a source (at $y_2 = 0.5$) in linearly sheared flow, with $U_0 = 0.3U_\infty$, for two different sound speeds. All plots use the same set of frequencies, scaled with the free-stream velocity U_∞ and boundary-layer thickness δ . The data is normalised so that the maximum in θ is 1. A lobe-like structure is in evidence for high frequencies, though it is not possible from these plots to determine which lengthscale is driving this, as both λ_a and λ_h are changing with ω (when everything else is held fixed). At low Mach numbers there is a broad frequency-independent coalescence of the curves.

Given the wide variety of parameters that can be independently varied, a variety of far-field directivity plots are presented, mostly focusing on disturbances to a simple, slipping, linear profile. The first pair of plots, figures 4.4.4, consider varying the frequency ω with free-stream Mach number fixed. Low frequency disturbances have no (pressure) lobes with the convective effects of higher Mach number free-stream flow tend to move the primary directivity upstream. At low Mach numbers, this low-frequency plot directly reproduces a θ -independent directivity that we would expect of a normal monopole in the absence of flow, most obvious for $\omega = 1, 0.1$ in figure 4.4.4c with low Mach number.

The θ -independent directivity follows from the formula (4.4.1) in the limit $c_0 \rightarrow \infty$. In this limit, which is also the limit $\beta \rightarrow 1$, the Doppler-shifted observer angle Θ and the actual observer angle θ approach each other. Any deviation from a $\sin(\theta)$ directivity in

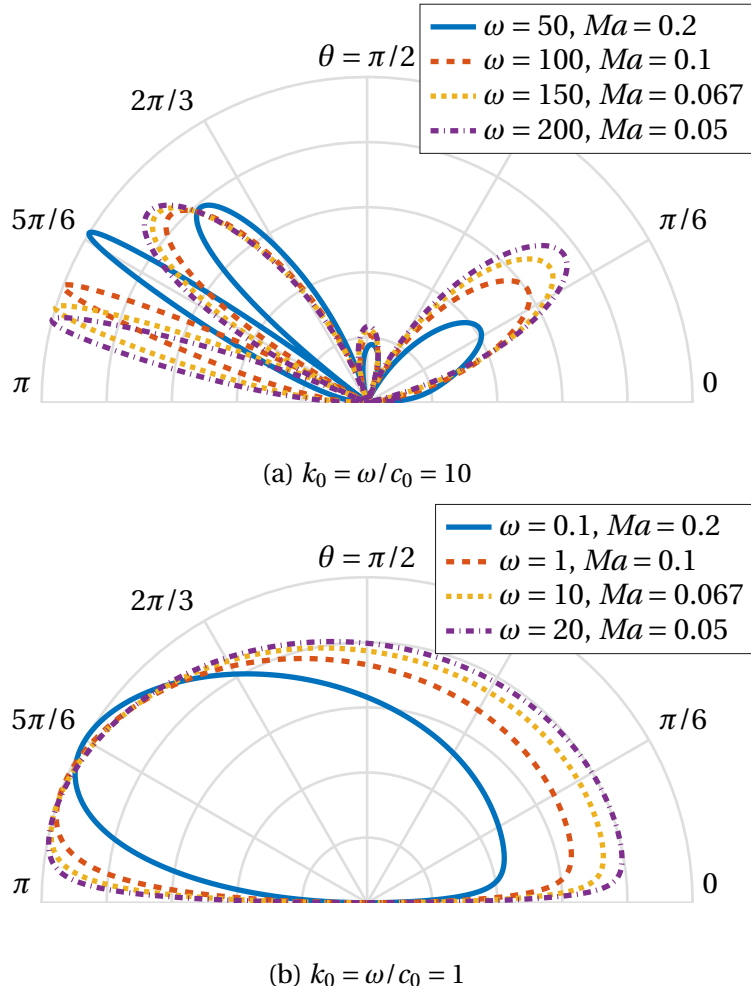


Fig. 4.4.5 For the same setup as figure 4.4.4, the hydrodynamic wavelength is varied whilst holding the acoustic wavelength/wavenumber constant, and $|\mathcal{P} I_{FF}|$ is plotted. For shorter wavelengths comparable to the boundary-layer thickness, the lobe-like structure develops, but the broad direction of the modes broadly invariant, though there is variation in the magnitude of each lobe. This confirms that the lobe-like behaviour is a function more of acoustic wavelength, as might be expected. For longer wavelengths, the compact dipole-like directivity is obtained, which varies little with changing λ_h .

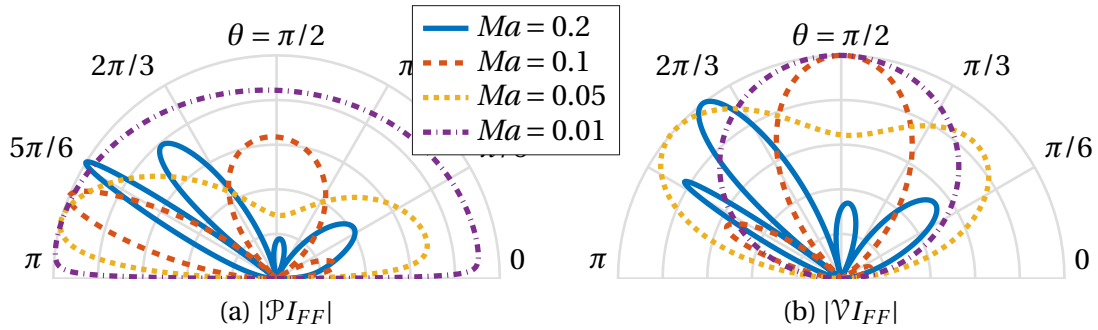


Fig. 4.4.6 For the same setup as figure 4.4.4, the free-stream Mach number is instead varied at fixed frequency $\omega = 50U_\infty/\delta$. Though the hydrodynamic wavelength is unchanged, the acoustic wavelength lengthens as c_0 is increased (and Ma decreased), and the multi-lobed high frequency behaviour tends towards the single-lobed dipole-type behaviour seen in the earlier section.

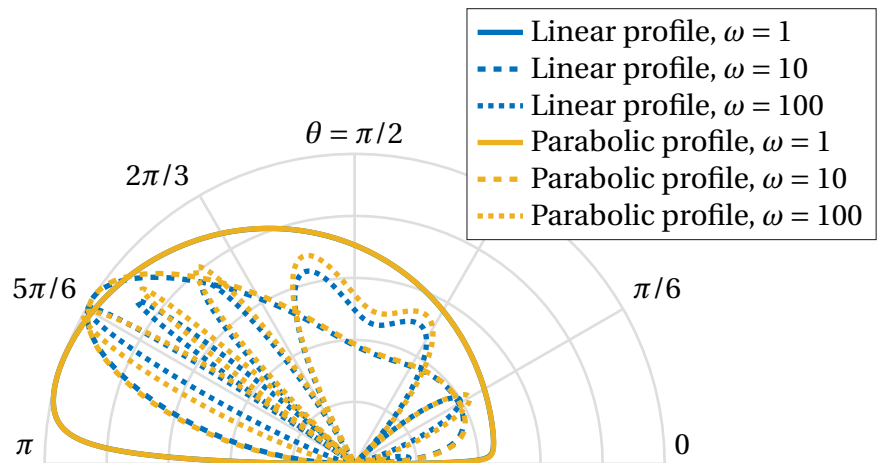


Fig. 4.4.7 The effect of profile shape is investigated, by construction of a linear and parabolic profile with $U(y_2)$ identical. Here, $y_2 = 0.3$ and $U_0 = 0.3$ for the linear case, making $U_0 = 0$ exactly for the parabolic case. In both cases the speed of sound is constant $c_0 = 5$, so have reasonably high $Ma = 0.2$. The resultant pressure directivity shows very little variation with background profile, despite the difference in shear throughout and differing slip velocity.

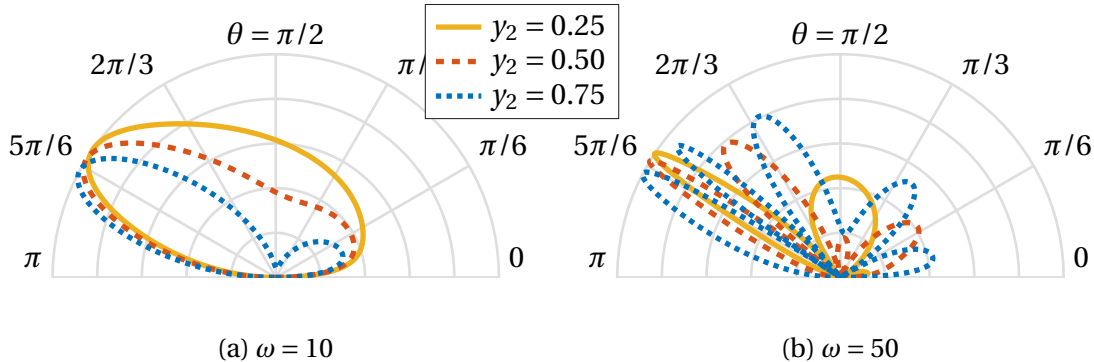


Fig. 4.4.8 For the same setup as figure 4.4.4 with fixed speed of sound $c_0 = 5$. $|\mathcal{P}_{IFF}|$ is plotted for two chosen frequencies: $\omega = 10$ so the acoustic wavelength $\lambda = \pi > \delta$, but not by much; and $\omega = 50$ with acoustic wavelength shorter than boundary-layer thickness. The source position y_2 is varied, with a near-wall source generating a more lobe-like solution proximity to its own image source. When the source is further from the wall, the tendency towards a monopole-like disturbance (with little direct interaction between the source and wall) is regained, though at this choice of parameters this effect isn't particularly clear.

pressure perturbations are therefore generated by

$$\phi_h(k_s)K(k_s) = \frac{\phi_h(y_2; k_s)}{D_h(k_s)} \frac{C(y_2; k_1)^4}{C(0; k_1)^4} \frac{1}{k_1 - \kappa_1(y_2)}. \quad (4.4.5)$$

In the limit $c_0 \rightarrow \infty$, $k_s \rightarrow 0$ for all θ , though we would expect D_h to rapidly change in the narrowing interval between the acoustic branch cuts. The ratio $C(y_2; k_1)/C(0; k_1) \rightarrow 1$, as it can be simply written down, and the Cauchy-type term tends to $-U(y_2)/\omega$. Deviation is then contained within $\phi_h(y_2)/D_h$, which can be approximated using results from the previous chapter. Since ϕ_h is defined by boundary-conditions at $x_2 = 0$, it depends little on the acoustic variables, and thus is broadly constant across the range of saddle points. Finally, $D_h \sim \gamma = \sin(\theta)$, which exactly cancels out the $\sin(\theta)$ dependence from the steepest descent integration parameterisation. This γ contribution is exactly cancelled out when considering \mathcal{V}_{IFF} , with the velocity operator bringing a factor of γ from the wall-normal derivative, and so a dipole with $\sin(\theta)$ directivity is obtained, which is the result we would also get from considering a free-stream acoustic potential, φ , with $p \sim \varphi$ and $v' \sim \partial\varphi/\partial x_2$.

For higher frequencies, multiple lobes appear, with the number increasing with Mach number. The lengthscale discussions earlier, however, highlight a limitation with varying frequency alone: it fails to isolate either variation in λ_h or λ_a , with both varying linearly with ω . To isolate these effects, figure 4.4.6 varies the Mach number alone (and thus only the acoustic wavelength λ_a) and figure 4.4.5 holds the acoustic wavenumber k_0 constant whilst varying frequency and speed of sound, thereby allowing variation of λ_h alone.

The number of lobes, and the silent points of far-field directivity vanishing, are clearly dependent on the acoustic wavelength as opposed to the hydrodynamic wavelength, though the amplitude of each lobe might vary with λ_h , as in figure 4.4.5a. In this figure, the acoustic wavelength $\lambda_a = 2\pi/10 \approx 0.6$ is comparable to δ and to y_2 . This lobe-like structure arises when the acoustic lengthscale is comparable to the boundary-layer thickness, or smaller. This is unsurprising, recalling the long-wavelength analysis before when only a dipole (a single-lobed structure) is observed.

Whilst we have established that the acoustic directivity depends almost entirely on the acoustic wavenumber, there are still other parameters to investigate the behaviour of. The first we consider, in figure 4.4.7, is whether or not the shape of the background profile affects the far-field directivity. As we shall see, the choice of y_2 affects directivity, so two profiles were constructed so that, for a given y_2 , $U(y_2)$ is the same in both profiles. In this example, a linear slipping profile (as in all images as yet) and a non-slipping parabolic profile are considered, with source at $y_2 = 0.3$. The two profiles are respectively shown with solid and dashed lines, for a selection of frequencies. Even at high frequency, where the lobe-like structure (corresponding to short acoustic wavelengths) is essentially unchanged by the choice of background profile, though small changes are observed that vanish at lower frequencies. This observation, that shape of background profile can be broadly ignored, justifies the focus on a single profile shape for all the far-field images generated so far.

We have identified short acoustic wavelengths give rise to lobe-like structures. This, however, need not be the only cause. There is still a freedom in specifying the source location, and this is investigated in figure 4.4.8. If the acoustic wavelength is much larger than the boundary-layer thickness, monopole-like behaviour persists independently of y_2 . However, if y_2/δ is small and λ_a is not large, then there might the development of lobe-like structures that don't exist for larger y_2 , or the enhancement of the lobe-like nature as seen in figure 4.4.8b. Whilst the exact reasoning behind these structures requires further research, a potential hypothesis is that were the solution to be constructed via imposition of an "image" source in $x_2 < 0$, the increased interference due to the source and its image as y_2 decreases causes a constructive and destructive interference pattern in the far-field pressure. Whilst there would be more simple cancellation in the uniform flow case, the small distortion due to the background shear potentially suffices to provide a suitable small difference in perceived phase in the far-field.

4.4.3 Far-field sound: downstream of source

We have computed the sound far beyond the boundary-layer, though we haven't considered the propagation of waves within the boundary-layer itself, driven by the critical layer contribution. Denoting $C_{CL,U}$ and $C_{CL,L}$ the parts of the critical layer contour in the $U/Lk_1 P$ respectively (both traversed left-to-right), we have

$$I_{CL} = \left(\int_{CL,U} - \int_{CL,L} \right) K_h(k_1; x_2) e^{-ik_1 x_1} dk_1, \quad (4.4.6)$$

giving the critical layer contribution, with K_h , whilst combining a variety of terms, "known". K_h has the additional property that $K_h(k_1^*) = K_h^*(k_1)$: essentially deriving from the fact that the problem requires the solution of a real differential equation with real boundary condition (which doesn't necessarily hold in the impedance case, below, for complex Z).

Deforming the critical-layer contours onto the critical layer itself (potentially indented around poles), gives

$$\begin{aligned} I_{CL} &= \int_{\omega/U_\infty}^{\omega/U_0} [K_h(s+i0) - K_h(s-i0)] e^{-isx_1} ds \\ &= 2 \int_{\omega/U_\infty}^{\omega/U_0} \text{Im}(K_h(s)) e^{-isx_1} ds \end{aligned} \quad (4.4.7)$$

with $\pm i0$ indicating evaluation just above or below the critical-layer respectively, and the evaluation in the latter integral taken on the upper side of the branch cut (with in the limit of small, positive imaginary part). This can be computed accurately numerically by deforming the branch to below the real axis, as outlined in §4.2.4, which allows precise evaluation on the branch cut (without numerical errors from the critical point of the differential equation). A general example of this integrand (without the Fourier oscillation e^{-isx_1}) is shown in figure 4.4.9.

For large x_1 , the integrand oscillates rapidly, and contributions from smooth regions of K_h cancel rapidly (which can be made concrete via the Riemann-Lebesgue lemma). The integral is therefore dominated by the end points. Consider the general case

$$J(x) = \int_{s_1}^{s_2} f(s) e^{-ixs} ds, \quad (4.4.8)$$

for large x , supposing $f \sim \beta_j(s-a)^{\alpha_j}$ for $j = 1, 2$, where $\alpha_j > -1$ for convergence of the integral. For f infinitely differentiable (or, at least, suitably differentiable for end points to

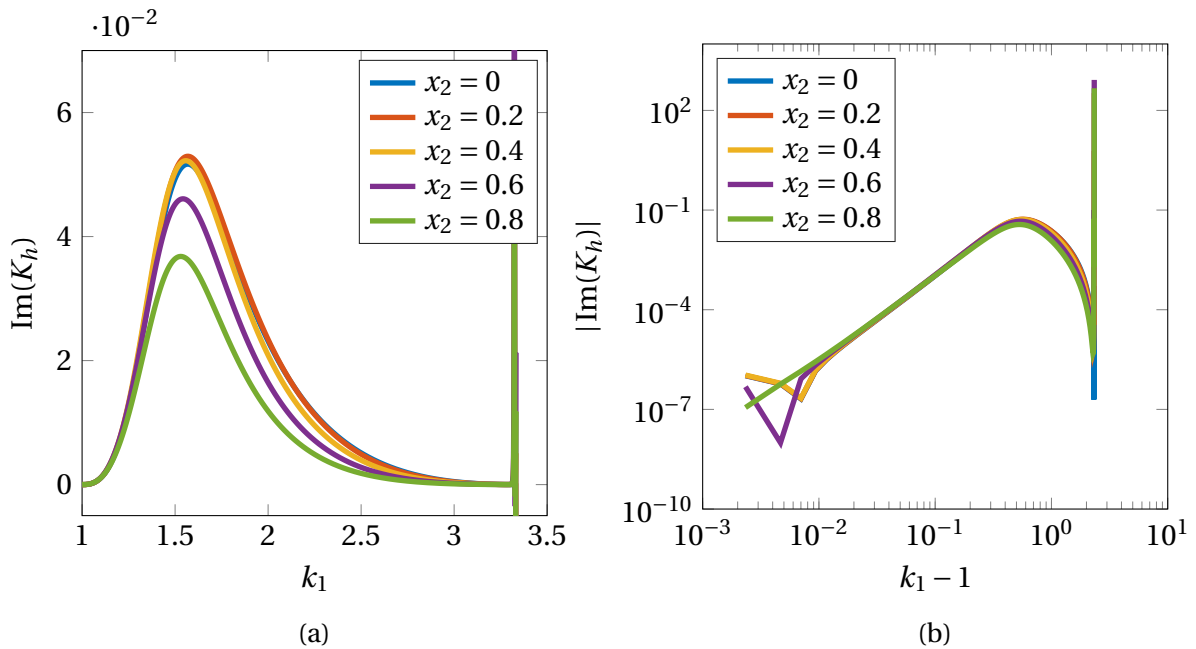


Fig. 4.4.9 For a parabolic profile ($U_0 = 0.3U_\infty$, $\omega = 1$, $c_0 = 5U_\infty$), the integrand K_h of the critical-layer integral (for pressure fluctuations) is shown for a variety of fixed x_2 (with source location $y_2 = 0.5$). The evaluation is just above the critical-layer contour (with $\text{Im}(k_1) = 0.001$), which removes computational errors near poles of the complete integrand. As can be seen, this imaginary part is *smooth* (despite the singularities in the real part, at poles of K_h). Fluctuations near $k_1 = \omega/U(0) = 3.333$ are due to numerical error due to the regular singular point in computing the ODE solution. Near $k_1 = 1$, the integrand looks like $(k_1 - 1)^2$, demonstrated by the log plot.

dominate), application of both Watson's and Jordan's lemma gives

$$J(x) \sim \beta_1 e^{iax} \Gamma(1 + \alpha_1)(ix)^{-(1+\alpha_1)} - e^{ibx} \Gamma(1 + \alpha_2) \beta_2 (-ix)^{-(1+\alpha_2)}. \quad (4.4.9)$$

Decay is therefore dominated by the end with smaller α_j . If the integrand is otherwise continuous, the remaining integrand decays, at its slowest, like $1/x$ and thus any integrable singularities ($-1 < \alpha_j < 0$) dominate the integral. The integrand decays more strongly than this at either end, as demonstrated by the earlier figure, with decay like $(k_1 - \omega/U_\infty)^2$ near $k_1 = \omega/U_\infty$. Careful comparison with the numerical solution shows that this end does, however, dominate (with the other end point contribution decaying even more rapidly in k_1) and thus $p'_{CL} \sim x_1^{-3}$ for the case plotted. This algebraic decay is consistent with earlier work [22].

That the critical-layer decays algebraically downstream is not a new result, but it is worth remphasising. Firstly, it decays comparatively slowly compared with any stable modes, and thus might be important at moderate distances downstream (where there are no unstable modes). Secondly, there is a clear distinction with the piecewise linear case. In the earlier case, neutrally stable modes, along where a critical-layer would be, could easily be identified, which did not decay downstream of the source. For a continuously sheared profile, however, all critical-layer disturbances decay. This highlights a great danger in a discontinuity in shear: a δ -function in shear gives rise to propagating solutions that cannot exist for smoothly varying shear.

4.5 Pressure-release and impedance boundaries

The routines outlined for the hard-wall section generalise in a straightforward manner for more complicated, linear, boundary conditions applied at $x_2 = 0$, though care must be taken with the existence of boundary-layer modes, which typically show either exponential growth or decay, arising as isolated zeros of D_ℓ .

The routines set up to analyse the dispersion function and to invert the integral essentially depend only on the boundary conditions through the definition of relevant ℓ_1 and ℓ_2 (so that $\ell_1\phi' + \ell_2\phi = 0$ on $x_2 = 0$). For the wall-normal velocity we imposed $\ell_1^h = -C_0^2 = -[i(\omega - U(0)k_1)]^2$ and $\ell_2^h = -3C_0C'_0 = -3(i(\omega - U(0)k_1)) \times (-iU'(0)k_1)$, implicitly dividing out a constant C_0^2 . Pressure-release conditions are obtained via $\ell_1^p = 0, \ell_2^p = -C_0^3$ and general impedance conditions are straightforward to synthesis by summing these coefficients. For impedance Z , $\ell_j^Z = i\omega Z \ell_j^h - C_0 \ell_j^p$. Fundamentally the routine is un-

changed, aside from the excitation of modal solutions away from the critical-layer, which must be included separately.

4.5.1 Pressure-release conditions

The two pairs of figures, figures 4.5.1 and figures 4.5.2, both consider disturbances to a parabolic profile, above a pressure-release wall. With lengths scaled by boundary layer thickness δ , and all speeds by free-stream velocity U_∞ , we have slip velocity $U_0 = 0.3$ and free-stream Mach number $M_\infty = 0.2$, corresponding to (constant) speed of sound $c_0 = 5$.

The dispersion function (and thus the majority of singularities of the Fourier transformed disturbance) are shown in figures 4.5.1 for two frequencies, $\omega = 1$ and $\omega = 20$, chosen to display two distinct characteristics. The former is linearly unstable, with a pair of conjugate modes lying on either side of the branch cut (with real part ≈ 1 and imaginary part ≈ 0.3). Either by including these within the branch cut integration contour, or by calculating the residue at each zero (and thus at each pole of the integrand), it is straightforward to include this contribution in the fully computed solution, shown in figure 4.5.2a, with a disturbance growing exponentially downstream. Conversely, the higher frequency case $\omega = 20$ is stable (see figure 4.5.2b), with the instability modes subsumed into the critical-layer, and no such exponentially growing disturbance visible. This is directly analogous to the linearly sheared, incompressible case, where the behaviour and stabilisation of conjugate modes could be tracked as the frequency was varied.

In fact, it is straightforward to show that these roots of the compressible dispersion relation are the same modal solutions as in the incompressible case, and are thus hydrodynamic in nature (rather than acoustic). Consider a simple piecewise linear profile, for example, with $U_0 = 0.2$ and $U_\infty = 1$. Using methods outlined in the previous chapter, this has a pair of conjugate modes in the long-wavelength limit at $k_1 = 1.3843 \pm 0.3621i$. Similar zero finding can be done with finite speed of sound. If $c_0 = 5$ is constant, so reasonably high Mach number of 0.2, we have zeros at $k_1 = 1.3855 \pm 0.3607i$: there is negligible effect of finite speed of sound on the location of these modes. Even with a more complicated boundary-layer profile, for example a parabolic boundary-layer profile with the same slip and free-stream velocities, we have only small displacement with $k_1 = 1.2071 \pm 0.3413i$, though the effect of varying the profile is clearly a lot greater than of varying the speed of sound.

Finally, for the higher-frequency case a series of poles appear near the acoustic branch cut. Poles of the dispersion function do not in themselves contribute to the solution (since they correspond only to zeros of the integrand), and will not feature in this discussion.

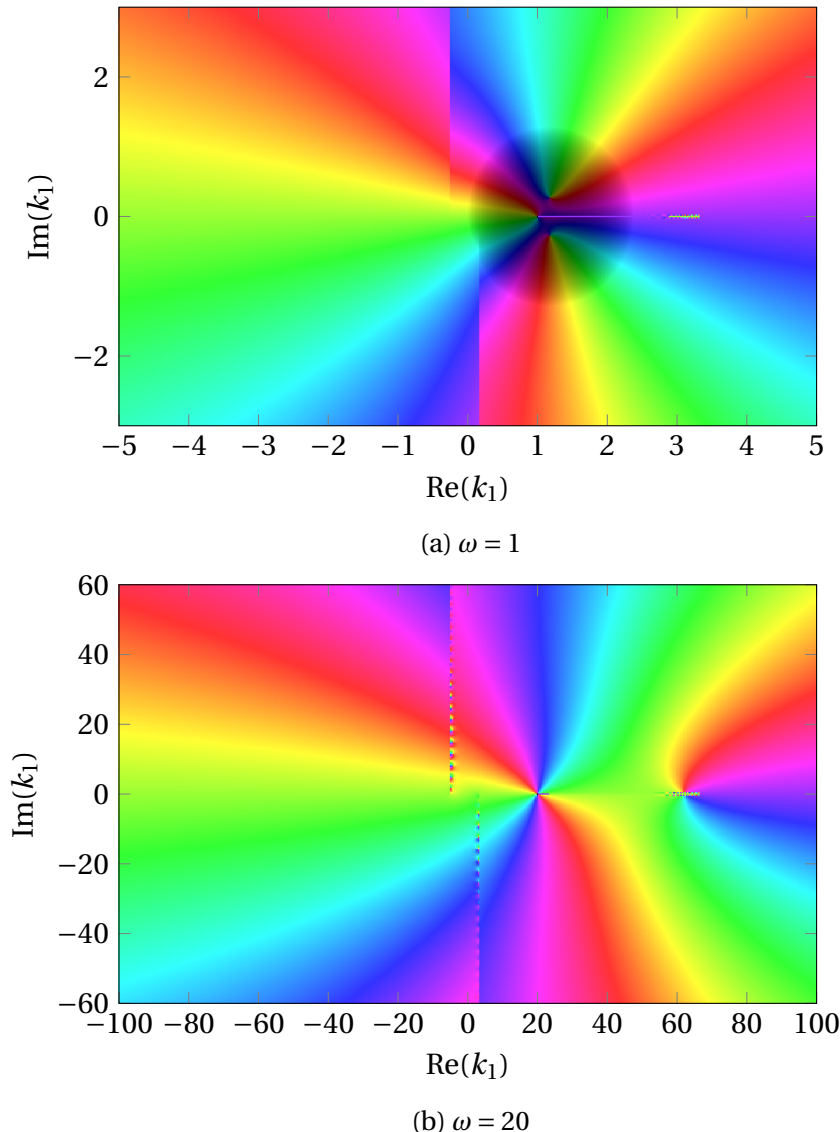


Fig. 4.5.1 Phase plot of dispersion function, D_p , as outlined in the text, for two different frequencies, one unstable and one stable. Since the axes are both stretched with ω , the acoustic and critical-layer branch cuts are in the same location on the image in each plot.

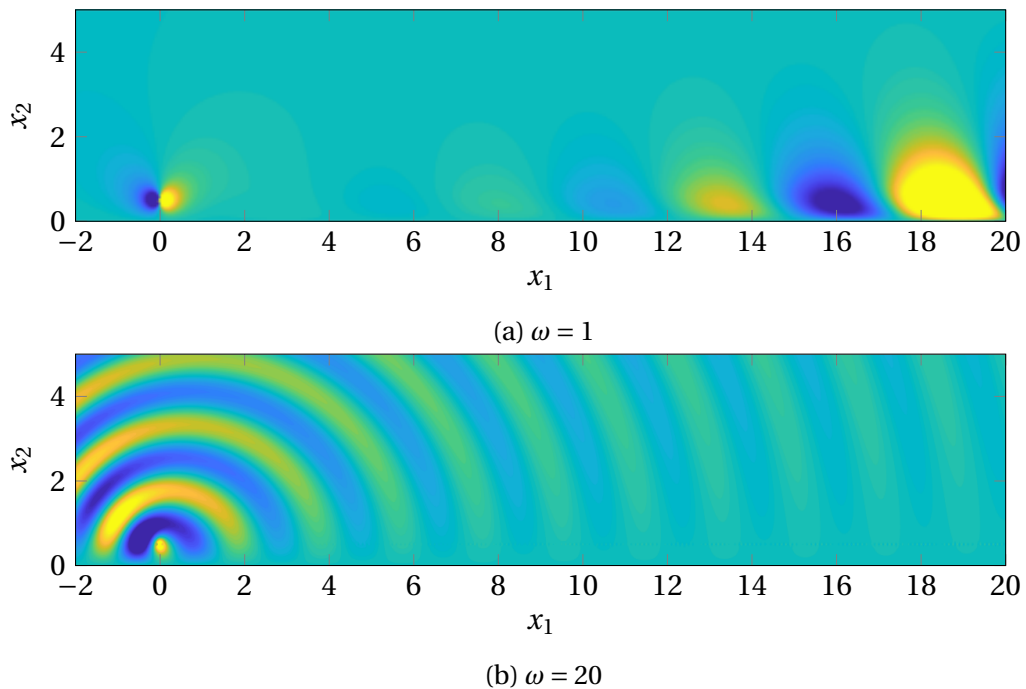


Fig. 4.5.2 The pressure perturbation above a pressure-release wall, in an unstable configuration. We have the standard parabolic profile ($U_\infty = \delta_\infty = 1$), with $U_0 = 0.3$, and $M_\infty = 0.2$, and two frequencies, $\omega = 1$ and $\omega = 20$ chosen so that unstable modes exist in the former case, figure 4.5.2a (but not the latter, figure 4.5.2b), growing exponentially downstream.

Far-field noise

As previously, we can compute the far-field acoustic response through evaluation at a saddle point. This process is identical to the hard-wall procedure, with suitable replacement of functions, and so is not repeated here. In the long-wavelength case, we expect a dipole-like directivity in pressure due to the boundary-condition now being imposed on pressure, which mathematically comes out of the evaluation of I_{FF} since D_p , unlike D_h , is broadly constant in the limit $c_0 \rightarrow \infty$ at the saddle point location.

A sample of far-field directivities has been computed. Firstly, the speed of sound is increased while holding frequency constant, increasing only the acoustic wavelength, in figure 4.5.3, showing a similar lobe-like structure to the hard-wall equivalent (though it is worth noting the number of lobes is generally reduced in all cases, suggesting a reduction in interference between the source and the reflection from the wall). Similarly, it is easy to show the far-field dependence on exact flow profile is small analogously to the hard-wall case (figure 4.4.7). The effect of varying source location is again investigated, and again (for higher frequencies than previously) a source close to a wall induces lobe-like far-field behaviour. Direct comparisons between hard-wall and pressure-release directivities will be investigated below, through variation of impedance Z from ∞ to 0. This also allows reinvestigation of the far-field results found in the incompressible case in the previous chapter, §3.6, where the mathematics of the far-field sound calculation were not clear.

4.5.2 General impedance boundary condition

The impedance case arises from taking the boundary condition

$$\mathcal{L}_{01}^Z = i\omega Z \mathcal{V}_{01} - C_0 \mathcal{P}_{01}. \quad (4.5.1)$$

Other required functions drop out readily from the previous work, for example we can write

$$D_Z = \mathcal{L}_{01}^Z \phi_d = i\omega D_h - C_0 D_p. \quad (4.5.2)$$

This allows use of previously computed dispersion functions, if desired. Other than the loss of symmetry in $k_1 \rightarrow k_1^*$, the process of determining zeros, numerical inversion and evaluation of far-field acoustics generalises directly from the preceding cases. As with the long-wavelength case in §3, we expect some number of zeros of D_Z , though the precise number of these boundary-layer modes depends on the precise setup, as does their resultant stability.

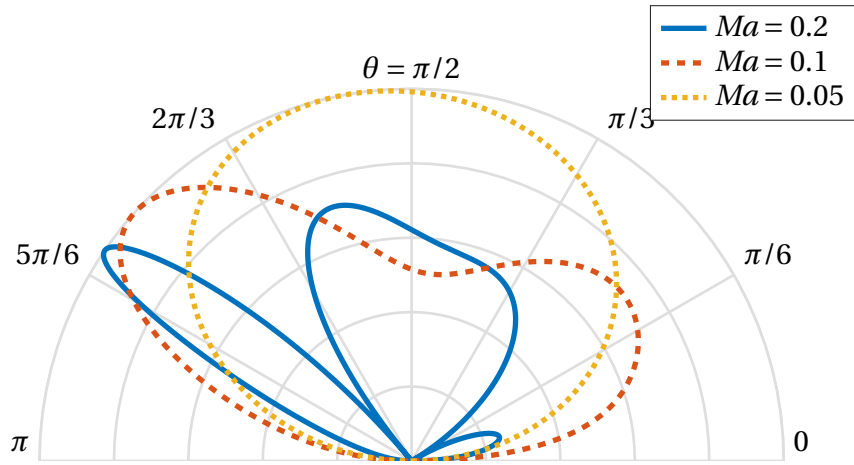


Fig. 4.5.3 Perturbation far-field noise due to a point source at $y_2 = 0.5$ to a slipping linear profile ($U_0 = 0.3U_\infty$) above a pressure-release wall, for frequency $\omega = 50$, as the speed of sound c_0 is increased (and thus free-stream Mach number, $U_\infty/c_0 = 1/c_0$ is decreased). This should be compared to figure 4.4.6. The lobe-like behaviour is less developed. In the incompressible limit $c_0 \rightarrow \infty$, a $\sin(\theta)$ dipole directivity is obtained.

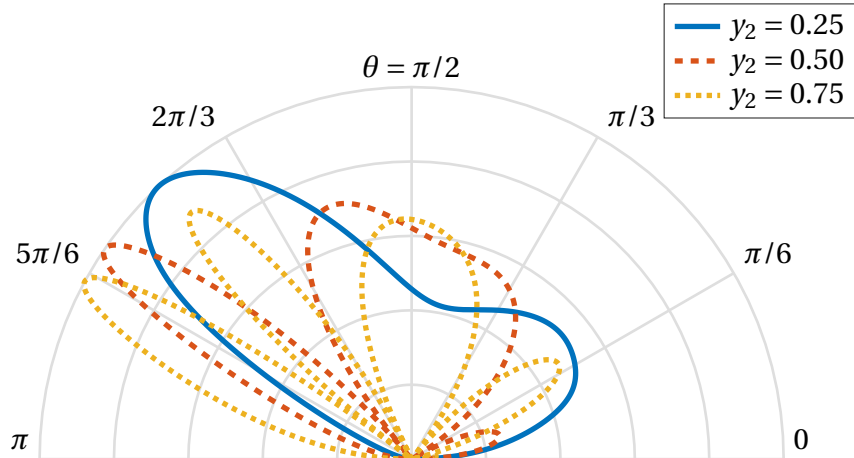


Fig. 4.5.4 Variation of source location y_2 , exactly as figure 4.4.8b, save with a pressure-release boundary. The higher frequency case $\omega = 50$ is shown as it is more interesting, the lower frequency case results in single-lobe, $\sin(\theta)$ -type profiles for all y_2 chosen. Again, we get increased lobe-like behaviour as y_2 decreases, though the number of lobes is always less than the corresponding hard-wall case.

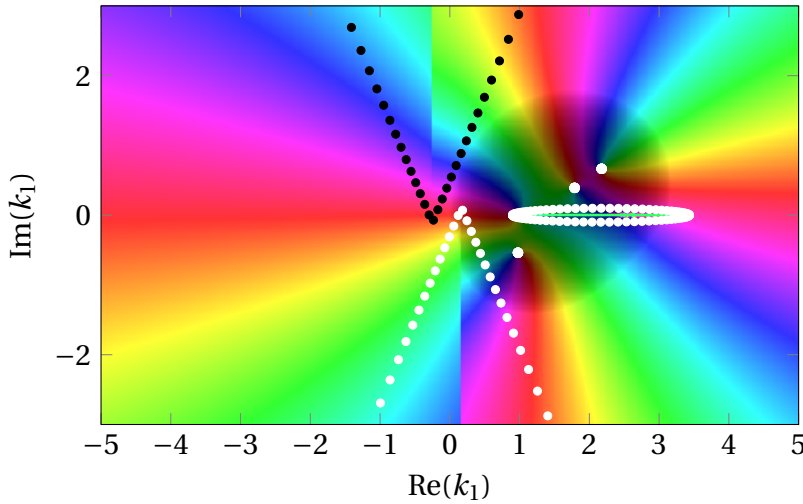


Fig. 4.5.5 Dispersion function for the setup discussed in the text and in figure 4.5.6. The three modal solutions are visible, two above the critical layer and one beneath. A selection of quadrature points are also shown, white for $x_1 > 0$ and black for $x_1 < 0$, though they have been thinned out to increase visibility.

To demonstrate the viability of this method, the case $Z = 0.1 + 0.1i$. at unit frequency, is considered². This has three boundary-layer modes, two in the UH k_1 P and one in the LH k_1 P as can be seen by the dispersion function in figure 4.5.5, and the two in the UH k_1 P are convectively unstable (as a Briggs-Bers analysis shows). The full inversion plot is computed and the pressure disturbance plotted in figure 4.5.6. The far-field noise for this setup can also be computed, but it is a simple single-lobe disturbance and is uninteresting, due to the low frequency chosen.

Finally, we can use this impedance formulation to validate earlier results, with $Z = 0$ regaining the pressure-release and $Z = \infty$ regaining the hard-wall case. We recall earlier work when the location of critical-layer modes was investigated as $|Z|$ was varied in the long-wavelength case (§3.6, specifically figures 3.6.6), and the observation that whilst the modal behaviour as $Z \rightarrow 0$, $Z \rightarrow \infty$ was the same, the exact modes that correspond to the limiting modes varied.

Similarly, we can investigate the lobe-like structure for shorter acoustic wavelengths, and how this depends on Z , as per figures 4.5.7. We have previously seen that pressure-release disturbances typically have fewer lobes than hard-wall solutions, and a dipole-like directivity rather than a monopole directivity. There is clear distinction between lobes in both cases, with certain directions in which no sound is radiated. For finite,

²In ν' the factor ρ_0 has been taken to be 1, which scales Z . For consistency, what is referred to here as Z is strictly $c_0^2 Z$. Whilst this doesn't affect specific results, it must be borne in mind when comparing different values of background speed of sound. This scaling cannot be imposed if c_0 is a function of x_2 .

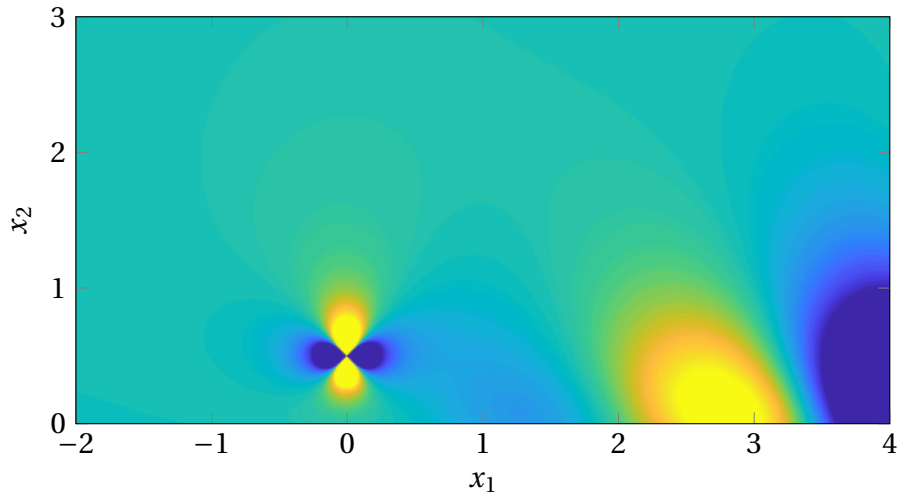
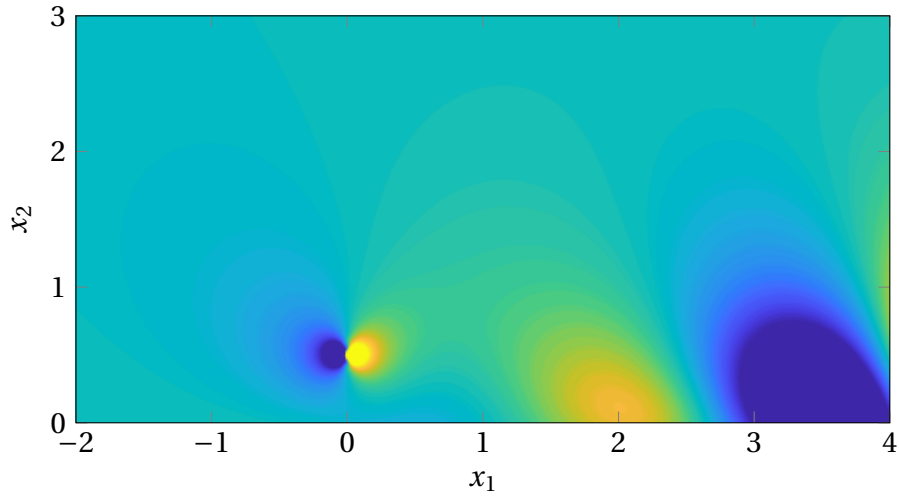
(a) Real part of pressure disturbance (at $t = 0$)(b) Imaginary part of pressure disturbance (at $t = 0$)

Fig. 4.5.6 The full inversion for a slipping parabolic profile with $U_0 = 0.3U_\infty$ and free stream Mach number 0.2, above a lined wall with (scaled) impedance $0.1 + 0.1i$. This setup has two unstable boundary-layer modes, dominated for large x_1 by the one with the largest imaginary part.

non-zero Z these lobes are no longer distinct. Whilst there is a clear gradual change from pressure-release to hard-wall regardless of the sign of $\text{Im}(Z)$, the exact variation in lobe-like structure is completely different between the two cases. For $\arg(Z) = \pi/4$ (figure 4.5.7a), the large pressure-release mode around $\theta = \pi/2$ quickly splits into two, with the hard-wall mode with θ slightly larger than $2\pi/3$ quickly forming, even for small $|Z|$. The downstream propagating and normal propagating modes are slower to develop. Conversely, the wall-normal propagating mode develops immediately if $\arg(Z) = -\pi/4$ (figure 4.5.7b), centred on $\theta = \pi/2$, whereas the downstream pressure-release lobe only slowly separates into two downstream lobes for large $|Z|$. This observation reinforces what we have seen before in §3.6: there appears to be no consistent map between $Z = 0$ and $Z = \infty$ that can match lobes (or modes) between the two cases.

4.6 Wake solutions

For completeness, the disturbance due to a point source in an unbounded region should also be considered, relevant to the wake of the trailing-edge of an aerofoil in §6 later. This has been considered for the the piecewise-linear, long-wavelength case before in §3.7, though a slightly different approach is considered here due to the limitations of the code constructed for integration of the governing transformed ODE. The basic setup is shown in figure 4.6.1.

4.6.1 Auxiliary functions

For the piecewise linear case, we constructed two auxiliary functions to satisfy the boundary conditions, namely decay as $x_2 \rightarrow \pm\infty$ upon transformation, corresponding to outgoing waves only. This required little extra work, as routines had been constructed to cope with non-continuous shear, it being the cornerstone of the chapter. However, the code utilised in this chapter implicitly assumes continuity of U' throughout the boundary-layer, manually taking care of any jump in shear at the edge of the boundary-layer $x_2 = \delta$. Most profiles of interest in the doubly-infinite case have a discontinuity in shear at $x_2 = 0$. Without developing methods of integration to cope with this shear jump, it is possible to utilise earlier code. We describe the background flow profile as

$$U(x_2) = \begin{cases} U_\infty^+ & x_2 > \delta^+ \\ U^+(x_2) & 0 < x_2 < \delta^+ \\ U^-(-x_2) & \delta^- < x_2 < 0 \\ U_\infty^- & x_2 < \delta^- \end{cases} \quad (4.6.1)$$

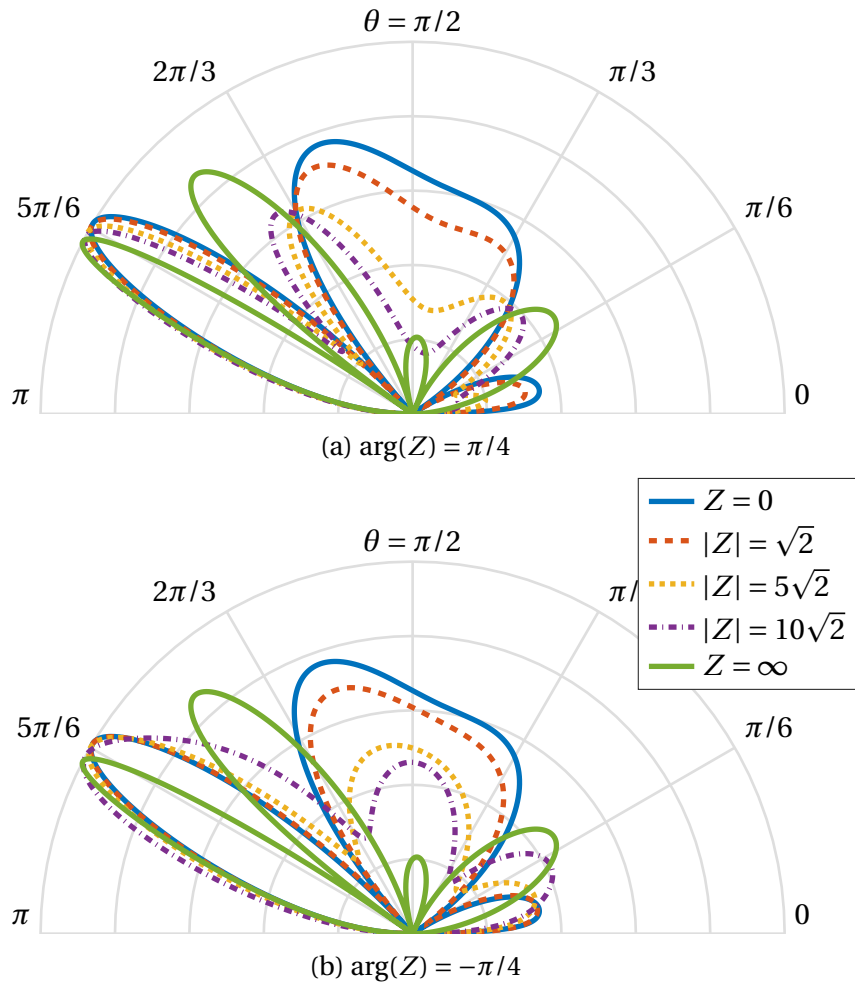


Fig. 4.5.7 For the typical parabolic slipping profile, with $U_0 = 0.3U_\infty$, $c_0 = 5U_\infty$, and $\omega = 50$ (chosen to ensure behaviour differing from a single lobe) the effect on far-field pressure directivity through variation of Z is investigated, with $Z = 0$ regaining the pressure-release solution and $Z = \infty$ the hard-wall solution shown for reference.

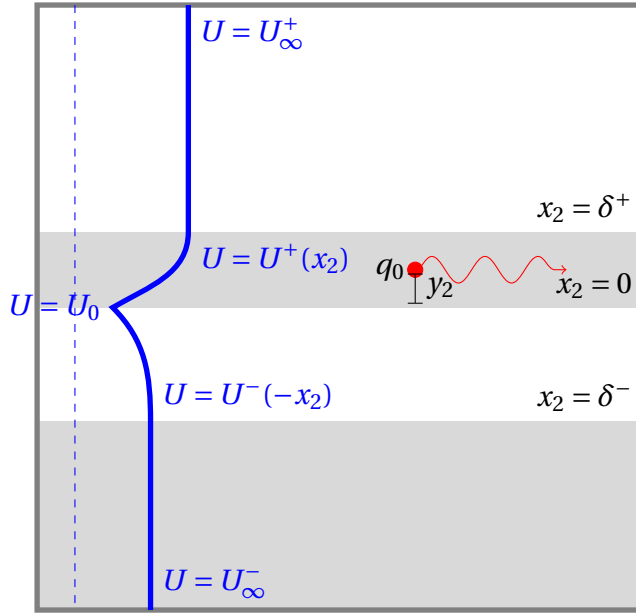


Fig. 4.6.1 Setup: a point source above a wake. There is a finite region of shear for $\delta^- < x_2 < \delta^+$, potentially with a discontinuity in shear at $x_2 = 0$ (and $x_2 = \delta^\pm$). As before, we place a point mass source at $(x_1, x_2) = (0, y_2)$, assuming $y_2 > x_2$.

with $\delta^- < 0 < \delta^+$, and U^\pm both defined for positive arguments $z \in (0, \delta^\pm)$ respectively. We can then define decaying auxiliary functions on these half-profiles, as before, with $\phi_d^\pm(z)$ the decaying auxiliary function for profile $U^\pm(z)$. The need now is to extend the $\phi_d(-x_2)$, which takes negative values of x_2 , into the region $0 < x_2 < y_2$, to construct what has hitherto been referred to as ϕ_ℓ . We can do this via the imposition

$$\mathcal{V}_{01}^{0+} \phi_\ell(0^+) = \mathcal{V}_{01}^{0-} \phi_d^-(0^-) \quad (4.6.2a)$$

$$\mathcal{P}_{01}^{0+} \phi_\ell(0^+) = \mathcal{P}_{01}^{0-} \phi_d^-(0^-), \quad (4.6.2b)$$

which is simply continuity of pressure and of vertical velocity across the wake, and takes into account the jump in shear in the difference between the pressure operators $\mathcal{V}^{0\pm}$. We can now essentially think of ϕ_ℓ as the inner auxiliary function with boundary conditions on $x_2 = 0$ of the form $\ell_1 \phi'_\ell + \ell_2 \phi_\ell = 0$, exactly as before. These functions ℓ_j are driven by the flow beneath the plate, but reduce to routines already used throughout this chapter.

Explicit determination of ℓ_1 and ℓ_2 is required. Writing $\mathcal{V}^{0\pm} = \ell_1^{h\pm} d/dx_2 + \ell_2^{h\pm}$, and similarly $\mathcal{P}^{0\pm} = \pm \ell_1^{p\pm} d/dx_2 + \pm \ell_2^{p\pm}$ we have the linear system

$$\ell_1^{h+} \phi'_\ell + \ell_2^{h+} \phi_\ell = \ell_1^{h-} \phi_d'^- + \ell_2^{h-} \phi_d^- \quad (4.6.3a)$$

$$\ell_1^{p+} \phi'_\ell + \ell_2^{p+} \phi_\ell = \ell_1^{p-} \phi_d'^- + \ell_2^{p-} \phi_d^- \quad (4.6.3b)$$

This can be solved to give

$$\begin{pmatrix} \phi'_\ell \\ \phi_\ell \end{pmatrix} = \frac{1}{\ell_1^{h+}\ell_2^{p+} - \ell_1^{p+}\ell_2^{h+}} \begin{pmatrix} \ell_2^{p+}\ell_1^{h-} - \ell_2^{h+}\ell_1^{p-} & \ell_2^{p+}\ell_2^{h-} - \ell_2^{h+}\ell_2^{p-} \\ \ell_1^{h+}\ell_1^{p-} - \ell_1^{p+}\ell_1^{h-} & \ell_1^{h+}\ell_2^{p-} - \ell_1^{p+}\ell_2^{h-} \end{pmatrix} \begin{pmatrix} \phi_d^{-'} \\ \phi_d^- \end{pmatrix}. \quad (4.6.4)$$

We now note the earlier normalisation chosen as per (4.3.7), with

$$\ell_1 = \phi_\ell(0) = \frac{(\ell_1^{h+}\ell_1^{p-} - \ell_1^{p+}\ell_1^{h-})\phi_d^{-'} + (\ell_1^{h+}\ell_2^{p-} - \ell_1^{p+}\ell_2^{h-})\phi_d^-}{\ell_1^{h+}\ell_2^{p+} - \ell_1^{p+}\ell_2^{h+}}, \quad (4.6.5a)$$

$$\ell_2 = -\phi'_\ell(0) = \frac{(\ell_2^{h+}\ell_1^{p-} - \ell_2^{p+}\ell_1^{h-})\phi_d^{-'} + (\ell_2^{h+}\ell_2^{p-} - \ell_2^{p+}\ell_2^{h-})\phi_d^-}{\ell_1^{h+}\ell_2^{p+} - \ell_1^{p+}\ell_2^{h+}}. \quad (4.6.5b)$$

Whilst this expression is messy, it is readily computable as a function of k_1 . Simplification follows from the simple form of \mathcal{P} , with $\ell_1^{p\pm} \equiv 0$ and $\ell_2^{p+} = \ell_2^{p-}$, with (for generalised acoustic potential ϕ , $\mathcal{P}_{01}^{0\pm} = -C_0^3$). In fact, the simple form of \mathcal{P} greatly simplifies the above expression, and we have

$$\ell_1 = \phi_d^-(0^-) \quad (4.6.6a)$$

$$\ell_2 = \phi_d^{-'}(0^-) + 3 \left(\frac{C_0^{+'} + C_0^{-'}}{C_0} \right) \phi_d^-(0^-) \quad (4.6.6b)$$

with $C_0 = i(\omega - U(0)k_1)$ continuous and $C_0^{\pm'} = -ik_1 U^{\pm'}(0)$.

The resulting ϕ_ℓ is therefore the continuation of ϕ_d^- into $x_2 > 0$, satisfying the same jump condition as at the edge of the boundary-layer in §4.2. Therefore, we can use the earlier representation of the disturbance due to the point source, (4.3.8), with

$$\phi_- = \begin{cases} \phi_\ell(x_2) & x_2 > 0 \\ \phi_d^-(x_2) & x_2 < 0 \end{cases} \quad (4.6.7)$$

and all earlier constructions carry over with no further difficulty. Care is needed when taking transverse derivatives due to the argument of ϕ_d^- taking negative values. There is a slight penalty in numerical efficiency, as to compute $\phi_\ell(x_2, k_1)$ an additional computation of $\phi_d^-(0, k_1)$ is required. Further, different steepest descent contours are required for $x_2 > \delta^+$ and $x_2 < \delta^-$, driven by the free-stream velocity above and below the wake.

4.6.2 Complete inversion

As a specific example for complete inversion, we consider the following group of background profiles. We define $U_1(x_2)$ to be a slipping parabolic profile with vanishing shear at the edge of the boundary layer, $x_2 = \delta = 1$ (defining the length scale), with $U(0) = U_0 = 0.3$ and $U(\delta) = U_\infty = 1$ (thereby providing the velocity scaling). Similarly, define U_2 to be the parabolic profile with the *same* slip velocity and boundary-layer thickness and free-stream velocity 0.5. We can then consider three cases: firstly that both $U^\pm = U_1$, so that the flow profile is symmetric in $x_2 \leftrightarrow -x_2$, or that $U^+ = U_1$ and $U^- = U_2$ or vice versa.

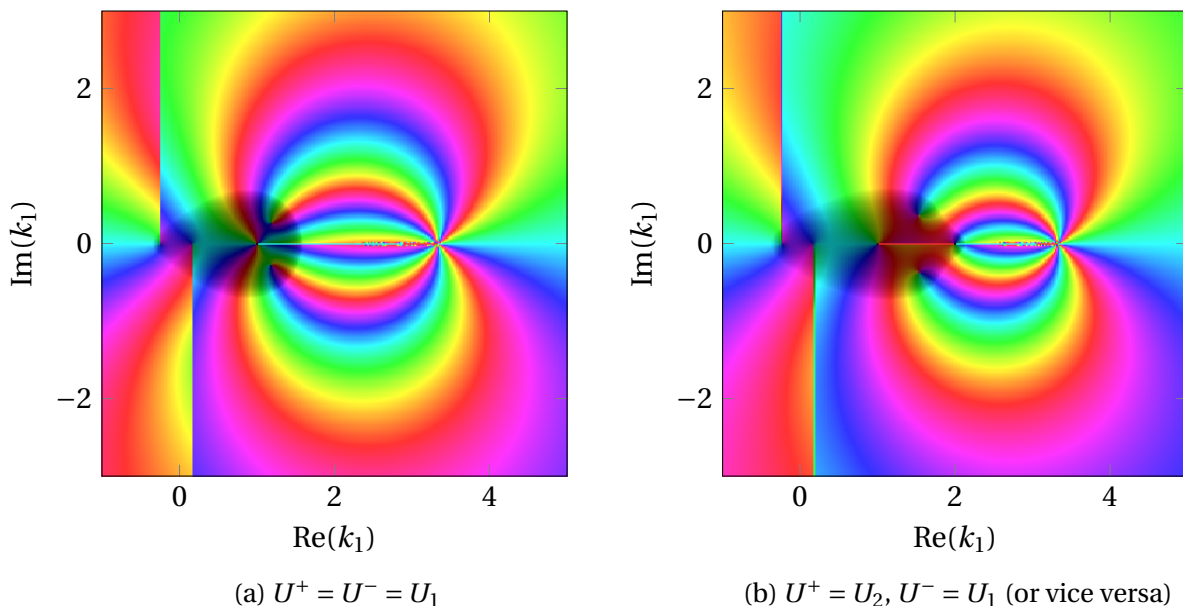


Fig. 4.6.2 For $\omega = 1$ and $c_0 = 5$, the wake dispersion functions for the symmetric and asymmetric cases is plotted, as discussed in the text.

In both cases, the profile is unstable at $\omega = 1$, with strong inflection at $x_2 = 0$ driving this instability. The dispersion functions are shown in figure 4.6.2, for the symmetric and asymmetric cases (the latter independent of which of U^\pm is $U^{(1,2)}$). A variety of features of these functions should be identified, firstly noting the conjugate zeros near $\omega/U_\infty = 1$ away from the real axis, corresponding to an unstable and a stable mode. In the asymmetric case, these are drawn back towards $\omega/U_{2\infty} = 2$, but still lie in the same broad region of the complex plane. They grow faster in the asymmetric case, with larger imaginary part.

The dispersion function also has points of note near both types of branch cuts. An additional branch point exists at $\omega/U_{2\infty} = 2$ in the asymmetric case, though as it lies on the critical-layer between $\omega/U_{1\infty}$ and ω/U_0 it is not easy to see. Essentially, we have two superimposed branch cuts lying along the critical-layer branch cut for $x_2 \geq 0$ separately.

This does not occur in the symmetric case when both critical-layer branch cuts lie in the same place. Lastly, and hard to make out on the given plots, the acoustic branch cuts divide into two in the asymmetric case: the one driven by the cuts of γ with $U = U_1(\delta^+)$, and the one driven by cuts of γ with $U_2(\delta^-)$. If these substantially differ, care is required that the steepest descent contours, which loop their appropriate acoustic branch cut, do not cross the “new” acoustic branch cut from the flow on the other side of the wake. For low Mach number flow this is not an issue, as the cuts lie very close to each other, but it might be an issue at higher Mach numbers with greatly differing flow speeds.

Finally, in the symmetric case we note that, as with the long-wavelength case, we can relate this dispersion function D_ℓ to the product $D_h D_p$ for the flow profile restricted to $x_2 > 0$, and thus any hard-wall or pressure-release modes naturally arise as wake modes.

Inversion, up to the caveat that the inversion contour should not cross any additional acoustic branch cuts, then proceeds as throughout in this chapter. There may be benefits from using different contours for the branch cut inversion depending on whether $x_2 \gtrless 0$. For the cases we are considering, the full inversion is computed and displayed across figures 4.6.3 and 4.6.4, picking up modal contributions from the dispersion zeros identified in figures 4.6.2. The source is always placed at $y_2 > 0$, in the upper flow. The strength of the source is clearly reduced when the upper flow is slower, even with amplification by the factor $1/U(y_2)$, which is directly related to the reduction in shear at the source location.

Notwithstanding this, the increased growth rate of the unstable (Kelvin-Helmholtz) mode is clear in the asymmetric cases (figures 4.6.3b, 4.6.3c), with downstream development of the perturbation barely visible in the symmetric case (figure 4.6.3a). Further, it is possible to eyeball a physical “location” of the resulting instability (at least in the pressure plots, figure 4.6.3), with the instability localised on the side of $x_2 = 0$ with the largest free-stream velocity. Conversely, the growth of the wall-normal velocity perturbation (figure 4.6.4) is always centred on the shear discontinuity itself, at $x_2 = 0$, and shows more aggressive growth.

4.6.3 Far-field noise

Far-field noise can be computed as before, driven by the saddle point contribution. As noted, however, the steepest descent contour is a function of the free-stream velocity, and therefore differs for $x_2 \gtrless 0$ if we have an asymmetrical wake, which extends to the location of the saddle point too. This leads to interesting lobe-like behaviour of the far-field noise of an asymmetric wake.

Initially, however, it is worth focusing on a symmetric wake, or at least a wake with $U_\infty^- = U_\infty^+$, though the structure of the shear-layer may differ for $x_2 \gtrless 0$. This is done in

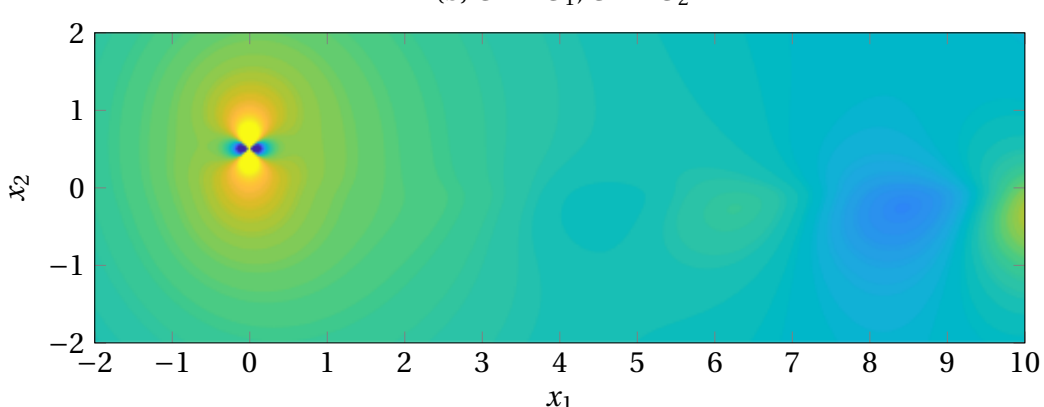
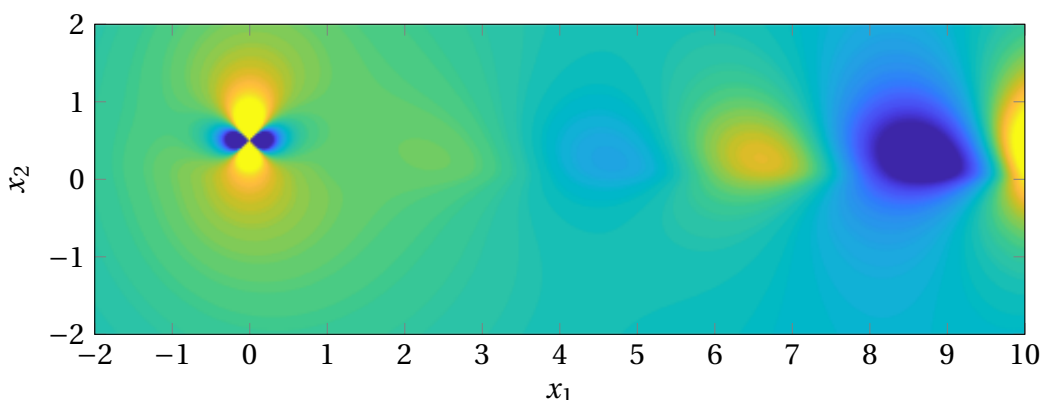
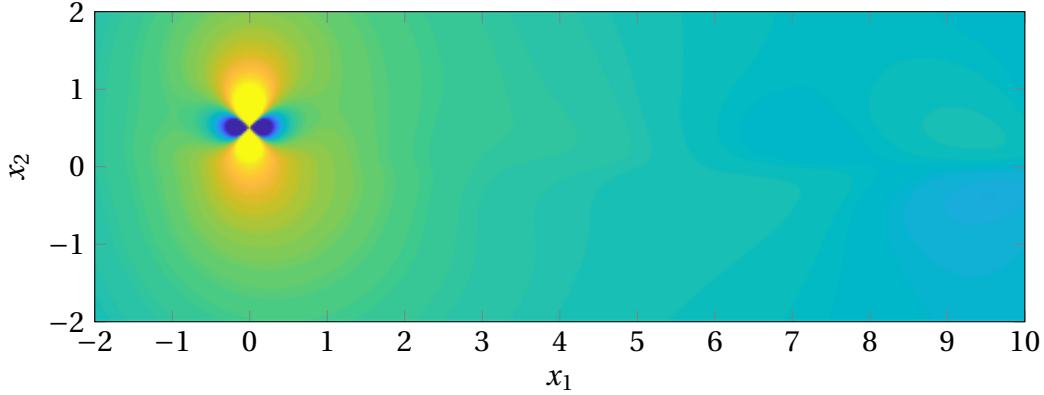
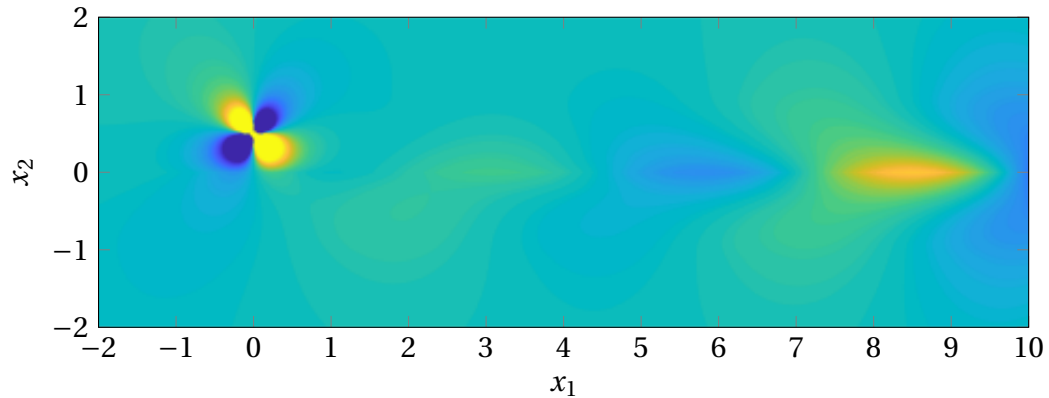
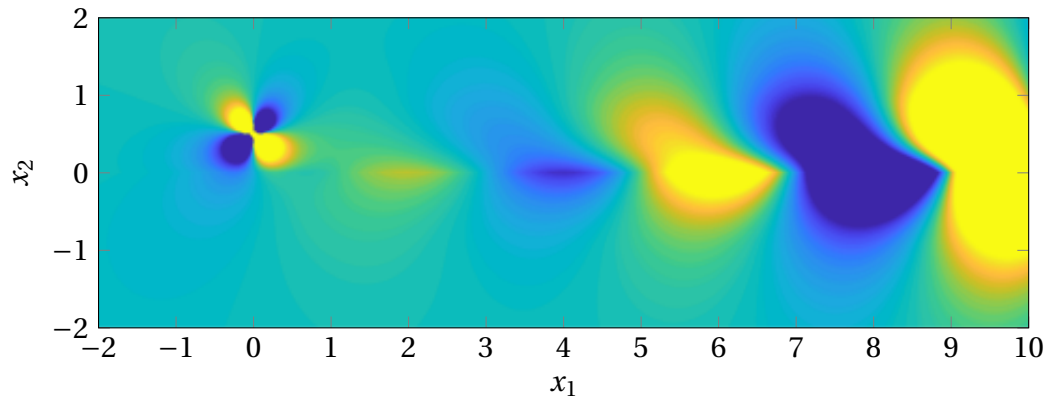
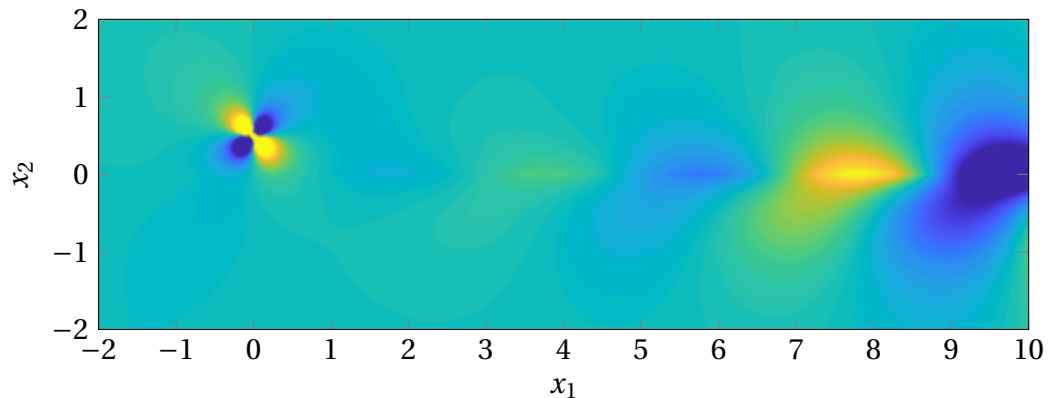


Fig. 4.6.3 $\text{Re}(p'_0)$ for a point source at $y_2 = 0.5$ (above the wake) of unit frequency, with free-stream Mach number 0.2 for the fastest flow (i.e. $c_0 = 5$ is constant). Here the shear is non-zero for $x_2 \in (-1, 1)$, with a discontinuity in shear along $x_2 = 0$.

(a) $U^+ = U^- = U_1$ (b) $U^+ = U_1, U^- = U_2$ (c) $U^+ = U_2, U^- = U_1$ Fig. 4.6.4 $\text{Re}(v'_0)$ for the setup as previous (figure 4.6.3)

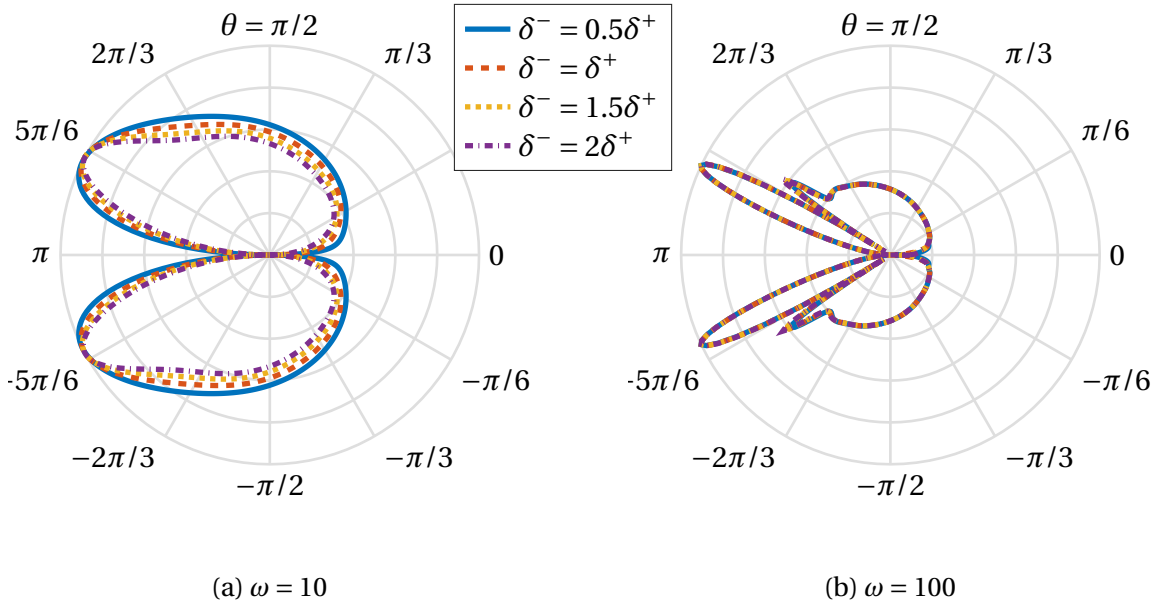


Fig. 4.6.5 The far-field pressure directivity, $|\mathcal{P}I_{FF}|$. If the free-stream velocity is the same above and below the plate, the radiation profile is symmetric. Here, the effect of only changing δ^- is investigated. Above and below the plate, we have a parabolic profile with $U_0 = 0.3U_\infty$ and constant speed of sound $c_0 = 5$.

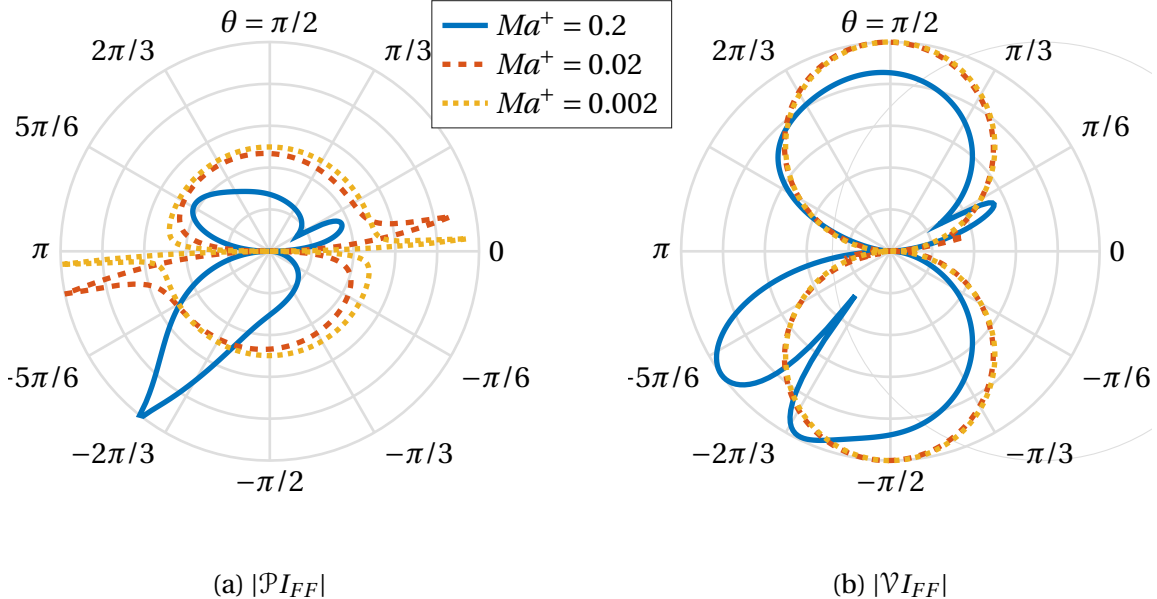


Fig. 4.6.6 The (constant) speed of sound c_0 is varied, for an asymmetric wake, with Mach number shown for the free-stream velocity above the wake. Both above and below $x_2 = 0$, where $U_0 = 0.3$, we have a parabolic profile, with $U_\infty^- = 2U_\infty^+$, with the latter U_∞^+ scaling the speed of sound. $\delta^\pm = 1$ and $\omega = 10$, producing a lobe-like behaviour for high Mach numbers. For lower Mach numbers, a monopole-like directivity in pressure (and dipole-like in v') is regained, as the acoustic wavelength increases.

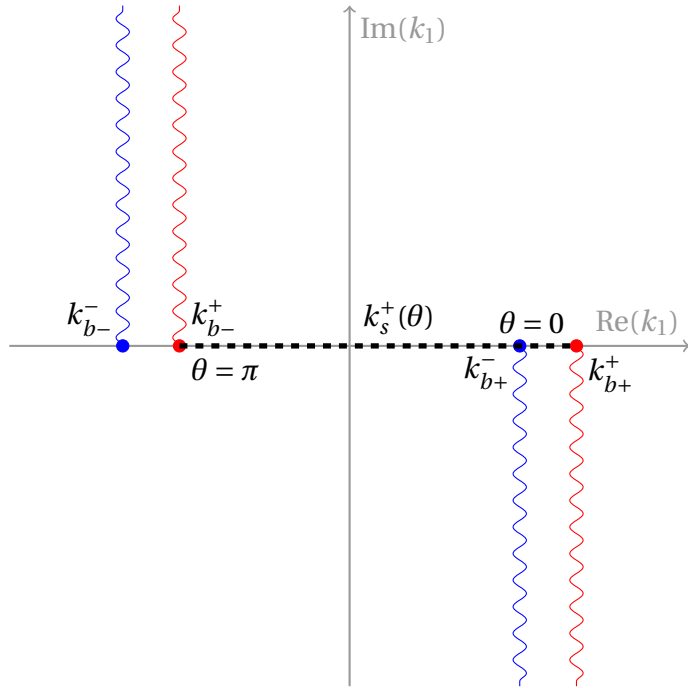


Fig. 4.6.7 Variation of saddle point location for $x_2 > 0$, including crossing over indicative acoustic branch points generated from lower flow.

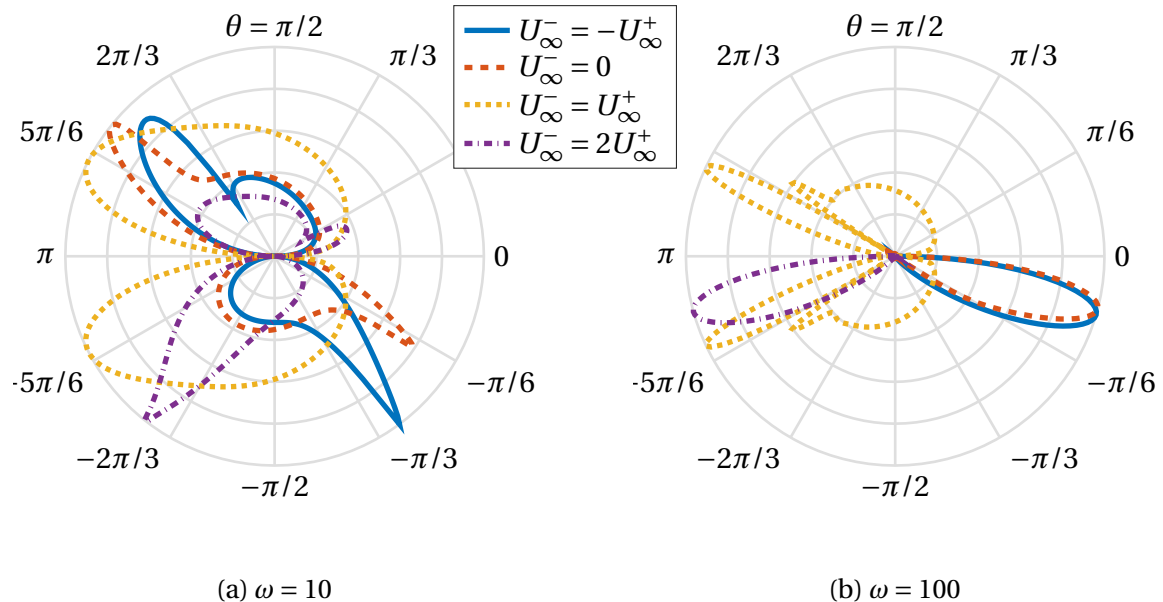


Fig. 4.6.8 If there is asymmetry in the free-stream velocity above and below a shear layer, a (predictable) lobe-like structure develops, as discussed in the text. Here, we have a parabolic profile above and below a wake with $U_0 = 0.3U_{\infty}^+$ and $c_0 = 5U_{\infty}^+$, and the free-stream velocity below the wake is varied. At higher frequencies there is a very strong, directed lobe against the direction of the (beneath wake) flow.

figure 4.6.5, where only the width of the lower layer, δ_∞^- , is varied. For low frequencies (long acoustic wavelengths) there is a simple pattern with single lobe for each of $x_2 \geq 0$ and a symmetry in $x_2 \mapsto -x_2$, or $\theta \mapsto -\theta$. This is to be expected: the saddle point location is unchanged under this transformation, since it is a function only of free-stream speed of sound and free-stream velocity, neither of which are modified in this example. For long acoustic wavelengths a monopole-like structure (in pressure) is obtained, essentially following from the acoustics not noticing the thin shear layer and therefore radiating equally in all directions (up to some modifications by the uniform background flow).

For higher frequencies, as per figure 4.6.5b, an upstream propagating lobe structure appears, with thin lobes developing, and the count increasing for larger ω , though this is confined to large $|\theta|$ and there is always a single downstream propagating lobe, with the directivity essentially independent of δ^- . This differs from the case with boundaries, where we saw putting the source near the wall (be it lined or not) generated lobe-like directivity in all directions. We do not have the same image source construction here (as we have no boundaries) and there is direct potential interference source to generate this pattern.

The monopole, θ -independent directivity is emphasised as we increase the acoustic wavelength in figure 4.6.6, for a slightly asymmetric profile. For large λ_a , i.e. large c_0 , we obtain a clear $\sin(\theta)$ directivity, as expected from an acoustically compact shear layer (though the source strength and thus amplitude is a function of background shear). As the wavelength is decreased, a clear lobe-structure develops in the asymmetric case. This can be explained mathematically by noting the behaviour of the saddle points as the observer angle, $\theta = \tan^{-1}(x_2/x_1)$, varies, schematically shown in figure 4.6.7. There are four acoustic branch points, driven by the branch points of γ with U_∞^\pm , explicitly given by (for general background flow speed U)

$$k_{b\pm} = \frac{U\omega}{c_0^2 - U^2} \pm \frac{1}{c_0} \sqrt{\frac{\omega^2}{(c_0^2 - U^2)^2} - \frac{k_3^2}{c_0^2 - U^2}}. \quad (4.6.8)$$

With two free stream velocities U_∞^\pm , we therefore get four such k_b , which shall be denoted $k_{b\pm}^\pm$ with each \pm independent. We can then note the behaviour of the saddle point. For example, for $x_2 > 0$, the saddle point $k_s^+(\theta)$ goes from k_{b+}^+ to k_{b-}^- as θ varies from 0 to π , which is exactly as the case has previously been. For some θ , however, $k_s^+ = k_{b+}^-$ (as per the sketch, though the branch cuts could be swapped). Since D_ℓ is minimal here, it is reasonable to expect singular behaviour, and indeed we see in the directivity plots

this critical value of $\theta = \theta_0$ amplifies far-field radiation. There is a corresponding angle, approximately $\theta_0 - \pi$, for $x_2 < 0$ generating the peak beneath the wake.

This lobe-like structure is made most obvious when asymmetry is considered directly, as per figure 4.6.8, where the free-stream velocity below the plate is varied. Two values of ω are considered, to emphasise the strength of this singular lobe for higher frequencies. The code is perfectly capable of coping with the background profile becoming negative, and as such we can consider monotonic shear layers on $\delta^- < x_2 < \delta^+$, which (as expected) has the effect of swapping the direction of the new lobe from positive streamwise direction to negative streamwise direction, consistent with swapping the positions of the two pairs of branch cuts. At high frequencies, this single directed lobe dominates the far-field solution, and is a direct result of the asymmetry.

4.7 Discussion and conclusions

The principal strength of this chapter lies in the extension of previous analytic modelling methods, focused on simple boundary-layer profiles and restrictive physical assumptions, to a far more generic case of arbitrary, continuous, background profiles and speeds of sound (as a proxy for background density), whilst ensuring the numerical methods are not computationally expensive. The success of this method was demonstrated on the same physical setup as in the previous chapter, §3, namely of a mass source above a flat surface, which may or may not be lined. The primary goal of this model problem was to evaluate the strength of the numerical routines used, including the (numerical) Fourier inversion methods as well as integration across a boundary-layer, both of which will be used throughout the scattering problems in the next two chapters, §5 and §6, as well as in the far-field computation of acoustic radiation through the method of steepest descent.

Whilst this chapter consists primarily of preliminary mathematical work, it does result in an array of interesting physical results. Firstly, in relation to the preceding chapter, §3, we have a chance to reanalyse the far-field noise in the limit $c_0 \rightarrow \infty$, and we have another chance to observe surface modes, be they unstable modes above a pressure-release surface or above a more general lined surface with impedance Z . The surface modes highlighted in the previous chapter reoccur in this more general framework, even with c_0 finite, and correspond closely to the (necessarily hydrodynamic) modes found in the previous chapter. Previous work varied $|Z|$ from 0 (pressure-release) to ∞ (hard-wall). The relaxation of pressure-release modes to hard-wall modes depended very sensitively on the argument of Z . An alternative analysis is tested in this chapter, considering the lobe-like nature of the far-field noise at relative short acoustic wavelengths λ_a . The lobe-

structure for the pressure-release wall continuously varies as $|Z|$ is increased, limiting to the hard-wall structure at $|Z| = \infty$, though the precise nature of the lobe decomposition again depends sensitively on $\arg(Z)$, providing another note of caution in attempting to match surface modes with pressure-release or hard-wall equivalents.

By allowing finite c_0 and short acoustic wavelengths, it is possible to investigate the much richer far-field noise structure than in the previous chapter. The steepest descent method explicitly identifies a saddle point lying between the two acoustic branch point, and numerical methods for finite c_0 allow evaluation at exactly this saddle point, unlike the previous difficulties arising from direct evaluation at $k_1 = 0$ in the incompressible limit. A noticeable difference arises, however, in the nature of the far-field noise (and, indeed, the near-field solution) as per §3 and within this chapter. Consider, for example, a point mass source above a hard-wall. In the limit $c_0 \rightarrow \infty$, this generates an acoustic wave through the interaction with the background vorticity, which is not the case in this chapter. For finite, if large, c_0 , the point mass source generates a pressure wave directly, through the coupling between perturbation density and pressure through entropy conservation, regardless of the existence, or not, of background shear. This fundamental difference is borne out in the both the near-field solution (compare, for example, figures 3.5.5b and 4.4.3a, particularly in the vicinity of the source) and in the far-field directivity. Above a hard-wall, we have a pressure monopole-like directivity in the large (but finite) c_0 limit, due to constructive interference between the monopole source and its image. Conversely, there is destructive interference in the infinite c_0 case, generating a dipole. For these reasons, it is difficult to comment on the accuracy of the far-field analysis in the preceding chapter.

The code and mathematics in this chapter has focused on the assumption of a monotonic, finite, boundary-layer. This assumption of finite boundary-layer not physically reasonable in practice. For reasonably small Reynolds numbers, we might expect a developed Blasius-type boundary-layer to have evolved. Whilst this asymptotes to a constant value as $x_2 \rightarrow \infty$, it does not fit with the finite δ assumption inherent in the numerics. This is not an insurmountable problem, as the same methods can be developed to include a boundary-layer profile stretching to $x_2 \rightarrow \infty$, and provides a useful example of a straightforward extension to the current work. This is not the only limitation as presented here. Whilst the code as written can cope with both variable c_0 (as a proxy for background density) and spanwise wavenumber k_3 , the solutions presented in this chapter focus on the purely two-dimensional case, under the assumption that the Mach number is sufficiently low that the background speed of sound can be regarded as constant.

Chapter 5

Scattering from a junction

A fundamental problem of acoustics is the generation of sound from the interaction of a vortical gust solution with a sharp change in boundary conditions. Utilising the Wiener-Hopf technique, this chapter focuses on the scattering of a hydodynamic disturbance at an abrupt change to the treatment of a surface, for example the leading- or trailing-edges of a section of lining. The effect of lining on scattered noise is investigated, including when a convectively unstable surface mode is excited over a finite region of lining.

5.1 Introduction

So far, we have focused on *streamwise homogeneous* boundary conditions, more generally applicable to any problem for which the boundary lies along a streamline of the background flow, and on which the boundary condition is a function linking ϕ and $\partial\phi/\partial n$ which is independent of position along this streamline. The setup in §3 and §4 permits the use of the Fourier transform, exploiting the x_1 -independence of the boundary condition, which in turn is defined for all $x_1 \in (-\infty, \infty)$, with the perturbation being driven by some point forcing within the body of the fluid.

In many applications we might expect an abrupt change in boundary condition, most noticeably at the sharp trailing-edge of an aerofoil. This is a well-understood source of sound, with an efficient conversion of vortical motion to far-field acoustic noise, via the insistence that the scattered solution is non-singular at the discontinuity itself [31] and the imposition of the unsteady Kutta condition. Scattering by a sharp trailing-edge is only one example of the generation of acoustic disturbances by a boundary-layer discontinuity, and this chapter focuses firstly on the generic junction between two boundary conditions, before developing the theory to transition between two lined surfaces (or potentially no-penetration (hard) or pressure-release surfaces), so that there is one boundary condition

(along $x_2 = 0$) for $x_1 < 0$ and a different one for $x_1 > 0$. The Wiener-Hopf technique and half-range Fourier transforms allow many of the previous methods to transfer to this problem, which gives great control over the behaviour at the scattering point, without loss of generality at $x_1 = x_2 = 0$.

Scattering by the transition between a hard and soft surface has been considered previously, though typically in the framework of a duct. In 2007 Rienstra [89] considered the scattering of a hard-wall duct mode at a hard-soft transition within a duct, identifying components reflected and transmitted within the duct and drawing parallels with scattering from the end of a duct. The surface modes previously identified are problematic in this case, though, with causality analysis difficult in the uniform-flow case, and so a vortex-sheet type boundary layer (separating zero flow from the mean flow near the boundary) was considered. More recent work by Singh and Rienstra [93, 101] has considered directly including a shear layer in the scattering problem with both hard-soft and soft-hard transitions, using the incompressible limit as considered previously by Rienstra and Darau [91]. This formulation raises some questions, both of *causality*, the direction in which neutrally stable modes propagate, and in the loss of a cleanly identifiable Wiener-Hopf strip. The problem therefore requires revisiting as the limit of a well-understood numerical problem, which is part of what this chapter aims to do.

Via the inclusion of a finite shear layer, the excitation of surface modes is precisely understood, since they are no longer confined to lie exactly along the wall and instead propagate within the (now non-infinitesimal) boundary-layer. As well as allowing precise solution of the scattering problem, this allows discussion of the restabilisation of an unstable surface mode, for example at the end of a lined section. Downstream of the lined section we do not expect to find such an unstable mode, which is borne out in the mathematical analysis. However, if the surface mode is excited for a finite downstream extent the resulting amplification of the mode can lead to strong acoustic scattering as it restabilises. Therefore, whilst the surface mode itself might not be a source of sound, the restabilisation thereof may well be. This is investigated in the limit of acoustically-decoupled junctions in §5.6.

This chapter begins with an outline of the Wiener-Hopf method and its application to single-junction scalar problems, for generic differential operators in §5.2. This illustrates a few technicalities that require care in the Wiener-Hopf process, for example insisting on continuity of the logarithm along the separation contour, and provides an intuitive representation of the Wiener-Hopf kernel as the ratio of upstream and downstream dispersion functions. This is then applied to the scattering of an incident vortex sheet, from which a more general gust solution could be constructed (see §6.3) across a hard-soft junction,

exciting modes when the downstream boundary condition is unstable (a function of frequency and background profile, as determined in §4). In particular, the limits of $c_0 \rightarrow \infty$ (the incompressible limit) and of $U_0 \rightarrow 0$ (the no-slip limit) are considered numerically and, where appropriate, analytically in §5.4. Once the method has been shown to work in the near-field, and readily gives far-field scattered noise with little computation required through similar methods to §4, it is generalised to the generic scattering between two lined surfaces in §5.5, which happens to be mathematically more straightforward as the Wiener-Hopf kernel is better behaved. Finally, the restabilisation of a convectively unstable surface mode is discussed in §5.6, as the result of an upstream junction. Provided coupling between the scattered solutions themselves can be ignored, the impact on the excited mode can be analysed.

5.2 The generic scattering problem

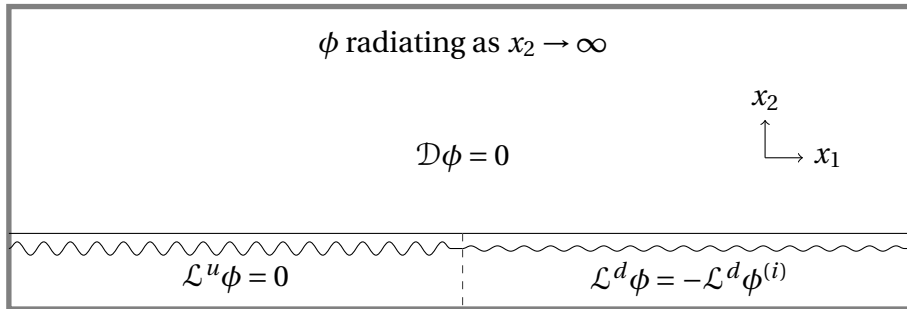


Fig. 5.2.1 The setup for the solution of the generic scattering problem considered in this section, with a scattered quantity ϕ driven by forcing or some incident solution on the downstream boundary ($x_1 > 0$).

Before application of the method to scattering of a disturbance from a junction between two boundaries, it is instructive to consider the generic scattering problem for a two-piece boundary. The setup is sketched in figure 5.2.1. For some scattered quantity ϕ , the problem we consider is a mixed boundary-value problem, namely

$$\mathcal{D}\phi = 0 \quad x_2 > 0, -\infty < x_1 < \infty \quad (5.2.1a)$$

$$\mathcal{L}^u\phi = 0 \quad x_2 = 0, x_1 < 0 \quad (5.2.1b)$$

$$\mathcal{L}^d\phi = -\mathcal{L}^d\phi^{(i)} \quad x_2 = 0, x_1 > 0 \quad (5.2.1c)$$

coupled with a radiation condition at infinity. The solution is driven by $\phi^{(i)}$, which we will relate to the upstream solutions derived in the previous section. All differential operators,

\mathcal{D} , and $\mathcal{L}^{u,d}$, are linear and independent of the coordinate x_1 (which will continue to be referred to as the streamwise coordinate even for this more general problem), though they mainly contain streamwise derivatives $\partial/\partial x_1$.

5.2.1 Half-range Fourier transforms and the Wiener-Hopf method

We can solve this problem, provided the integrals converge, using half-range Fourier transforms and applying the Wiener-Hopf method. Given the mixed nature of the boundary conditions, it is natural to introduce half-range Fourier transforms, defined as

$$f_1^+(k_1, x_2, t) = \int_0^\infty f(\mathbf{x}, t) e^{+ik_1 x_1} dx_1, \quad (5.2.2a)$$

$$f_1^-(k_1, x_2, t) = \int_{-\infty}^0 f(\mathbf{x}, t) e^{+ik_1 x_1} dx_1, \quad (5.2.2b)$$

which together sum to give the full Fourier transform. They behave similarly to Laplace transformations and can be inverted by considering an inversion contour passing above or below all singularities as appropriate. Further, they have the property that f_1^+ is analytic in the upper-half complex k_1 plane (UH k_1 P) and f_1^- in the lower-half complex k_1 plane (LH k_1 P), a fact that will be exploited in later analysis.

Using these transformations on the boundary condition along $x_2 = 0$ allows recasting of the problem in k_1 -space, with as before subscript 1 denoting the streamwise transform of a quantity and \pm (either sub- or superscript) denoting the domain of analyticity of the function. In Fourier space, (5.2.1) becomes

$$D_1 \phi_1 = 0 \quad x_2 > 0 \quad (5.2.3a)$$

$$\mathcal{L}_1^u \phi_1^+ + p_u(k_1) = 0 \quad x_2 = 0 \quad (5.2.3b)$$

$$\mathcal{L}_1^d \phi_1^- + p_d(k_1) = -\mathcal{L}_1^d \phi_1^{(i)+} \equiv -I^+ \quad x_2 = 0 \quad (5.2.3c)$$

The functions p_u and p_d are end-point contributions, from the truncation of the Fourier transform. Analogously to the Laplace transform, we have

$$\left(\frac{\partial^n f}{\partial x_1^n} \right)_1^\pm = (-ik_1)^n f_1^\pm \mp \sum_{j=1}^n (-ik_1)^{n-j} \frac{\partial^{j-1} f}{\partial x_1^{j-1}}(x_1 = 0^\pm) \quad (5.2.4)$$

with the contributions from $x_1 = 0^\pm$ (in real space) contributing to the half-range transformation, though have no impact on analyticity (as polynomials are entire), and they cancel

out in the analysis that follows. This allows definition of the transforms of the operators $\mathcal{L}_1^{u,d}$ by the substitution $\partial/\partial x_1 = -ik_1$.

We now have an ordinary differential equation for ϕ_1 , with a radiation condition at infinity. With the chosen convention for temporal Fourier transforms, this becomes a decay condition as $x_2 \rightarrow \infty$ in k_1 space. Denoting the decaying solution of $\mathcal{D}_1\phi_1 = 0$ as ϕ_d , we have

$$\phi_1 = A(k_1)\phi_d \quad (5.2.5)$$

with A to be determined from the boundary conditions. Critically, this means

$$\mathcal{L}_1^{u,d}\phi_1 = A(k_1)\mathcal{L}_1^{u,d}\phi_d \quad (5.2.6)$$

Using this fact, and splitting¹ via $\mathcal{L}_1^{u,d}\phi_1 = \mathcal{L}_1^{u,d}\phi_1^+ + \mathcal{L}_1^{u,d}\phi_1^-$ (see (5.2.12) below) allows writing down

$$A\mathcal{L}_1^u\phi_d = -p_u + (\mathcal{L}_1^u\phi_1)^+ \quad (5.2.7)$$

$$A\mathcal{L}_1^d\phi_d = -p_u + (\mathcal{L}_1^d\phi_1)^- - I^+ \quad (5.2.8)$$

We define the two unknown functions $U^+ = (\mathcal{L}_1^u\phi_1)^+$ and $U^- = (\mathcal{L}_1^d\phi_1)^-$, analytic in the upper and lower half-planes respectively. We further define the two dispersion functions, $D_{u,d} = \mathcal{L}_1^{u,d}\phi_d$, analogous to the previously defined functions. Finally, we define the Wiener-Hopf kernel

$$K = \frac{D_d}{D_u} = \frac{\mathcal{L}_1^d\phi_d}{\mathcal{L}_1^u\phi_d} \quad (5.2.9)$$

linking together the upstream and downstream solutions. With this, we can eliminate A to give

$$K(U^+ - p_d) = (U^- - p_u) - I^+. \quad (5.2.10)$$

Since the end-point polynomials are entire functions of k_1 , this is an equation of the form

$$KB^+ = C^- - I^+ \quad (5.2.11)$$

with B^+ and C^- unknown, except for their domain of complex analyticity. This is a Wiener-Hopf equation [79], and can be solved for both B^+ and C^- by appealing to known physical behaviour of the solution near the boundary discontinuity, or equivalently for large k_1 . We suppose, for the time being without proof, that we can decompose any complex analytic

¹We assume that the \mathcal{L} are (in Fourier space) a polynomial in k_1 and therefore entire in k_1 , so that $\mathcal{L}^u\phi_1^\pm = (\mathcal{L}_1\phi_1)^\pm$.

function additively:

$$F = F^+ + F^- \quad (5.2.12)$$

with superscript \pm denoting the half-plane of analyticity (UH k_1 P or LH k_1 P respectively). This is unique up to the addition of an entire function to one side of the factorisation (and the subsequent subtraction from the other component).

We similarly define the multiplicative factorisation of a function as

$$F = F_+ F_- \quad (5.2.13)$$

with the *splitfunctions* F_\pm analytic and *non-zero* in their respective half-planes. Armed with this, we recast the Wiener-Hopf equation (5.2.11) into the following form

$$K_+ B^+ + \left(\frac{I^+}{K_-} \right)^+ = \frac{C^-}{K_-} - \left(\frac{I^+}{K_-} \right)^-. \quad (5.2.14)$$

We now suppose that K and I are free of singularities in some strip of the complex plane containing the real axis², and as such so are their factorisations. The left-hand side of the previous equation is analytic in the UH k_1 P and the right-hand side on the LH k_1 P, and the above construction ensures they agree exactly on the this complex strip, an open set in the complex plane. By analytic continuation, they define components of the same function. The LHS indicates the function is analytic in the UH k_1 P and the RHS the LH k_1 P, so this function must be entire, analytic on the entirety of the k_1 plane. We denote this function E , and thus can write down B^+ and C^- in terms of this entire function, namely

$$B^+ = -\frac{1}{K_+} \left(\frac{I^+}{K_-} \right)^+ + \frac{E}{K_+}, \quad (5.2.15)$$

$$C^- = K_- \left(\frac{I^+}{K_-} \right)^- + K_- E. \quad (5.2.16)$$

We can say something about E if slightly more is known, namely the large k_1 behaviour of B^+ and C^- . If we can bound their growth by some polynomial, we can use this to bound E . By (the extended form of) Liouville's theorem, if we can bound E by a polynomial, then E is a polynomial of at most that order. In the ideal case, we can bound E by a decaying function and set it to be zero.

²A little care is required here when the frequency ω is real, and can be compared to imposition of the Briggs-Bers criterion earlier. This is discussed in §5.2.3 below.

Applying these principles to the generic Wiener-Hopf equation we derived earlier gives

$$A = -\frac{1}{K_+ D_u} \left(\frac{I^+}{K_-} \right)^+ + \frac{E}{K_+ D_u} \quad (5.2.17)$$

and the solution to the differential equation is thus

$$\phi(x_1, x_2) = \frac{1}{2\pi} \int_{F_1} \left[-\frac{1}{K_+} \left(\frac{I^+}{K_-} \right)^+ + \frac{E}{K_+} \right] \frac{\phi_d(x_2; k_1)}{D_u} e^{-ik_1 x_1} dk_1 \quad (5.2.18)$$

where F_1 is an integration contour that stretches along the strip of analyticity. We can directly verify that this does, in fact, describe a solution to the differential equation, by directly applying the boundary conditions. Applying the upstream operator \mathcal{L}^u on $x_2 = 0$ gives

$$\mathcal{L}^u \phi(x_1, 0) = \frac{1}{2\pi} \int_{F_1} \left[\frac{1}{K_+} \left(\frac{I^+}{K_-} \right)^+ + \frac{E}{K_+} \right] \frac{D_u}{D_u} e^{-ik_1 x_1} dk_1 \quad (5.2.19)$$

with the remaining integrand analytic in the UH k_1 P. We can thus close the contour, for $x_1 < 0$, by a semicircle in the UH k_1 P, with the contribution decaying exponentially and thus the integral vanishing as required. Similarly, noting $D_u K_+ = D_d / K_-$ allows rewriting of the integral as

$$\phi = \frac{1}{2\pi} \int_{F_1} \left[-I^+ + K_- \left(\frac{I^+}{K_-} \right)^- + K_- E \right] \frac{\phi_d(x_2; k_1)}{D_d(k_1)} e^{-ik_1 x_1} dk_1 \quad (5.2.20)$$

and application of the downstream operator when $x_2 = 0$ separates the integrand into a component analytic in the lower-half plane and the term consisting purely of the inverse transform of $-I^+$, thereby closing in the lower-half plane (for $x_1 > 0$) directly reproduces $-I$, the term forcing the equation, as expected.

5.2.2 Explicit computation of splitfunctions

Both additive and multiplicative factorisations can be computed explicitly via application of Cauchy's integral formula, namely

$$f(a) = \oint_{\bar{C}} \frac{f(z)}{z - a} dz \quad (5.2.21)$$

where \bar{C} is a simple closed contour (traversed anticlockwise) with a in the interior, and f is analytic on the interior of \bar{C} .

Suppose $F(k_1)$ is a function which is analytic in the strip $-\sigma_+ < \text{Im}(k_1) < \sigma_-$, with $\sigma_\pm > 0$, and that $F \rightarrow 0$ as $k_1 \rightarrow \infty$. Consider the contours C_\pm parallel to the real axis, parameterised on $-\infty < t < \infty$ as

$$C_\pm(t) = \pm t \mp i s_\pm \quad (5.2.22)$$

with $0 < s_\pm < \sigma_\pm$, shown schematically in figure 5.2.1.

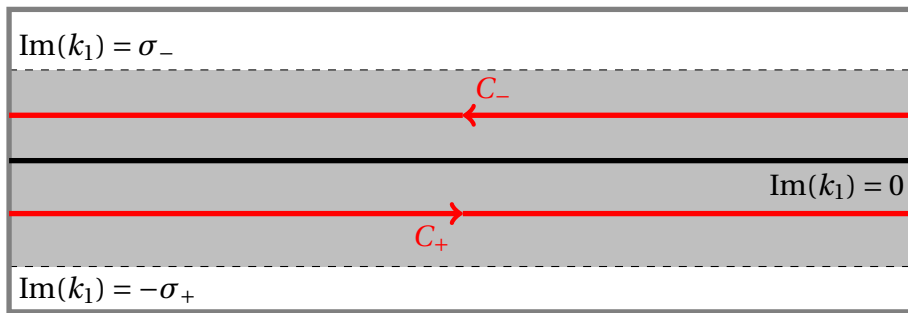


Fig. 5.2.2 Contours for additive factorisation.

We then claim

$$F^\pm(k_1) = \int_{C_\pm} \frac{F(z)}{z - k_1} dz \quad (5.2.23)$$

gives a constructive way of determining the additive factorisation. On the strip contained by the contours they sum to give F , since this is equivalent to integrating over the contour $C_+ \cup C_-$, which is closed (providing no contribution from infinity, which is ensured by the decay condition on F). Application of Cauchy's formula (5.2.21) directly returns F . Thus we need merely show the analyticity of these functions in their respective half-planes. This can be equivalently demonstrated with either splitfunction, and as such we focus on F^+ .

Consider the union of C_+ and the semicircular contour C_R , given by $z = Re^{i\theta} - s_+$, with θ running from 0 to π . Together, in the limit $R \rightarrow \infty$, these form a simple closed contour, and thus, using Cauchy's formula, we can derive the function analytic on the interior of this domain, which is exactly the UH k_1 P, extended to include all k_1 with $\text{Im}(k_1) > -s_+$. Since the integrand in Cauchy's formula can be bounded by $\max_\theta |F(Re^{i\theta})|$ and the length of C_R by πR , we can bound the semicircular contribution by $\max_\theta |F(Re^{i\theta})|$, which we've assumed decays to zero. This then regains the expression we have for F^+ , and thus F^+ is analytic in the UH k_1 P. In the alternate half plane, we can use analytic continuation to extend $F^\pm = F - F^+$. Whilst trivial, this property can be very useful.

Formulae for multiplicative factorisation follow directly from additive factorisation. If $F \rightarrow 1$ as $k_1 \rightarrow \infty$, then additive factorisation of $\log(F)$ gives the multiplicative factorisation, via

$$\log(F_+ F_-) = \log F_+ + \log F_- = (\log F)^+ + (\log F)^- \quad (5.2.24)$$

so that $F_{\pm} = \exp((\log F)^{\pm})$.

Some functions appear regularly, and it is useful to be able to factorise them efficiently.

A function with a single pole in one half-plane. Consider the function, for some G^- analytic on the LHk_1P ,

$$F(k_1) = \frac{G^-(k_1)}{k_1 - k_p} \quad (5.2.25)$$

with $\text{Im}(k_p) < 0$. The pole at k_p is therefore the only singularity in the LHk_1P . This can be additively factorised on sight to give

$$F^+(k_1) = \frac{G^-(k_p)}{k_1 - k_p} \quad (5.2.26a)$$

$$F^-(k_1) = \frac{G^-(k_1) - G^-(k_p)}{k_1 - k_p}. \quad (5.2.26b)$$

Factorisation of γ and $|k_1|$. Consider first the function γ , defined as (compare (4.2.12))

$$\gamma^2 = k_1^2 + k_3^2 - (k_0 - Mk_1)^2 \quad (5.2.27)$$

with square root branch cuts taken to avoid the real axis when ω has negative imaginary part. Here, $k_0 = \omega/c_0$ and $M = U/c_0$ and may both depend on wall-normal coordinate x_2 . For fixed x_2 , we can regard this as a function of k_1 with k_0 and k_3 parameters, writing

$$\begin{aligned} \gamma^2 &= (1 - M^2)k_1^2 + 2Mk_0k_1 + k_3^2 - k_0^2 \\ &= \beta^2 \left[\left(k_1 - \frac{Mk_0}{\beta^2} \right)^2 - \left(\frac{k_0^2}{\beta^4} - \frac{k_3^2}{\beta^2} \right) \right] \\ &= \beta^2 \left[\left(k_1 - \frac{Mk_0}{\beta^2} \right) - \sqrt{\frac{k_0^2}{\beta^4} - \frac{k_3^2}{\beta^2}} \right] \left[\left(k_1 - \frac{Mk_0}{\beta^2} \right) + \sqrt{\frac{k_0^2}{\beta^4} - \frac{k_3^2}{\beta^2}} \right] \end{aligned} \quad (5.2.28)$$

with $\beta^2 = 1 - M^2$, and so

$$\gamma = \beta \left(\left(k_1 - \frac{Mk_0}{\beta^2} \right) - \sqrt{\frac{k_0^2}{\beta^4} - \frac{k_3^2}{\beta^2}} \right)^{1/2} \left(\left(k_1 - \frac{Mk_0}{\beta^2} \right) + \sqrt{\frac{k_0^2}{\beta^4} - \frac{k_3^2}{\beta^2}} \right)^{1/2}. \quad (5.2.29)$$

This expression has two branch points, at

$$k_1 = k_{b\pm} = \frac{Mk_0}{\beta^2} \pm \sqrt{\frac{k_0^2}{\beta^4} - \frac{k_3^2}{\beta^2}} \quad (5.2.30)$$

which unambiguously lie in a complex half-plane when k_0 is non-real. So as the resulting cut of the complex plane does not cross the real axis, these are therefore linked through infinity when defining the branch cut, provided they lie on either side of the real axis, which is always the case for subsonic flows ($M < 1$), real k_3 and negative imaginary part of k_0 . Provided the square root defining $k_{b\pm}$ is chosen so that it returns k_0/β^2 when $k_3 = 0$ (as opposed to the negative), we have $k_{b\pm}$ lying in the Lower/Upper Half k_1 Plane (L/UH k_1 P), respectively. Then defining

$$\gamma_\pm = \beta^{1/2} (k_1 - k_{b\pm})_\pm^{1/2} \quad (5.2.31)$$

we have exactly that $\gamma = \gamma_+ \gamma_-$ and further that γ_\pm are analytic and nonzero in the U/LH k_1 P respectively. We have introduced a new notation for a function

$$(z - z_0)_\pm^\alpha \quad (5.2.32)$$

which (for some complex constant z_0) denotes raising complex number $(z - z_0)$ to the non-integral power α , with the branch cut chosen to go from z_0 to $\mp i\infty$. If z_0 is in the L/UH z P, this function is analytic in the U/LHzP respectively.

This function is useful for factorising $|k_1|$, which comes up frequently in incompressible applications. For application of the Wiener-Hopf procedure a strip of analyticity is required, which necessitates regularisation of $|k_1|$ (which is analytic nowhere on the imaginary axis). We define

$$|k_1|_\epsilon = (k_1 + i\epsilon)_+^{1/2} (k_1 - i\epsilon)_-^{1/2}. \quad (5.2.33)$$

This regularised function multiplicative factorises into a + and a - function, given by each bracket in turn, and satisfies $|k_1|_\epsilon \rightarrow |k_1|$ as $\epsilon \rightarrow 0$, and so we factorise $|k_1|$ as

$$|k_1|_\pm = (k_1)_\pm^{1/2} \quad (5.2.34)$$

though care is needed when performing this regularisation, and other regularisations are permitted.

5.2.3 Generalised half-planes

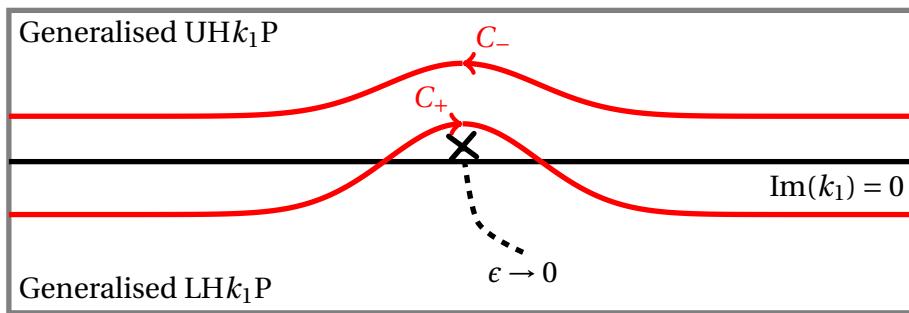


Fig. 5.2.3 Schematic representation of generalised half-planes, required to satisfy causality in the Wiener-Hopf solution.

Neither γ nor $|k|$ have the strip of analyticity posited for factorisation, as per figure 5.2.2, when the frequency ω is real. However, there is a clear continuity argument for what the factorisation should be as a parameter is relaxed. We therefore generalise the additive factorisation slightly, and in turn generalise the idea of the Upper and Lower half-planes.

Suppose $F = F(k_1; \epsilon)$ is a function of k_1 , decaying as $k_1 \rightarrow \infty$, parameterised by some ϵ , for example $\epsilon = \text{Im}(\omega)$ in the case of γ , and F varies continuously as a function of ϵ . For certain values of ϵ , we suppose there is a strip of analyticity, enclosing the real axis, on which $F = F^+ + F^-$ is well-defined via the Cauchy formula. We want to insist that, as ϵ varies, F^\pm vary *continuously*. This causes issues if F has a singularity at some location, which for some ϵ crosses the contour C_\pm defining the splitfunction. However, it is straightforward to maintain continuity by deforming this contour in turn, so it still passes on the same side of the singularity as before. This is illustrated, with $\epsilon \rightarrow 0$ causing a pole to cross the real axis, in Figure 5.2.3.

A caveat is that the resulting splitfunctions F^\pm aren't respectively analytic on the U/LH k_1 P when the contour has been deformed across the real axis, with no guarantee of analyticity on the closed region between the real axis and the contour (in the case of the figure, contour C_+). We thereby define *generalised* half-planes by the locations of these new contours, namely the generalised UH k_1 P (gUH k_1 P) consisting of all k_1 lying beneath the deformed C_- contour (a function of parameter ϵ and the gLH k_1 P similarly above C_+). These overlap on the open set between C_+ and C_- , which we assume exists for the Wiener-Hopf procedure to hold. Any inverse Fourier transforms must be performed

in this strip of analyticity to preserve causality, and by generalising in this sense we are essentially using the Briggs-Bers criterion.

5.2.4 Numerical computation of splitfunctions

Consider the Cauchy-type formula for factorisations (5.2.23), generalised to consider C_{\pm} any (suitable) contour linking $-\infty$ to ∞ . This formula will be used repeatedly and it is useful to have a consistent method of numerical computation of splitfunctions. Suppose the contour is parameterised as a function of t , running from $-\infty$ to ∞ , so that

$$F^{\pm} = \pm \frac{1}{2\pi i} \int_{-\infty}^{\infty} \frac{F(C(t))}{C(t) - k_1} \frac{dC}{dt} dt \quad (5.2.35)$$

where we suppose $C(t) \rightarrow \pm\infty$ as $t \rightarrow \infty$. For most of this work, we treat contours of the form $C(t) = t + if(t)$, for some f , and so this condition trivially holds provided f is bounded.

Motivated by Veitch and Peake [109], which were in turn suggested by Rienstra, we make the substitution³

$$t = \frac{s}{(1-s^2)}. \quad (5.2.36)$$

Provided $F(k_1) = O(k_1^{-1})$ as $k_1 \rightarrow \infty$, we have the resulting finite integral to determine the splitfunctions, which can be solved using normal Gaussian quadrature methods (noting the integrand is finite at the end points of the integration with the decay of F specified), namely

$$F^{\pm} = \pm \frac{1}{2\pi i} \int_{-1}^1 \frac{F(C(s/(1-s^2)))}{C(s/(1-s^2)) - k_1} \frac{dC(s/(1-s^2))}{d(s/(1-s^2))} \frac{1+s^2}{(1-s^2)^2} ds. \quad (5.2.37)$$

This integral has integration points bunched for smaller k_1 , which is typically the most important contribution to the integral, and thus naturally has the behaviour required, even for a reasonably low number of quadrature points. Examples of using this in practise are demonstrated in later sections.

5.2.5 Multiplicative factorisation: Winding numbers, continuity of log and curved branch cuts

An earlier comment noted that, if $F \rightarrow 1$ as $k_1 \rightarrow \infty$, then additive factorisation of $\log(F)$ suffices to determine the multiplicative factorisation of F . This is easily illustrated to be

³This differs slightly from the reference text, and is valid for all t , both positive and negative.

an oversimplification, by considering for example

$$F(z) = \frac{z - z_+}{z - z_-} \quad (5.2.38)$$

with z_{\pm} in the U/LHzP respectively. Whilst this is trivially factorisable, and $F \rightarrow 1$ in all directions, we cannot say that $\log(F) \rightarrow 0$ in all directions, due to the change in argument of the function. If $\arg(F) = 0$ as $z \rightarrow \infty$ along the positive real axis, then if we move leftwards along the real axis we find that $\arg(F) = -2\pi$ as $z \rightarrow -\infty$. These two limits only have $\log(F) \rightarrow 0$ if a branch cut of \log has been crossed, which invalidates the factorisation method (which assumes the function, in this case $\log(F)$, is continuous along the factorisation contour).

The fundamental problem with this function is that the winding number of the function around 0 is non-zero: there is an overall gain or loss of argument along the separation contour. If we were to plot $F(z)$ in the complex plane as z varies along the real axis, it would go from 1 to 1 by making a loop around $z = 0$. There is therefore no way to determine a branch cut of $\log(F)$, beginning at 0 and stretching to ∞ , such that $F(z)$ does not at some point cross the cut. This is relatively straightforward to deal with, as suggested by the example given which can be trivially factorised. We extend this to deal with other cases [79].

Suppose we only impose that $|F| \rightarrow 1$ as $z \rightarrow \infty$, and is analytic on the real axis (or whichever contour we choose that asymptotes to the real axis for large z). For some real μ , ν , we have

$$F \rightarrow \begin{cases} e^{i\mu} & z \rightarrow -\infty, \\ e^{iv} & z \rightarrow +\infty. \end{cases} \quad (5.2.39)$$

Picking two useful branch points (which will depend on the function of choice) z_{\pm} (in the U/LHzP), the reduced function \bar{F} , defined as

$$\bar{F}(z) = F(z)e^{-i\mu}(z - z_-)_+^{\alpha}(z - z_+)^{-\alpha}, \quad (5.2.40)$$

satisfies $F \rightarrow 1$ as $z \rightarrow \pm\infty$. Here, α is defined as

$$\alpha = \frac{1}{2\pi}(\nu + \mu). \quad (5.2.41)$$

As before, the branch cuts of $(z)_{\pm}^{\alpha}$ are defined to connect 0 and $\mp i\infty$, so that, for example, $(z - z_+)^{\alpha}$ is a --function, analytic in the LHzP. \bar{F} is then amenable to numerical factorisation. If \bar{F} is shown to have non-zero winding number after this analysis, it is

straightforward to increase or decrease α by an integer amount. With \bar{F} factorised, then

$$F_{\pm}(z) = e^{i\mu/2} \bar{F}_{\pm}(z)(z - z_{\mp})_{\pm}^{\pm\alpha} \quad (5.2.42)$$

follows, the leading $e^{i\mu/2}$ chosen for symmetry though as a constant its splitting between F_{\pm} is somewhat arbitrary.

This elimination of the nonzero winding number ensures that, provided \log is fixed to be continuous along the factorisation contour, \bar{F} can be factorised numerically. Constructing such a logarithm is numerically tricky, as some degree of automation determining whether a branch cut has been crossed is needed. A more readily useable approach is to use a curved branch cut of \log , which is applicable in most circumstances, provided a path can be found from 0 to ∞ without the complex curve $w = F(z)$ (for z along the separation contour) being crossed, though we do not need to use this method in this work.

Whilst we have assumed μ and ν are real, this constraint is not necessary and they can be complex indices. This greatly expands the number of problems that can be directly dealt with using this method, though issues of boundedness need to be carefully considered when α is complex. This is first done in §5.4, though appears throughout this chapter and the following one.

5.2.6 Linking small x_1 and large k_1 behaviour

Generalising the method of stationary phase, we can relate the near-field physical behaviour of a function with its far-field behaviour in Fourier space. For a function $f \sim x^{\alpha}$ as $x \rightarrow 0$, the resulting half-range transform is dominated near $x = 0$ as $k \rightarrow \infty$, with transformed function $F(k) \sim k^{-(1+\alpha)}$. If we use physical arguments to bound real variables near a junction ($\mathbf{x} = \mathbf{0}$), then we obtain large k_1 bounds on the resulting half-range transforms. This will in turn provide a bound on the entire function $E(k_1)$.

In the presence of mean flow, it is typically possible to impose a Kutta condition [31], by which we prescribe that (physical) perturbation quantities are *finite* at the junction $\mathbf{x} = \mathbf{0}$, and so $\alpha > 0$ for both velocity and pressure perturbations. As discussed by [31], this is not necessarily possible to impose if there is no background flow, which naturally arises if we have a non-slipping profile. In this case, typically finite pressure and (integrably) singular velocities would be expected, so that $\alpha > -1$ for the velocity field. Were we to not impose such conditions, the addition of eigensolutions, singular at the junction, driven by the value of the entire function E , would contribute to the solution. Alternative considerations involve insisting the energy generated from the junction is suitably well-defined.

5.3 Slipping sheared flow: Hard-soft transition

We cement these ideas by focusing first on the transition between a *hard* wall, upstream (which supports no wall-normal velocity perturbations) and a *soft* wall downstream (supporting no pressure fluctuations), before generalising to generic impedance boundaries both up and downstream. There is a fundamental difference between whether the imposed background profile, assumed to be a function of wall-normal coordinate x_2 alone is slipping (so that $U_0 = U(0) \neq 0$, or if it satisfies a no-slip condition $U_0 = 0$). This distinction is important when bearing in mind the ill-posed nature of the impedance boundary condition with slipping flow, which the construction of a full shear profile attempts to alleviate. That said, there are fewer mathematical difficulties with the slipping case and it is that problem that shall be considered first.

5.3.1 Problem setup and incident field

We take the generic mixed setup, as per (5.2.1), with $\mathcal{L}^u = \mathcal{V}$ and $\mathcal{L}^d = \mathcal{P}$, which depend slightly on the choice of potential for the potential or fluid quantity of interest. For the governing differential operator we simply pick \mathcal{D}_R^\dagger , the adjoint Rayleigh operator, as per (2.3.11), with background profile $U = U(x_2)$. We define the particular quantities $U_0 = U(0)$ and $U_\infty = \lim_{x_2 \rightarrow \infty} U(x_2)$, where the latter is typically the value of U at the edge of the boundary-layer $x_2 = \delta$, with U constant for $x_2 > \delta$, though this formulation again permits more general profiles.

For the incident unsteady disturbance we take the simple case of a time-stationary harmonic vortex sheet, with transients decaying and any sources expected to be far upstream. We then take, for the continuous shear case, $\phi^{(i)}$ as satisfying

$$\mathcal{D}_{R0}\phi_0^{(i)} = \frac{c_0^2(y_2)q_0}{U(y_2)}\delta(x_2 - y_2)\exp(-i\kappa_1(y_2)x_1). \quad (5.3.1)$$

As in previous chapters, $\kappa_1 = \omega/U(y_2)$ is the convected wavenumber of a disturbance propagating with the mean flow at the location of the vortex sheet. We seek solutions proportional to $e^{-i\kappa_1 x_1}$. If we are instead considering the piecewise-linear case and therefore the perturbation streamfunction as the potential to be solved, we instead consider (the equivalent) incident streamfunction satisfying

$$\nabla^2\psi_0^{(i)} = \frac{U'(y_2)q_0}{\rho_0 U(y_2)}\delta(x_2 - y_2)\exp(-i\kappa_1(y_2)x_1). \quad (5.3.2)$$

This section will primarily focus on the former, though the intricacies introduced by the latter will be remarked upon later (primarily with issues of $|k_1|$ in the incompressible case).

Using earlier notation and computed functions, we write down the solution to (5.3.1), satisfying the upstream hard-wall boundary condition, as

$$\phi_0^{(i)} = \frac{c_0^2(y_2)q_0}{U(y_2)} \exp(-i\kappa_1(y_2)x_1) \frac{\phi_{\gtrless}(x_2; \kappa_1)\phi_{\leqslant}(y_2; \kappa_1)}{W(y_2)} \quad (5.3.3)$$

with $\phi_{\gtrless}(x_2; k_1) = \phi_d$ for $x_2 > y_2$ and ϕ_h for $x_2 < y_2$ (with ϕ_{\leqslant} the other of these functions) – the only difference for more general boundary-conditions is the replacement of ϕ_h by the appropriate solution satisfying the upstream boundary condition. We can then use (4.3.6) to write this in terms of the hard-wall dispersion function, evaluated at $k_1 = \kappa_1 = \omega/U(y_2)$, and so

$$\phi_0^{(i)} = \frac{c_0^2(y_2)q_0}{U(y_2)} \frac{\exp(-i\kappa_1(y_2)x_1)}{D_h(\kappa_1)} \frac{c_0(y_2)^2 C(y_2)^4}{c_0(0)^2 C(0)^4} \phi_{\gtrless}(x_2; \kappa_1)\phi_{\leqslant}(y_2; \kappa_1) \quad (5.3.4)$$

Since much of this is a function of y_2 alone (either directly or through κ_1) and does not materially effect the scattering problem, we consider the generic incident field

$$\phi_0^{(i)} = Q_0(y_2)\phi_{\gtrless}(x_2; \kappa_1)\phi_{\leqslant}(y_2; \kappa_1)\exp(-i\kappa_1 x_1) \quad (5.3.5)$$

noting that due to linearity the solution is proportional to Q_0 . There are issues with evaluating the auxiliary functions at $k_1 = \kappa_1$ due to the critical-layer, and so deformed contour methods should be utilised as per §4.2.4 to avoid the singularity in the governing equations, with consistency needed between the direction the contour loops the regular singular point in calculation of ϕ_d , ϕ_h and D_h .

The scattered problem, in Fourier-space, is forced by

$$I^+ = \left(\mathcal{P}_0 \phi_0^{(i)} \right)_1^+. \quad (5.3.6)$$

Since the only x_1 dependence of the incident field is through the oscillatory term $\exp(-i\kappa_1 x_1)$ and \mathcal{P} does not explicitly depend on x_1 , $\mathcal{P}_0 \phi_0^{(i)}$ depends on x_1 only through this oscillatory term. The half-range transform can then be computed as

$$\begin{aligned} I^+ &= Q_0(y_2)\phi_{\leqslant}(y_2; \kappa_1) [\mathcal{P}_{01}(\kappa_1)\phi_{\gtrless}(x_2; \kappa_1)] \int_0^\infty e^{-i\kappa_1 x_1} e^{ik_1 x_1} dx_1 \\ &= Q_0(y_2)\phi_d(y_2; \kappa_1) [\mathcal{P}_{01}(\kappa_1)\phi_h(0; \kappa_1)] \frac{i}{(k_1 - \kappa_1)}. \end{aligned} \quad (5.3.7)$$

Aside from the single pole in the LHk_1P at $k_1 = \kappa_1$, this function is analytic. Note that this pole lies on the real axis when ω is real, but should be considered as lying in the (generalised) lower half k_1 -plane.

5.3.2 The Wiener-Hopf kernel and factorisation

The Wiener-Hopf kernel is given by

$$K(k_1) = \frac{D_p(k_1)}{D_h(k_1)} \quad (5.3.8)$$

with zeros at zeros of D_p and poles at zeros of D_h , and a typical pair of acoustic branch cuts. Numerical formulae for multiplicative factorisation exist from (5.2.21), though these require a normalised kernel such that $\tilde{K} \rightarrow 1$ as $k_1 \rightarrow \infty$, and thus require an understanding of the large- k_1 behaviour of K , which can be obtained from the asymptotic analysis in §4.2.5, which exactly gives large k_1 expressions for ϕ_d , from which large k_1 expressions for $\mathcal{P}\phi_d$ and $\mathcal{V}\phi_d$ can easily be derived. We have

$$D_p \sim -C^3\phi \quad (5.3.9a)$$

$$D_h \sim \gamma C^2\phi \quad (5.3.9b)$$

where ϕ can be computed, but is common to both functions. Both γ and C are evaluated for $U = U_0$, and importantly are both large as $k_1 \rightarrow \infty$. This is where there is a difference for the non-slip case, with D_h missing terms that are here smaller in k_1 , but of equal importance when $U_0 = 0$ (so that C is $O(k_1^0)$ and is small). The resulting large k_1 kernel is then

$$K_f = -\frac{C}{\gamma}. \quad (5.3.10)$$

There are other functions (less physically motivated) that have the same large k_1 -behaviour as K , however this choice of K_f can be factorised directly from earlier work. $C = i(\omega - U_0 k_1)$ has a single zero in the (generalised) lower half plane, and is thus already a + function, and γ has previously been factorised in section 5.2, so that

$$K_{f+} = -\frac{C}{\gamma_+}, \quad (5.3.11a)$$

$$K_{f-} = \frac{1}{\gamma_-}. \quad (5.3.11b)$$

The normalised kernel $\bar{K} = K/K_f$ can then be factorised numerically (with care to ensure poles and zeros of the kernel are correctly assigned a half-plane), to give $\bar{K} = \bar{K}_+ \bar{K}_-$ and thus

$$K_{\pm} = \bar{K}_{\pm} K_{f\pm}. \quad (5.3.12)$$

Whilst the factorisation needs to be done, we can use this expression to determine the large k_1 -behaviour of the factorised kernel, which will allow bounding of the entire function $E(k_1)$. We note that factorisation via the Cauchy formula, (5.2.23), implies that if $F \rightarrow 0$ as $k_1 \rightarrow \infty$ then both $F^{\pm} \rightarrow 0$ as $k_1 \rightarrow \pm\infty$. This convenient choice of factorisation, applied to $\log \bar{K}$, implies $\bar{K}_{\pm} \rightarrow 1$ as $k_1 \rightarrow \infty$, and hence far-field behaviour is determined by far-field behaviour of $K_{f,\pm}$. This presupposes the condition outlined in §5.2.5 has been satisfied, that the winding number of \bar{K} about 0 is 0 and $\log(K)$ can be chosen to be continuous along the separation contours, with suitable decay at infinity. This can be demonstrated to be valid under the choice of K_f for this slipping case, by plotting $\log(K)$ in the complex plane along the separation contour, as done later for the no-slip kernel in figure 5.4.1b. We therefore have

$$K_{\pm} \sim k_1^{\pm 1/2} \quad (5.3.13)$$

as $k_1 \rightarrow \infty$. This allows bounding of the entire function $E(k_1)$.

Numerical factorisation of reduced kernel

A generic example of the unreduced Wiener-Hopf kernel K is shown in figure 5.3.1, for a simple parabolic profile (unstable above a pressure-release wall). It has a similar structure to previously seen dispersion functions, with zeros at zeros of the pressure-release dispersion function and branch cuts along the critical layer and acoustic branch cuts corresponding to those of γ . Factorisation requires that the (convectively unstable) pressure-release zeros remain in the generalised lower half-plane, and thus factorisation contours must be deformed as indicated schematically in figure 5.3.2. It is worth noting the same factorisation contour can be used for both + and - factorisations, though this removes the self-checking strip on which $K_+ = K/K_-$ (and vice versa).

A typical factorisation contour used is a “tanh” contour, with

$$C(t) = t + i \left[a + b \tanh \left(\frac{2}{t_+ - t_-} \left(t - \frac{t_+ + t_-}{2} \right) \right) \right]. \quad (5.3.14)$$

This gives a contour with imaginary part tending to $a \pm b$ as $t \rightarrow \pm\infty$, with t_+ and t_- controlling the steepness and centre of the contour, and allowing it to be chosen to pass

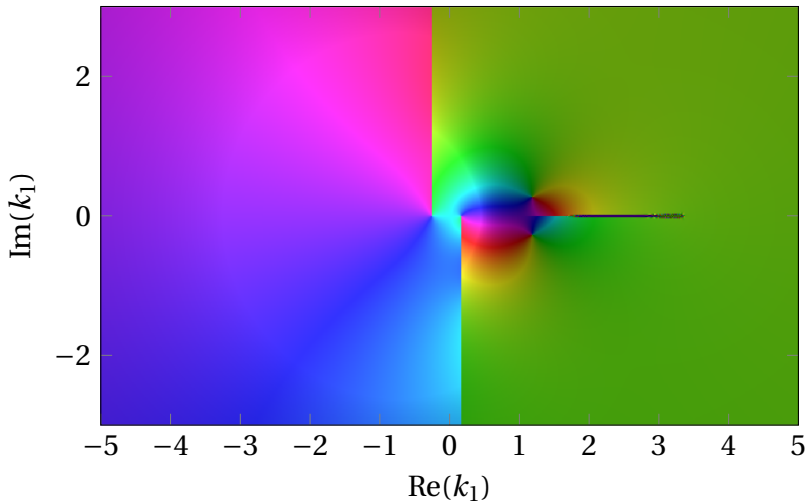


Fig. 5.3.1 Phase plot of the Wiener-Hopf kernel $K = D_p/D_h$ for a slipping parabolic profile ($U_0 = 0.3$, with $\delta = U_\infty = 1$ and constant speed of sound $c_0 = 5$), for frequency $\omega = 1$ ensuring the existence of unstable pressure modes. The features are generic: the pair of branch cuts near the origin to $\pm i\infty$, corresponding to acoustic γ ; the critical layer between ω/U_∞ and ω/U_0 along the real axis, and the possible existence of hydrodynamic modal solutions (in this case, two pressure release zeros above and below $k_1 \approx 1$). As per the §3, these modes are at worst convectively unstable, and therefore belong to a generalised lower half plane.

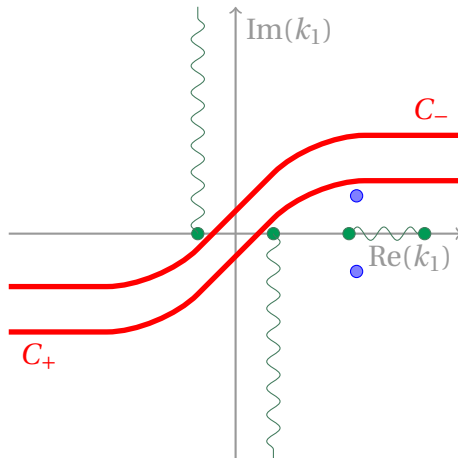


Fig. 5.3.2 Schematic representation of possible locations of C_{\pm} for the slipping hard/soft kernel, passing between the acoustic branch cuts and above the critical layer and any (downstream propagating) singularities or zeros, here the zeros of D_p . K_- is analytic beneath C_- and similarly K_+ above C_+ , so on the strip between contours $K = K_+K_-$.

between acoustic branch cuts. With quadrature points chosen to cluster for smaller t , this is most accurate between acoustic branch cuts, which is the most relevant location for far-field noise. For large $|t|$, these contours do not lie on either half of the real axis, which is different from as assumed in §5.2.3, though this is not a worry provided $\log(\bar{K})$ decays as $k_1 \rightarrow \infty$ along almost all rays, which is the case here.

The resulting numerical factorisation of the generic K above is done using a single case of the above tanh contour, with the results shown in figures 5.3.3. Relatively few quadrature points (100) are used to highlight the behaviour of the factorised functions near the factorisation contours, namely that there is a thin region around the integration contour, widening with the spacing of quadrature points, in which precise evaluation of the splitfunctions K_{\pm} requires care. A line of poles is visible along the separation contour, which arises from the singularity of the Cauchy kernel $(k_1 - k_q)^{-1}$ near quadrature points k_q upon discretisation.

An alternative contour, that does indeed asymptote to the real axis and includes deformations about clusters of singularities, can be found in Veitch and Peake [109]. The imaginary part of the contour is a rational function of polynomials in t .

Additive factorisation of the incident disturbance

The Wiener-Hopf procedure requires additive factorisation of I^+ / K_- . Since I^+ has a single pole when $k_1 = \kappa_1$, in the (generalised) LH k_1 P, we can use the note in the preceding section to write down the factorisation:

$$\frac{I^+}{K_-} = \frac{I_0}{k_1 - \kappa_1} \times \frac{1}{K_-} = \frac{I_0}{K_-(\kappa_1)(k_1 - \kappa_1)} + \left(\frac{1}{K_-(k_1)} - \frac{1}{K_-(\kappa_1)} \right) \frac{I_0}{k_1 - \kappa_1} \quad (5.3.15)$$

with the first term on the RHS a + function and the second a - function. Here, $I_0 = Q_0(y_2)\phi_d(y_2; \kappa_1)[\mathcal{P}_{01}(\kappa_1)\phi_h(0; \kappa_1)]$ gathers the k_1 -independent terms in I^+ . Both terms decay like k_1^{-1} as $k_1 \rightarrow \infty$ in their respective half-planes.

Determining the entire function, $E(k_1)$

All that remains for writing down the scattered solution is determination of the entire function E . To do so, we must consider the functions B^+ and C^- , respectively the upper/lower half-range transformations of the *scattered wall-normal velocity* on the soft, downstream surface, and the *scattered pressure* on the hard, upstream surface. We apply a Kutta condition, as per the end of the preceding section, insisting that both pressure and velocity are finite at the junction. As such, in the k_1 -plane, both B^+ and C^- decay at least as rapidly as k_1^{-1} in their respective half-planes. We recall (5.2.14) defining a representation

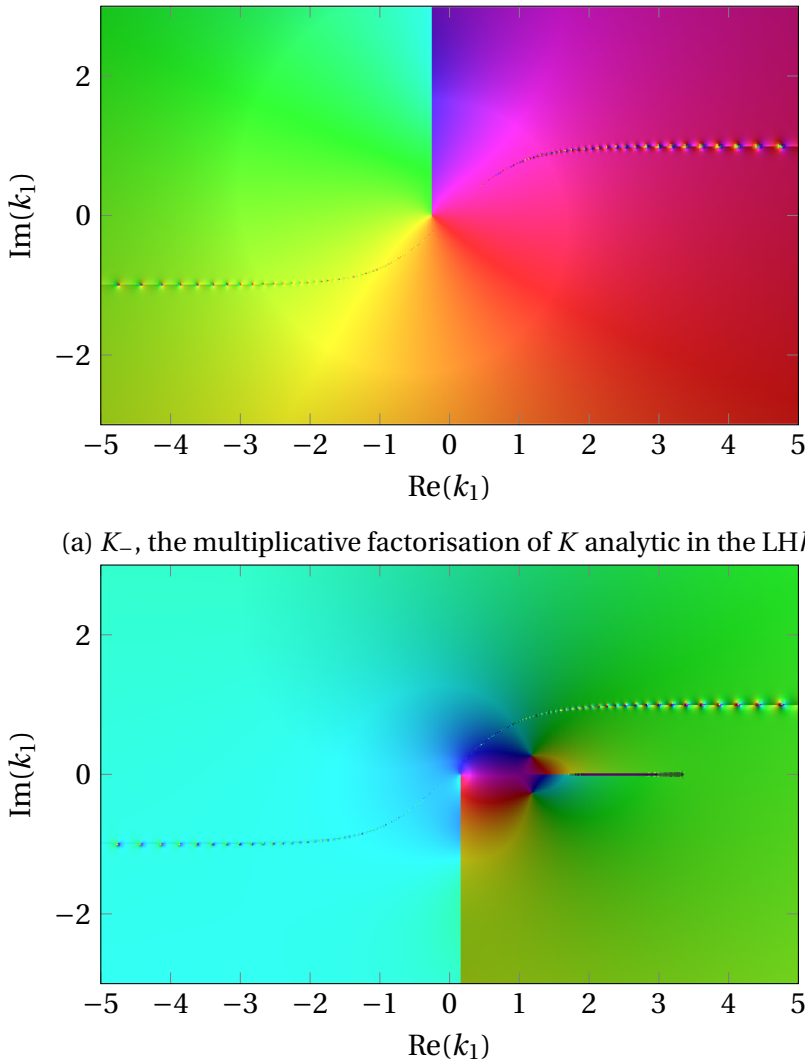


Fig. 5.3.3 Phase plots of the multiplicative factorisation of K as per figure 5.3.1, using a tanh contour (visible as a line of singularities) and relatively low number of integration points $N = 100$. In practice, the number of integration points will be around 10 times this. The functions are analytic on either side of this integration contour, and (other than singularities at integration points) analytically continue across the contour until singularities of K are encountered. On the side of the contour in which they are not analytic, we have constructed $K_{\pm} = K/K_{\mp}$. With most quadrature points focused on $k_1 \approx 0$, the jump in the function at the integration contour is least noticeable here.

of E in either half-plane. We have two observations: that B^+ and C^- , and thus K_+B^+ and C^-/K_- , both decay as $k_1 \rightarrow \infty$ (though only as $k_1^{-1/2}$); and that the forcing term, $(I^+/K_-)^\pm$ also decays, and thus $E(k_1) \rightarrow 0$ in all directions as $k_1 \rightarrow \infty$. By Liouville's theorem, E (an entire function bounded by 0 at ∞) is identically zero.

Combination of the above with the final expression in the generic derivation, (5.2.18), gives the scattered solution

$$\phi = -\frac{1}{2\pi} \int_{F_1} \frac{I^+(k_1)}{K_+(k_1)K_-(\kappa_1)} \frac{\phi_d(x_2; k_1)}{D_h(k_1)} e^{-ik_1 x_1} dk_1. \quad (5.3.16)$$

The inversion contour F_1 must lie in the generalised UHk_1P , that is above the C_+ contour, and thus above the pole of I^+ (which lies on the real axis when ω is real). It may also have to lie above all downstream propagating singularities of the Wiener-Hopf kernel K (for example zeros of D_p that correspond to unstable solutions, but are in the LHk_1P for ω with large negative imaginary part, and thus in the generalised LHk_1P).

5.3.3 Numerical inversion

Numerical inversion directly extends the point source inversion in §4, with a very similar integrand. The far-field noise is controlled by the steepest descent contour due to the exponential term, $\exp(-\gamma_\infty x_2 - ik_1 x_1)$ (outside the boundary-layer), and thus deformation onto this steepest descent contour is both numerically useful (ensuring there is no oscillatory exponent) and analytically useful for determination of far-field noise.

Away from the acoustic branch cuts, the singularities of this integrand arise from singularities either of D_h or D_p , or the single forcing pole at $k_1 = \kappa_1$. This can be made explicit by considering two different, equivalent expressions for the integrand, noting

$$\frac{1}{K_+(k_1)D_h(k_1)} = \frac{K_-(k_1)}{D_p(k_1)}. \quad (5.3.17)$$

If $x_1 < 0$, we deform into the UHk_1P as shown in figure 5.3.4, picking up any singularities only of D_h since K_+ is, by construction, singularity free. Conversely, for $x_1 > 0$ deforming into the LHk_1P picks up singularities only of D_p since, again, K_- is singularity free. It therefore makes sense to use these two, equivalent, expressions respectively for $x_1 < 0$ and $x_1 > 0$, as the location of the singularities is straightforward to determine (and has been done before in the point source case above a homogeneous boundary). The last thing to insist is that the deformed contours do not cross the separation contours C_\pm . Whilst this is straightforward for near-field evaluation, where (as previous) the exact steepest descent

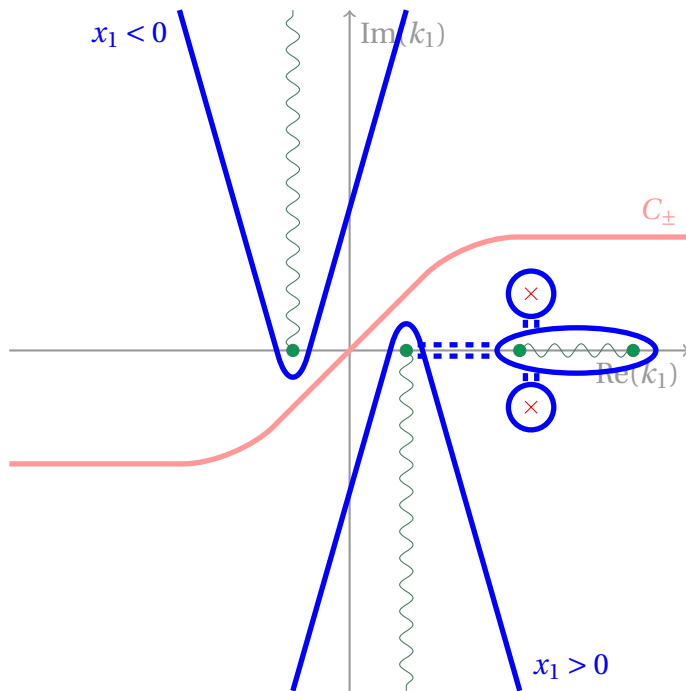


Fig. 5.3.4 Schematic of contour deformation for inversion of the scattering integrand, assuming factorisation contours $C_+ = C_-$. Contours are chosen to remain in their respective half planes. Singularities of the integrand come from singularities of D_h (above C_+) and D_p (below C_-) only, and so contour deformation is identical to the pressure-release point source case. Different forms of the integrand used in the each generalised half-plane, here defined as above and below C_{\pm} , are discussed in the text. The acoustic forcing pole at $k_1 = \kappa_1$ is not shown, but would lie on the critical layer branch cut.

contour is not used, when doing far-field evaluation this will require care with quantifying where the saddle point is with respect to the separation contour, as discussed below.

We are now in a position to compute the near field solution by numerically computing the inversion. The unstable case treated as a generic example is inverted and shown in figures 5.3.5, with the excited pressure mode growing exponentially downstream seen in the scattered component figure 5.3.5b. The full solution (figure 5.3.5a) clearly shows the satisfaction of the pressure-release boundary condition for $x_1 > 0$, and the purely acoustic radiating component can be isolated by focus purely on the steepest descent contours (or, in this case, the approximation looping each acoustic branch cut).

The same scattering problem (with the same slipping parabolic background flow) is shown for higher frequency in figure 5.3.6, a stable configuration (as shown in the pressure-release considerations in §4). In this case, the incident vortex sheet is changed little over the junction and dominates the solution, and so only the scattered component is shown. A clear radiating wavefront can be seen, due to the steepest descent contours, and in turn the saddle point.

5.3.4 Far-field noise

Noting the clear radiation pattern from the junction point itself, the natural question is to investigate the acoustic radiation generated by the junction itself. If this is large, any noise-reduction advantage to use of a short section of lining may be removed by the leading- and trailing-edges of the lining itself. This analysis can be performed using the steepest descent method, and in turn focusing on the saddle point contribution, due to the identical exponent in the integrand (outside the boundary-layer) as the point source integrand (see, for example, (4.3.8)) and thus we proceed using the same saddle point method, and steepest descent contours, as §4.3.1.

Given the work already done on steepest descent and far-field noise, previous work transfers across with only the single caveat of being careful with generalised half planes. This is sketched in figure 5.3.7, showing the saddle point passing from one half plane to the other. To avoid numerical error near the separation contours, the two different, equivalent, expressions in (5.3.17) are used respectively in the (generalised) Upper and Lower Half k_1 -planes, with a check that the two routines agree for θ such that the saddle point, $k_{1s}(\theta)$, lies between the two separation contours.

The junction itself is the primary acoustic source. This leads to a single lobe in far-field directivity plots, as there is no corresponding image source to consider (as per the point source case) since the acoustic source lies on the wall itself. When considering, for example, $|p'|$, it is reasonable to expect this directivity to be directed upstream, as

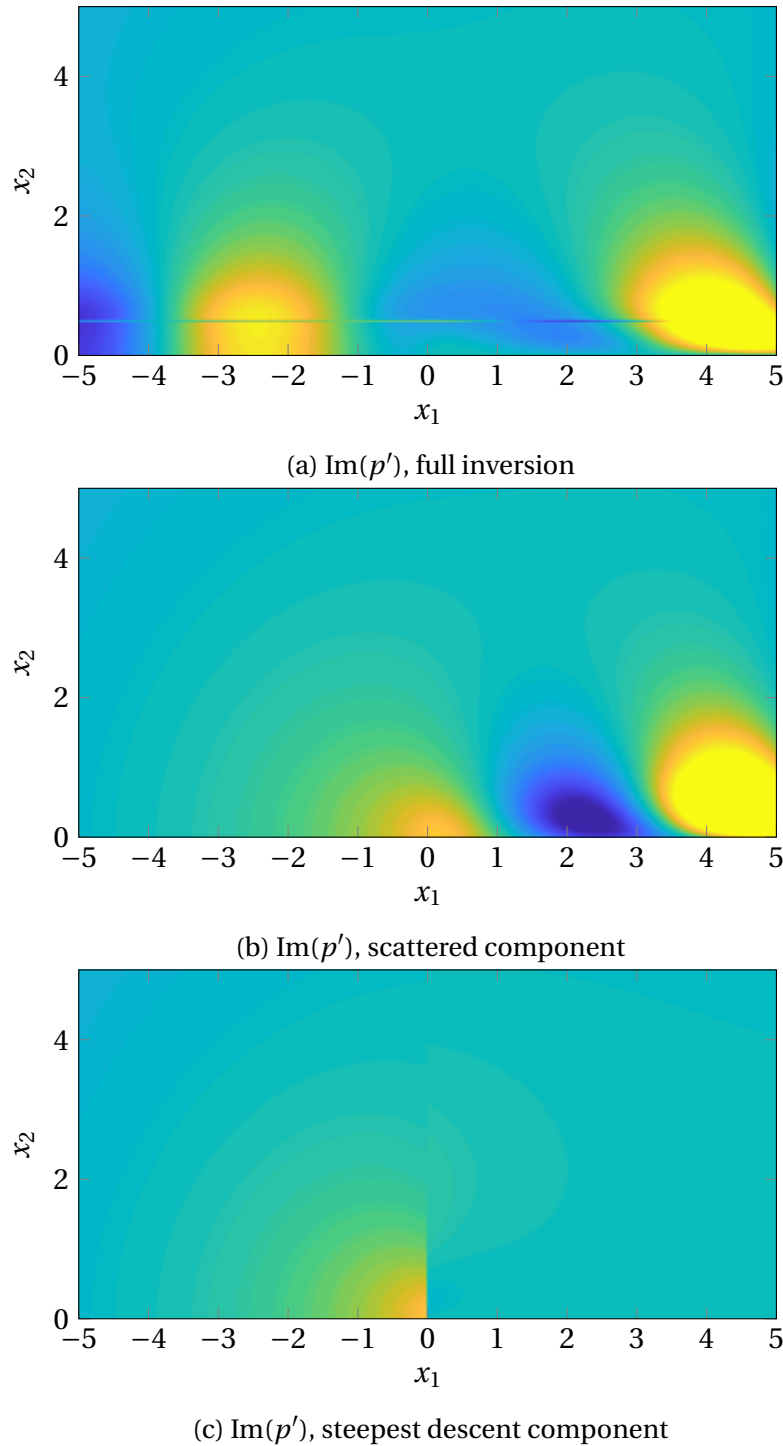


Fig. 5.3.5 The scattering of a vortex sheet disturbance from a hard to a soft boundary is shown for the unstable case outlined in figure 5.3.1, at frequency $\omega = 1$, with the source located at $y_2 = 0.5\delta$. Following the contour deformation, figure 5.3.5c neglects the modal and critical-layer contributions.

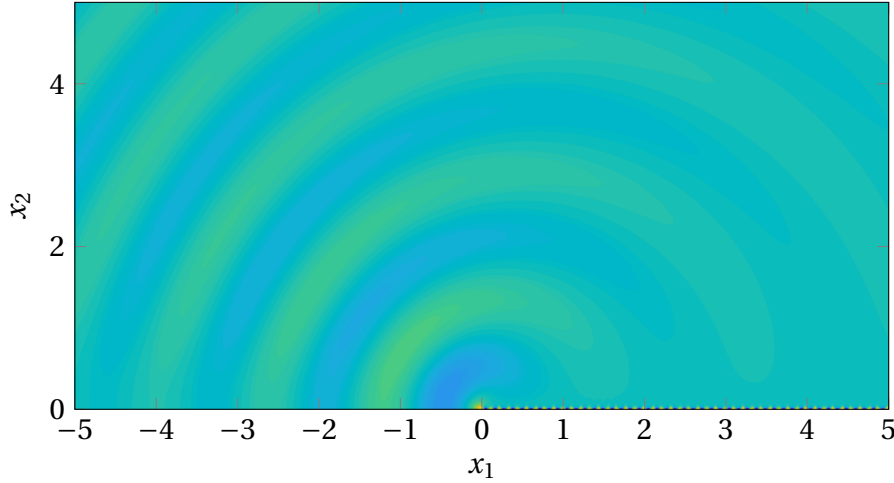


Fig. 5.3.6 The scattered component, $\text{Im}(p')$, for $\omega = 20$ and $y_2 = 0.1\delta$. Since the vortex sheet dominates the solution (as can be seen by the reaction downstream of $x_1 = 0$, very close to $x_2 = 0$), only the scattered component is shown for this stable configuration. The clear acoustic radiation pattern from the junction is visible.

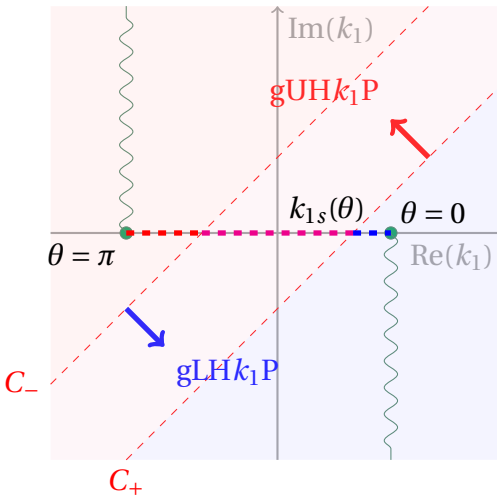


Fig. 5.3.7 Zooming in to the acoustic branch cuts of the inversion integrand, with separation contours C_{\pm} (and thus their respective upper (red) and lower (blue) generalised half-planes) shown. The saddle point, as a function of θ , moves between acoustic branch cuts, and thus between gHPs. For θ small, so that $k_{1s}(\theta)$ is in the gLH k_1 P, we use the form of the integrand containing $K_-(k_1)$ only, and conversely for θ “large”. This ensures that the separation contour is never crossed as θ varies. The two solutions necessarily agree on the overlap between the two generalised half-planes (magenta), on which all of K , K_{\pm} are analytic.

$p' = 0$ downstream on the wall, and thus a downstream suppression of pressure would be expected. Directivity (though not strength) of the disturbance broadly doesn't depend on vortex sheet "location" y_2 from the point of view of an observer in the far-field, since the source is concentrated at the origin, which is demonstrated in figure 5.3.8, which as expected shows an upstream directivity for a case chosen to amplify acoustic effects. With this in mind, all further analysis in this section fixes the source location $y_2 = 0.5\delta$, since this choice is essentially arbitrary.

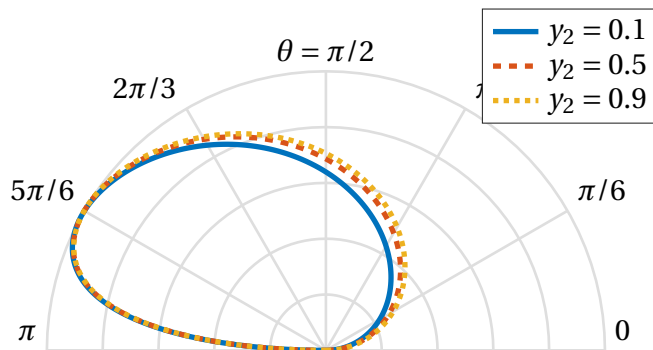


Fig. 5.3.8 The effect of varying source location on far-field directivity, here $|p'|$ normalised by the highest value as a function of θ , is shown, for a simple, slipping parabolic profile $U_0 = 0.2U_\infty$, at reasonably high Mach number $U_\infty/c_0 = 0.2$. The frequency $\omega = 5$ is chosen to give acoustic wavelength comparable to boundary-layer thickness $\delta = 1$, though the limited variation with y_2 is consistent across all choices of frequency.

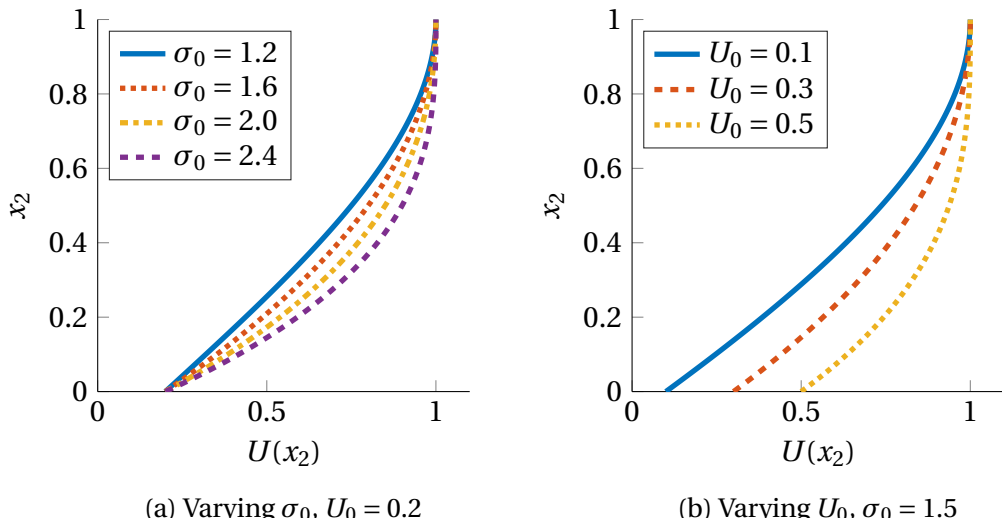


Fig. 5.3.9 Two pairs of cubic profiles, continuous with continuous shear at the edge of the boundary-layer, chosen so that U_0 and $\sigma_0 = U'(0)$ can be varied independently. The range of U_0 and σ_0 is chosen so that no profile is inflecting, and thus hard-wall stability is ensured.

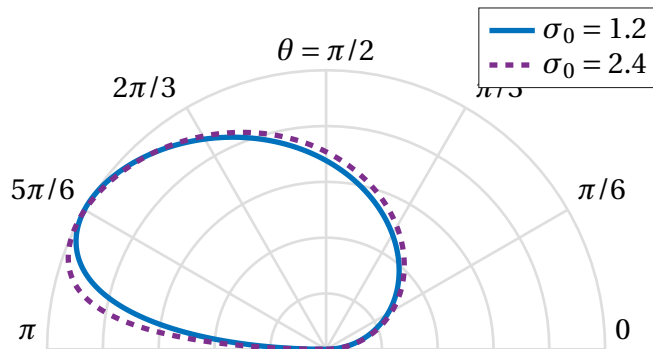


Fig. 5.3.10 By construction of a cubic, non-inflecting, profile, the effect of variation of wall-shear, without varying slip velocity ($U_0 = 0.2$), is investigated. The far-field pressure $|p'|$, normalised by the maximum, is shown for $\omega = 5$ and free-stream Mach number 0.2, and the resulting directivity plot shows little effect of wall-shear variation.

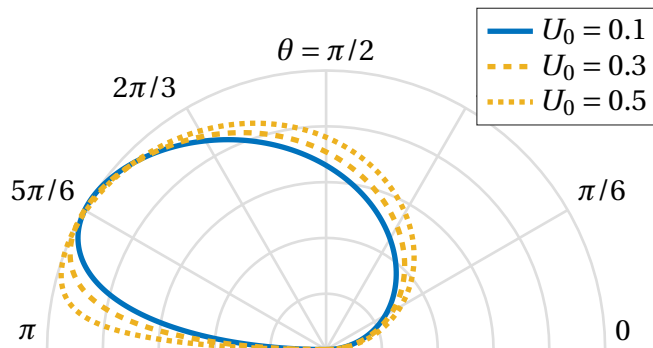


Fig. 5.3.11 By construction of a cubic, non-inflecting, profile, the effect of variation of slip velocity without varying wall-shear ($\sigma_0 = 1.5$) The far-field pressure $|p'|$, normalised by the maximum, is shown for $\omega = 5$ and free-stream Mach number 0.2, and the resulting directivity plot shows a noticeable effect of varying slip velocity, with a much wider lobe for higher slip velocities.

It is important to investigate the *shape* of the boundary-layer on the far-field directivity. As yet, this work has focused on linear profiles (with a jump in shear at the edge of the boundary-layer) and parabolic profiles, chosen to be smooth at the edge of the boundary-layer. Both of these have a necessary variation in slip velocity U_0 with wall-shear $\sigma_0 = U'(0)$, as there are insufficient degrees of freedom to separate these quantities (for fixed $U_\infty = \delta = 1$, a scaling assumed throughout). With this in mind, a cubic profile is constructed allowing independent variation of U_0 and σ_0 : indeed, these parameters alone are enough to specify the problem. The profile considered here is

$$U(x_2) = U_0 + \sigma_0 x_2 + (3 - 3U_0 - 2\sigma_0)x_2^2 + (2U_0 + \sigma_0 - 2)x_2^3. \quad (5.3.18)$$

This profile has $U(1) = 1$ and $U'(1) = 0$, and is non-inflecting provided, simultaneously, $3U_0 + \sigma_0 < 3$ and $3U_0 + 2\sigma_0 > 3$. Two examples of this type of profile are shown in figures 5.3.9, respectively for fixed slip velocity and for fixed wall-shear. The separation of these parameters, albeit via the construction of a more complicated profile, allows direct investigation of the effect of changing each of them, seen respectively in figures 5.3.9a and 5.3.9b, both for reasonably high frequency $\omega = 5$. The effect of changing the slip velocity is considerably more pronounced, which is partially as this more broadly changes the flow profile across the entire boundary-layer. For slipping flow, the effect of varying wall shear is comparatively minimal. It is worth noting that these plots, normalised by the highest value, show only the *directivity* of the far-field noise, and thus show nothing about whether or not near-wall shear can reduce the amplitude of the noise.

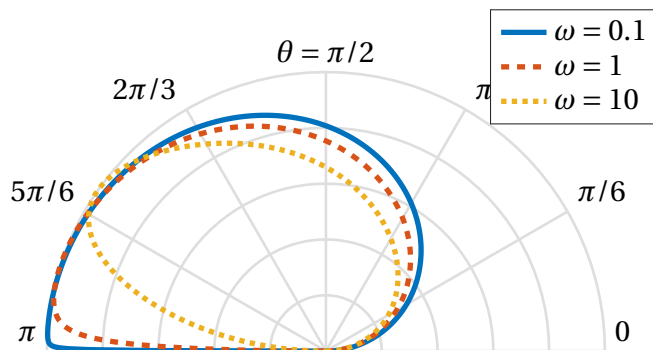


Fig. 5.3.12 For y_2 fixed, with the same parabolic profile as figure 5.3.8, with instead the frequency (and thus both the *hydrodynamic* and *acoustic* wavelengths) being varied, here scaled with boundary-layer thickness and free-stream velocity, as usual. Low frequency directivity tends towards a $\sin(\theta/2)$ cardioid, whereas high-frequency directivity tends towards a single, upstream-directed lobe.

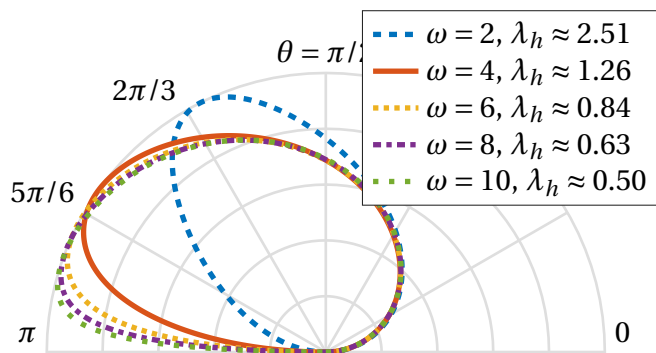


Fig. 5.3.13 The acoustic wavelength is fixed at 2π , so that $c_0 = \omega$ for each plot. The hydrodynamic lengthscale $\lambda_h \equiv 2\pi U(y_2)/\omega$ is then allowed to vary.

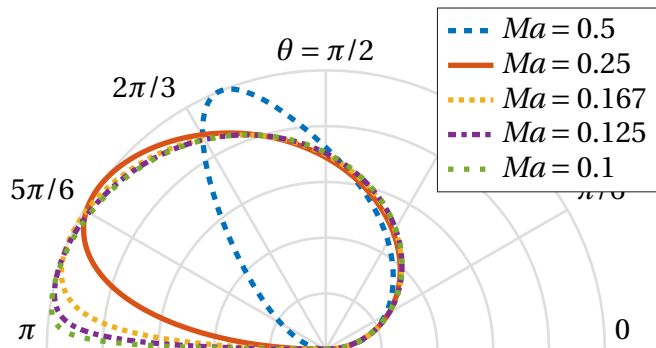


Fig. 5.3.14 As figure 5.3.13, except $\omega = 4$ is fixed, fixing the hydrodynamic wavelength at approximately 1.26 (and in turn, ensuring the red (solid) curves on both plots are the same). The speeds of sound are as in the preceding plot, with acoustic wavelength here varying from π to 5π .

For a point source in sheared flow, the directivity was broadly controlled by the acoustic wavelength $\lambda_a = 2\pi/k_0 = 2\pi c_0/\omega$, with some contributions from the hydrodynamic wavelength $\lambda_h = 2\pi/\kappa_1 = 2\pi U(y_2)/\omega$, which is smaller a factor of the Mach number. With this, we focus on the effect of frequency variation on the far-field directivity, having identified the lack of impact from variation of source location and comparatively little effect from variation of background profile. Varying frequency alone (whilst holding c_0 and U constant) produces figure 5.3.12, showing a broad trend from a cardioid $\sin(\theta/2)$ profile for low frequencies, to the single downstream-directed lobe for higher frequencies. As before, there is only a single lobe: there is no real lengthscale imposed by the source to cause an interference pattern as seen before (any “image” sources would be coincident with the actual scattered source at the origin).

As before, it is useful to focus on varying each imposed lengthscale independently, since varying ω varies both λ_h and λ_a . We firstly vary the hydrodynamic wavelength while holding the acoustic lengthscale constant in figure 5.3.13. A short acoustic wavelength is chosen to maximise any effect of the boundary-layer on the far-field acoustics, though this in turn limits the possible range of values of λ_h (limited by required $Ma < 1$). Surprisingly, even with the acoustic behaviour fixed, changing this alone has a large effect on the far-field directivity. Shorter wavelength disturbances propagate more upstream. Whilst at first glance this is linked to the boundary layer becoming more “incompressible” as c_0 increases, this cannot entirely explain the effect as incompressibility is determined more by the acoustic *lengthscale* which remains constant. This highlights the importance of the source: even if its location might not be important, the induced lengthscale is.

Finally, focus on varying only the free-stream Mach number (and thus acoustic wavelength) produces the very similar figure 5.3.14, chosen to overlap with the preceding case. Whilst the qualitative trend is the same as holding the acoustic wavelength constant, the effect is of a more directed high Mach number flow and of a more cardioid low Mach number flow, emphasising the importance of the acoustic wavelength on the scattering from the junction: for a larger acoustic wavelength (smaller Mach number) the boundary-layer effect is reduced, even for the same hydrodynamic wavelength, and a cardioid-type directivity profile is seen. This reduction to the “expected” incompressible/uniform solution being more pronounced when the boundary-layer is acoustically compact (i.e. $\lambda_a \gg \delta$) holds for even moderately large Mach number Ma , and is a far more pronounced effect than the similar result for longer hydrodynamic wavelengths.

5.4 Non-slipping sheared flow: Hard-soft transition

The previous section relied on the assumption that $U_0 \neq 0$. This assumption is not critical to the Wiener-Hopf analysis, indeed the resulting Wiener-Hopf equation (in the non-slip case) is identical, with the kernel having the same definition, $K = D_p/D_h$. Issues arise only from attempts to factorise this kernel, since the large k_1 behaviour differs. This fundamentally arises from the presence (or lack of) the term $U_0 k_1$ in the transformed convective derivative C , evaluated at the wall. For large k_1 this term grows and dominates (if $U_0 \neq 0$) and so the non-appearance of this term in the non-slip kernel leads to greatly differing large k_1 asymptotics, and thus factorisation is more involved.

Otherwise, the mathematics for a non-slipping flow is identical, and the scattered solution, due to a vortex sheet, is again given by (5.3.16), with suitably redefined K_{\pm} .

5.4.1 Far-field kernel

Determination of the far-field behaviour can be determined by analogy with the piecewise-linear, incompressible case. In this case, with exponential terms decaying rapidly, we have

$$K \sim \frac{i(k_1 \sigma_0 - |k_1| \omega)}{|k_1|^2} \quad (5.4.1)$$

which can immediately be seen by comparing the expressions for p' and v' in (3.3.7), for example. Generalisation to the compressible case naïvely requires replacement of $|k_1|$ with γ , which has identical far-field behaviour anyway (since $U_0 = 0$ and so $\gamma_0 = \sqrt{k_1^2 - \omega^2/c_0^2}$, at least for two-dimensional disturbances). With this, we have a far-field approximation, for large k_1 , as

$$K \sim \frac{i(k_1 \sigma_0 - \gamma_0 \omega)}{\gamma_0^2} \quad (5.4.2)$$

with $\gamma_0^2 = k_1^2 - k_0^2$ and wall shear $\sigma_0 = U'(0)$. Unlike the previous case, there is no trivial factorisation of this kernel as the difference $k_1 \sigma_0 - \gamma_0 \omega$ has not been previously factorised. We can, however, use the method outlined in §5.2.5, and find a numerical reduction of the total kernel, which tends to unity at either end of the factorisation contour, using the far-field behaviour from above.

We assume we have a separation contour (or contour) $C_{(\pm)}(s)$ tending towards $\pm\infty$ as $s \rightarrow \pm\infty$. Along this contour, we have

$$K \sim \frac{i}{|s|} (\sigma_0 \mp \omega). \quad (5.4.3)$$

This is the same far-field behaviour as

$$K_f = i(\sigma - \omega)(k_1 - k_{b+})_+^{-1/2+\alpha}(k_1 - k_{b-})_-^{-1/2-\alpha} \quad (5.4.4)$$

with exponent α defined as

$$\alpha = \frac{1}{2\pi i} \log \left(\frac{\sigma_0 + \omega}{\sigma_0 - \omega} \right). \quad (5.4.5)$$

This is a complex number for ω complex. It is defined only up to the addition of a real integer, which can be fixed to ensure that the winding number of $\bar{K} = K/K_f$ is 0 along the integration contour. The two branch points $k_{b\pm}$ are essentially arbitrary, provided they lie respectively in the gL/UHk₁P. In practice, we identify them with the branch points of γ_0 as $k_{b\pm} = \pm\sqrt{\omega^2/c_0^2 - k_3^2}$, which avoids complication from multiple branch points of \bar{K} in different locations. The resulting reduced kernel, $\bar{K} = K/K_f$, therefore tends to 1 at either end of the separation contour, and we can thus compute the multiplicative factorisation of \bar{K} by computing the additive factorisation of $\log(K)$, as before. The factorisation of K itself then follows from the trivial factorisation of K_f , with

$$K_{f+} = i(\sigma - \omega)(k_1 - k_{b+})_+^{-1/2+\alpha}, \quad (5.4.6a)$$

$$K_{f-} = (k_1 - k_{b-})_-^{-1/2-\alpha}. \quad (5.4.6b)$$

The assignment of the leading constant $i(\sigma - \omega)$ is arbitrary, but for definiteness is included in (5.4.6a). This factorisation is shown for a simple, non-slipping parabolic profile in figure 5.4.1. Importantly, the continuity of \log is demonstrated in figure 5.4.1b with the principal value of α taken, demonstrating in this case no amendment due to winding number is required.

5.4.2 Numerical inversion

As noted in the caption to figure 5.4.1, the critical layer for any no-slip profile extends along $k_1 \in [\omega/U_\infty, \infty)$, if we integrate the governing differential equation along real x_2 . By integrating along complex z (generalising x_2 to the complex plane) we can deform this critical-layer branch cut to a location of choice, with the leading branch cut fixed at ω/U_∞ but the path to ∞ changed. This allows not only a more accurate evaluation of K_\pm , by deforming the critical-layer (and the main source of numerical error) away from the separation contour C_\pm , but it allows more precise evaluation of the inversion integral along the branch cut itself. Extending figure 5.3.4, the inversion contours for the no-slip case are indicated, with colours here used to denote if the critical-layer is deformed into

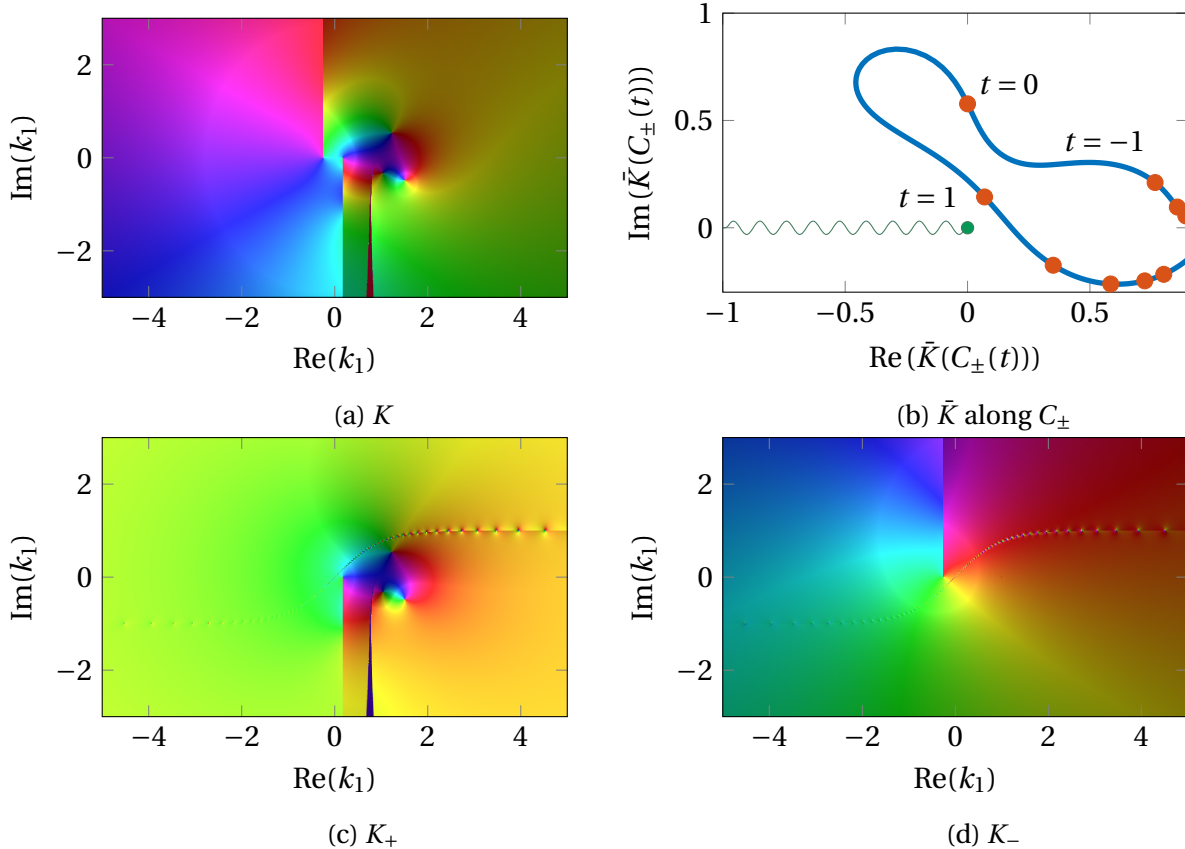


Fig. 5.4.1 The no-slip kernel for a parabolic profile at unit frequency. In this case, wall shear is $2 > \omega = 1$, which should be compared to the slipping case, figures 5.3.1 and 5.3.3. The numerical factorisation is also shown, with a simple tanh contour and 100 quadrature points, which is a lower accuracy than used when computing inversion and far-field noise, but demonstrates again the numerical accuracy near the separation contour. For clarity, the behaviour of the reduced kernel $\bar{K} = K/K_f$ is shown in figure 5.4.1b as we move along the separation contour. Since this curve does not enclose 0, a branch cut of log can be chosen to ensure $\log(\bar{K})$ is continuous and vanishes at either end of the contour, as shown. Unlike in the earlier slipping case, here the critical layer extends downwards from the leading branch point, $k_1 = \omega/U_\infty = 1$, as we choose to integrate the differential equation through a semicircular arc in the complex z -plane (with $\text{Re}(z) = x_2$). Since the second branch point moves to infinity as $U_0 \rightarrow 0$, this ensures K is numerically accurate along the entirety of C_{\pm} .

the U/LH k_1 P (by deforming the z contour into the L/UHzP respectively). With the critical layer contribution, the jump in the integrand over the critical-layer branch cut, tending towards zero as $|k_1|$ gets large, this allows truncation of the critical-layer integral at some finite, large, real k_1 .

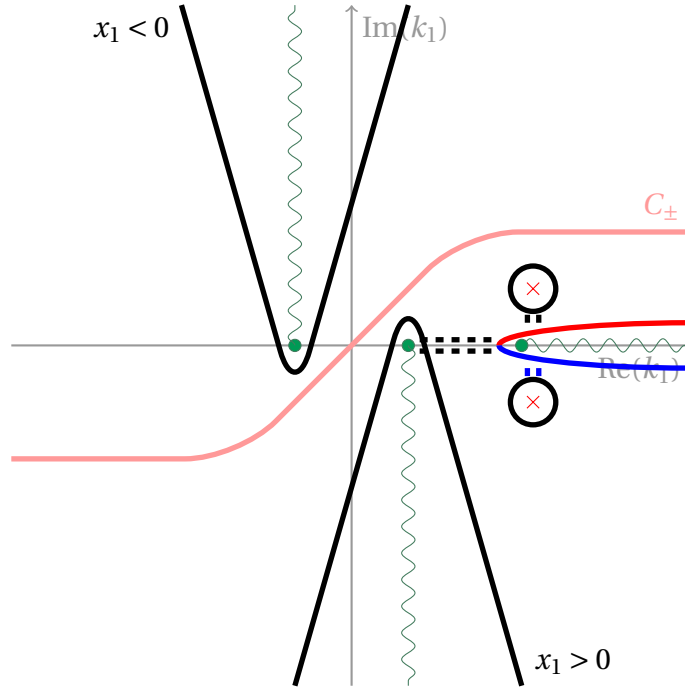


Fig. 5.4.2 Schematic of contour deformation in the no-slip case. Here, red contours (including the separation contour) indicate the integrand should be computed by integration in the UHzP, so that the critical-layer is deformed into the LH k_1 P, and blue contours indicate the converse. This allows precise evaluation of the integrand along both contours, and thus reduces numerical error in computation of the critical-layer contribution.

The final step required in the inversion process is to ensure the entire function, $E(k_1)$, is suitably understood. This is made slightly more difficult by the complex exponent in the far-field representation of the kernel $K_{f\pm}$ (as per (5.4.6)), which can be used as a proxy for the far-field behaviour of K_\pm where relevant, as computed \tilde{K}_\pm are analytic and tend to unity at infinity in all directions.

We recall the definition of α in (5.4.5). If $\sigma_0 > \omega > 0$, then we have the logarithm of a real number, and so α is imaginary (and with negative imaginary part, as $\sigma_0 - \omega > \sigma_0 + \omega$). If, instead, $\omega > \sigma_0 > 0$, then α has a non-zero real part. The principal value gives this as 1/2, though if checking the curve $\tilde{K}(C(t))$ showed a non-zero winding number around zero, this can be modified by an integer, though as per figure 5.4.1b, with $\omega = 1 < \sigma_0 = 2$, the principal value suffices for this case. With this imaginary part negative in both cases,

we split $\alpha = \operatorname{Re}(\alpha) - i b$ and then

$$K_{f\pm} \sim (k_1)_+^{-1/2 \mp ib} \quad (5.4.7)$$

for $\omega > \sigma$, and

$$K_{f+} \sim (k_1)_+^{-ib}, \quad (5.4.8)$$

$$K_{f-} \sim (k_1)_-^{-1+ib} \quad (5.4.9)$$

for $\omega < \sigma_0$. We now claim

$$(z)^{ix} \quad (5.4.10)$$

is bounded, regardless of choice of branch cut, for any real x . For $z = r e^{i\theta}$, we have

$$|z^{ix}| = |r^{ix}| e^{-x\theta}. \quad (5.4.11)$$

The second part, $e^{-x\theta}$, is bounded either by its value at the minimum value of θ (for $x < 0$) or at its maximum (for $x > 0$) as θ is sampled from some closed and bounded interval (for a straight branch cut from 0 to ∞ in any direction). Then $|r^{ix}| = |e^{ix\log r}| = 1$, as r is real and positive. Thus, $K_{f\pm}$ is, in the worst case, bounded by a constant, though $1/K_-$ might grow like k_1 . Provided B^+ , the pressure on the upstream surface, does not grow faster than $k_1^{1/2}$ (essentially arguing it is bounded, or at least is not particularly singular) then the UH k_1 P definition of the entire function

$$E(k_1) = K_+ B^+ + \left(\frac{I^+}{K_-} \right)^+ \quad (5.4.12)$$

must decay in the UH k_1 P, with the additive factorisation of the incident source inheriting the behaviour of I^+ only, and decaying as k_1^{-1} . Since any polynomial E will grow in the UH k_1 P, E must be identically zero and we obtain exactly the same integrand as before, up to replacement of K_\pm .

Inverting along the slightly altered contours produces figure 5.4.3, for a parabolic profile unstable above the pressure-release boundary downstream of $x_1 = 0$. Two cases are shown, with $\omega = 1$ and $\omega = 4$, respectively smaller and larger than wall shear $\sigma_0 = 2$, to demonstrate the validity of the solution in both cases.

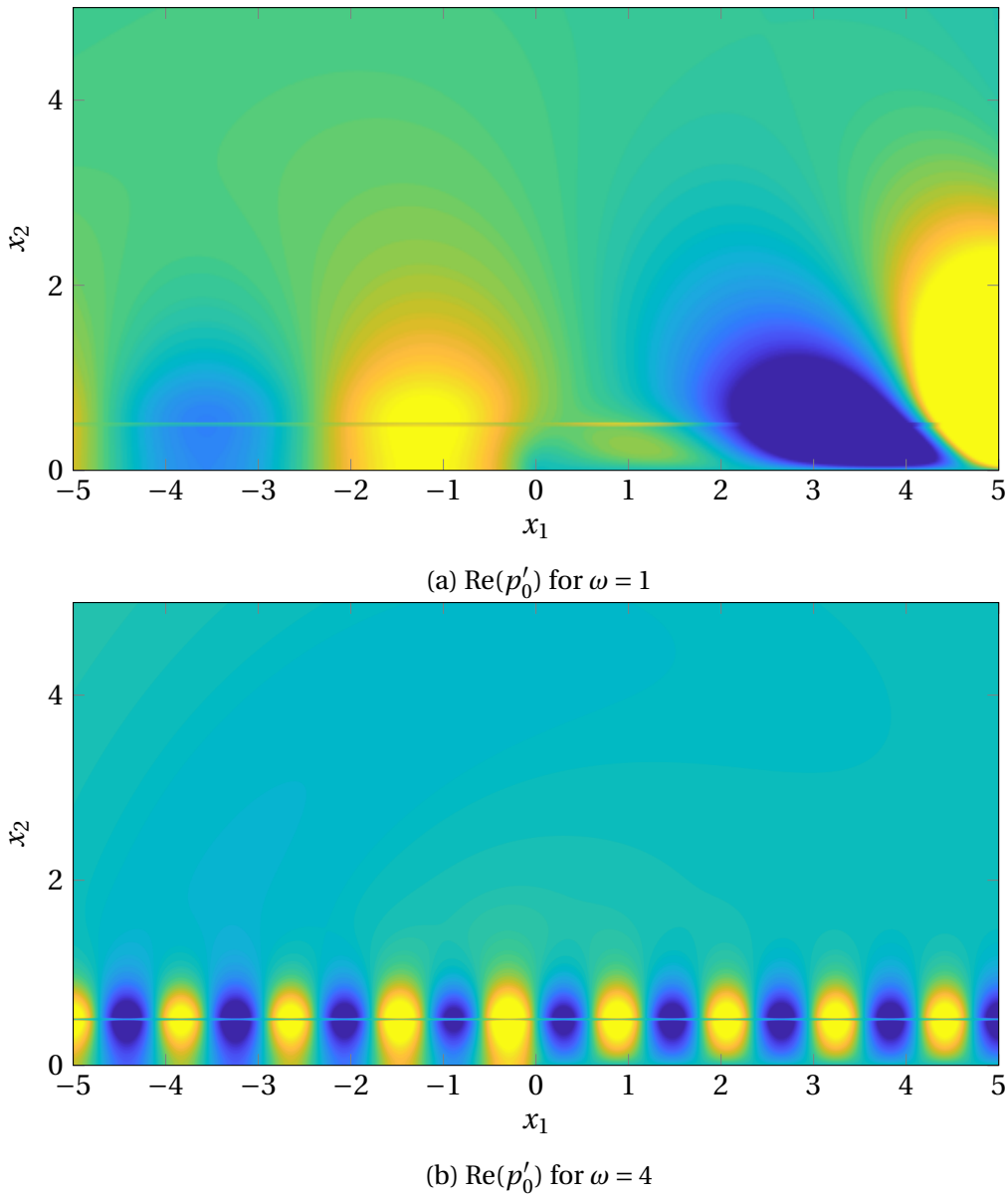


Fig. 5.4.3 The computed inversion (both incident vortex sheet and scattered) of a vortex sheet at $y_2 = 0.5\delta$ in a non-slipping parabolic profile, with $c_0 = 5U_\infty$, at frequencies above and below the wall shear. The latter case is stable, with stability reached when $\omega = \sigma_0$, which ensures the latter plot is unexciting (though the change to vanishing pressure on the wall is clearly visible). These plots show the more complicated factorisation routine is perfectly valid.

5.4.3 Behaviour of scattered solution near the junction

Of interest is the growth of the scattering at the scattering point, and in particular how this is affected by the relationship between ω and σ_0 . We have previously used conditions in physical space as $x_1 \rightarrow 0$ to bound the entire function in wavenumber space as $k_1 \rightarrow \infty$, and the inversion of this process can be used to compute the behaviour of the scattering solution near the junction, $x_1 = x_2 = 0$, by considering large k_1 behaviour of the integrand. As a function of k_1 , along $x_2 = 0$ the integrand for the pressure component of the solution, $p'_0 = \mathcal{P}_0 \phi_0$ (including both incident and scattered contributions), behaves like $K_- e^{-ik_1 x_1} / k_1$ for k_1 large, and so the behaviour locally to the junction can exactly be related to the behaviour of K_- for k_1 large, which has been computed directly through the far-field behaviour of K and the imposition of non-zero winding number.

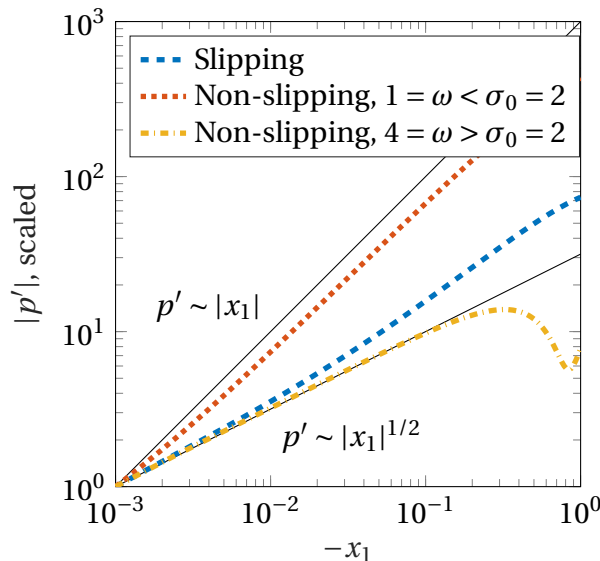


Fig. 5.4.4 Growth of scattered pressure solution upstream from junction point $x_1 = x_2 = 0$. In all cases a parabolic background profile is considered, with continuous shear at the edge of the boundary-layer. Either the slip velocity vanishes, or $U_0 = 0.1$, as appropriate. The total pressure is scaled by the value evaluated at $x_1 = 10^{-3}$, so that it is 1 here. As expected, the perturbation to the slipping profile grows as $(-x_1)^{1/2}$ and for the non-slipping profile it depends sensitively on the interplay between wall-shear and frequency.

For a *slipping* profile, we have $K_- \sim k_1^{-1/2}$ exactly, and so the streamwise transform of p' behaves as $k_1^{-3/2}$ for large k_1 . Via the discussion of §5.2.6, this corresponds to a scattered solution growing like $x_1^{1/2}$ near $x_1 = 0$, which is borne out numerically. For a *non-slipping* profile, the picture is not quite as clear. We recall $K_- \sim k_1^{-1/2-\alpha}$, where α is complex. If the frequency is less than the wall shear, $|\omega| < \sigma_0$ (assuming the background profile is increasing, so $\sigma_0 > 0$), then α is purely imaginary. Otherwise, it has a real part of

$1/2$ (to ensure that the winding number criterion is satisfied). In either case, $p' \sim x_1^{1/2+\alpha}$. When the frequency is large, larger than the wall shear, the scattered pressure grows (upstream, since it vanishes downstream) like x_1 , with some modifications from the remaining imaginary power. These three cases, slipping and non-slipping with $\omega \gtrless \sigma_0$ are considered numerically in figure 5.4.4, producing the results expected. In particular, for low frequency growth is much more like $|x_1|$, though the complex contribution ensures it is slightly less than this. This is consistent with previous work suggesting a growth rate between $|x_1|^{1/2}$ and $|x_1|$.

5.4.4 Far-field noise

Computation of far-field noise proceeds exactly as in the previous section §5.3, with suitably modified K , and as such there is no need to go into details here. Since evaluation of the far-field noise requires, for each observer angle, evaluation at single wavenumber $k_s(\theta)$, it is much more rapid than computing the full near-field inversion. With this in mind, we can use the far-field noise to focus on two specific problems of this setup: firstly whether the no-slip limit is in fact the limit of the preceding section as $U_0 \rightarrow 0$, which physically we would expect; and secondly what happens in the long-wavelength limit (comparing to previous work such as [101], which suggested non-trivial far-field behaviour when directly factorising the incompressible kernel K , rather than considering the limit of large finite c_0).

5.4.5 The consistency of the no-slip limit

The mathematical routine is fundamentally different depending on whether $U_0 = 0$ or $U_0 \neq 0$, though physically we wouldn't expect any abrupt change in the solution. Computation of far-field noise readily allows testing of this limit. This is readily investigated as per figure 5.4.5, which uses both the slipping and non-slipping mathematical routines. In the limit $U_0 \rightarrow 0$, the solution changes continuously, as physical intuition might suggest. This holds broadly across all frequencies, the choice of frequency is to emphasise the similarity in the limit.

5.4.6 The incompressible (long-wavelength) limit

This chapter has, as yet, been focused on the compressible case and the associated acoustic potential ϕ , in contrast to the opening work of §3, which looked at long-wavelength disturbances which could be regarded as, on the boundary-layer scale, incompressible.

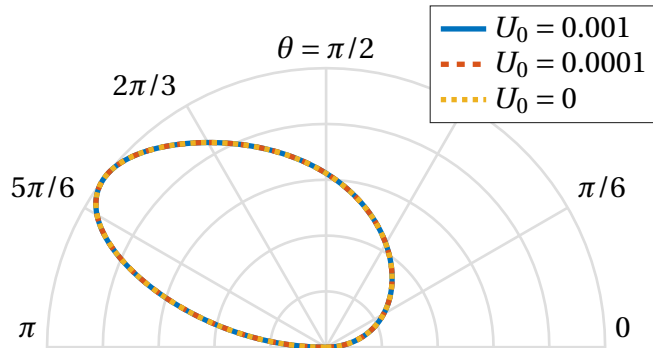


Fig. 5.4.5 Considering a parabolic profile with frequency $\omega = 5$ and free-stream Mach number 0.2. The slip velocity U_0 is relaxed to zero and the directivity of the resulting scattered sound is plotted. The curves are essentially indistinguishable. There is thus no physical change in the far-field behaviour of the no-slip case. This result still holds if $\omega < \sigma_0$.

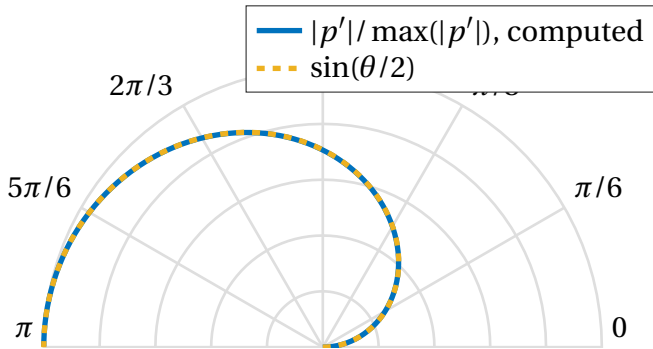


Fig. 5.4.6 The far-field directivity for large speed of sound c_0 , here chosen to be $500U_\infty$. Scattering from linear, non-slipping, background profile with unit shear, and frequency $\omega = 10$ (though the result is consistent across all frequencies). For reference, the cardioid directivity $\sin(\theta/2)$ is plotted, which shows precise agreement across for all $\theta < \pi$.

For a piecewise linear profile this substantially reduced the numerical complexity in solving the governing ODE. Difficulties arise in the scattering problem, however, due to the relaxation of $\gamma = \sqrt{k_1^2 - k_0^2}$ to $|k_1|$. The latter function has no contour stretching from $-\infty$ to ∞ on which it is analytic, since any contour must either pass over a branch cut or through the branch point at 0. This causes problems with the Wiener-Hopf factorisation, which implicitly assumes a strip of analyticity of the Wiener-Hopf kernel K , and therefore some regularisation of $|k_1|$ is required to create a well-posed Wiener-Hopf problem.

This limit can be taken, however, in the numerical work we have already done, by way of taking c_0 to infinity. Strictly, we require the dual condition (as per the derivation in §3) that $k_0^{-1} = c_0/\omega \gg \delta$ (long acoustic wavelength, so that the boundary-layer is acoustically compact) and that $Ma_\infty^2 = U_\infty^2/c_\infty^2 \ll 1$, which permits non-negligible free-stream velocities. For large but finite c_0 , there is nothing that prevents the derived routines from being used, and an example of the far-field directivity is shown in figure 5.4.6. For reference, the cardioid profile $p' \sim \sin(\theta/2)$ is also shown, which is exactly the profile that would be expected for the scattering from a trailing-edge in no flow (with no boundary-layer shear). As we shall see in the next chapter, the (symmetric) trailing-edge case is analogous to the hard-soft junction, and so this result is unsurprising.

The incompressible framework is consistent in this limit. This resolves earlier difficulties in factorising the apparent incompressible kernel directly [93, 101], which runs into two problems. Firstly, the separation contours C_\pm are pinched between the branches of $|k_1|$ at the origin, which removes a well-defined Wiener-Hopf strip, and thus the factorisation can only be ever thought of in a limit, either of $k_3 \rightarrow 0$ (so $\sqrt{k_1^2 + k_3^2} \rightarrow |k_1|$) or the limit of $c_0 \rightarrow \infty$ (so $\gamma = \sqrt{k_1^2 - \omega^2/c_0^2} \rightarrow |k_1|$). It is possible to find factorisations that seem to converge everywhere in this limit (in fact, the far-field factorisation used to reduce the kernel for numerical evaluation), but the difficulty arises in evaluation of this resulting kernel at $k_1 = 0$. This is critical for far-field evaluation, as we saw in the earlier chapter §3.

Further, far-field evaluation in the *compressible* case with c_0 finite requires evaluation at the saddle point k_s , which lies along a line connecting the two acoustic branch points. This cannot possibly be done when c_0 is infinite, as all these points collapse to $k_1 = 0$. It is therefore difficult to extract far-field information from a purely incompressible framework, especially when evaluation of K at $k_1 = 0$ is ill-defined.

With these two problems identified, the solution is to evaluate K alone as if it were compressible, with c_0 large (noting the convergence in the limit $c_0 \rightarrow \infty$). All other functions can be evaluated as if incompressible, which allows some analytic representation of the solution, and preserves the useful modal structure seen in §3. However, given factorisation of K is the most numerically difficult part of the computation, this approach

seems unnecessarily roundabout and, unless the exact benefits of the modal structure from a piecewise linear profile are required, there are insufficient gains from this approach for it to be worthwhile.

5.5 Transition between two different lined surfaces

The hard-soft transition has been covered in detail primarily because of the straightforward application of the derived formulas, with the relevant dispersion functions D_h and D_p covered in detail in previous chapters. The generic setup in the opening section, §5.2, allows for more complicated linear boundary conditions with little further work, the majority of the work focusing on identification of the far-field behaviour of the relevant Wiener-Hopf kernel (and relating concerns of winding numbers and behaviour of the entire function E). With this in mind, this section focused on the generic case of scattering from a transition between two lined surfaces, with arbitrary impedances Z_u and Z_d , upstream and downstream respectively. It opens with a brief discussion of the special case of a soft-hard transition, the inverse of the case seen above, which is the special case $Z_u = 0$ and $Z_d = \infty$.

5.5.1 Soft to hard transition

We previously considered generalised Upper and Lower Half Planes. For the generic kernel $K = D_d / D_u$, we required that zeros of D_d and of D_u , respectively zeros and poles of K , lie in the half-plane as determined by a Briggs-Bers analysis (i.e. the half-plane they lie in for large negative $\text{Im}(\omega)$). The alternate problem of scattering from the formerly downstream boundary condition to the formerly upstream boundary condition involves the inverse kernel K^{-1} , which has zeros and poles at the zeros of D_u and D_d respectively, but which lie in exactly the same generalised half planes as before. The factorisation of K^{-1} then follows exactly the same procedure as factorising K , with resulting factors simply K_{\pm}^{-1} , which are trivially synthesised from the already computed splitfunctions. Essentially, the careful causality considerations in the preceding section ensure that the problem with flipped boundary conditions is a trivial extension of the previous problem.

5.5.2 Impedance to impedance transition

We now consider the generic case of an upstream boundary with impedance Z_u (for $x_1 < 0$) and a downstream boundary with impedance Z_d . Provided these are not 0 (a pressure-release boundary) or ∞ (a hard-wall boundary) the analysis that follows is in

many ways more straightforward than in the hard-soft transition, due to the cleaner form of the kernel K . Defining the up/downstream dispersion functions as $D_{Z_{u,d}}$ respectively, we have

$$K = \frac{D_{Z_d}}{D_{Z_u}} = \frac{i\omega Z_d D_h - C_0 D_p}{i\omega Z_u D_h - C_0 D_p}. \quad (5.5.1)$$

The linearity of the impedance boundary condition, explicitly $i\omega Z v' = (i\omega + U(0)\partial/\partial x_1) p'$, leads directly to linearity of the dispersion function. The critical step for numerical factorisation is as before identification of the large k_1 behaviour of K . There are two distinct cases to consider.

Firstly, if $U_0 \neq 0$, then $p' \sim k_1^3 \phi$ and $v' \sim \gamma k_1^2 \phi$, following from $\phi' \sim -\gamma \phi$ and ignoring scaling constants. The pressure term (multiplied by another factor of k_1) thus dominates unless $Z = \infty$ (in either case) and in the slipping case

$$K \sim 1. \quad (5.5.2)$$

No work is therefore required to prepare this function for numerical factorisation, other than checking the winding number around 0 along the factorisation contour vanishes.

The non-slip case with $U_0 = 0$ instead has $p' \sim \phi$ as $C_0 = i\omega$ has no k_1 dependence. v' therefore dominates for large k_1 (driven in part by the shear term), and $D_Z \sim i\omega Z D_h$, and so

$$K \sim \frac{Z_d}{Z_u} \quad (5.5.3)$$

and we can introduce the straightforward reduced kernel

$$\bar{K} = \frac{Z_u K}{Z_d} \quad (5.5.4)$$

which can be factorised numerically subject to the usual caveats. This limit does not work in the pressure-release case $Z = 0$.

If either $Z = \infty$ (so one surface is hard), then in the far-field, slipping case we merely regain the far-field hard-soft or soft-hard kernel, as appropriate (since the pressure dominates the impedance term, asymptotically giving the equivalent to a soft wall). Conversely, if either $Z = 0$ (so one surface is a pressure-release soft wall) the no-slip case reduces again to the hard-soft or soft-hard (no-slip) kernel in the far-field. In both cases, the preceding two sections have dealt with the factorisation of this far-field kernel (or its inverse) and the numerics proceeds analogously, so won't be directly considered in this section.

The full near-field inversion for a simple example is shown in figure 5.5.1, showing a transition from $Z = 1 - i$ upstream to $Z = 2 - 2i$ downstream, mainly to demonstrate the

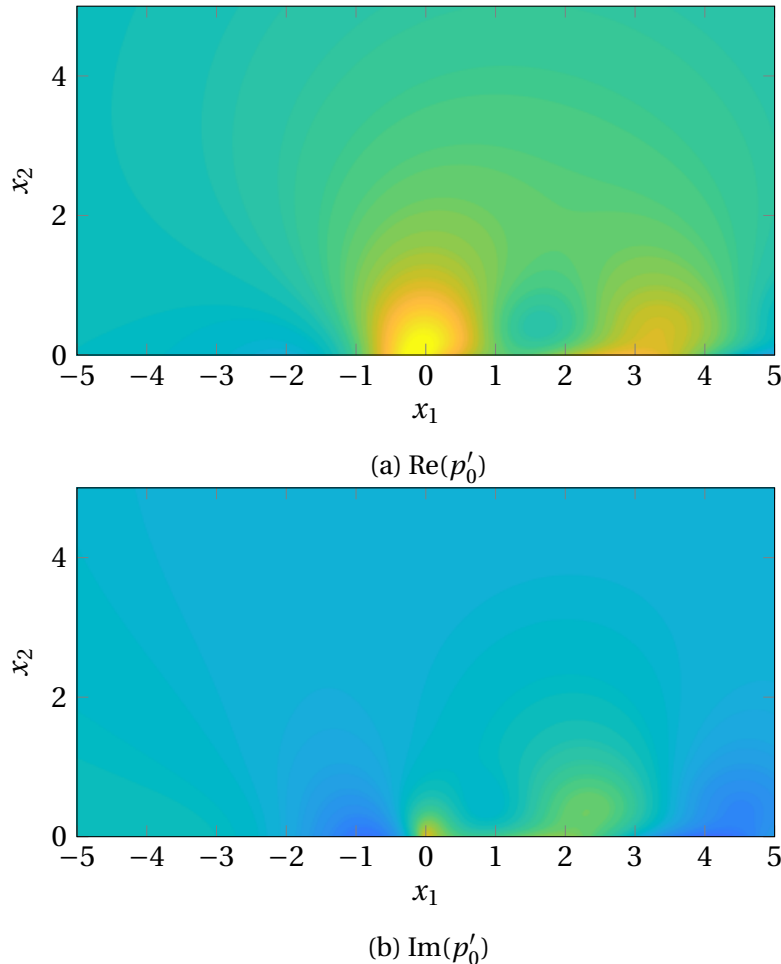


Fig. 5.5.1 A vortex sheet disturbance to a non-slipping parabolic profile, with continuous shear at the edge of the boundary-layer, above a lining with $Z_u = 1 - i$ for $x_1 < 0$ and $Z_d = 2 - 2i$ for $x_1 > 0$. The linings are convectively stable for $\omega = 1$, but both (and importantly D_u) have an upstream propagating mode which is picked up when integrating in the UH k_1 P.

validity of the code, and in particular the answer is consistent for $x_1 \geqslant 0$ (when the choice of contours changes). Only the scattered component, focused on the origin, is displayed, since the scattered solution is much smaller in magnitude than the incident solution (and so is essentially not visible on the full plot). This case differs slightly from previous work, since, with the frequency and profile chosen, the lined walls have two surface mode solutions, one with $\text{Re}(k_1) < 0$. This can be shown to be upstream propagating, and thus the zero of D_u should be picked up when integrating in the UH k_1 P. Two modal solutions therefore originate at $x_1 = 0$, one propagating to the right (a zero of D_d) and one to the left (a zero of D_u), both exponentially decaying downstream.

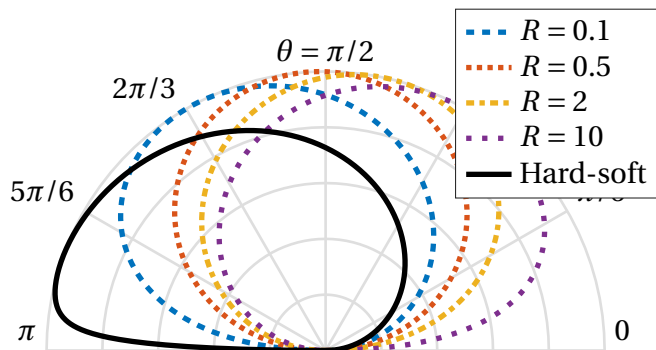


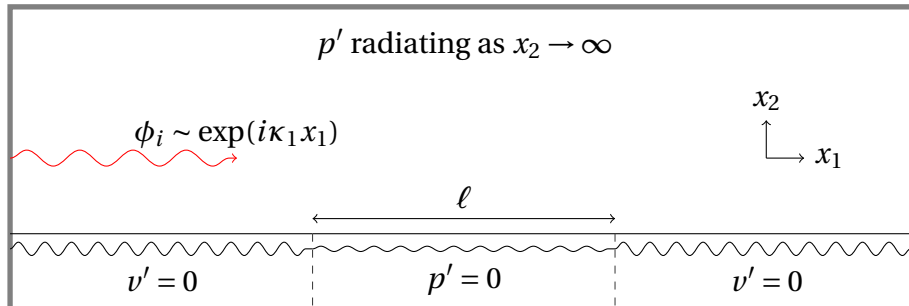
Fig. 5.5.2 The scattering from an impedance-impedance junction, with $Z_u = (1 - i)/R$ and $Z_d = R(1 - i)$. A non-slipping parabolic background profile, with free-speed $Ma = 0.2$, is considered as before, at frequency $\omega = 1$.

Finally, far-field scattered noise can be computed in the usual way. We can use this to demonstrate the consistency of $Z \rightarrow 0$ (pressure-release) and $Z \rightarrow \infty$ (hard-wall). This is done in figure 5.5.2, with Z_u increasing as Z_d decreasing, showing the single lobe directivity moving from upstream to downstream. It is worth noting the plot is not quite symmetric in $R \rightarrow R^{-1}$, with a general downstream lean to the lobes. For reference the hard-soft junction is plotted, which is the limit of vanishing R , and can indeed be shown to be obtained in the limit of small, non-zero R . We are satisfied that the impedance case accurately recaptures the previous hard-soft transition, despite the fundamentally different factorisation routines.

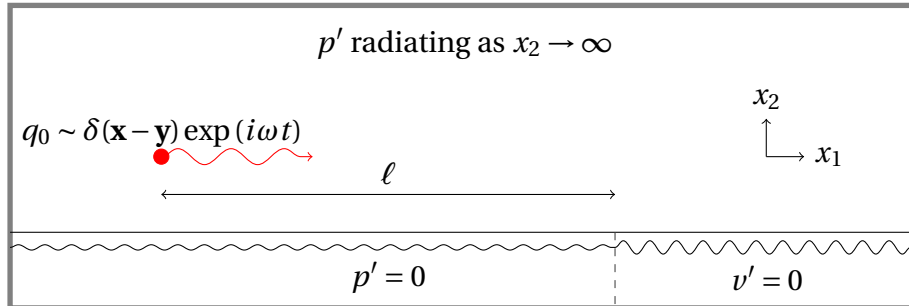
5.6 Restabilisation of unstable modes

It was briefly noted in the previous section, §5.5.1, that the soft-to-hard transition is mathematically a straightforward extension of the hard-to-soft transition, with the all-important Wiener-Hopf kernel simply the reciprocal of the earlier kernel. We can take

this to the next level by firstly imposing different upstream boundary conditions of an excited unstable mode, and from this consider the problem of a finite section of lining, under the assumption that the streamwise lengthscales imposed by this problem, denoted by ℓ , are sufficiently large that all contributions that are neither unstable nor neutrally stable have decayed. The problem to be considered is illustrated in figure 5.6.1a, though we could similarly discuss the problem of an upstream point source, shown in 5.6.1b, as a generalisation of §4.



(a) Scattering exciting an unstable mode, as per previous work in this chapter.



(b) A unstable mode excited by a point mass source, as per §4.

Fig. 5.6.1 Two related problems, both assuming an unstable mode is incident on some junction. Both cases pictured show the generation of a pressure-release mode, assumed unstable, generated at some streamwise distance ℓ before a soft-hard junction, though the exact forms of the various boundary conditions are essentially arbitrary up to insistence that they are linear and locally-reacting. It is assumed this distance ℓ is such that the disturbance incident on the (second) junction can be regarded as the sum of unstable and neutrally stable modes and that any scattering of acoustic solutions (i.e. scattering of terms generated at the other junction) can be ignored. The conditions for the validity of these assumptions is discussed in the text.

5.6.1 Restabilisation of an unstable mode

We first consider the scattering problem with incident wave of the form

$$\phi_i = A(x_2; \kappa_u) \exp(-i\kappa_u x_1) \quad (5.6.1)$$

with κ_u a wavenumber corresponding to a modal solution of the upstream boundary condition and thus if A is a multiple of ϕ_d the upstream boundary condition is automatically satisfied. Now suppose we have a transition at $x_1 = 0$ from boundary condition $\mathcal{L}^u \phi = 0$ to $\mathcal{L}^d \phi = 0$. The problem as discussed in all the preceding sections is essentially unchanged, save for the replacement of $(k_1 - \kappa_1)$ by $(k_1 - \kappa_u)$ in the denominator of the streamwise-transformed solution, both arising from the half-range transformation of the incident field and both κ_1 and κ_u constrained to be in the generalised LHK₁P (even if κ_u is unstable and has positive imaginary part, we assumed it is only convectively so).

With $\phi^{(i)} = B\phi_d(x_2; \kappa_u)e^{-i\kappa_u x_1}$ we therefore have have complete solution

$$\begin{aligned} \phi &= \phi^{(i)} + \phi^{(s)} \\ &= B \left[\phi_d(x_2; \kappa_u) e^{-i\kappa_u x_1} + \frac{1}{2\pi i} \int_{F_1} \frac{K_-(k_1)}{K_-(\kappa_u)} \frac{D_d(\kappa_u)}{D_d(k_1)} \frac{\phi_d(x_2; k_1) e^{-ik_1 x_1}}{k_1 - \kappa_u} \right]. \end{aligned} \quad (5.6.2)$$

We have written the split kernel in terms of the downstream dispersion function via the note (5.3.17), with the extra $D_d(\kappa_u)$ from I^+ and evaluation of $\mathcal{L}^d \phi_d$ on the downstream boundary. For $x_1 > 0$ we close in the gLHK₁P picking up residual contribution at $k_1 = \kappa_u$ (and acoustic contributions from the branch cuts and saddle point), and contributions from any other singularities of D_d . However, the residual contribution at κ_u is trivial to compute. The contour deformation indicates we loop this pole in a clockwise sense, picking up a contribution with negative sign that exactly cancels out the upstream incident solution. Therefore, the downstream solution consists solely of acoustic and critical-layer contributions, and the unstable modal solution is completely removed. This is to be expected, as the downstream boundary condition cannot support such a modal solution, and therefore it has no ability to persist. If the downstream boundary is stable (coupled with the background profile) then this exponentially growing disturbance is removed and the resulting disturbance doesn't grow downstream.

The above mathematical derivation is limited, in that it supposes (for $\text{Im}(\kappa_u) > 0$) an exponentially growing solution incident from $x_1 = -\infty$, where this disturbance will be infinitesimal. By introducing a finite length of growth, ℓ , this problem can be made more concrete. We do this by supposing we are a finite distance downstream of some disturbance that has excited a convectively unstable propagating solution, but far enough

downstream that any decaying solutions have decayed sufficiently that they can be ignored.

5.6.2 Finite unstable lining

We consider the setup as per figure 5.6.1a, with a hard-soft transition at $x_1 = x_{1u}$ and a soft-hard transition at $x_1 = x_{1d}$. Based on the above analyses, we expect an incident vortex sheet to scatter from the first transition, potentially generating unstable modes. At the section junction, any scattered modes will be restabilised, having only the effect of potentially amplifying the initial vortex sheet and of scattering noise to the far-field. This analysis neglects the effect of secondary scattering effects from the second junction of ignored terms from the first junction (e.g. critical-layer and branch point contributions) and in turn the reverse scattering effects from the second scattered solution at the leading junction. We assume that we can focus on the purely *modal* behaviour and solely the corresponding scattering at each junction, which could be motivated by direct consideration of the upstream point source problem.

We define, as previously, incident wave from $x_1 = -\infty$ given by (5.3.5), namely

$$\phi_0^{(i)} = Q_0(y_2) \phi_{\gtrless}(x_2; \kappa_1) \phi_{\lessgtr}(y_2; \kappa_1) \exp(-i\kappa_1 x_1) \quad (5.6.3)$$

for $x_2 \gtrless y_2$, with $\phi_{\gtrless} = \phi_h$. This satisfies the boundary condition for $x_1 < x_{1u}$ (and, incidentally, for $x_1 > x_{1d}$). We then define $\phi^{(s1)}$ to be the *first* scattered solution, driven by the junction at x_{1u} . As per §5.2, this can be written down exactly, namely

$$\begin{aligned} \phi_0^{(s1)} &= -\frac{Q_0(y_2) [\mathcal{P}_{01}^0 \phi_h(0; \kappa_1)] \phi_d(y_2; \kappa_1)}{2\pi i K_-(\kappa_1)} \int_{F_1} \frac{\phi_d(x_2; k_1)}{K_+(k_1)(k_1 - \kappa_1) D_h(k_1)} e^{-ik_1(x_1 - x_{1u})} dk_1 \\ &= -\frac{Q_0(y_2) [\mathcal{P}_{01}^0 \phi_h(0; \kappa_1)] \phi_d(y_2; \kappa_1)}{2\pi i K_-(\kappa_1)} \int_{F_1} \frac{K_-(k_1) \phi_d(x_2; k_1)}{(k_1 - \kappa_1) D_p(k_1)} e^{-ik_1(x_1 - x_{1u})} dk_1. \end{aligned} \quad (5.6.4)$$

These equivalent representations are exact, with hard-soft kernel

$$K = \frac{D_p}{D_h}. \quad (5.6.5)$$

Downstream of this junction, within the boundary-layer, we suppose this solution is dominated by some unstable pressure modal solution $\phi_{m1}^{(s1)}$ with wavenumber κ_p , which

has exactly the form

$$\phi_{0m1}^{(s1)} = \frac{Q_0(y_2) [\mathcal{P}_{01}^0 \phi_h(0; \kappa_1)] \phi_d(y_2; \kappa_1)}{K_-(\kappa_1)} \frac{K_-(\kappa_p) \phi_d(x_2; \kappa_p)}{(\kappa_p - \kappa_1) D'_p(\kappa_p)} e^{-i\kappa_p(x_1 - x_{1u})} \quad (5.6.6)$$

which is simply the residual contribution from the pole at $k_1 = \kappa_p$, traversed clockwise. The combination $\phi^{(i)} + \phi_m^{(s1)}$ doesn't satisfy the boundary condition on $x_2 = 0$ for $x_1 > x_{1u}$, so we include the forced contribution with wavenumber κ_1 within the modal scattered solution, namely

$$\phi_{0m2}^{(s1)} = \frac{Q_0(y_2) [\mathcal{P}_{01}^0 \phi_h(0; \kappa_1)] \phi_d(y_2; \kappa_1)}{D_p(\kappa_1)} \phi_d(x_2; \kappa_1) e^{-i\kappa_1(x_1 - x_{1u})} \quad (5.6.7)$$

The sum $\phi_m^{(s1)} = \phi_{m1}^{(s1)} + \phi_{m2}^{(s1)}$ then exactly cancels out the pressure fluctuations due to $\phi^{(i)}$ on the lined section of wall. Aside from the loss of smooth transition over $x_1 = x_{1u}$, these represent the dominant downstream contribution of the solution.

We now, in turn, define $\phi_m^{(s2)}$, due to the scattering of $\phi_m^{(s1)}$ at the second junction $x_1 = x_{1d}$ (noting that the incident wave will not scatter here, as it satisfies the downstream hard-wall boundary condition). This neglects the scattering due to any other components of the initial scattered solution: the critical-layer, the acoustic contribution and any other modal contributions. Using the above decomposition of $\phi_m^{(s1)}$ we have two contributions to $\phi_m^{(s2)}$. Firstly, due to the unstable mode

$$\begin{aligned} \phi_{0m1}^{(s2)} &= \bar{Q}_0 \int_{F_1} \frac{K_+(k_1) \phi_d(x_2; k_1)}{(k_1 - \kappa_p) D_p(k_1)} e^{-i k_1 (x_1 - x_{1d})} dk_1 \\ &= \bar{Q}_0 \int_{F_1} \frac{\phi_d(x_2; k_1)}{(k_1 - \kappa_p) K_-(k_1) D_h(k_1)} e^{-i k_1 (x_1 - x_{1d})} dk_1 \end{aligned} \quad (5.6.8)$$

with leading coefficient

$$\bar{Q}_0 = \frac{Q_0(y_2) [\mathcal{P}_{01}^0 \phi_h(0; \kappa_1)] D_h(\kappa_p) \phi_d(y_2; \kappa_1)}{2\pi i K_-(\kappa_1)} \frac{K_-(\kappa_p)^2 e^{-i\kappa_p \ell}}{(\kappa_p - \kappa_1) D'_p(\kappa_p)} \quad (5.6.9)$$

reduced purely for clarity, with $\ell = x_{1d} - x_{1u}$ the distance between the junctions. As per the introduction to this section, the pole at $k_1 = \kappa_p$ exactly cancels the modal solution for $x_1 > x_{1d}$.

The second contribution, due to the forcing solution, is

$$\begin{aligned}\phi_{0m2}^{(s2)} &= \frac{Q_0(y_2) [\mathcal{P}_{01}^0 \phi_h(0; \kappa_1)] \phi_d(y_2; \kappa_1)}{2\pi i K_+(\kappa_1)} e^{-i\kappa_1 \ell} \int_{F_1} \frac{K_+(k_1) \phi_d(x_2; k_1)}{(k_1 - \kappa_1) D_p(k_1)} e^{-ik_1(x_1 - x_{1d})} dk_1 \\ &= \frac{Q_0(y_2) [\mathcal{P}_{01}^0 \phi_h(0; \kappa_1)] \phi_d(y_2; \kappa_1)}{2\pi i K_+(\kappa_1)} e^{-i\kappa_1 \ell} \int_{F_1} \frac{\phi_d(x_2; k_1)}{(k_1 - \kappa_1) K_-(k_1) D_h(k_1)} e^{-ik_1(x_1 - x_{1d})} dk_1\end{aligned}\quad (5.6.10)$$

Again, the pole at $k_1 = \kappa_1$ exactly cancels out the solution for $x_{1u} < x_1 < x_{1d}$. In both cases, the Wiener-Hopf kernel is the reciprocal of the hard-soft kernel, and as such the splitfunctions are the reciprocal of what would normally be used. Far downstream of the second junction, only the incident wave persists (assuming the decay of any critical-layer and acoustic contributions). The unstable mode doesn't propagate beyond the section of lining, and it therefore appears to have no strong effect on the solution. However, if the desire is to control far-field noise, then its contribution is noticeable. We have three scattering contributions computed: the scattering of the incident field off the first junction, and the scattering of the two propagating fields off the second junction. The far-field noise due to all three can be computed using the steepest descent method as previously. Importantly, if $\text{Im}(\kappa_u) > 0$, for large ℓ we expect a large amplification of the scattered solution.

The complete solution (up to the approximations made) is shown in figure 5.6.2, for $\ell = 5$. This is not sufficiently large for the critical-layer contribution from the first junction to decay, but shows the broad accuracy of the method, including the dominance on downstream scattering due to the unstable mode excited at the upstream junction. The second plot, figure 5.6.2b shows the solution only due to the first scattering point, with the excited modal contribution only shown between the junctions ($-5 < x_1 < 0$).

Far-field evaluation directly generalises §4.3.1. Neglecting the scaling functions

$$Q_0(y_2) [\mathcal{P}_{01}^0 \phi_h(0; \kappa_1)] \phi_d(y_2; \kappa_1) / 2\pi i,$$

common to all terms, outwith the boundary-layer we have an integral of the form

$$\int_{F_1} \left(I^{(s1)}(k_1) + I_1^{(s2)}(k_1) + I_2^{(s2)}(k_1) \right) e^{-ik_1 x_1 - \gamma_\infty x_2} \quad (5.6.11)$$

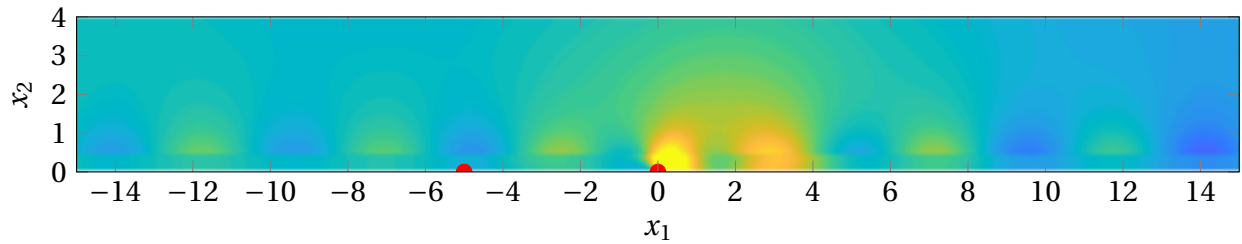
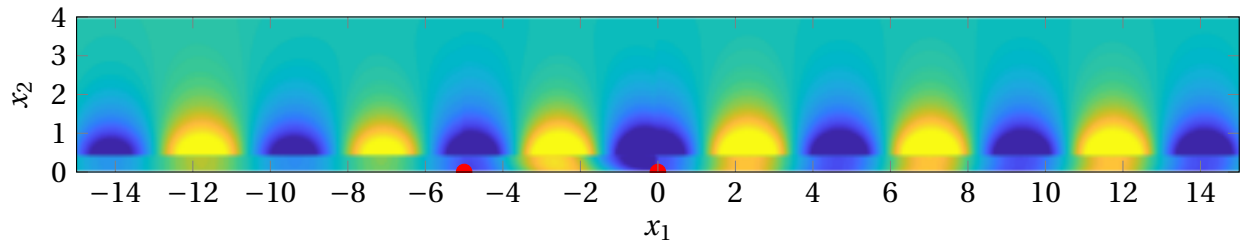
(a) $\text{Im}(p')$, all components(b) $\text{Im}(p')$, only scattering from upstream junction (colour scale enhanced by a factor of 5)

Fig. 5.6.2 Two junction scattering, subject to the approximation of ℓ large. There are two junctions, at $x_1 = -5$ and $x_1 = 0$. The background flow is a slipping parabolic profile ($U_0 = 0.3U_\infty$) with free-stream $Ma = 0.2$ and $\omega = 1$. The profile is unstable above the pressure-release wall. Discontinuities are visible in the full plot at $x_1 = 0$, due to the neglect of the critical-layer contribution. The second junction dominates the acoustics, even though the unstable mode (visible in the second plot for $x_1 \in (-5, 0)$, particularly for $x_2 < y_2$) still broadly appears weaker than the incident vortex sheet.

with

$$I^{(s1)} = \frac{e^{+ik_1x_{1u}}}{K_-(\kappa_1)(k_1 - \kappa_1)K_+(k_1)D_h(k_1)} \quad (5.6.12a)$$

$$I_1^{(s2)} = \frac{e^{-i\kappa_p\ell + ik_1x_{1d}} D_h(\kappa_p) K_-(\kappa_p)^2}{K_-(\kappa_1) D'_p(\kappa_p) (\kappa_p - \kappa_1) (k_1 - \kappa_p) K_-(k_1) D_h(k_1)} \quad (5.6.12b)$$

$$I_2^{(s2)} = \frac{e^{-i\kappa_1\ell + ik_1x_{1d}}}{K_+(\kappa_1)(k_1 - \kappa_1)K_-(k_1)D_h(k_1)} \quad (5.6.12c)$$

and far-field sound can be determined from evaluation of these functions at the saddle point k_s as per (4.4.1). Further, since each component can be dealt with separately, it is straightforward to determine the source of the far-field noise. This is done in figure 5.6.3 for two frequencies, with the same setup as the near-field plot in figure 5.6.2. The pressure-release wall is unstable in the first plot, figure 5.6.3a, and the restabilisation of the unstable mode, given by the yellow dotted line, dominates the far-field noise. In contrast, the contribution from both scattering points is comparable in the stable case, displayed in figure 5.6.3b, though the downstream junction is stronger than the upstream.

5.7 Discussion and conclusions

Inclusion of a realistic shear layer has permitted solution of the hard-soft scattering problem through well-developed Wiener-Hopf techniques. Even though computation of the various functions dependent on wall-normal coordinate x_2 must be done numerically, this does not prevent their use in the Wiener-Hopf framework, permitting relatively fast computation of the scattering from a boundary discontinuity, with complete control of the singularity at the junction via the entire function E . Further, by generalising the Briggs-Bers process to the Wiener-Hopf process, via the introduction of generalised Upper and Lower Half Planes, there is no ambiguity in whether a modal solution propagates upstream or downstream. This highlights a difficulty in the earlier work of Singh [93, 101], who suggested that the hard-soft and soft-hard transitions might have a different behaviour other than that suggested by reversal of space and time. This arose from the difficulty of identifying the half-plane of a mode in the incompressible limit, a difficulty that doesn't arise in the continuous shear, compressible case.

The most computationally expensive step is typically the factorisation of K , particularly when attempting to understand the far-field noise (for which most other evaluations are comparatively trivial). However, once the kernel has been computed along the separation contour, factorisation for any given values of k_1 follows from a simple matrix

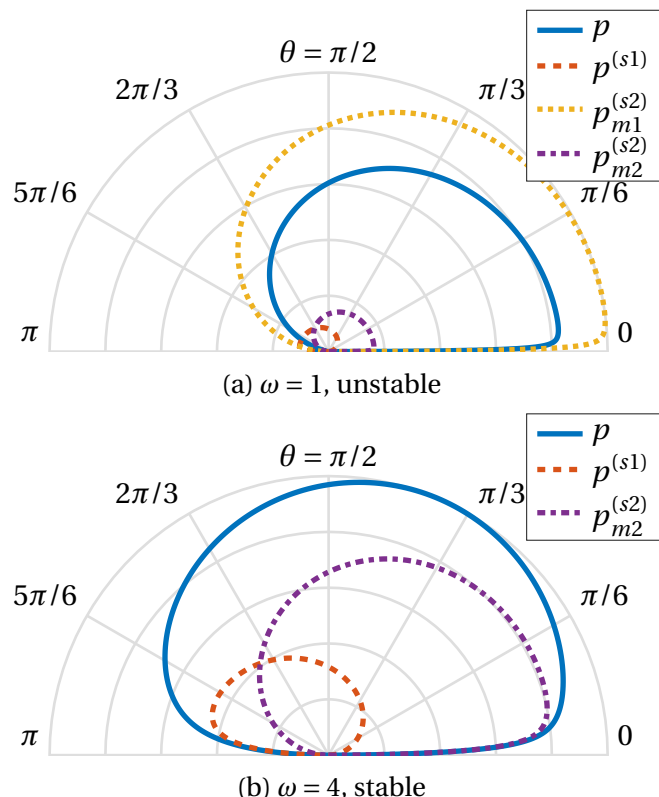


Fig. 5.6.3 $|p'|$ for the two-junction problem as per the previous figure, figure 5.6.2. The downstream unstable mode (represented by $p_{m1}^{(s2)}$) dominates the total acoustic field p , whereas in the stable case the non-surface mode contributions from both junctions ($p^{(s1)}$ and $p_{m2}^{(s2)}$ respectively) are broadly comparable (though pointed in opposite directions, as we would expect by the inversion of the junction type from hard-soft to soft-hard).

multiplication, and is thus relatively rapid. Therefore, once the factorisations have been computed once, it is straightforward to determine on any inversion contours of interest. In fact, since the x_2 -dependence of the scattered solution depends on the source location only in amplitude, if regarding this vortex sheet scattering as a Green's function, integration for generic vorticity distribution is straightforward to generalise, without revaluation of K_{\pm} or $\phi_d(x_2; k_1)$ being required, which will be exploited in the next chapter when the slightly more difficult trailing-edge scattering problem is tackled.

Previous work [89] has noted that the hard-soft scattering problem is essentially equivalent to the trailing-edge scattering problem. Whilst the distortion of radiation by boundary-layer shear has an effect on the radiation direction from the junction, this result remains true in this case, up to the caveat that the background profile is *symmetric* in the trailing-edge case, which will be discussed in the next chapter §6. This is most obvious from the $\sin(\theta/2)$ -type profile seen for low Mach numbers and long acoustic wavelengths, for which the effect of boundary-layer shear on radiation is least. This is exactly the pressure-scattering profile that would be expected at the trailing-edge of a hard-plate, and there are clear symmetry reasons why that should be the case as outlined below.

The most difficult step, mathematically, is determination of some function which, for large k_1 , behaves as the Wiener-Hopf kernel, but which can be factorised analytically. Typically, inspired by Noble [79] and Veitch [109], it is possible to compare behaviour with some product of complex powers of $(k_1 - k_{b\pm})$. Indeed, this is the approach taken by Singh [101]. This appears to provide an analytic result in this case, in fact exactly this product, though it suggests far-field sound behaving like $(x_1 + ix_2)^{\alpha}$ where α is non-real, which is curious on physical grounds. This is an artifact of the incompressible limit, however, for which the two acoustic branch points “pinch” together. This removes the possibility of defining a Wiener-Hopf strip, in this limit, and therefore the whole process breaks down. However, in this chapter we considered the solution for finite c_0 and allowed it to be large. As shown by figure 5.4.6, we get exactly the $\sin(\theta/2)$ dependence that we would expect from a trailing-edge, which is simply the symmetric extension of the hard-soft problem. Essentially, the complex powers in the far-field kernel asymptotic approximation are cancelled out when the numerical factorisation is computed, and do not persist into the final solution, though this numerical factorisation can only be computed when c_0 is finite (or under some other regularisation, e.g. k_3 non-zero).

The final section highlights how some essentially invisible surface mode can lead to a strong source of far-field acoustic noise. This highlights the importance of understanding the hydrodynamic forcing solution within the boundary-layer in the computation of the resulting far-field sound, which relates to the central thrust of this thesis, in understanding

how turbulence displacement within the boundary-layer can affect far-field noise. This is more explicitly evaluated in the next chapter §6, which considers scattering of a similar vortex sheet, and more generalised solutions, from a trailing-edge, through development of the methods in this chapter.

Chapter 6

Scattering from a sharp trailing-edge

Extending the analysis from the previous chapter, the scattering of a vortex sheet (and, in turn, more general vorticity distributions) from a sharp trailing-edge is computed. Previous models are enhanced by the inclusion of a background flow profile, which further allows consideration of asymmetric profiles (potentially with different free-stream velocities above and below the plate), and scattering from a lined plate.

6.1 Introduction

The problem of scattering from a trailing-edge, with the inclusion of background shear, has motivated this work from the outset. As outlined in the introduction, a variety of noise control methods exist which, through either the deflection of turbulence, or the shielding of the hard, scattering surface of the aerofoil, reduce surface pressure fluctuations near the trailing-edge, which in turn (either theoretically [3, 106] or, less frequently, experimentally measured [24]) reduces the far-field noise.

Due to both its importance in understanding the noise of sharp edges, and its mathematical elegance, the trailing-edge scattering problem is well-studied, with a variety of different models suggested for dealing with it. Most experimental work predicts far-field noise through the utilisation of an acoustic analogy, for example that of Ffowcs Williams and Hawking [35], which allows known acoustic perturbations in some control region to be propagated to the far-field, a similar approach to that used by Amiet [5]. These methods are useful numerically and experimentally, the former to overcome difficulties with propagating waves near the edge of computational domains, the latter to remove the need to directly measure far-field noise, instead utilising the measurable surface pressure spectrum. A variety of mathematical models exist, including varying degrees of physical complexity, for example that of Howe [56] and Ffowcs Williams and Hall [34].

The fundamental mechanism through which vorticity is converted into far-field noise is the (unsteady) Kutta condition [31] and is well-understood. It generalises the well-understood classical Kutta-Joukowsky hypothesis, which brings together the effect of viscosity on a steady flow about an aerofoil into a single condition at the trailing-edge, allowing unique choice of the circulation about the aerofoil. In *unsteady* aerodynamics it has similarly come to mean the removal of a velocity singularity at some distinguished point, typically a sharp trailing-edge or corner, or (as we saw in the previous chapter) at a boundary discontinuity. The Wiener-Hopf procedure gives the desired control of this tip singularity, and the analysis in the previous extension can be extended, incorporating background asymmetry and upstream lining, though if the upstream boundary is different on either side of the (flat) upstream plate, standard methods are typically unavailable.

This analysis makes the simplifying assumption, previously made throughout this work, that we are considering linearised perturbations to a parallel mean background flow. This is problematic in two obvious ways: firstly it doesn't allow the mean flow to develop rapidly as it passes the trailing-edge, as we assume it remains frozen as it passes over the trailing-edge. It therefore cannot satisfy realistic non-slip conditions upstream and be a developing wake downstream of the trailing-edge, and as such we generally focus on the case considered by Schuster [96] with the background slip velocity, U_0 , being non-zero, in an attempt to model both the upstream and downstream mean flow. It is possible to develop a theory in which the background flow is developing on some slow scale, which, locally to the trailing-edge, result in the same perturbation equations as being solved in this work. The parallel flow assumption also somewhat limits the geometries that can be considered, with any (no-penetration) conditions needing to be aligned with the background flow. This essentially limits consideration to flat plate geometries, though interesting trailing-edge geometries could be considered, for example serrations [7]. Again, through consideration of perturbations to slowly developing background flow this assumption can be relaxed somewhat to include more realistic aerofoil geometries [11].

This chapter begins by solving the scattering of a upstream gust by a sharp trailing-edge, on either a hard, or a pressure-release or a lined aerofoil. This idealised vortex sheet is then associated with vortical perturbations in the wake, and the scattering of a more general convected disturbance is generated in §6.3. This is then related to the central hypotheses of this work: the mechanism behind which deflection of turbulence reduces surface pressure, and in turn the transfer of this disturbance to far-field noise.

6.2 Scattering from a generic trailing-edge

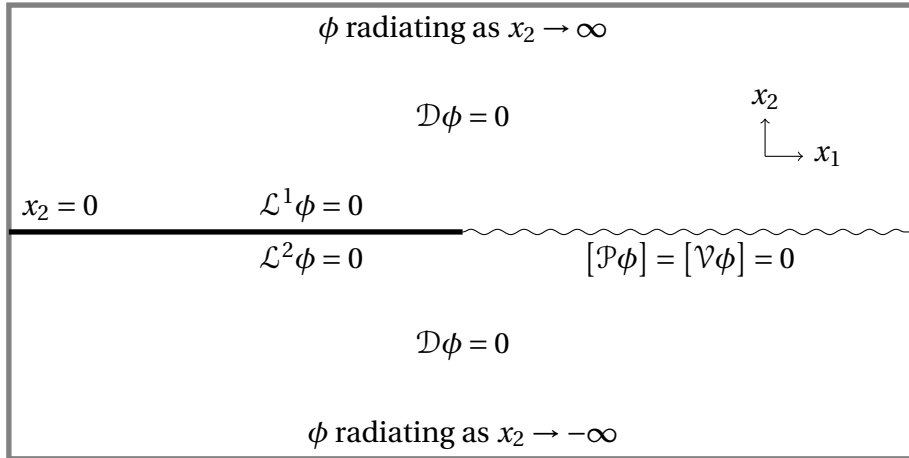


Fig. 6.2.1 The generic setup for a trailing-edge scattering problem, with square brackets denoting the jump across the wake for $x_1 > 0$. This can be thought of as two separate problems in $x_2 \gtrless 0$, linked across the wake.

Consider the setup in figure 6.2.1. A fixed background profile $U(x_2)$, defined for $-\infty < x_2 < \infty$, passes over the trailing-edge of a flat plate, defining \mathcal{D} as the adjoint Rayleigh operator as previously. We consider an incident vortex sheet perturbation, as in the preceding chapter, but any generic incident field $\phi^{(i)}$ perturbs the background flow, assumed to satisfy the upstream boundary condition on the top side of the plate. For definiteness, we define $\phi^{(i)} \equiv 0$ for $x_2 < 0$. If disturbances below the plate are of interest, the mapping $x_2 \mapsto -x_2$ allows consideration of this case.

6.2.1 Scattering from a generic, harmonic, incident field

The scattered field $\phi^{(s)}$ satisfies the governing equation for the potential, $\mathcal{D}\phi^{(s)} = 0$ and an outgoing radiation condition. On the plate, $x_2 = 0$ and $x_1 < 0$, we have

$$\mathcal{L}^1 \phi^{(s)} = 0 \quad x_2 = 0^+ \quad (6.2.1a)$$

$$\mathcal{L}^2 \phi^{(s)} = 0 \quad x_2 = 0^- \quad (6.2.1b)$$

for generic linear operators \mathcal{L}^j , though more precision will be needed later. Downstream of the the plate a wake develops. Across the wake, we insist on continuity of velocity and of pressure, the former a proxy for continuity of particle displacement (when background flow U is continuous across the wake), which is exactly the setup considered for wake disturbances in earlier chapters, §3.7 and §4.6. Explicitly, we have, for $x_1 > 0$ (arguments

indicating location of x_2 evaluation)

$$\mathcal{P}^{0^+}\phi^{(s)}(0^+) - \mathcal{P}^{0^-}\phi^{(s)}(0^-) = -\mathcal{P}^{0^+}\phi^{(i)}(0^+) \quad (6.2.2a)$$

$$\mathcal{V}^{0^+}\phi^{(s)}(0^+) - \mathcal{V}^{0^-}\phi^{(s)}(0^-) = -\mathcal{V}^{0^+}\phi^{(i)}(0^+). \quad (6.2.2b)$$

As in the previous chapter, we can take half-range transformations of these conditions. For clarity, we define Φ_1 to be the Fourier transform of $\phi^{(s)}$, evaluated at $x_2 = 0^+$, and similarly Φ_2 of $\phi^{(s)}$ evaluated at $x_2 = 0^-$. Further, $\mathcal{P}^{1,2} = \mathcal{P}^{0^\pm}$, and the same for \mathcal{V} . Essentially we reduce the problem into two regions: 1 denoting $x_2 > 0$ and 2 denoting $x_2 < 0$, linked across the wake. Taking half-range transforms (and assuming time-harmonic dependence) gives

$$\mathcal{L}_{01}^1 \Phi_1^- = 0 \quad (6.2.3a)$$

$$\mathcal{L}_{01}^2 \Phi_2^- = 0 \quad (6.2.3b)$$

$$\mathcal{P}_{01}^1 \Phi_1^+ - \mathcal{P}_{01}^2 \Phi_2^+ = -I_p^+ \quad (6.2.3c)$$

$$\mathcal{V}_{01}^1 \Phi_1^+ - \mathcal{V}_{01}^2 \Phi_2^+ = -I_v^+ \quad (6.2.3d)$$

with I_p and I_v respectively the Fourier transformed pressure and wall-normal velocity perturbations due to the incident field $\phi^{(i)}$. Finally, we note the radiation condition implies the solution decays as $x_2 \rightarrow \pm\infty$. Defining $\phi_{1,2}$ to be the decaying solution as $x_2 \rightarrow \pm\infty$, normalised so that $\phi_{1,2} \rightarrow \exp(\mp\gamma_\pm x_2)$ as per §4.6, we must have

$$\phi^{(s)} = \begin{cases} A_1(k_1)\phi_1(x_2; k_1) & x_2 > 0 \\ A_2(k_1)\phi_2(x_2; k_1) & x_2 < 0. \end{cases} \quad (6.2.4)$$

and so $\Phi_j = A_j(k_1)\phi_j(0; k_1)$ for $j = 1, 2$.

Using (6.2.3), we find four equations for A_j in terms of unknown functions, namely

$$A_1 \mathcal{L}_{01}^1 \phi_1 = \mathcal{L}_{01}^1 \Phi_1^+ \equiv B_1^+, \quad (6.2.5a)$$

$$A_2 \mathcal{L}_{01}^2 \phi_2 = \mathcal{L}_{01}^2 \Phi_2^+ \equiv B_2^+, \quad (6.2.5b)$$

$$A_1 \mathcal{P}_{01}^1 \phi_1 - A_2 \mathcal{P}_{01}^2 \phi_2 = \mathcal{P}_{01}^1 \Phi_1^- - \mathcal{P}_{01}^2 \Phi_2^- - I_p^+ \equiv C_p^- - I_p^+, \quad (6.2.5c)$$

$$A_1 \mathcal{V}_{01}^1 \phi_1 - A_2 \mathcal{V}_{01}^2 \phi_2 = \mathcal{V}_{01}^1 \Phi_1^- - \mathcal{V}_{01}^2 \Phi_2^- - I_v^+ \equiv C_v^- - I_v^+. \quad (6.2.5d)$$

All ϕ_j are evaluated at $x_2 = 0$, above or below the plate or wake as appropriate.

We have four equations and six unknowns: the coefficients $A_{1,2}$, the downstream extension of the boundary conditions $B_{1,2}^+$, and the pressure and velocity jumps in scattered

solution across the plate, $C_{p,v}^-$. Eliminating $A_{1,2}$ gives two coupled Wiener-Hopf equations, namely

$$B_1^+ \frac{\mathcal{P}_{01}^1 \phi_1}{\mathcal{L}_{01}^1 \phi_1} - B_2^+ \frac{\mathcal{P}_{01}^2 \phi_2}{\mathcal{L}_{01}^2 \phi_2} = C_p^- - I_p^+, \quad (6.2.6a)$$

$$B_1^+ \frac{\mathcal{V}_{01}^1 \phi_1}{\mathcal{L}_{01}^1 \phi_1} - B_2^+ \frac{\mathcal{V}_{01}^2 \phi_2}{\mathcal{L}_{01}^2 \phi_2} = C_v^- - I_v^+. \quad (6.2.6b)$$

Whilst this equation can be written in the form $\mathbf{KB}^+ = \mathbf{C}^- - \mathbf{I}^+$, a matrix equation which exactly extends (5.2.11), factorising the matrix \mathbf{K} is non-trivial. We therefore make the assumption that the upstream boundary condition corresponds to some impedance condition \mathcal{L}^Z , with Z the same on both sides of the plate. In the asymmetric case, this is *not* setting $\mathcal{L}^1 = \mathcal{L}^2$, since the shear (and therefore \mathcal{P}) may be different for $x_2 = 0^\pm$. Explicitly,

$$\mathcal{L}_{01}^Z = i\omega Z \mathcal{V}_{01} - C_0 \mathcal{P}_{01}. \quad (6.2.7)$$

If we impose this boundary condition above and below the plate, then trivially the quantity $\mathcal{L}^Z \phi$ is continuous across the plate, vanishing on both sides. Further, since \mathcal{L} is a linear combination of pressure and (wall-normal) velocity operators, and both these are continuous across the wake, we end up with the strong condition that

$$\mathcal{L}_{01}^1 \Phi_1 - \mathcal{L}_{01}^2 \Phi_2 = 0. \quad (6.2.8)$$

Via (6.2.5a) and (6.2.5b), this is simply the condition that $B_1^+ = B_2^+$. A similar relationship could be written down linking C_p^- and C_v^- , but it is worth noting that now we have a decoupled Wiener-Hopf system, namely

$$\left(\frac{\mathcal{P}_{01}^1 \phi_1}{\mathcal{L}_{01}^1 \phi_1} - \frac{\mathcal{P}_{01}^2 \phi_2}{\mathcal{L}_{01}^2 \phi_2} \right) B_1^+ = C_p^- - I_p^+. \quad (6.2.9)$$

This is appropriate for $Z \neq 0$, including the hard-wall case, but it is trivial in the case $Z = 0$ and the alternative representation with $\mathcal{P} \rightarrow \mathcal{V}$ should be used. The Wiener-Hopf kernel can be simplified:

$$K = \left(\frac{\mathcal{P}_{01}^1 \phi_1}{\mathcal{L}_{01}^1 \phi_1} - \frac{\mathcal{P}_{01}^2 \phi_2}{\mathcal{L}_{01}^2 \phi_2} \right) = i\omega Z \frac{\mathcal{P}_{01}^1 \phi_1 \mathcal{V}_{01}^2 \phi_2 - \mathcal{V}_{01}^1 \phi_1 \mathcal{P}_{01}^2 \phi_2}{\mathcal{L}_{01}^1 \phi_1 \mathcal{L}_{01}^2 \phi_2}. \quad (6.2.10)$$

Previously, the Wiener-Hopf kernel was written cleanly in terms of dispersion functions, and it can be again here. We have previously seen the wake dispersion function

$$D_w = \mathcal{P}_{01}^1 \phi_1 \mathcal{V}_{01}^2 \phi_2 - \mathcal{V}_{01}^1 \phi_1 \mathcal{P}_{01}^2 \phi_2, \quad (6.2.11)$$

and, defining the impedance dispersion function for the flow above/below the plate with a superscript (1, 2) respectively, we have

$$K = i\omega Z \frac{D_w}{D_Z^1 D_Z^2}. \quad (6.2.12)$$

As per the previous chapter, factorisation allows solution of this problem, up to some (possibly known) entire function E , namely (for $j = 1, 2$, for which respectively define $\bar{j} = 2, 1 = 3 - j$)

$$A_j = \frac{B^+}{D_Z^j} = \frac{1}{D_Z^j K_+} \left(E - \left(\frac{I_p^+}{K_-} \right)^+ \right) \quad (6.2.13a)$$

$$= \frac{D_Z^{\bar{j}} K_-}{i\omega Z D_w} \left(E - \left(\frac{I_p^+}{K_-} \right)^+ \right). \quad (6.2.13b)$$

These two expressions are equivalent. The former is appropriate for $x_1 < 0$, with non-analyticity in the UH $k_1 P$ driven by zeros of D_Z^j , and thus surface modes. Conversely, for $x_1 > 0$ the latter expression is more useful, with modal solutions arising as roots of the wake dispersion relation D_w , as would be expected.

The entire function vanishes if we insist the pressure jump across the tip of the plate is at worst integrably singular, which controls the possible size of C_p^- as $k_1 \rightarrow \infty$. This analysis, at least for scattering from either a hard or a soft plate, identically follows §5.3.2, due to the similarities in the kernel. We can therefore write down the exact scattered solution in the form of a Fourier inversion of $A_j \phi_j$, and computation proceeds exactly as in the preceding chapter (though with the extension of different representations for $x_2 \gtrless 0$).

6.2.2 The Green's function: incident vortex sheet

We now consider explicitly the incident vortex sheet, either for its own merits or from which to construct a more general vortical solution. As per §5, we therefore have

$$I_p^+ = -\frac{1}{i(k_1 - \kappa_1)} [Q_0(y_2)\phi_d(y_2; \kappa_1)\mathcal{P}_{01}\phi_Z(0; \kappa_1)] \equiv -\frac{I_0}{i(k_1 - \kappa_1)}. \quad (6.2.14)$$

We now define $g = g^{(i)} + g^{(s)}$ to be exactly the solution to this problem, as a function of y_2 and $\kappa(y_2)$, so that $g^{(i)}$ gives rise to the above forcing (with an explicit choice of Q_0 noted in §6.3 below). We have four exact representations for the scattered solution depending on the signs of x_1 and x_2 , namely

$$g^{(s)} = \frac{I_0(y_2)}{2\pi i K_-(\kappa_1)} \int_{F_1} \frac{\phi_1(x_2; k_1)}{D_Z^1(k_1)} \frac{e^{-ik_1 x_1}}{K_+(k_1)(k_1 - \kappa_1)} dk_1 \quad x_1 < 0, x_2 > 0 \quad (6.2.15a)$$

$$g^{(s)} = \frac{I_0(y_2)}{2\pi i K_-(\kappa_1)} \int_{F_1} \frac{\phi_2(x_2; k_1)}{D_Z^2(k_1)} \frac{e^{-ik_1 x_1}}{K_+(k_1)(k_1 - \kappa_1)} dk_1 \quad x_1 < 0, x_2 < 0 \quad (6.2.15b)$$

$$g^{(s)} = \frac{I_0(y_2)}{(2\pi i)(i\omega Z)K_-(\kappa_1)} \int_{F_1} \frac{\phi_1(x_2; k_1)D_Z^2(k_1)}{D_w(k_1)} \frac{K_-(k_1)e^{-ik_1 x_1}}{(k_1 - \kappa_1)} dk_1 \quad x_1 > 0, x_2 > 0 \quad (6.2.15c)$$

$$g^{(s)} = \frac{I_0(y_2)}{(2\pi i)(i\omega Z)K_-(\kappa_1)} \int_{F_1} \frac{\phi_2(x_2; k_1)D_Z^1(k_1)}{D_w(k_1)} \frac{K_-(k_1)e^{-ik_1 x_1}}{(k_1 - \kappa_1)} dk_1 \quad x_1 > 0, x_2 < 0. \quad (6.2.15d)$$

F_1 is, as usual, the causal deformation of the real axis as $\text{Im}(\omega) \rightarrow 0$ from below and, as before, can be deformed to the relevant steepest descent contours (dependent on whether $x_1 \gtrless 0$), picking up contributions from the poles of the dispersion relationships, and from the forcing wavenumber κ_1 . Further, the branch cut along the critical-layer always contributes for positive x_1 (assuming $U > 0$ throughout). It is worth being explicit about this contribution.

Let the zeros of D_Z^1 be labelled $\kappa_{Zj}^{1\pm}$, with N_Z^{1+} in the gUH k_1 P and N_Z^{1-} in the gLHK $_1$ P, so that j runs from 1 to $N_Z^{1\pm}$ respectively. Similarly, we label the zeros of D_Z^2 as $\kappa_{Zj}^{2\pm}$, and the zeros of the wake κ_{wj}^\pm . Which half-plane they lie in is determined by the Briggs-Bers procedure, and in practice defines the generalised half-planes. Explicitly picking up the

modal contributions, we have for example for $x_1, x_2 > 0$, (so using (6.2.15c))

$$\begin{aligned} g^{(s)} = & \frac{I_0(y_2)}{(2\pi i)(i\omega Z)K_-(\kappa_1)} \left(\int_{C_{L1}} + \int_{C_{CL}^1} \right) \frac{\phi_1(x_2; k_1) D_Z^2(k_1)}{D_w(k_1)} \frac{K_-(k_1) e^{-ik_1 x_1}}{(k_1 - \kappa_1)} dk_1 \\ & - \frac{I_0(y_2)}{i\omega Z K_-(\kappa_1)} \sum_{j=1}^{N_w^-} \frac{\phi_1(x_2; \kappa_{wj}^-) D_Z^2(\kappa_{wj}^-)}{D'_w(\kappa_{wj}^-)} \frac{K_-(\kappa_{wj}^-)}{(\kappa_{wj}^- - \kappa_1)} e^{-i\kappa_{wj}^- x_1}. \quad (6.2.16) \end{aligned}$$

The contour $C_{L,U}^{1,2}$ is the steepest descent contour, a function of observer angle $\theta = \tan^{-1}(x_2/x_1)$, based on the free-stream velocity above the plate (superscript 1) or below the plate (superscript 2), which might differ if there is asymmetry. The (L, U) subscript indicates it is in either the lower or upper half k_1 plane respectively, directly corresponding to $x_1 \gtrless 0$. The critical layer integral $C_{CL}^{1,2}$ loops the branch cut from $k_1 = \omega/U_0$ to $\omega/U_\infty^{1,2}$, with $U_\infty^{1,2}$ respectively the free-stream velocity above or below the plate. The critical-layer integral contains the modal contribution from $k_1 = \kappa_1$.

The above expression is *not* uniformly correct, given it assumes that deformation from F_1 to C_L^1 picks up all modal contributions. For some observer angles θ , particularly steep angles with $x_2 \gg x_1$, the steepest descent contour may remain above some modal contributions. Recalling (4.3.21), describing the steepest descent in terms of parameter t running from -1 to 1 , in terms of Mach shifted angle $\Theta = \tan^{-1}(\beta x_2/x_1)$, the steepest descent contours look like complex rays as $t \rightarrow \pm 1$.

For $x_1, x_2 > 0$ (so $\cos(\Theta) > 0$, $\Theta = (0, \pi/2)$), the rays make an angle of $-\pi/2 \pm \Theta$ with the real axis, so that for $x_2 \gg x_1$, they are asymptotically the real axis, and for $x_1 \gg x_2$ they are either side of the negative imaginary axis (and thus looping the acoustic branch cut). Therefore a zero with complex argument ϕ is picked up through the steepest descent deformation if approximately $-\pi/2 + \Theta < \phi$, so that $\Theta < \phi - \pi/2$. Since the steepest descent contour rapidly asymptotes to this ray, this is a good approximation of whether or not the contribution from this pole should be included in the integral. In the far-field each unstable disturbance is therefore confined to a limited segment extending from the origin, with well-understood width. Since the free-stream velocity above the plate, U_∞^1 , differs from that below the plate, U_∞^2 , this scattered, modal segment may be asymmetric for larger Mach numbers, given the Mach shift factor β in the definition of Θ .

6.2.3 Simplification in the symmetric case

In general, we can separate the background profile (and analogously the background speed of sound) as

$$U(x_2) = \begin{cases} U_1(x_2) & x_2 > 0 \\ U_2(x_2) & x_2 < 0 \end{cases} \quad (6.2.17)$$

preserving the consistency of (1, 2) denoting $x_2 \gtrless 0$. The wake dispersion relationship simplifies greatly if the background profile U is symmetric, so that $U_1(x_2) = U_2(-x_2)$, as noted in §3.7, where $\phi_2(-x_2) = \phi_1(x_2) = \phi_d(x_2)$, and so

$$D_w = -2\mathcal{P}_{01}\phi_d\mathcal{V}_{01}\phi_d. \quad (6.2.18)$$

We also have $D_Z^1 = D_Z^2$ and as such the scattered solution is symmetric in $x_2 \mapsto -x_2$, as might be expected.

In the case of a rigid plate upstream with a no-penetration condition (the limit $Z \rightarrow \infty$), $D_Z \rightarrow i\omega Z D_h$ and the Wiener-Hopf kernel is exactly

$$K = \frac{1}{i\omega Z} \frac{2D_p}{D_h} \quad (6.2.19)$$

and, by putting the $i\omega Z$ into K_- and noting it will always cancel, we can consider the reduced kernel

$$K^* = \frac{2D_p}{D_h}. \quad (6.2.20)$$

This almost exactly reproduces the hard-soft scattering kernel seen in §5.3, save for the factor of 2, which scales the downstream solution by a factor of half. This is not a surprise. If we were to consider this wake problem with two vortex sheets, above and below the plate, with opposite strengths, then the induced pressure on $x_2 = 0$ would exactly cancel, and we would be left with exactly the hard-soft scattering problem defined on $x_2 > 0$. Similar image arguments could be made for the other problems considered in the previous chapter. With this in mind, it is prudent to focus primarily on the asymmetric case in this chapter, which genuinely generalises the previous work.

6.2.4 Kernel far-field behaviour and factorisation

The work in the previous chapter highlights the majority of the difficulties faced when factorising the kernel, with the large k_1 -asymptotics being the most important thing to determine. There are multiple cases to consider.

$Z = \infty$. The rigid plate case will be the most used, where we consider the rescaled kernel

$$K^* = \frac{D_w}{D_h^1 D_h^2} = \frac{D_p^1}{D_h^1} - \frac{D_p^2}{D_h^2}. \quad (6.2.21)$$

A little care is needed with signs, compared to earlier dispersion relationships, as D_h^2 , for example, is defined for a background flow beneath the plate (unlike previous definitions of D_h for a flow above a boundary). With this, we note that K^* is simply the sum of two hard-soft kernels, respectively for $U_1(x_2)$ and for $U_2(-x_2)$, the far-field asymptotics of which have already been determined. Importantly, they are functions of background flow parameters at the wall only, and so if $U_0 \neq 0$

$$K^* \sim \frac{2C_0}{\gamma_0} \sim \mp \frac{2iU_0}{\beta_0}. \quad (6.2.22)$$

If, however, $U_0 = 0$, we've seen previously that the far-field behaviour of the hard-soft kernel is a function of wall shear. Defining then $\sigma_1 = U'_1(0)$ and $\sigma_2 = U'_2(0)$ (so that, for example, if the profile is symmetric $\sigma_1 = -\sigma_2$ and if the shear is continuous $\sigma_1 = \sigma_2$), then

$$K^* \sim \frac{2i}{|k_1|} \left(\frac{1}{2}(\sigma_1 - \sigma_2) \mp \omega \right), \quad (6.2.23)$$

both evaluated as $k_1 \rightarrow \pm\infty$. The factor of 2 has no effect on the factorisation procedure, which can therefore proceed exactly as in §5.3, redefining the wall shear

$$\sigma_0 = (\sigma_1 - \sigma_2)/2 \quad (6.2.24)$$

as the *average* of the shears seen above and below the plate (by flipping the sign of σ_2 by considering $U_2(-x_2)$).

$Z = 0$. For a pressure-release plate, attempting to use the same method as before simply gives $K = 0$. This is unsurprising, as $I_p^+ = 0$ and the scattered solution cannot be determined. Instead, replacing I_p with I_v by using (6.2.5d) instead of (6.2.5c) as the basis for determining the Wiener-Hopf equation, we have kernel (scaling out any factors of Z , which will cancel in the limit $Z \rightarrow 0$)

$$K^* = \frac{D_h^1}{D_p^1} - \frac{D_h^2}{D_p^2}. \quad (6.2.25)$$

Since this is just the sum of the soft-hard kernels above and below the plate, the far-field behaviour is straightforwardly

$$K^* \sim \frac{2\gamma_0}{C_0} \sim \pm \frac{2i\beta_0}{U_0} \quad (6.2.26)$$

for $U_0 \neq 0$, and

$$K^* \sim -i|k_1| \left(\frac{1}{\sigma_1 \mp \omega} + \frac{1}{-\sigma_2 \mp \omega} \right) = -2i|k_1| \frac{\sigma_0 \mp \omega}{(\sigma_1 \mp \omega)(-\sigma_2 \mp \omega)} \quad (6.2.27)$$

for $U_0 = 0$, both in the limits $k_1 \rightarrow \pm\infty$. σ_0 is as defined above in (6.2.24).

We note in the symmetric case indicated above, the kernel is simply twice the hard-soft kernel for the flow defined on $x_2 > 0$, and there is essentially a reduction to the soft-hard scattering problem. The symmetry could allow for more complicated flow profiles to be solved as done by Rawlins [83], who considered a plate with different boundary conditions above and below.

Z finite, non-zero, $U_0 \neq 0$. If upstream impedance Z is finite and non-zero and the background flow is slipping, for large k_1 we have

$$D_Z^j \sim -C_0 D_p^j \quad (6.2.28)$$

The kernel therefore appears to vanish for large k_1 . However, we can be careful, and if we note

$$D_w \sim 2D_p D_h \quad (6.2.29)$$

for large k_1 , where D_p and D_h are the large k_1 -behaviour which depends only on the background flow velocity at $x_2 = 0$. Hence,

$$K \sim \frac{2i\omega Z D_h}{C_0^2 D_p} \quad (6.2.30)$$

which does indeed vanish for large k_1 , though we have a stronger handle on the behaviour, and we can write down

$$K \sim \frac{2i\omega Z \gamma_0}{C_0^3} \sim \pm \frac{2\beta_0(i\omega Z)}{U_0^3 |k_1|^2}. \quad (6.2.31)$$

Z finite, non-zero, $U_0 = 0$. Conversely, if $U_0 = 0$, the dispersion function $D_Z \sim i\omega D_h$. This reduces to the problem considered above, up to some factors of $i\omega Z$, and

$$K \sim \frac{1}{i\omega Z} \frac{2i}{|k_1|} (\sigma_0 \mp \omega) \quad (6.2.32)$$

as per (6.2.23). None of the above collection of far-field behaviours present any new problems with factorisation, up to checking the winding number along the contour in the multiplicative factorisation of K , as previously.

6.2.5 Near- and far-field inversion for $g^{(s)}$

To demonstrate the validity of this solution, the scattered Green's function is numerically computed in the near-field, and the resulting far-field sound is then determined. Without loss of generality the hard-plate case is focused on, which reduces the mode-finding required (as the upstream boundary is stable) but otherwise has little effect on the numerics, the main aim here being to show the decomposition of the solution does, in fact, constitute the scattered solution above and below the plate, particularly if we have an asymmetric flow field.

With that in mind, near-field inversion is computed for a slightly asymmetric background profile, consisting of a parabola for both $x_2 \geq 0$, so that the resultant shear is smooth at the edge of the boundary-layer. In both cases, the boundary-layer thickness $\delta = 1$ with source at $x_2 = y_2 = 0.5$, and, scaling all velocities by the free-stream velocity above the plate, the slip velocity is 0.3 and the free-stream velocity below the plate is 1.5. For frequency $\omega = 1$, the resultant downstream wake is unstable, with a complex conjugate pair of zeros of D_w , explicitly at $\kappa_w = 0.8720 \pm 0.2618i$. This has been written down explicitly to highlight that the real part of this corresponds to a background flow velocity only beneath the plate, since $\omega/U_\infty^+ = 1$ is larger than this. This intuitively suggests the modal solution should dominate beneath the plate, if there is some physical correspondence in location. A selection of outputs is shown in figure 6.2.2, decoupling the effect of the vortex sheet in the total solution from the purely scattered solution, and as predicted the growing wake mode is centred on $x_2 < 0$. Some other points to note include that the vertical velocity v'_0 induced solely by the vortex sheet (upstream of the trailing-edge) is very small for $x_2 \in (0, 0.5)$, though the corresponding pressure fluctuations, which drive the scattering, do not.

It is hard to see the purely acoustic (steepest descent driven) fluctuations on these plots, and so figure 6.2.3 shows an enlarged plot of only this contribution, approximating the steepest descent contours by fixed hyperbolae, which do not vary with observer location. Slight discontinuities are visible across $x_1 = 0$, which is to be expected as the modal contributions are excited here but not included in this component of the solution. For large $|\mathbf{x}|$ a vaguely cardioid-type directivity can be seen, which will be analysed directly below.

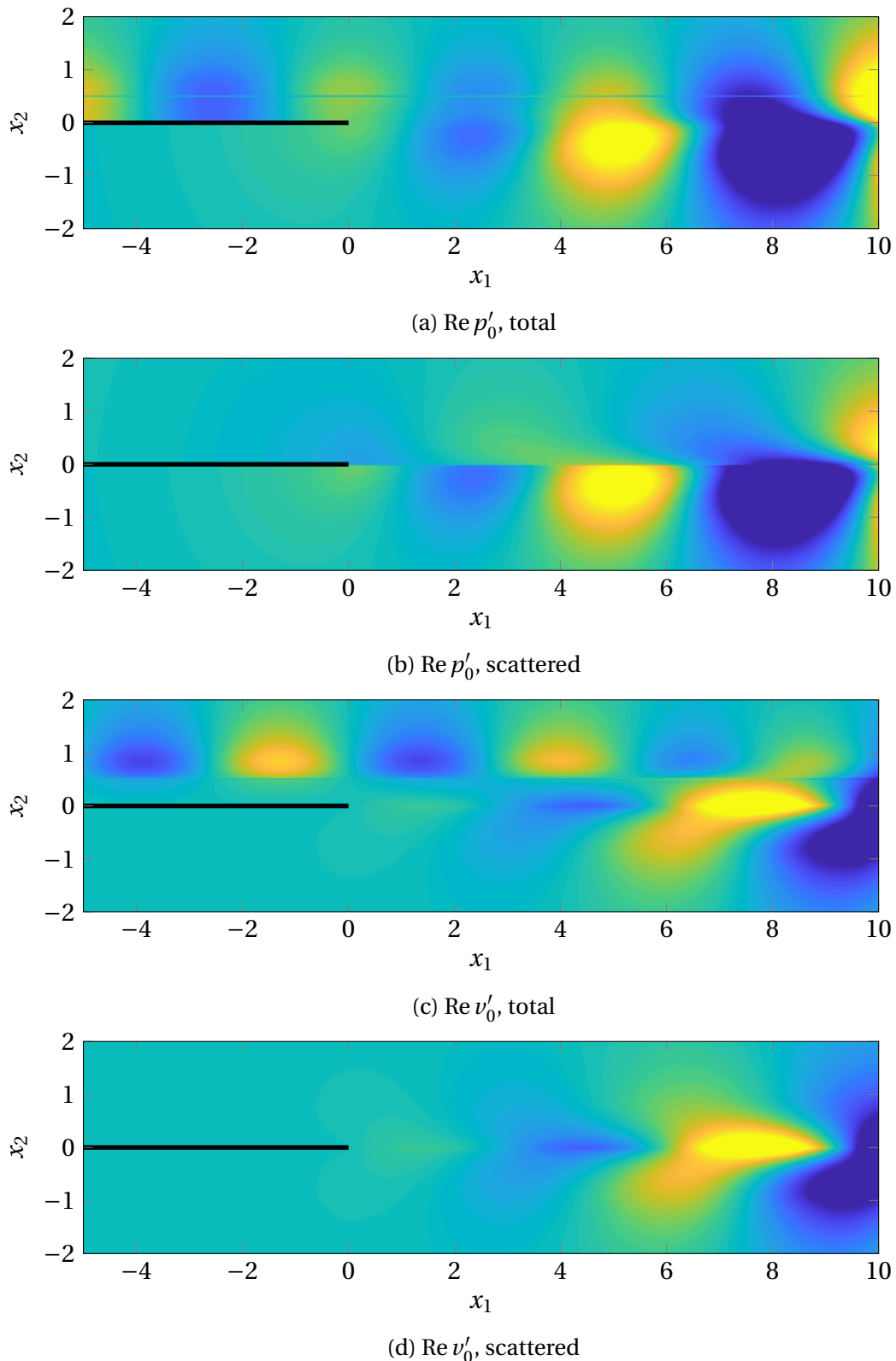


Fig. 6.2.2 Pressure and wall-normal velocity perturbations due to an upstream incident vortex sheet on the trailing-edge of a flat plate, as described in the text.

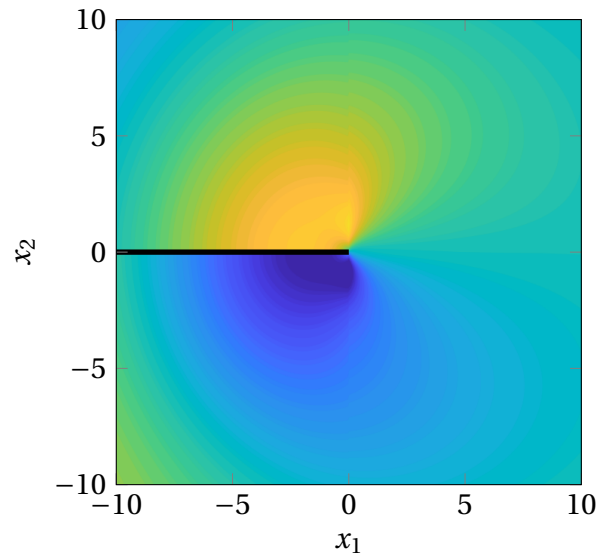


Fig. 6.2.3 The purely acoustic component of the scattered field as per the previous setup, described in the text.

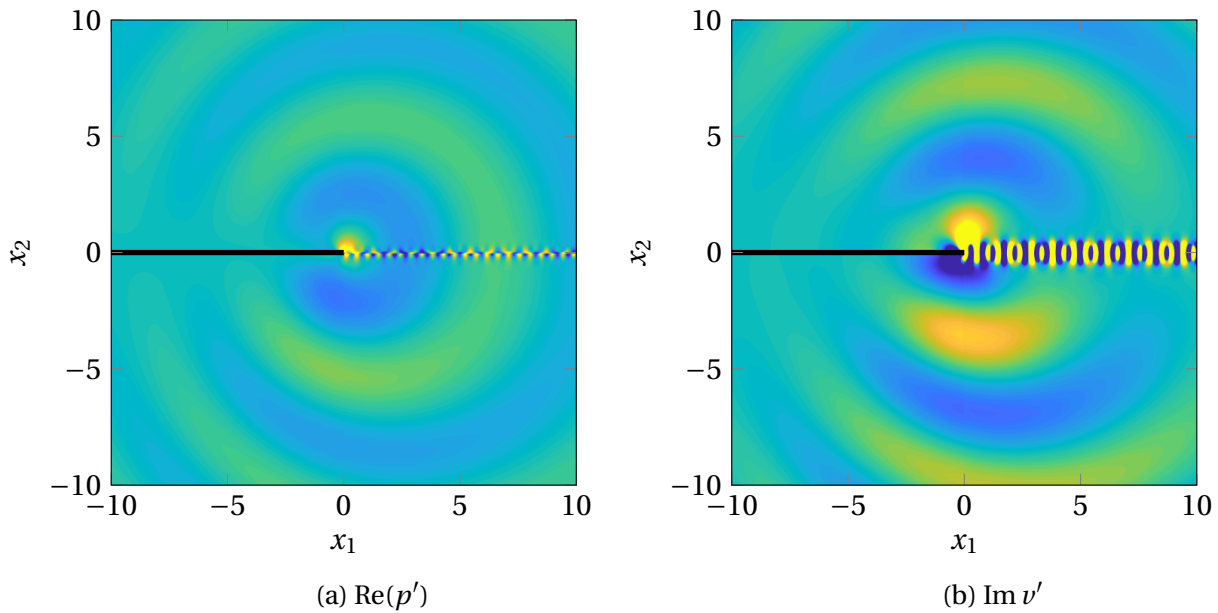


Fig. 6.2.4 Scattered component of solution for $Z = 1 - i$ at frequency $\omega = 5$, over a slightly asymmetric profile consisting of constant shear on in both boundary layers, as indicated in the text.

The above analysis considers only a hard-wall. Since the model has been developed for a lined wall, the case $Z = 1 - i$ is considered for a profile with constant shear (described below) above and below the plate. For frequency $\omega = 5$, this leads to neutrally stable modes propagating into the wake (and no modes propagating upstream, in this case), and the near field inversion proceeds in the same way as previously. The scattered pressure and velocity fields are shown, with here $U_\infty^+ = 1$, $U_\infty^- = 1.5$ and $U_0 = 0.3$, with $c_0 = 5$ throughout. Both above and below the plate boundary-layer thickness is $\delta^\pm = 1$. At this higher frequency, the acoustic radiation can clearly be seen, and in particular, for this value of Z , it is broadly orientated downstream. Further, in this case we should note that the perturbations are singular at the tip, $x_1 = x_2 = 0$, showing $x_1^{-1/2}$ type behaviour. This is integrably singular, as the analysis suggested. The Kutta condition does not completely eliminate this singularity, which follows from the large k_1 -behaviour of the Wiener-Hopf kernel in this case. In this case, uniquely, $K \sim k_1^{-2}$ as $|k_1| \rightarrow \infty$. The near tip behaviour in physical space is linked to the far-field behaviour in wavenumber space, exactly as per §5.2, and $1/K_+$ grows in this case, which ensures the Fourier inversion integral does not converge at $x_1 = 0$.

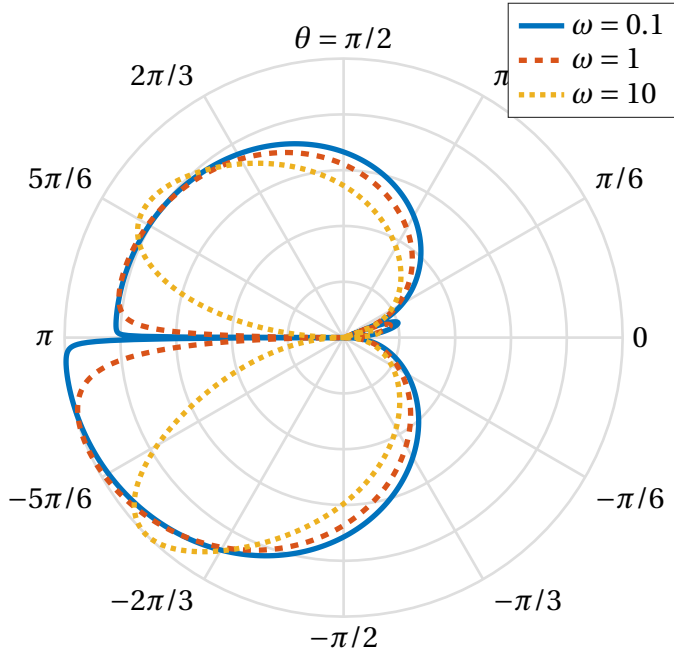


Fig. 6.2.5 With slightly asymmetric profile as per the previous setup, the far-field directivity (here, $|p'|$, normalised by the maximal value), is computed as frequency is varied.

The directivity can be analysed in the normal way, as per the directivity when the wake profile was considered earlier in §4.6, with saddle points based on the free-stream

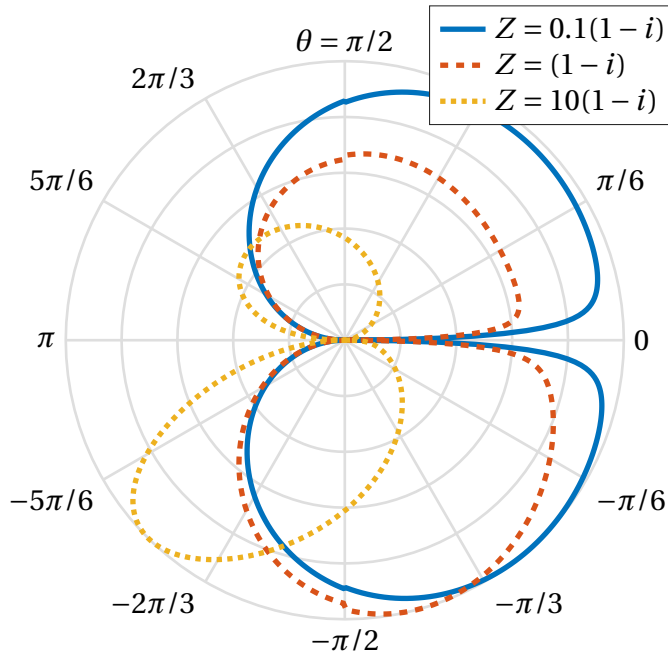


Fig. 6.2.6 At frequency $\omega = 5$, with a symmetric parabolic setup as per the flow above the plate in the previous figure, the impedance Z is varied.

flow above and below the shear layer. This is done for the case considered above as the frequency is varied (and thus both hydrodynamic and acoustic wavelengths) and the resulting directivity is plotted (normalised by the maximal value in θ) in figure 6.2.5. There are no particular surprises when comparing with either scattering from a junction, as per the preceding section, or with the point source in unbounded flow. The lower region, with higher free-stream velocity, is generally louder. As with the wake case, there is an extra lobe formed due to the asymmetry, here pointing downstream and slightly towards the direction with the lower free-stream velocity. On both sides, as the frequency is lowered and the acoustic wavelength increases, a cardioid-type, $\sin(\theta/2)$ profile is attained, though with different magnitudes above and below the plate. As the frequency is raised, this moves towards a single, upstream-orientated, lobe.

Similarly, we consider the variation of Z in figure 6.2.6. This setup considers a symmetric profile, with parabolic slipping profiles both above and below the wake, with $U_0 = 0.3U_\infty$. This choice of symmetric profile highlights the fundamental asymmetry of the scattering direction for finite, non-zero, Z . In both the limit $Z \rightarrow \infty$ and $Z \rightarrow 0$, a symmetric profile is attained. However, for finite Z , the profile is non-symmetric, in this case the radiation profile favours the region beneath the wake, on the opposite side of the plate to the forcing term. That we have asymmetry is not in itself a surprise, with the

symmetry in the hard-wall and pressure-release trailing-edge cases arising directly from the reduction, in these cases, of the problem to either the hard-soft or soft-hard scattering problem (up to a factor of two), with either symmetry or asymmetry in scattered pressure across the wake.

For $|Z|$ large, the solution tends towards the cardioid structure, orientated downstream, as seen in figure 6.2.5. Conversely, for small $|Z|$ this profile is flipped. As noted above, this follows from the reduction of the scattering kernel to either the hard-soft or soft-hard kernel, and the solution is essentially that discussed in detail in the previous chapter, §6. Finally, the slight discontinuity across $\theta = \pi/2$ must be noted. This is purely numerical, and results from the slow decay of $\log(K/K_f)$, which causes difficulties in precise factorisation of the Wiener-Hopf kernel.

A final caveat is that this plot and all preceding directivity plots, in both this chapter and §5, show only the *direction* of radiated sound. For a concrete comparison of the magnitude, it is important that we suitably normalise the forcing source term, which shall be done carefully in the next section. This is important, for example when investigating the importance of vortex sheet height y_2 , since this has very little effect on directivity but a great effect on the magnitude of the radiating noise.

6.3 Distributed boundary-layer vorticity

Earlier, we defined g to be the Green's function for the scattering problem, due to a vortex sheet. Explicitly, we require g to be the solution of

$$\mathcal{D}_{R0}^\dagger g_0 = e^{-i\kappa_1(y_2)x_1} \delta(\mathbf{x}_T - \mathbf{y}_T) \quad (6.3.1)$$

which fixes the scaling factor Q_0 . Recalling (2.3.15), the acoustics, or at least the generalised potential ϕ which determines p' and v' , is driven by some convected quantity

$$\mathcal{D}_{R0}^\dagger \phi_0 = e^{-i\omega x_1/U(x_2)} F_{01}(x_2, x_3) \quad (6.3.2)$$

assuming a harmonic disturbance like $e^{i\omega t}$, which fixes the streamwise dependence. Therefore, if g_0 satisfies the same boundary conditions as ϕ_0 , we can trivially write down

$$\phi_0 = \int g_0(\mathbf{x}; \mathbf{y}_T) F_{01}(\mathbf{y}_T) d\mathbf{y}_T \quad (6.3.3)$$

which takes care of the forcing convected quantity.

An important caveat must be noted here. Previously, we have defined the adjoint Rayleigh operator via (2.3.11). Upon streamwise transformation, however, we instead determined the auxiliary functions via solution of the ODE given by (4.2.4), which arose upon division by $c_0^2 C$. The forcing for the Green's function must therefore also be divided by this quantity, so that

$$Q_0(y_2) = -\frac{C(y_2; \kappa_1)^3}{c_0(0)^2 C(0; \kappa_1)^4} \frac{1}{D_Z^1(\kappa_1(y_2))}. \quad (6.3.4)$$

This is important for the resulting g to be well-defined. Essentially, we note that $C(y_2; \kappa_1)$ is, by definition, zero. The above choice of Q_0 consistently gives a value for $I_0(y_2)$, in the limit $k_1 \rightarrow \kappa_1$, that is neither zero nor infinite, essentially driven by $\phi_d(y_2; k_1) \sim C^{-3}$ as $k_1 \rightarrow \kappa_1$. With this, we have (taking the limit $k_1 \rightarrow \kappa_1$)

$$I_0 = \frac{C(y_2; \kappa_1)^3}{c_0(0)^2 C(0; \kappa_1)} \frac{\phi_d(y_2; \kappa_1) \ell_1^Z(\kappa_1)}{D_Z^1(\kappa_1(y_2))} \quad (6.3.5)$$

since $\mathcal{P}\phi_Z = -C_0^3 \phi_Z(0)$ and we normalised $\phi_Z(0) = \ell_1^Z$.

We have a convergent integral expression for g , including both the incident and scattered components. Assuming two-dimensional disturbances for clarity, we define the boundary-layer integrated quantity

$$\bar{F}(k_1) = \int_0^\infty \frac{I_0(y_2; \kappa_1) F(y_2)}{K_-(\kappa_1(y_2)) (k_1 - \kappa_1(y_2))} dy_2. \quad (6.3.6)$$

which could alternatively be formulated as an integral in κ_1 . This is the combination of all source-dependent terms, weighted by F within the boundary-layer. Integration across the boundary-layer then gives the scattered solution, with $j = 1, 2$ for $x_2 \gtrless 0$ as usual, as

$$\phi^{(s)} = \frac{1}{2\pi i} \int_{F_1} \frac{\phi_j(x_2; k_1)}{D_Z^j(k_1)} \frac{\bar{F}(k_1)}{K_+(k_1)} e^{-ik_1 x_1} dk_1. \quad (6.3.7)$$

This can be rearranged for $x_1 < 0$ as previously. Importantly, this is exactly the same expression as previously, upon replacement of $I_0(y_2)/K_-(\kappa_1)(k_1 - \kappa_1)$ with \bar{F} , and therefore earlier routines can readily be used.

It is worth looking at the physical meaning of the terms in \bar{F} . I_0 is exactly the wall-pressure due to a point source. F is a generalisation of the perturbation velocity, scaled by mean-flow parameters. By, for example, explicitly computing the vorticity in terms of ϕ ,

and comparing terms between this ω and $F = \mathcal{D}_R^\dagger \phi$, we can note

$$F \rightarrow -\frac{c_0^2}{U'} \omega_3 \quad (6.3.8)$$

as we relax to the two-dimensional, constant shear case. We therefore have a generalised vortical quantity, ω_c , which we define via

$$\omega_c = -\frac{U'}{c_0^2} F. \quad (6.3.9)$$

We can use this to rewrite the integral for \bar{F} in terms of the wavenumber spectrum of ω_c , as

$$\bar{F}(k_1) = -\omega c_0^2 \int_{|U_\infty^+}^{\omega/U_0} \frac{I_0(y_2(\kappa_1); \kappa_1) \omega_c(\kappa_1)}{K_-(\kappa_1)(k_1 - \kappa_1) U(y_2(\kappa_1))^2} d\kappa_1. \quad (6.3.10)$$

Secondly, there is the contribution from K_- which, in part, governs the acoustic response. In the uniform flow, hard-wall case, this would be compared with γ_- , which shall be done below. The behaviour of this function quantifies the effect of the boundary-layer on radiated acoustic noise due to surface pressure, a quantity which is often readily measurable.

6.3.1 Numerical solutions

The upstream Green's function is exactly

$$g_0^{(i)} = \frac{C(y_2; \kappa_1)^3}{c_0(0)^2 C(0; \kappa_1)^4} \frac{\phi_{\geq}(x_2; \kappa_1) \phi_{\leq}(y_2; \kappa_1)}{D_Z(\kappa_1)} \exp(-i\kappa_1 x_1) \quad (6.3.11)$$

with $\phi_{\geq} = \phi_d, \phi_Z$ for $x_2 \geq y_2$ respectively, where ϕ_Z satisfies the above-plate impedance condition with $\phi_Z(0) = \ell_1^Z$. This expression has been repeated to highlight the numerical difficulty of $C \equiv 0$ at $y_2 = \kappa_1$. We navigate this problem by considering instead the *pressure* at $x_2 = y_2$, with

$$\mathcal{P}_0 g_0^{(i)} = \frac{1}{c_0(0)^2 C(0; \kappa_1)^4} \frac{p_{\geq}(x_2; \kappa_1) p_{\leq}(y_2; \kappa_1)}{D_Z(\kappa_1)} \exp(-i\kappa_1 x_1) \quad (6.3.12)$$

with $p_{01} = -C^3 \phi_{01}$ regular as $x_2 \rightarrow y_2$ from the desired side. From this, if desired, the acoustic potential ϕ can be rederived under division by C^3 (which is clearly singular, with a triple pole, $x_2 = y_2$). However, if it is only physical variables that are of interest, namely that of pressure fluctuations and vertical velocities (since streamwise velocities are not

completely defined in this setup), consideration of the pressure streamfunction above suffices (noting $v' \sim \partial p'/\partial x_2$).

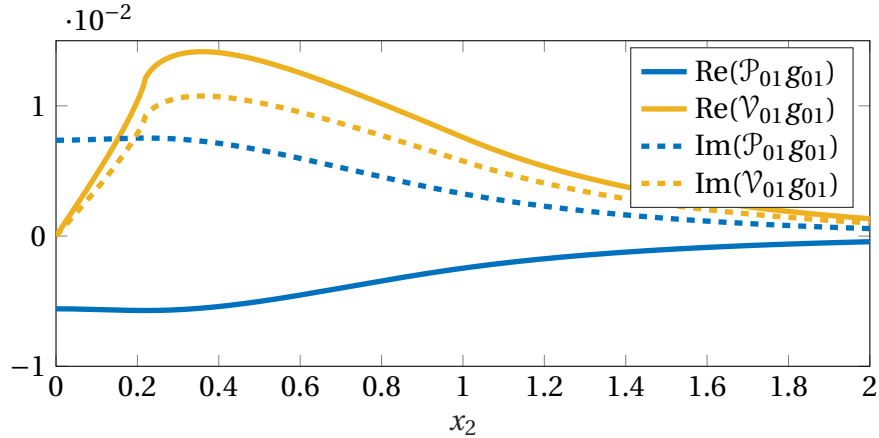


Fig. 6.3.1 Demonstration of computed Green's function for $\omega = 1$, with slipping parabolic profile throughout this section maintained ($U_0 = 0.3U_\infty$, $Ma_\infty = 0.2$). For frequency $\omega = 1$, the pressure and velocity due to a source at $y_2 = 0.2193\delta$ (so $\kappa_1 = 1.7440$) are shown. The pressure is continuous across the vortex sheet, and the vertical velocity has a discontinuity in derivative at $x_2 = y_2$ (and, as expected, vanishes on the wall $x_2 = 0$ due to the imposed hard-wall condition).

The results presented in this section focus on a slipping parabolic profile above a hard-wall, in much the same way as the above-plate flow in the preceding section, but there is nothing particularly special about this configuration. A demonstration of the shape of the Green's function, or at least the derived pressure and vertical velocity, is shown in figure 6.3.1. This was attained by evaluating the p_d at $x_2 = y_2 + \epsilon$ and p_Z at $x_2 = y_2 - \epsilon$, in the limit of small ϵ . This was done due to the singularity in ϕ , though if directly computing p' (for example from the direct Rayleigh equation) it would be possible to integrate directly to y_2 .

By way of demonstration the progression, above a hard wall, of a vorticity distribution $\omega_c = 1$, for all $y_2 \in (0, \delta^+)$, is considered in figure 6.3.2. Since the imposed vorticity is real, this corresponds to it being in phase for $x_1 = 0$, and thus this is where the solution is strongest. The vorticity is completely in phase for $x_1 = 0$, and so the resulting disturbance is strongest here. Since the vorticity convects with the background flow, that further away from the hard-wall along $x_2 = 0$ convects faster, and this gradual movement out of phase leads to the decay in the disturbance. The decay is roughly, in this case, like x_1^{-2} .

We supplement the upstream solution with the fully scattered solution in figure 6.3.3, which requires computation of \bar{F} for any new ω_c , which can then be fed back into the

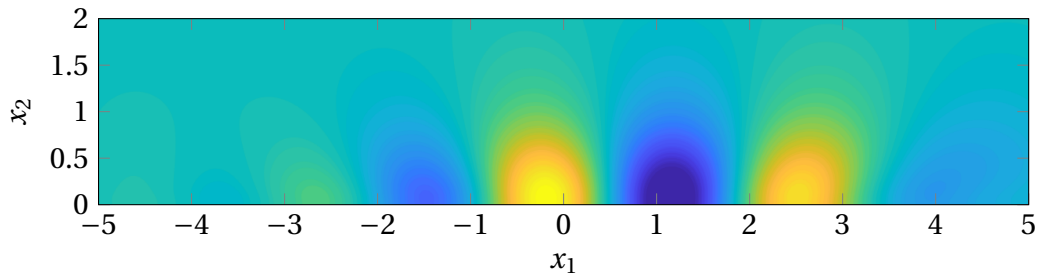


Fig. 6.3.2 $\text{Re}(p')$ for a constant distribution of generalised perturbation vorticity across the usual parabolic boundary-layer, with frequency $\omega = 1$.

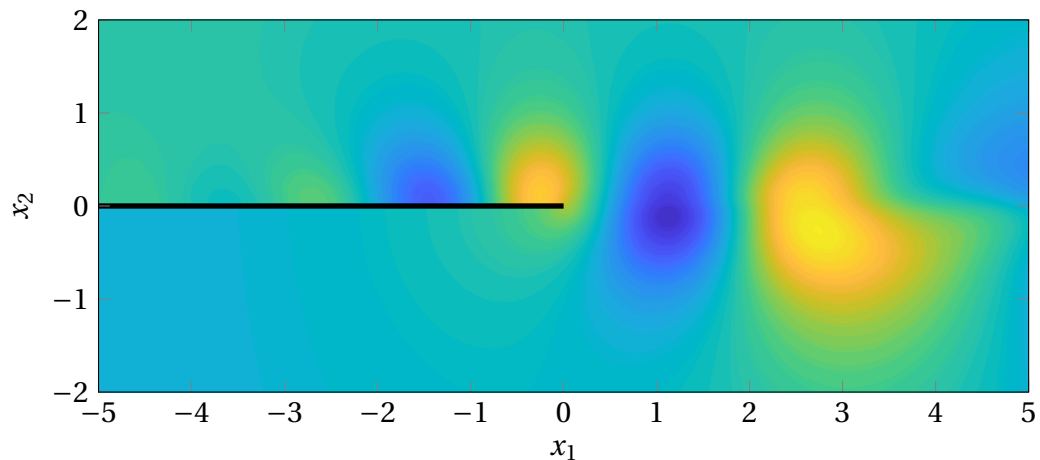


Fig. 6.3.3 Scattering of upstream perturbation figure 6.3.2 by the trailing-edge of a hard plate. As with figure 6.2.2, the background profile is asymmetric with a higher free-stream velocity below the plate.

integration routines. This makes it slower than redefining the vorticity distribution for the upstream case, which requires only a single summation for new ω_c .

Suppose we have a set of quadrature points κ_{1j} and weights w_j , so that $y_2(\kappa_{1j}) = y_{2j}$. Then, \bar{F} is approximated as the sum

$$\bar{F} \approx \sum_j A_j B_j. \quad (6.3.13)$$

with $A_j = -w_j \omega c_0^2 I_0(y_{2j}) \omega_c(\kappa_{1j}) / K_-(\kappa_{1j}) U(y_{2j})^2$, and $B_j = 1/(k_1 - \kappa_{1j})$. For evaluation at general k_1 , A_j need only be evaluated once for given flow parameters, and then $\bar{F}(k_1)$ requires only a simple summation for given values of k_1 . This ensures this problem, once A_j has been computed, is nearly as quick to evaluate as the vortex sheet scattering problem, replacing each (single) evaluation of $1/(k_1 - \kappa_1)$ by a single summation over κ_j .

6.4 Analysis of noise-reduction hypotheses

In the introduction, a variety of trailing-edge noise control devices were introduced. A mechanism for noise reduction was highlighted, namely the displacement of boundary-layer turbulence. The careful construction of the scattering model in the previous chapters allows precise investigation of this mechanism, and evaluation of whether this simple gust model can capture the underlying turbulence. Further, the effect of background shear on the transfer of surface pressure fluctuations to far-field pressure fluctuations is revisited.

It is worth here revisiting Amiet's equation, discussed in the introduction. Recall (1.1.1), linking the surface pressure fluctuation spectrum with the far-field radiated spectrum

$$S_{pp}(x_1, x_2, 0, \omega) \approx b \left(\frac{\omega c x_2}{4\pi c_\infty r_e^2} \right)^2 l_p(\omega) S_{pp}(0, \omega) |\mathcal{L}^2|. \quad (6.4.1)$$

We repeat this equation here to highlight the two primary points of interest: firstly, the effect of background shear on the transfer function \mathcal{L} , which has hitherto been undefined in this work. This essentially requires comparison of K_- with the hard-wall, uniform flow equivalent, which drives the acoustic far-field response (though there are further issues of defining convected wavenumber). We expect, particular for larger acoustic wavelengths, that this function will only have minor corrections, in that the acoustic behaviour essentially does not see the acoustically compact boundary-layer.

Secondly, and more importantly, we are in a position to consider the reduction in $S_{pp}(0, \omega)$, the surface fluctuating pressure spectrum. In essence, the question is whether

we can match displacement of boundary-layer turbulence above noise control devices, an effect repeatedly borne out in experimental investigations, with a corresponding reduction in surface pressure fluctuations, using the vortex sheet (and distributed vorticity) models outlined above, and the resulting wall-pressure due to a known “strength” of vorticity.

6.4.1 Modification of the transfer function by shear layer

In uniform flow, we regain the classical Schwarzschild solution [97, 95] to the trailing-edge scattering problem, from which Amiet’s transfer function can be constructed. In uniform flow U , $\phi_d = e^{-\gamma x_2}$ exactly, and the pressure generated from a vortex sheet, via the earlier calculations, is

$$\begin{aligned}\mathcal{P}_0 g_0^{(s)} &= \frac{I_0(y_2)\gamma_-(\kappa_1)}{2(2\pi i)} \int_{F_1} \frac{e^{-\gamma(k_1)x_2 - ik_1x_1}}{\gamma_-(k_1)(k_1 - \kappa_1)} dk_1 \\ &= -\frac{e^{-\gamma(\kappa_1)y_2} C(\kappa_1)^2}{4\pi i \gamma_+(\kappa_1) c_0^2} \int_{F_1} \frac{e^{-\gamma(k_1)x_2 - ik_1x_1}}{\gamma_-(k_1)(k_1 - \kappa_1)} dk_1\end{aligned}\quad (6.4.2)$$

A gust convecting at the free-stream velocity is silent, since $C(\omega/U) = 0$ by definition, and so κ_1 must be chosen to correspond to some convected velocity $U_c < U$, an artificial constraint bypassed by this more sophisticated calculation. This method is slightly more general than Schwarzschild’s solution, which merely determines the pressure on the upstream hard plate, as this incorporates the wall-normal dependence and therefore allows direct evaluation of far-field sound.

The Wiener-Hopf kernel in the uniform flow case is simply

$$K = \frac{2D_p}{D_h} = -\frac{2C}{\gamma}. \quad (6.4.3)$$

This is factorised as $K_+ = 2\gamma_+/C$ and $K_- = 1/\gamma_-(k_1)$, and the former appears outside the integrand, evaluated at convected wavenumber κ_1 , and the latter within the integrand. The effect of shear can then be quantified in the effect on the behaviour of $K_+(\kappa_1)K_-(k_1)$. An ideal consideration would be investigation of the behaviour of source-independent functions $\gamma_-(k_1)$ and $K_-(k_1)$, but this runs into issues with the ability to arbitrarily scale the factorised kernel by an arbitrary constant. This, essentially, is the same as the previous computation of far-field noise, but we are interested here only in the transmission of wall-pressure fluctuations to far-field pressure fluctuations, which arises from fixing $I_0 \equiv 1$, considering the scattering of the gust-induced wall-pressure $e^{i(\omega t - i\kappa_1 x_1)}$, where we now

must prescribe κ_1 . Fixing $U_c = 0.8U_0$ for all plots¹, the far-field sound in two cases for unit I_0 , as the boundary-layer profile is consistently varied, is shown in figure 6.4.1.

We consider the two distinct cases of an acoustically compact boundary-layer, and one which is less so. In both cases, we consider a slipping parabolic profile though there is no reason the results will not be generic. Identification of the source strength (here, $I_0 = 1$) allows far-field directivity to be exactly plotted including magnitude, and both plots show the magnitude of far-field pressure $|p'|$, up to the decay as $r^{-1/2}$. In the first case, the acoustic wavelength $\lambda_a = 20\pi\delta$, much larger than the boundary-layer thickness, whereas in the second case $\lambda_a = 2\pi\delta$, which is a comparable size to the boundary-layer thickness. As previously identified, the directivity of the scattering is essentially unmodified by the compact boundary-layer, though there is variation for shorter acoustic wavelengths. In both cases, we compare with the cardioid profile obtained for uniform flow ($U_0 = U_\infty$), slightly shifted from a $\sin(\theta/2)$ profile by Mach number effects.

Allowing for observation of the magnitude variation allows identification of a small enhancement in sound by boundary-layer shear, with the lowest slip velocity, in both cases, leading to the highest radiation. The effect is noticeably reduced in the compact case, and is only maximally up to 2 dB in the shorter wavelength case. As hypothesised, there is little effect on radiation directly from the boundary-layer shear, particularly in the longer wavelength cases of interest (driven by low free-stream Mach number, rather than low frequency). This highlights the need to directly consider the effect of source on reducing wall-pressure fluctuations (and therefore, by this analysis, far-field pressure fluctuations).

6.4.2 Reduction of wall pressure by vorticity displacement

Having identified \tilde{F} with generalised convected vorticity ω_c , we can turn attention to a fundamental question of this thesis, namely the potential reduction of far-field noise through the displacement of boundary-layer turbulence. For an infinitesimal vortex sheet at location $x_2 = y_2$, of strength ω_0 , we have an explicit expression for the induced wall-pressure p_w given by

$$p_w = -\frac{\omega_0 c_0(y_2)^2 I_0}{U'(y_2)} = \frac{\omega_0}{C(0; \kappa_1) U'(y_2)} \frac{p_d(y_2; \kappa_1) \ell_1^Z(\kappa_1)}{D_Z^1(\kappa_1(y_2))}. \quad (6.4.4)$$

¹This value of U_c is somewhat arbitrary, and is merely used as an example. Measured convection velocities are a function of frequency, with Rogers and Moreau [94] incorporating $U_c = 0.6U_\infty$ in their extension of Amiet's models, and $U_c = 0.7U_\infty$ often used.

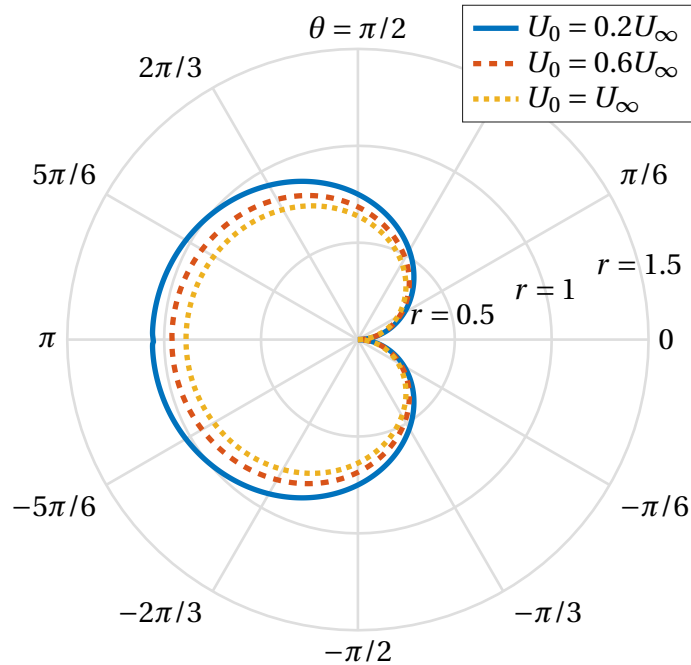
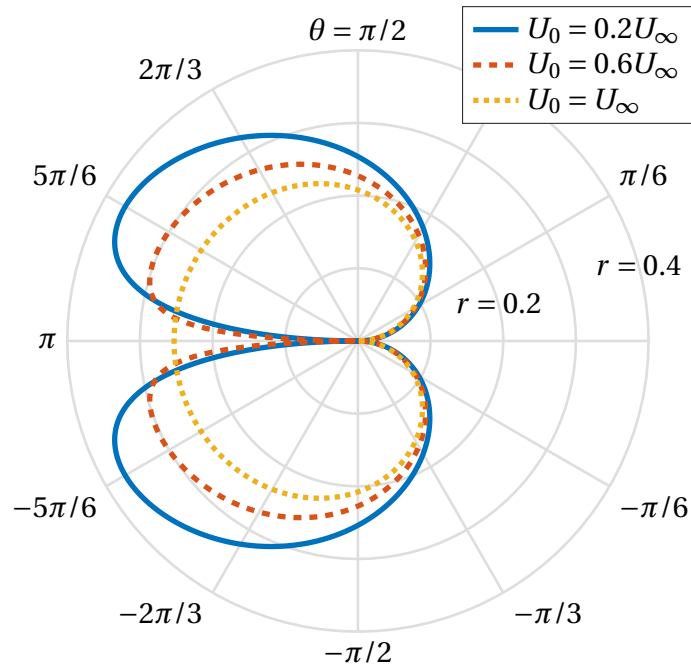
(a) Acoustically compact boundary-layer, $c_0 = 50U_\infty$.(b) Acoustically non-compact boundary-layer, $c_0 = 5U_\infty$.

Fig. 6.4.1 The transfer of wall-pressure to the far-field for a parabolic slipping profile, at frequency $\omega = 5$, with gust wavenumber $\kappa_1 = \omega/(0.8U_\infty)$.

The far-field sound is a directly driven by this quantity, as per either Amiet (1.1.1) or as directly computed previously in (6.2.15). Subject to the caveat in evaluation of $p_d(y_2)$ (namely the limit as $x_2 \rightarrow y_2$ from above, as per §6.3.1), we can evaluate this as a function of ω and of y_2 , fixing $\omega_0 = 1$ (that is, a “point” vortex sheet).

Figure 6.4.2 demonstrates the wall-pressure for three different boundary-layer setups, as a function of source location y_2 and frequency ω . In dimensional form, we should consider $y_2 \mapsto y_2\delta$ and $\omega \mapsto \omega U_\infty / \delta$, so if estimating boundary-layer thickness on the order of centimetres and free-speed flow speed around 10 ms^{-1} , then $\omega = 1$ corresponds to a (temporal) frequency of around $f \approx 100 \text{ Hz}$, which is at the lower end of human hearing. For fixed y_2 location there is the same broad trend: a maximum at some intermediate frequency, with algebraic decrease in wall pressure for lower frequencies (so linear in $\log(\omega)$), and a faster than algebraic decrease at higher frequencies. Similarly, for fixed y_2 , there is normally a maximal intermediate value of $|p_w|$ with monotonic behaviour on either side of this maximum, with the wall-pressure decaying to zero both due to a source at the wall and due to a source in the free-stream.

The location of this maximum in y_2 is heavily frequency and profile dependent. For the linear profile, figure 6.4.2b, the peak tracks the location of the modal solution as found in §3, and is finite only due to the approximation in taking $y_2 + \epsilon$ in the evaluation of ϕ_d . However, for higher frequencies this modal solution (tending towards $y_2 = \delta$) becomes negligible in comparison to the wall-pressure induced by near-wall vorticity, a trend seen in the slipping parabolic case too. Interestingly, the drift of the peak in y_2 location as ω varies is not seen in the non-slip case (figure 6.4.2c, which has broadly the same wall-pressure to frequency profile for all y_2). Finally, for very low frequencies the slipping parabolic profile, figure 6.4.2a, appears to have a modal-type solution hitherto unnoticed, lying exactly on the critical-layer.

This offers some support for the idea that deflection of boundary-layer turbulence, and therefore vorticity, can result in a reduction of far-field noise. Certainly, we have a strong dependence on the location of boundary-layer turbulence and wall-pressure. For higher frequencies, broadly of more interest, given the low flow speeds of consideration, near-wall turbulence has a much higher coupling with observable wall-pressure, with the impact decaying rapidly in y_2 . Therefore, movement of near-wall vorticity further into the boundary-layer, without changing its fundamental strength (or permitting mild increases in turbulence) can achieve a great reduction in wall-pressure and therefore far-field noise. Whilst this picture is not as clear at lower frequencies, where the wall-pressure is dominated by turbulence much further from the wall, it offers support of previously suggested mechanisms at the frequencies of interest.

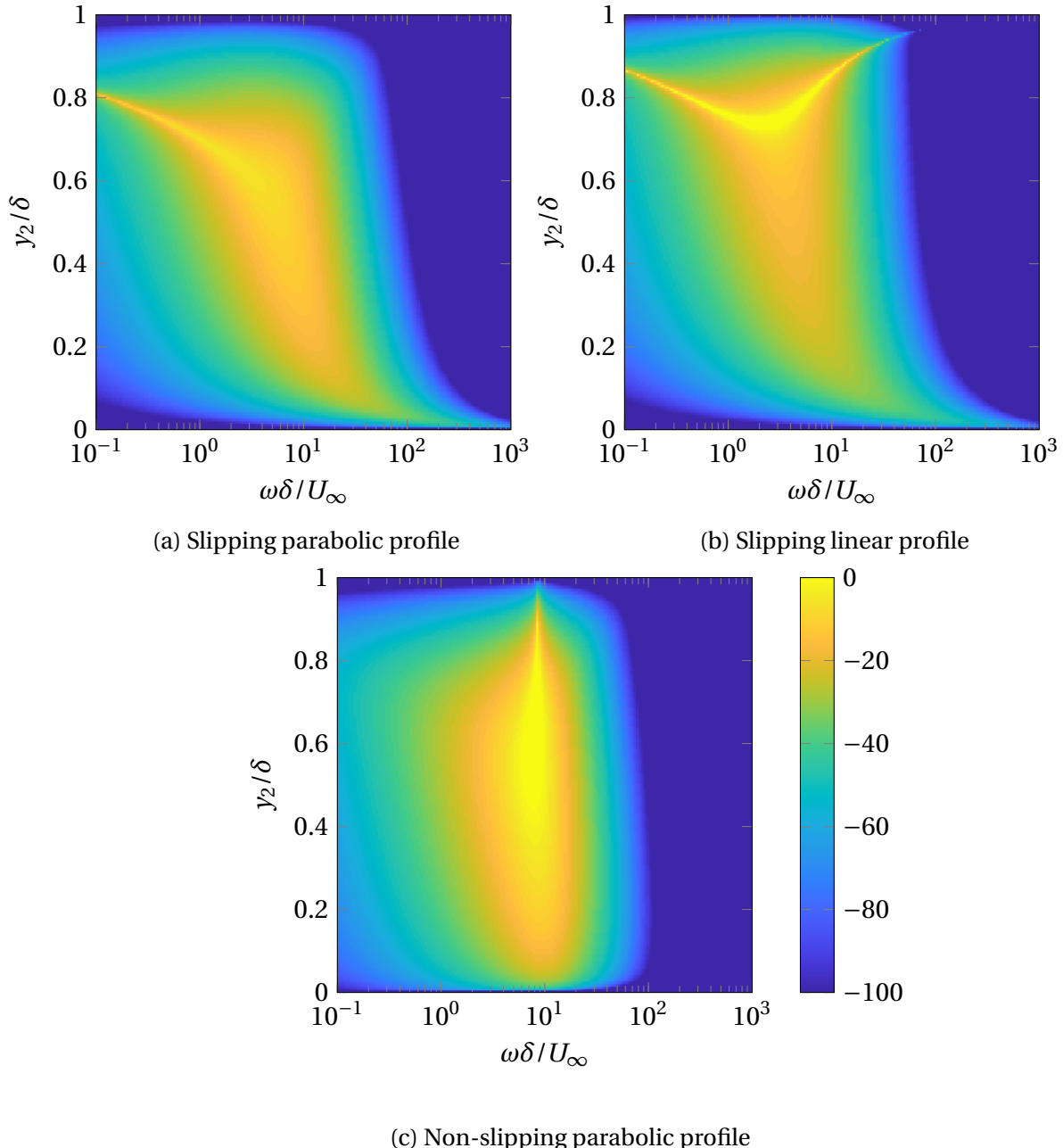


Fig. 6.4.2 The wall-pressure, $20\log_{10}(|p_w|)$ (in dB) for a variety of boundary-layers, due to a vortex sheet of unit strength at $x_2 = y_2$. All have $c_0 = 5U_\infty$, with parabolic profiles having continuous shear at the edge of the boundary-layer, with a jump in shear at the edge in the linear case. If the profile is slipping, $U_0 = 0.3U_\infty$.

6.4.3 Wall-pressure and far-field noise prediction from a physically motivated boundary-layer

We would like to combine the above two thoughts: what is the effect of varying boundary-layer shear on wall-pressure fluctuations (due to a vortex sheet fixed at some location) and in turn on far-field noise, and within the framework what is the effect of variation of y_2 . We consider the two profiles shown in figure 6.4.3, motivated by those experimentally observed above fence-like noise control devices [3], see figure 3.3.3. The profiles are broadly similar, constructed from two parabolae with continuous background velocities and shear at some intermediate point, which means the numerical code need not be modified for a jump in shear.

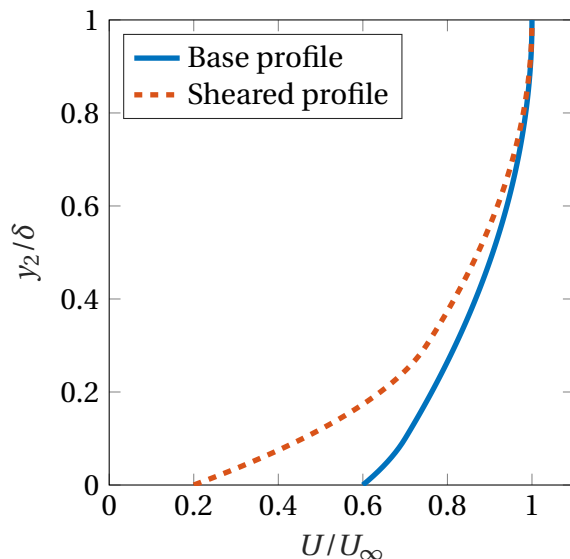


Fig. 6.4.3 Two flow profiles, consisting of two parabolic pieces, inspired by figure 3.3.3 with the imposition of continuous shear.

We then consider a vortex sheet at a variety of fixed y_2 locations for both of these setups, as the frequency is varied, in figure 6.4.4. The frequency, displayed in Hz, is based on a free-stream velocity of 10 ms^{-1} and boundary-layer thickness 20 mm, and is shown to give some physical meaning to the scaled frequency hitherto considered. For both plots and for all locations, both the wall-pressure p_w and the far-field pressure, measured at $\theta = \pi/2$ directly above the plate, is shown. For this analysis, the speed of sound is large, $c_0 = 35U_\infty$, and so we expect the far-field directivity to be a simple $\sin(\theta/2)$ profile, so measurement at a single observer angle can easily be generalised. It is computed assuming the background profile is symmetric for $x_2 \geq 0$. The computed far-field sound is

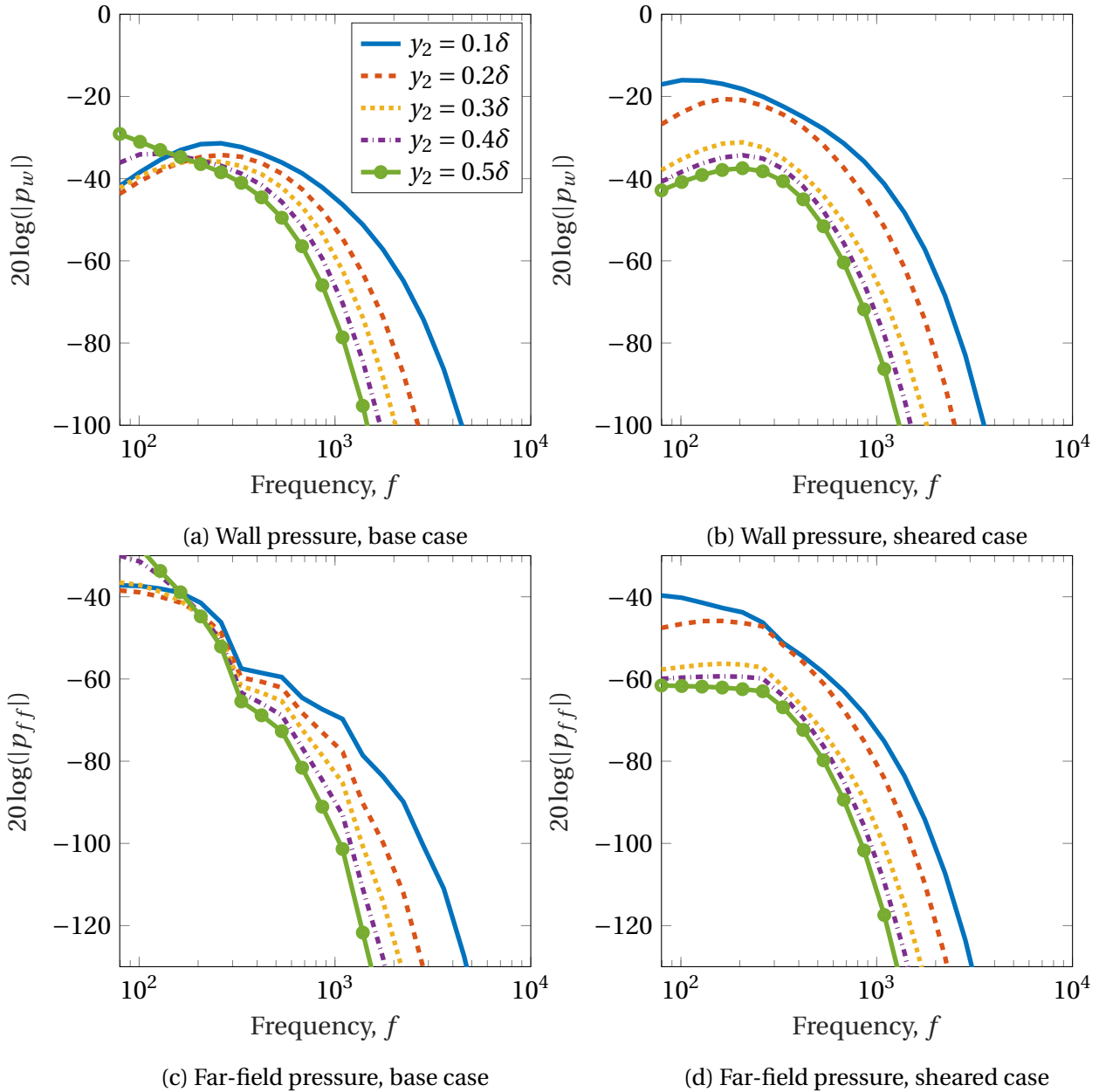


Fig. 6.4.4 Pressure fluctuations in dB at both the surface and the far-field, for a range of source locations and frequencies (in Hz). The two background profiles are outlined in figure 6.4.3, with the remaining parameters discussed in the text.

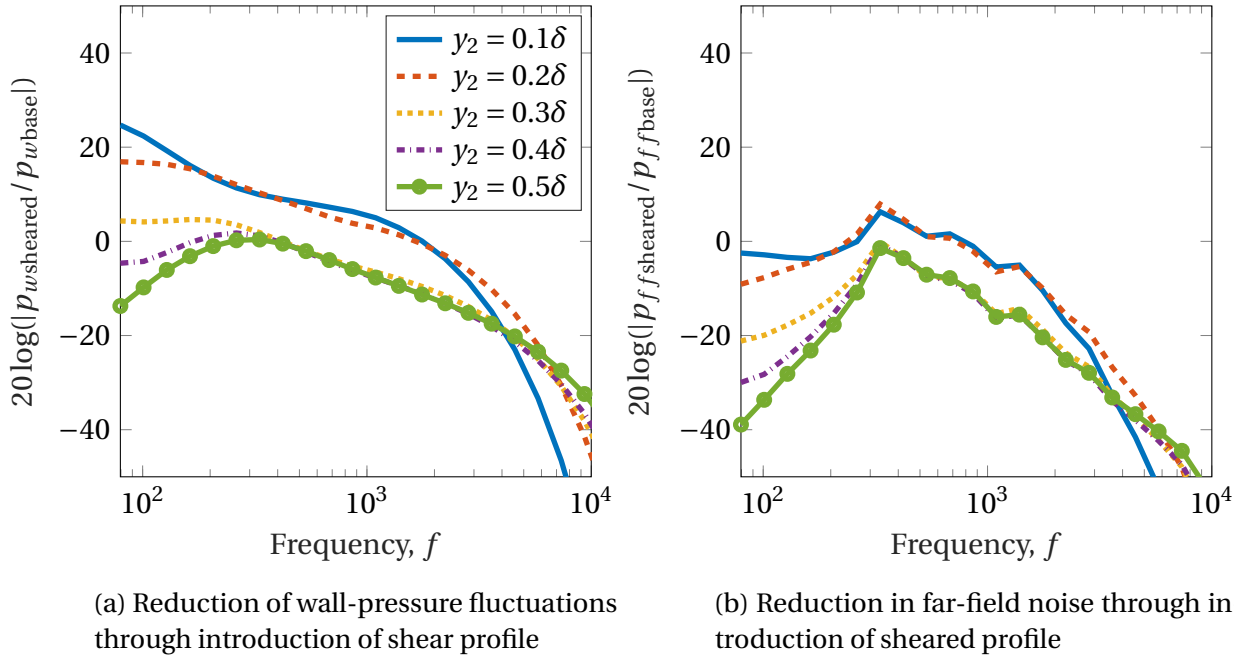


Fig. 6.4.5 Change in pressure fluctuations (in dB) due to the change in background profile, as figures 6.4.3 and 6.4.4.

the magnitude of a wave decaying as $r^{-1/2}$, and this factor (and other scaling constants, irrelevant on a logarithmic scale) have been ignored. The far-field noise is derived as a multiplier of the wall-pressure, which does depend to a limited extent on frequency and source location (as well as boundary-layer shape).

There are features common to all the plots. As before, for fixed y_2 there is a maximal value of wall-pressure at some intermediate frequency (both figures 6.4.4a and 6.4.4b), though this property doesn't neatly transfer to far-field noise. The magnitude of this peak is monotonic in y_2 , with the wall-pressure decreasing as y_2 increases. Indeed, this is common to almost all frequencies of interest: a vortex sheet further from the wall, with the same magnitude of vorticity, induces a smaller wall-pressure. This monotonicity is preserved in the far-field, figures 6.4.4c and 6.4.4d. At low frequencies, the increase in wall-pressure with frequency does not transfer to an increase in far-field pressure with frequency.

At physically realisable frequencies, the common decrease in wall-pressure with increase in y_2 lends a great deal of support to the hypothesis that turbulence deflection leads to a reduction in wall-pressure and, through this scattering model, far-field noise. The reduction is not insubstantial, particularly at higher frequencies, though it is worth noting it is at these frequencies we might expect the viscous terms, hitherto neglected, to become important.

We can use the choice of two background profiles to investigate the effect of background shear on both wall-pressure and radiated noise directly, as per figure 6.4.5, which looks at the decibel increase in both wall-pressure and far-field noise in the sheared case, compared with the base case. This highlights an important warning about use of wall-pressure as a proxy for far-field noise: whilst there is broadly, for all frequencies, a reduction in far-field noise (with some small increase at some y_2 when $\log(f) \approx 2.5$), there appears to be an increase in wall-pressure at low frequencies when the source is near the wall, amplified by the increase in shear. This is consistent with the work in §3.5, which looked at the effect of a (piecewise linear) background profile with increased shear near the wall, and showed an increase in wall-pressure. That this need not translate into increased far-field noise adds substance to the effect of shear-shielding, even if there is some apparent increase in wall-pressure. An increase in wall-pressure directly due to the background profile could be directly cancelled out in the scattering to the far-field.

With this we have established that both a change in background profile, and a movement of vorticity within the boundary-layer, can lead to a substantial reduction in observed far-field noise. The movement of vorticity consistently and predictably leads to a reduction in far-field noise, where the change of the background profile is less clear-cut, which supports the work presented in the previous two sections.

6.5 Conclusions and discussion

By extension of the Wiener-Hopf process introduced in §5, this chapter outlines the solution to the generic scattering problem from a trailing-edge. Typical analyses of this kind of problem assume the underlying differential equation, under a suitable integral transformation (be it Fourier or equivalently Laplace, as in this work, or for example the Mellin transform when considering wedge scattering), can be reduced to an ODE for which analytic solutions can be obtained. The numerical work then arises from the need to factorise the Wiener-Hopf kernel, but with a complete understanding of the complex analytic behaviour of this kernel. The work in §5 and this chapter has generally kept the factorisation and therefore the solution of the problem quite simple, by only considering a single junction (or, in the trailing-edge case, two junctions linked by the behaviour of the solution across the wake). However, complexity has arisen as the governing transformed ODE does not permit simple, analytic, closed form solutions, and therefore numerical routines have been introduced to allow the Wiener-Hopf framework to be used, which was the fundamental basis for the work of §4.

Through the framework developed throughout this work, it is numerically inexpensive to quickly determine the far-field noise due to scattering of a vortex sheet, and indeed a more generic “gust” solution, from a sharp trailing-edge. This extends the typical work concerning uniform flow, or symmetric flow with constant shear [96], to more general background profiles, which may be both asymmetric and have smoothly varying shear. Further, this work has extended typical considerations of scattering from a hard- or a pressure-release wall to scattering from a generic lined wall, subject to the caveat that the impedance Z is equal on both surfaces of the plate, permitting solution (as a scalar Wiener-Hopf problem) through proportionality of pressure and velocity perturbations along $x_2 = 0$. The more generic case, with different impedances above and below the plate, requires use of more sophisticated matrix-based Wiener-Hopf techniques, and is unlikely to result in solutions that can easily be written down in closed form.

A primary outcome of this chapter is the construction of a more generic gust solution, given some known vorticity distribution at some physical location, following Goldstein’s work [46, 48]. Identifying the convected quantity with some generalised perturbation vorticity allows analysis of the effect of displacement of this vorticity within the boundary-layer. In the final section, §6.4, this was used to consider the questions outlined in the introduction to this thesis: namely can these reasonably simple models give some understanding of the workings of noise control devices, which appear to work via the deflection of boundary-layer turbulence away from the scattering wall, resulting in a reduction in surface pressure and in turn a reduction in far-field noise. Whilst direct modification of boundary-layer mean shear does little to the far-field radiation, in fact broadly increasing it, there is strong evidence that vorticity movement with the boundary-layer (and therefore movement of turbulence) has a strong effect on reduction of surface pressure. In particular, at high frequencies surface pressure is dominated by vorticity very near the scattering surface, so displacement of these disturbances, even if the effect is only small, can have a large effect on far-field noise.

Chapter 7

Conclusions

7.1 Summary and discussion

7.1.1 Implementation of quasi-numerical methods

This work fits between the two typical approaches to scattering problems.

The first, broadly analytic, relies on the the governing ODE having analytic solutions so the Wiener-Hopf process can be done almost entirely in terms of known functions. Any numerical computations in this procedure are normally focused on the factorisation of the Wiener-Hopf kernel. Alternatively, when there is more than one junction and the perturbations are governed by a matrix Wiener-Hopf equation (for example scattering by a thin plate of finite length), iterative methods can be used to compute the solution via a series of scalar Wiener-Hopf problems. Other problems consider a background flow that is some small irrotational perturbations to some uniform flow, for example the noise of a cambered, angled or thick aerofoil [75, 76, 9]. However, in the limit chosen for acoustic perturbations, these perturbations are generally governed by Helmholtz equation, or can at least be reduced to this form, or alternative asymptotic limits can be considered which give rise to analytic solutions (for example with background shear [10]). Only rarely has the case where the governing ODE itself cannot be solved analytically been considered.

Whilst this work began with a case for which analytically tractable solutions could be found (\$3), it was identified that as the number of piecewise linear pieces was increased this process was no longer practical. Similarly, in the compressible case, with a linearly sheared boundary-layer of finite extent, it is possible to find a solution to the governing ODE for pressure in terms of hypergeometric functions [96]. These are of no help when considering the scattering problem, as they are less well-understood functions that, broadly, can only be considered numerically. The Wiener-Hopf process, however, requires

only a limited amount of knowledge about the functions being considered: the far-field behaviour of the Wiener-Hopf kernel, whether or not this kernel has zeros and poles, and which generalised half-plane it lies in, as well as some knowledge of branch points. All of these can be gleaned from a function defined only as a solution to an ODE with specified boundary conditions, and it is this approach taken throughout this work.

For the problem considered, the branch cuts are imposed by the behaviour at the edge of the boundary-layer, and are therefore well-understood. The work of chapters 3 and 4 primarily considered the mass source problem, but also allowed consideration of roots of a variety of dispersion relations, which (as demonstrated in §5.2) have a direct link to zeros and poles of the Wiener-Hopf kernel. With this, the complete information required to solve the Wiener-Hopf kernel has been obtained without explicit analytic solution of the governing ODE. This comes at the cost of increased computational expense, though computation of the auxiliary functions for a governing ODE is comparatively inexpensive when compared with the kernel factorisation process (which does however have auxiliary function computation embedded within it).

The second approach is complete numerical computation of the scattered solution. Grid based methods struggle with scattering problems due to the large number of points required near the boundary-layer discontinuity. Indeed, for genuinely discontinuous boundary-conditions, the difficulty of eliminating eigenfunctions of the scattered solution, through an imposition of a Kutta condition, becomes difficult [8]. Aside from the comparatively inexpensive routines developed in this work, the satisfaction of the Kutta condition trivially requires specification of a single entire function E , which can be evaluated on physical grounds. Finally, this setup naturally leads to propagating wavelike solutions in an infinite domain, avoiding problems of reflection from the edge of the domain typically found in numerical applications.

Finding the middle ground between these approaches, as we have done in this thesis, vastly increases the number of problems for which the Wiener-Hopf technique can be used, across a wider range of the parameter space (in particular at all but the very high frequencies at which viscous effects become important).

7.1.2 Development of the understanding of scattering problems

The solution of scattering problems induced by a discontinuity in boundary conditions is not new, and neither is the use of the Wiener-Hopf technique in solving them. However, the inclusion of background shear within the scattering problem reduces many analytic complexities of the hard-soft scattering problem, at the expense of the a more complex governing ODE that does not necessarily permit analytical solutions, discussed above.

As noted in the introduction to §5, the scattering from lined surfaces has previously thrown up difficulties. Consideration of the hard-soft scattering problem, with mean flow, is not new [89, 93], though due to the presence of surface modes a variety of modelling simplifications have previously been made, for example assuming a thin region near the wall in which there is no background flow, or by considering an unbounded region of constant shear. These modelling simplifications are needed due to the presence of surface modes, which may be convectively unstable, and exist only in an exponentially thin region near the wall (when considering perturbations to uniform flow). Modifications to the Myers boundary condition have been proposed to deal with this difficulty [66], though little work has been done on the scattering problem with these new boundary conditions.

By allowing a non-infinitesimal boundary-layer, we have revisited the scattering problem, deriving a solution which, although it must be computed numerically, satisfies the boundary conditions and, more importantly, any conditions imposed at the scattering junction. That this solution is correct can readily be shown by verifying the computed solutions, though a considerable deal of work has been put into the generation of near-field solutions demonstrating the behaviour of the perturbation within the boundary-layer.

An important result is the clarification that, in the limit of $c_0 \rightarrow \infty$, the scattered solution across a hard-soft junction regains the cardioid-type scattering that would be expected of scattering from a hard trailing-edge, and indeed later we see the soft-hard scattering directivity is directly comparable to the scattering from a soft trailing-edge. This limit, the limit of long acoustic wavelength and the quasi-incompressible limit, has been analysed previously analytically [93, 101], though direct analysis of this setup is difficult. By direct numerical consideration of the limit, exact results have been generated.

Finally, it is worth reviewing the problem considered in §5.6, in which a convectively unstable surface mode (be it above an lined surface or a pressure-release wall) may restabilise at the trailing-edge of the lined section, as the hard-wall downstream cannot support such disturbances. It was demonstrated that such modes can lead to a large increase in scattered acoustic noise due to a finite section of lining, due to the exponential growth of the surface mode even over the comparatively short distances involved. Whilst this surface mode is in some sense invisible (since it doesn't propagate downstream), its large contribution to the acoustic scattering suggests a need for care, and highlights the importance in understanding these modes.

7.1.3 Explaining noise control devices

This work began with a discussion of novel devices for the control of trailing-edge noise. There was particular focus on two broad types of devices: firstly, blowing near the trailing-

edge [106], and secondly through streamwise-orientated devices structures upstream of the trailing-edge, be it fibres [28, 27], rails [25], or fence-like *finlets* [26, 24, 3, 4]. All these devices (both passive and active) reduce the pressure fluctuations on the scattering surface of the aerofoil, and thus (either directly measured or inferred via some modelled transfer function) result in a (sometimes substantial) reduction of far-field noise, with obvious practical applications including the blades of wind turbines. The passive devices took inspiration from the soft, downy coating on the upper side of an owl's wing, which has the effect of almost completely suppressing pressure fluctuations, and contributes substantially to the silent flight of larger owl species.

Experimental measurements of both blowing and streamwise-aligned passive devices results in two observations, common to both devices. As the flow passes over the device, there is a sharp increase in near wall mean shear. As the flow develops, there is a region of recirculation in the wake of the device. Flow-borne turbulence from upstream is therefore deflected further away from the wall, above this recirculation region, a result apparent in measurements of rms velocity perturbations within the boundary-layer. Some experimental setups allow measurement of both background shear and of turbulence intensity at a variety of streamwise locations, from which a reasonably complete understanding of the flow over such devices can be obtained [106].

A goal of this work was to construct an analytical framework that could utilise these experimental observations directly, importantly isolating the acoustically relevant mechanisms. This model was created through Goldstein's work on Rapid Distortion Theory [43, 44], which directly includes the effects of mean flow shear and provides a careful framework for gust solutions, namely generalised vortical solutions convected with the mean flow, which are the only contribution to the acoustic (pressure) components of the far-field disturbance. To some extent, all chapters of this thesis relate to applying this theory in a more and more complicated framework, in particular to the problem of scattering from a trailing-edge. With the mean flow profile and perturbation vorticity (as a proxy for turbulence intensity) now as inputs to the model, it has been demonstrated that it is possible to compute both the near- and far-field scattering of an arbitrary vorticity distribution to an arbitrary (continuous) mean flow.

This allows testing of both the experimental observations, which was done in §6.4, asking two questions. Firstly, how does mean background shear affect the transfer of wall-pressure fluctuations to far-field pressure fluctuations, and secondly can the reduction in wall-pressure fluctuations be explained by this simple model of boundary-layer turbulence (ignoring the effects of viscosity and nonlinearity in the mean flow, for example).

For longer acoustic wavelengths, corresponding to lower frequencies, there is little difference in radiation to the far-field, which would be predicted by scaling arguments. Indeed, there is evidence that mean shear enhances far-field noise due to wall-pressure fluctuations, though compared to observed noise reduction the effect is minimal. There is, however, a strong relationship between vorticity location within the boundary-layer and induced wall pressure, dramatically shown in figure 6.4.2. In particular, for higher frequencies (more comparable to frequencies of interest), disturbances close to the wall induce a considerably stronger wall-pressure. That this effect is highly dependent on background shear was investigated more thoroughly in the following section. This confirmed that displacement of boundary-layer turbulence can indeed result in a large reduction of wall-pressure, and therefore far-field noise, even for small displacements, provided any disturbance is moved out of this thin, “loud” region.

Whilst conclusions are as yet limited, this comparatively simple model, focusing on the underlying physics of noise induced by unsteady fluctuations within the boundary-layer, has successfully given rise to the required framework to which the experimental observations on noise control devices can be compared.

7.2 Future work

This work has primarily focused on the construction of a model of gust-junction interaction, rather than complete exploration of the possibilities offered by it. The model, as described mathematically and as numerically implemented, permits the background density to vary with the transverse coordinate x_2 (via the background speed of sound as a proxy), a condition that has not been utilised in this work but is appropriate at higher Mach numbers. Further, this work focused on the purely two-dimensional case, with U regarded as a function of wall-normal coordinate x_2 only. As noted in the introduction, the formulation permits spanwise dependence of U (and c_0), with the derivation relying only on the *parallel* nature of the background flow. Three-dimensionality is permitted in the perturbation via the spanwise wavenumber k_3 , and the code constructed for this work permits this to be non-zero though, again, this has not been directly studied in this work. Further work should consider non-zero k_3 , particularly as integration over spanwise lengthscales is important for the complete understanding of far-field noise.

In this work, only finite boundary-layers, with non-zero shear confined to some interval $x_2 \in (\delta^-, \delta^+)$, were considered. There is no fundamental need for this restriction. The derivation makes no assumption of it, save in the prescription that, in the mean flow, $\phi_d = \exp(-\gamma_\infty x_2)$. Replacing this with (integrated) ϕ_d satisfying $\phi_d \sim \exp(-\gamma_\infty x_2)$

as $x_2 \rightarrow \infty$, on the assumption that $U \rightarrow U_\infty$ in this limit, permits non-finite boundary-layers. The boundary-layer integration can be computed by making some mapping of the infinite integral $x_2 \in (0, \infty)$ to a finite integral, exactly as done with numerical inversion routines. In particular, this would allow consideration of tanh-like profiles and a Blasius-type boundary-layer profile, which in turn must be computed as the solution to the governing nonlinear ODE. At reasonably low Reynolds numbers, the Blasius boundary-layer is physically relevant, and therefore extension of this work to infinite boundary-layers is very desirable.

The indicative results on gust displacement are interesting, if currently only reasonably qualitative. This is not a limitation of the model as coded, as it happily permits scattering of arbitrary vorticity distributions from a trailing-edge or a junction, and further work should be done to quantify the link between vorticity location and scattered noise, particularly through utilisation of realistic experimental data, and at physically realisable frequencies. An important question is, however, raised: what is the link between (measurable) boundary-layer velocity fluctuations and boundary-layer vorticity (which drives the scattering process)? For a practical model that takes, as an input, background shear and boundary-layer turbulence, this link is a crucial step.

References

- [1] Ablowitz, M. J. and Fokas, A. S. (2003). *Complex Variables: Introduction and Applications*, volume XXXIII. Cambridge University Press.
- [2] Abramowitz, M. and Stegun, I. A. (1965). *Handbook of mathematical functions, with formulas, graphs, and mathematical tables.*, Dover Publications, New York.
- [3] Afshari, A., Azarpeyvand, M., Dehghan, A. A., and Szőke, M. (2016). Trailing Edge Noise Reduction Using Novel Surface Treatments. In *22nd AIAA/CEAS Aeroacoustics Conference*, page 2834. AIAA.
- [4] Afshari, A., Azarpeyvand, M., Dehghan, A. A., and Szőke, M. (2017). Effects of Streamwise Surface Treatments on Trailing Edge Noise Reduction. *23rd AIAA/CEAS Aeroacoustics Conference*.
- [5] Amiet, R. K. (1976). Noise due to turbulent flow past a trailing edge. *Journal of Sound and Vibration*, 47(3):387–393.
- [6] Amiet, R. K. (1978). Effect of the incident surface pressure field on noise due to turbulent flow past a trailing edge.
- [7] Ayton, L. J. (2017). An analytic solution for gust-aerofoil interaction noise for plates with leading-edge serrations. In *23rd AIAA/CEAS Aeroacoustics Conference*.
- [8] Ayton, L. J., Gill, J. R., and Peake, N. (2016). The importance of the unsteady Kutta condition when modelling gust-aerofoil interaction. *Journal of Sound and Vibration*, 378:28–37.
- [9] Ayton, L. J. and Peake, N. (2013). On high-frequency noise scattering by aerofoils in flow. *Journal of Fluid Mechanics*, 734:144–182.
- [10] Ayton, L. J. and Peake, N. (2015). On high-frequency sound generated by gust-aerofoil interaction in shear flow. *Journal of Fluid Mechanics*, 766:297–325.

- [11] Baker, D. I. and Peake, N. (2018). Trailing-edge noise in slowly-varying, sheared flow. In *2018 AIAA/CEAS Aeroacoustics Conference*, Reston, Virginia. American Institute of Aeronautics and Astronautics.
- [12] Batchelor, G. K. (2000). *An Introduction to Fluid Dynamics*. Cambridge University Press.
- [13] Batchelor, G. K. and Proudman, I. (1954). The effect of rapid distortion of a fluid in turbulent motion. *Quarterly Journal of Mechanics and Applied Mathematics*, 7(1):83–103.
- [14] Bender, C. M. and Orszag, S. A. (2013). *Advanced mathematical methods for scientists and engineers I: Asymptotic methods and perturbation theory*. Springer Science & Business Media.
- [15] Bodling, A., Agrawal, B. R., Sharma, A., Clark, I., Alexander, W. N., and Devenport, W. J. (2017). Numerical Investigation of Bio-Inspired Blade Designs at High Reynolds Numbers for Ultra-Quiet Aircraft and Wind Turbines. In *23rd AIAA/CEAS Aeroacoustics Conference*.
- [16] Bodling, A. and Sharma, A. (2018). Numerical investigation of low-noise airfoils inspired by the down coat of owls. *Bioinspiration & Biomimetics*, 14(1):016013.
- [17] Bornemann, F. (2011). Accuracy and Stability of Computing High-order Derivatives of Analytic Functions by Cauchy Integrals. *Foundations of Computational Mathematics*, 11(1):1–63.
- [18] Brambley, E. and Peake, N. (2006). Surface-Waves, Stability, and Scattering for a Lined Duct with Flow. In *12th AIAA/CEAS Aeroacoustics Conference (27th AIAA Aeroacoustics Conference)*, Reston, Virginia. American Institute of Aeronautics and Astronautics.
- [19] Brambley, E. J. (2009a). Fundamental problems with the model of uniform flow over acoustic linings. *Journal of Sound and Vibration*, 322(4-5):1026–1037.
- [20] Brambley, E. J. (2009b). Low-frequency acoustic reflection at a hard-soft lining transition in a cylindrical duct with uniform flow. *Journal of Engineering Mathematics*, 65(4):345–354.
- [21] Brambley, E. J. (2012). Review Of Acoustic Liner Models With Flow. In *Acoustics2012*, number April, pages 3429–3434.

- [22] Brambley, E. J., Darau, M., and Rienstra, S. W. (2012). The critical layer in linear-shear boundary layers over acoustic linings. *Journal of Fluid Mechanics*, 710:545–568.
- [23] Brown, C. E. and Michael, W. H. (1954). Effect of Leading-Edge Separation on the Lift of a Delta Wing. *Journal of the Aeronautical Sciences*, 21(10):690–694.
- [24] Clark, I., Alexander, W. N., and Devenport, W. J. (2017a). Bio-Inspired Finlets for the Reduction of Marine Rotor Noise. In *23rd AIAA/CEAS Aeroacoustics Conference*, page 3867.
- [25] Clark, I., Baker, D., Alexander, W. N., Devenport, W. J., Glegg, S. A., Jaworski, J., and Peake, N. (2016a). Experimental and Theoretical Analysis of Bio-Inspired Trailing Edge Noise Control Devices. In *22nd AIAA/CEAS Aeroacoustics Conference*.
- [26] Clark, I. A., Alexander, W. N., Devenport, W., Glegg, S., Jaworski, J. W., Daly, C., and Peake, N. (2017b). Bioinspired Trailing-Edge Noise Control. *AIAA Journal*, 55(3):740–754.
- [27] Clark, I. A., Daly, C. A., Devenport, W., Alexander, W. N., Peake, N., Jaworski, J. W., and Glegg, S. (2016b). Bio-inspired canopies for the reduction of roughness noise. *Journal of Sound and Vibration*, 385:33–54.
- [28] Clark, I. A., Devenport, W., Jaworski, J. W., Daly, C., Peake, N., and Glegg, S. (2014). The Noise Generating and Suppressing Characteristics of Bio-Inspired Rough Surfaces. In *20th AIAA/CEAS Aeroacoustics Conference*, number June.
- [29] Corless, R. M., Gonnet, G. H., Hare, D. E. G., Jeffrey, D. J., and Knuth, D. E. (1996). On the Lambert W function. *Advances in Computational Mathematics*, 5:329–359.
- [30] Crighton, D. G. (1972). Radiation from vortex filament motion near a half plane. *Journal of Fluid Mechanics*, 51(2):357–362.
- [31] Crighton, D. G. (1985). The Kutta Condition in Unsteady-Flow. *Annual Review of Fluid Mechanics*, 17(1979):411–445.
- [32] Crighton, D. G. (1991). Airframe Noise. In *Aeroacoustics of Flight Vehicles: Theory and Practice*, volume 1, pages 391–447. NASA Langley Research Centre.
- [33] Drazin, P. G. and Reid, W. (1985). *Hydrodynamic Stability*. Cambridge University Press.

- [34] Ffowcs Williams, J. E. and Hall, L. H. (1970). Aerodynamic sound generation by turbulent flow in the vicinity of a scattering half plane. *Journal of Fluid Mechanics*, 40(4):657–670.
- [35] Ffowcs Williams, J. E. and Hawkings, D. L. (1969). Sound generation by turbulence and surfaces in arbitrary motion. *Philosophical Transactions of the Royal Society of London. Series A, Mathematical and Physical Sciences*, 264(1151):321–342.
- [36] Gerhard, T., Erbslöh, S., and Carolus, T. (2014). Reduction of airfoil trailing edge noise by trailing edge blowing. In *Journal of Physics: Conference Series*, volume 524.
- [37] Geyer, T., Sarradj, E., and Fritzsche, C. (2014). Measuring owl flight noise. *43rd International Congress on Noise Control Engineering*, 1904(3):1–16.
- [38] Geyer, T. F., Sarradj, E., and Fritzsche, C. (2011). Vergleichende Überflugmessungen an Eulen und nicht leise fliegenden Vögeln. In *DACA*.
- [39] Glauert, H. (1928). The Effect of Compressibility on the Lift of an Aerofoil. *Proceedings of the Royal Society A: Mathematical, Physical and Engineering Sciences*, 118(779):113–119.
- [40] Glegg, S. and Devenport, W. J. (2017a). Leading Edge Noise from Very Thick Airfoils with Vertical Fences. *23rd AIAA/CEAS Aeroacoustics Conference*.
- [41] Glegg, S. A. and Devenport, W. J. (2017b). *Aeroacoustics of low mach number flows*. Academic Press.
- [42] Goldstein, M. E. (1978a). Characteristics of the unsteady motion on transversely sheared mean flows. *Journal of Fluid Mechanics*, 84(2):305–329.
- [43] Goldstein, M. E. (1978b). Unsteady vortical and entropic distortions of potential flows round arbitrary obstacles. *Journal of Fluid Mechanics*, 89(3):433–468.
- [44] Goldstein, M. E. (1979). Scattering and distortion of the unsteady motion on transversely sheared mean flows. *Journal of Fluid Mechanics*, 91(4):601–632.
- [45] Goldstein, M. E. (2001). An exact form of Lilley’s equation with a velocity quadrupole/temperature dipole source term. *Journal of Fluid Mechanics*, 443:231–236.
- [46] Goldstein, M. E., Afsar, M. Z., and Leib, S. J. (2013). Non-homogeneous rapid distortion theory on transversely sheared mean flows. *J. Fluid Mech*, 736:532–569.

- [47] Goldstein, M. E. and Atassi, H. (1976). A complete second-order theory for the unsteady flow about an airfoil due to a periodic gust. *Journal of Fluid Mechanics*, 74(04):741.
- [48] Goldstein, M. E., Leib, S. J., and Afsar, M. Z. (2017). Generalized rapid-distortion theory on transversely sheared mean flows with physically realizable upstream boundary conditions: Application to trailing-edge problem. *Journal of Fluid Mechanics*, 824:477–512.
- [49] Graham, R. (1934). Silent Flight of Owls. *Journal of the Royal Aeronautical Society*, 38:837–843.
- [50] Heaton, C. J. and Peake, N. (2006). Algebraic and exponential instability of inviscid swirling flow. *Journal of Fluid Mechanics*, 565:279–318.
- [51] Hertel, H. (1966). *Structure, form, movement*. Reinhold, New York.
- [52] Hinch, E. J. (1991). *Perturbation methods*. Cambridge University Press.
- [53] Howe, M. (1996). Emendation of the Brown & Michael equation, with application to sound generation by vortex motion near a half-plane. *Journal of Fluid Mechanics*, 329:89–101.
- [54] Howe, M. (1999). Trailing edge noise at low Mach numbers. *Journal of Sound and Vibration*, 225(2):211–238.
- [55] Howe, M. S. (1975). Contributions to the theory of aerodynamic sound, with application to excess jet noise and the theory of the flute. *Journal of Fluid Mechanics*, 71(04):625.
- [56] Howe, M. S. (1978). A review of the theory of trailing edge noise. *J. Sound and Vibration*, 61(3):437–465.
- [57] Howe, M. S. (1991). Noise produced by a sawtooth trailing edge. *The Journal of the Acoustical Society of America*, 90(1):482–487.
- [58] Howe, M. S. (2002). *Theory of Vortex Sound*. Cambridge University Press, Cambridge.
- [59] Hubbard, H. (1994). *Aeroacoustics of flight vehicles, theory and practices Volume 1: Noise Sources and Volume 2: Noise Control*. NASA Langley Research Center.
- [60] Hunt, J. C. and Carruthers, D. J. (1990). Rapid distortion theory and the ‘problems’ of turbulence. *Journal of Fluid Mechanics*, 212(2):497–532.

- [61] Ingard, U. (1959). Influence of Fluid Motion Past a Plane Boundary on Sound Reflection, Absorption, and Transmission. *The Journal of the Acoustical Society of America*, 31(7):1035–1036.
- [62] Innes, D. and Crighton, D. (1989). On a non-linear differential equation modelling Helmholtz resonator response. *Journal of Sound and Vibration*, 131(2):323–330.
- [63] Jaworski, J. W. and Peake, N. (2013). Aerodynamic noise from a poroelastic edge with implications for the silent flight of owls. *Journal of Fluid Mechanics*, 723:456–479.
- [64] Jones, D. S. (1950). Note on diffraction by an edge. *Quarterly Journal of Mechanics and Applied Mathematics*, 3(4):420–434.
- [65] Jones, L. E. and Sandberg, R. D. (2012). Acoustic and hydrodynamic analysis of the flow around an aerofoil with trailing-edge serrations. *Journal of Fluid Mechanics*, 706:295–322.
- [66] Khamis, D. and Brambley, E. J. (2017). Viscous effects on the acoustics and stability of a shear layer over an impedance wall. In *Journal of Fluid Mechanics*, volume 810, pages 489–534. Cambridge University Press.
- [67] Koppen, E. and Fowler, K. (2015). International legislation for wind turbine noise. *Proceedings of the Euronoise*.
- [68] Kroeger, R., Grushka, H., Helvey, T., and Tullahoma., T. U. S. I. (1972). *Low speed aerodynamics for ultra-quiet flight*. Defense Technical Information Center.
- [69] Lighthill, M. J. (1952). On sound generated aerodynamically I. General theory. *Proceedings of the Royal Society of London. Series A. Mathematical and Physical Sciences*, 211(1107):564–587.
- [70] Lighthill, M. J. (1954). On Sound Generated Aerodynamically. II. Turbulence as a Source of Sound. *Proceedings of the Royal Society A: Mathematical, Physical and Engineering Sciences*, 222(1148):1–32.
- [71] Lilley, G. (1998). A study of the silent flight of the owl. In *4th AIAA/CEAS Aeroacoustics Conference*, volume 2340, page 1–6.
- [72] Lyu, B., Azarpeyvand, M., and Sinayoko, S. (2016). Prediction of noise from serrated trailing edges. *Journal of Fluid Mechanics*, 793:556–588.

- [73] Maslowe, S. (1986). Critical Layers in Shear Flows. *Annual Review of Fluid Mechanics*, 18(1):405–432.
- [74] Moreau, D. J. and Doolan, C. J. (2013). Noise-Reduction Mechanism of a Flat-Plate Serrated Trailing Edge. *AIAA Journal*, 51(10):2513–2522.
- [75] Myers, M. and Kerschen, E. J. (1995). Influence of Incidence Angle on Sound Generation by Airfoils Interacting with High Frequency Gusts. *Journal of Fluid Mechanics*, 292:271–304.
- [76] Myers, M. and Kerschen, E. J. (1997). Influence of camber on sound generation by airfoils interacting with high-frequency gusts. *Journal of Fluid Mechanics*, 353:221–259.
- [77] Myers, M. K. (1980). On the acoustic boundary condition in the presence of flow. *Journal of Sound and Vibration*, 71(3):429–434.
- [78] Neuhaus, W., Bretting, H., and Schweizer, B. (1973). Morphologische und funktionelle Untersuchungen über den lautlosen Flug der Eulen (*Strix aluco*) im Vergleich zum Flug der Enten (*Anas platyrhynchos*). *Biol Zbl*, 92:495–512.
- [79] Noble, B. (1958). *Methods based on the Wiener-Hopf technique for the solution of partial differential equations*. Pergamon Press Ltd., 1 edition.
- [80] Orr, F. (1907). The Stability or Instability of the Steady Motions of a Perfect Liquid and of a Viscous Liquid. Part II: A Viscous Liquid. *Source: Proceedings of the Royal Irish Academy. Section A: Mathematical and Physical Sciences*, 27:69–138.
- [81] Priddin, M. J., Baker, D. I., Ayton, L. J., and Peake, N. (2018). Vortex Sound Models: Passive and Active Noise Control. *24th AIAA/CEAS Aeroacoustics Conference*.
- [82] Pridmore-Brown, D. C. (1958). Sound propagation in a fluid flowing through an attenuating duct. *Journal of Fluid Mechanics*, 4(4):393–406.
- [83] Rawlins, A. D. (1975). The solution of a mixed boundary value problem in the theory of diffraction by a semi-infinite plane. In *Proceedings of the Royal Society of London A: Mathematical, Physical and Engineering Sciences*, pages 469–484. The Royal Society.
- [84] Rayleigh, L. (1879). On the Stability, or Instability, of certain Fluid Motions. *Proceedings of the London Mathematical Society*, s1-11(1):57–72.
- [85] Rienstra, S. and Peake, N. (2005). Modal scattering at an impedance transition in a lined flow duct. In *11th AIAA/CEAS Aeroacoustics Conference*, page 2852.

- [86] Rienstra, S. W. (1985). Irregular modes in a duct with an impedance wall. *Presented at the Dutch Acoustic Society on Flow Noise, Utrecht, The Netherlands, 11 Sep. 1985.*
- [87] Rienstra, S. W. (1987). *The acoustics of a lined duct with flow*. WD report. NLR.
- [88] Rienstra, S. W. (2003). A classification of duct modes based on surface waves. *Wave motion*, 37(2):119–135.
- [89] Rienstra, S. W. (2007). Acoustic scattering at a hard-soft lining transition in a flow duct. *Journal of Engineering Mathematics*, 59(4):451–475.
- [90] Rienstra, S. W. (2016). Sound Propagation in Slowly Varying 2D Duct with Shear Flow. In *22nd AIAA/CEAS Aeroacoustics Conference*.
- [91] Rienstra, S. W. and Darau, M. (2011). Boundary-layer thickness effects of the hydrodynamic instability along an impedance wall. *Journal of Fluid Mechanics*, 671:559–573.
- [92] Rienstra, S. W., Darau, M., and Brambley, E. J. (2013). The trailing vorticity field behind a line source in two-dimensional incompressible linear shear flow. *Journal of Fluid Mechanics*, 720:618–636.
- [93] Rienstra, S. W. and Singh, D. K. (2014). Hard wall-soft wall-vorticity scattering in shear flow. In *20th AIAA/CEAS Aeroacoustics Conference, 16-20 June 2014, Atlanta, Georgia, USA*.
- [94] Roger, M. (2008). Back-scattering correction and further extensions of Amiet ' s trailing-edge noise model . Part II : Application. *Journal of Sound and Vibration*, 323(2009):1–29.
- [95] Roger, M. and Moreau, S. (2005). Back-scattering Correction and Further Extensions of Amiet's Trailing Edge Noise Model, Part 1: Theory. *Journal of Sound and Vibration*, 286(3):477–506.
- [96] Schuster, W. B. (2002). *Trailing edge noise produced by the scattering of boundary layer turbulence*. PhD thesis, The University of Arizona.
- [97] Schwarzschild, K. (1901). Die Beugung und Polarisation des Lichts durch einen Spalt. I. *Mathematische Annalen*, 55(2):177–247.
- [98] Shi, Y. and Lee, S. (2018). Numerical Study of 2-D Finlets Using RANS CFD for Trailing Edge Noise Reduction. In *2018 AIAA/CEAS Aeroacoustics Conference*, Reston, Virginia. American Institute of Aeronautics and Astronautics.

- [99] Showkat Ali, S. A., Szoke, M., Azarpeyvand, M., and Ilario da Silva, C. R. (2018). Turbulent Flow Interaction with Porous Surfaces. In *2018 AIAA/CEAS Aeroacoustics Conference*, Reston, Virginia. American Institute of Aeronautics and Astronautics.
- [100] Siemens (2016). New Siemens Low-Noise Wind Turbine Inspired By Flight Of The Owls [Press Release].
- [101] Singh, D. K. (2016). Vorticity scattering in shear flows at soft wall–Hard wall transition. In *22nd AIAA/CEAS Aeroacoustics Conference*, page 2703.
- [102] Singh, D. K. and Rienstra, S. W. (2014). Nonlinear asymptotic impedance model for a Helmholtz resonator liner. *Journal of Sound and Vibration*, 333(15):3536–3549.
- [103] Smith, S. G. L. (2007). MAE207 Applications of complex analysis.
- [104] Sommerfeld, A. (1896). Mathematische Theorie der Diffraction. *Mathematische Annalen*, 47(2-3):317–374.
- [105] Sommerfeld, A. (1949). *Partial Differential Equations in Physics*. Academic Press.
- [106] Szőke, M. and Azarpeyvand, M. (2017). Active Flow Control Methods for the Reduction of Trailing Edge Noise. *23rd AIAA/CEAS Aeroacoustics Conference*.
- [107] Tam, C. K. and Auriault, L. (1998). Mean flow refraction effects on sound radiated from localized sources in a jet. *Journal of Fluid Mechanics*, 370:149–174.
- [108] Taylor, G. I. (1938). The Spectrum of Turbulence. *Proceedings of the Royal Society A: Mathematical, Physical and Engineering Sciences*, 164(919):476–490.
- [109] Veitch, B. and Peake, N. (2008). Acoustic propagation and scattering in the exhaust flow from coaxial cylinders. *Journal of Fluid Mechanics*, 613:275–307.
- [110] Vilenski, G. G. and Rienstra, S. W. (2007a). Numerical study of acoustic modes in ducted shear flow. *Journal of Sound and Vibration*, 307(3-5):610–626.
- [111] Vilenski, G. G. and Rienstra, S. W. (2007b). On hydrodynamic and acoustic modes in a ducted shear flow with wall lining. *Journal of Fluid Mechanics*, 583:45–70.
- [112] Watson, G. N. (1918). The Harmonic Functions Associated with the Parabolic Cylinder. *Proceedings of the London Mathematical Society*, s2-17(1):116–148.
- [113] Wegert, E. (2010). Phase Plots of Complex Functions: a Journey in Illustration. *arXiv.org*, 58(6):17.

- [114] Weisstein, E. W. (2018a). Helmholtz Differential Equation – Circular Cylindrical Coordinates.
- [115] Weisstein, E. W. (2018b). Runge-Kutta Method.
- [116] White, F. (2010). Fluid Mechanics. *McGraw-Hill, New York*, page 862.
- [117] Wiener, N. and Hopf, E. (1931). *Über eine Klasse singulärer Integralgleichungen*. Sitzungsberichte der Preussischen Akademie der Wissenschaften. Physikalisch-mathematische Klasse. Akad. d. Wiss.
- [118] Wolf, A., Lutz, T., Würz, W., Krämer, E., Stalnov, O., and Seifert, A. (2015). Trailing edge noise reduction of wind turbine blades by active flow control. *Wind Energy*, 18(5):909–923.

Appendix A

Appendices to Chapter 3

A.1 The existence N hard-wall modes

It was claimed in §3.5 that D_h typically has N zeros, for an N -piece profile. Naïvely this straightforward: D_h is uniformly unity for uniform flow, and the introduction of a pole, via the introduction of a jump in shear, should logically correspond to the introduction of a zero. We extend the usual methods of demonstrating stability of Rayleigh's equation [33] to prove the existence of these zeros and to say something about their location, in the special case of a concave decreasing background profile, i.e. $U''(x_2) \leq 0$ throughout (or, in the piecewise linear case, $\Delta\sigma_j \leq 0$ for all j).

Consider the equation satisfied by ψ_d , with the jump conditions included with the use of Dirac δ -functions, namely

$$\psi_d'' - k_1^2 \psi_d + \sum_{j=1}^N \frac{\Delta\sigma_j k_1}{\omega - U_j k_1} \delta(x_2 - \delta_j) \psi_d = 0. \quad (\text{A.1.1})$$

Multiplying this by ψ_d^* and integrating over x_2 gives

$$-\psi_d^*(0)\psi_d'(0) - \int_0^\infty |\psi_d'|^2 + k_1^2 |\psi_d|^2 dx_2 + \sum_{j=1}^N \frac{|\psi_d(\delta_j)|^2 \Delta\sigma_j k_1}{\omega - U_j k_1} = 0. \quad (\text{A.1.2})$$

For a modal solution, $\psi_d^*(0) = 0$. We can use this to limit the location of the poles. Firstly, with this assumption, taking the imaginary part of (A.1.2), with $k_1 = k_r + ik_i$, gives

$$2k_r k_i \int_0^\infty |\psi_d|^2 dx_2 = \omega k_i \sum_{j=1}^N \frac{|\psi_d(\delta_j)|^2 \Delta\sigma_j}{|\omega - U_j k_1|^2} \quad (\text{A.1.3})$$

where we are considering the case ω real and positive. If $\Delta\sigma_j < 0$ for all j , i.e. the concave case, we have solutions if either $k_i = 0$ or, since the integral is strictly positive and the right-hand side strictly negative, $k_r < 0$. We shall, for now, ignore the latter case and focus on real k_1 . This simply returns the result that a concave profile is stable.

For real k_1 , the real part of (A.1.2) can be written as

$$A(k_1) = - \sum_{j=1}^N \frac{C_j(k_1)}{\omega - U_j k_1} \quad (\text{A.1.4})$$

with $A(k_1) = \int |\psi'_d|^2 dx_2 + k_1^2 \int |\psi_d|^2$ and $C_j = -\Delta\sigma_j k_1 |\psi_d(\delta_j)|^2$. All of A and C_j are positive for all k_1 . This allows the immediate observation that there are no solutions for $k_1 < \omega/U_\infty$, since the right-hand side is negative and the left is positive. We now claim there are at least N solutions to this, with at least one solution lying in each interval $k_1 \in (\omega/U_j, \omega/U_{j-1})$. This follows from considering the behaviour of A near $k_1 = \omega/U_j$, where it has a pole, and is dominated by the term $-C_j/(\omega - U_j k_1)$. The sign must change over this pole, and since for $k_1 < \omega/U_j$ the denominator is positive, the sign must change from negative to positive. Between each pair of poles, A must therefore cross the real axis and give rise to a zero. Existence of this solution indicates that either $\psi_d(0) = 0$ or $\psi'_d(0) = 0$, which is not quite as strong a condition as required.

A.2 Numerical complex methods implementation

Most of these methods are based on the lecture course given by Llewellyn Smith [103], unless noted otherwise. We look at reasonably routine implementation of numerical routines for various aspects of complex variable theory, mainly focusing on performing integration and utilising integral formulae.

A.2.1 Integration

Suppose we have an integral of the form

$$J = \int_C I(z) dz \quad (\text{A.2.1})$$

and we can parameterise the contour C by $C(t)$, with $a \leq t \leq b$. Then

$$J = \int_a^b I(C(t)) \frac{dC}{dt} dt \equiv \int_a^b \bar{I}(t) dt \quad (\text{A.2.2})$$

somewhat trivially. In most applications, we can numerically approximate this using Gauss-Legendre quadrature, with

$$J \approx \sum_{j=0}^N w_j \bar{I}(t_j) \quad (\text{A.2.3})$$

with integration points t_j and weights w_j found in most reference texts [2] for simple Gaussian quadrature (where the function is well-behaved at the end points, with a linear mapping required to the interval $[-1, 1]$) with similar structures for integrably-singular end points. Most integrals in this work are computed using the “Legendre-Gauss Quadrature Weights and Nodes” Matlab package, by Greg von Winckel.

We have assumed finite integrals. If the range of the integral is infinite, we can typically map to a finite region. For example, the interval $(-\infty, \infty)$ is mapped to $(-1, 1)$ via the inverse of the substitution

$$t = \frac{s}{1 - s^2}. \quad (\text{A.2.4})$$

This mapping, and similar mappings, allows standard quadrature routines for finite intervals. Whilst the error of quadrature routines is hard to estimate, they are in practise rapidly convergent with quadrature points N , particularly for non-oscillatory integrals.

For integrals with a periodic integrand (for example integrals around closed contours) it is often sufficient to use the trapezium rule (as done in §B.1), with exponential accuracy. We have

$$\int_0^1 f(z) dz \approx \frac{1}{N} \sum_{j=1}^N f\left(\frac{j}{N}\right) \quad (\text{A.2.5})$$

if $f(z) = f(z + 1)$, which is straightforward to implement.

A.2.2 Pole/zero finding

Suppose we have a simple closed contour C in the complex plane, so that if a function $f : \mathbb{C} \rightarrow \mathbb{C}$ is analytic on the interior of C , then it satisfies the Cauchy integral theorem,

$$\int_C f(z) dz = 0. \quad (\text{A.2.6})$$

The number of zeros of f within C (if traversed anticlockwise) can then be calculated to be

$$N_Z = \frac{1}{2\pi i} \int_C \frac{f'(z)}{f(z)} dz, \quad (\text{A.2.7})$$

which is equivalent to determining the change in $\log(f(z))$ around C , where \log is defined to have continuous argument as C is traversed. If f is not analytic, but is instead meromorphic (analytic except at isolated complex poles), then this formula instead gives $N_Z - N_P$, the number of zeros minus the number of poles. Together, these two formulae quickly allow the number of zeros in a region to be calculated: first by confirming it is analytic (and there are no branch cuts) and secondly directly computing the zeros. Provided C is finite, it is straightforward to use previously introduced integration routines.

Once we have identified the number of zeros within a region, there are multiple methods to hone in on their location. Suppose f is analytic (without poles) within C , and has zeros z_j for $j = 1, \dots, N_Z$. Modifying the formula used to compute the number of zeros allows location of the zeros, via

$$\sum_{j=1}^{N_Z} z_j^n = \frac{1}{2\pi i} \int_C \frac{z^n f'(z)}{f(z)} dz \quad (\text{A.2.8})$$

using similar logic to before, for integer j . Thus, if $N_Z = 1$ (so that there is a single zero within C), completing this calculation for $n = 1$ immediately returns the location of the zero. For higher numbers of zeros, one can compute this for all orders up to $n = Z$ and then determine the location of the zeros by solving a series of polynomial equations. This is inefficient, however.

Instead, code has been written to locate the zeros via a bisection method, as illustrated in figure A.2.1. We begin with a box in the complex plane, bounded by C_0 . If there are no zeros within a box (as computed via (A.2.7)), that box is no longer subdivided and is ignored for future calculations. If there are multiple zeros within a box, the box is then subdivided into four and integral (A.2.7) is computed for each new box. If there is a single zero in the box, the summation formula (A.2.8) (with $n = 1$) is used to find the location of the zero. At each step, the integrals do not need to be particularly precise, so a low-order quadrature is typically appropriate, with the value of N_Z for a given box rounded to the nearest integer. For more precision, a range around each integer is treated as corresponding to that integer, for example if $N_Z \in (0.9, 1.1)$ we assume $N_Z = 1$ for that box. This allows low order quadrature and thus vastly reduces numerical complexity, though this will in turn introduce errors in (A.2.8). This suggests using iterative methods to precisely determine the zero location, once the approximate location has been determined via a bisection method. Further, if the zero lies near any grid lines, or in even worse cases on the lines, this method will fail as the integration cannot be suitably accurate. Further, N_Z is computed with multiplicity. This method will not work if there is, for example, a double zero at a single location, since N_Z will never be unity for any contour choice.

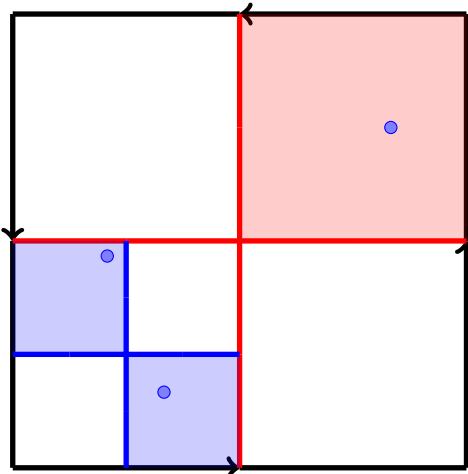


Fig. A.2.1 Contours for the bisection method, schematically shown in the case of f having three zeros (shown by open circles). Integration of (A.2.7) is done recursively, beginning with the black outer contour, followed by the red division (into quarters), followed by the blue division (into sixteenths), terminating when the number of zeros in each square is either one (schematically shown as shaded) or none. All contours are traversed anti-clockwise. In this case, two iterations are enough to broadly identify the location of the outer zero but three are required for the second and third. The closer the zeros, the more iterations are required to separate them.

Zeros can also be located using the standard Newton-Raphson iteration scheme. If f and f' are both known (potentially computing f' numerically via central differences or better methods) then the iterative scheme

$$z_{n+1} = z_n - \frac{f(z_n)}{f'(z_n)} \quad (\text{A.2.9})$$

gives a recursive method of finding the zero. If it converges, then it will converge to a zero of f , even in the complex plane. It does, however, require a good initial guess (which is where the bisection method is useful for beginning the analysis). If f has multiple zeros and we have found a single zero z_0 , then defining

$$\bar{f}(z) = \frac{f(z)}{z - z_0} \quad (\text{A.2.10})$$

which is regular at z_0 , allows repeated application of this and similar methods to find further zeros.

Typically in this work a coarse bisection method followed by Newton-Raphson will be used, with the bisection used to obtain an approximate zero location. Alternatively, it is possible to eyeball zeros of a function by using a phase plot, and using this as an

initial Newton-Raphson guess. Whilst this is often successful, it does not lend itself to automation. This is applicable to both functions for which there is an explicit expression for f and for which f is computed via solution of a differential equation, for example most dispersion relations in this work, provided the function can be efficiently evaluated along each contour for the variable of interest (typically the streamwise wavenumber k_1), as with the vectorised Runge-Kutta routines used throughout §4.2.3.

Appendix B

Appendix to Chapter 4

B.1 Numerical solution: Frobenius methods

As we saw in §4.2.3, the direct boundary-layer integration runs into difficulties near $C = 0$, for which $k_1 = \omega/U(x_2)$ for some $x_2 \in [0, \delta]$, where δ may be infinity. This occurs on along the line $k_1 \in [\omega/U_\infty, \omega/U_0]$ in the complex plane, which lies on the real axis when ω is real (assuming U is monotonic). When $C = 0$, we have a regular singular point, with the coefficient of ϕ' , $p(x_2)$, behaving like $1/(x_2 - x_0)$ (with x_0 the location of this critical point) [22]. Via the method of Frobenius, this means we can find an exact series expansion valid in the immediate proximity of this point. Under certain conditions, this expansion is valid across the width of the boundary-layer (from 0 to δ) and as such can be used to accurately evaluate, for example, the dispersion function near the critical layer.

Consider first the generic ODE

$$\phi''(z) + \frac{P(z)}{z - z_0} \phi'(z) + \frac{Q(z)}{(z - z_0)^2} \phi(z) = 0 \quad (\text{B.1.1})$$

with P and Q analytic in some radius around $z = z_0$. They can as such be expanded as

$$P(z) = \sum_{j=0}^{\infty} p_n (z - z_0)^n \quad (\text{B.1.2a})$$

$$Q(z) = \sum_{j=0}^{\infty} q_n (z - z_0)^n \quad (\text{B.1.2b})$$

and we try two solutions of the form

$$\phi_1 = \sum_{j=0}^{\infty} c_n (z - z_0)^{n+\sigma_1} \quad (\text{B.1.3a})$$

$$\phi_2 = D\phi_1 \log(z - z_0) + \sum_{j=0}^{\infty} d_n (z - z_0)^{n+\sigma_2} \quad (\text{B.1.3b})$$

with $\sigma_{1,2}$ determined by the condition that $c_0, d_0 \neq 0$. The constant due to degeneracy, D , might be zero, depending on the relationship between σ_1 and σ_2 . Substituting the expansion for ϕ_1 into the governing equation gives

$$\sum_{j=0}^{\infty} c_n (n+\sigma)(n+\sigma+1) z^{n+\sigma-2} + \left(\sum_{k=0}^{\infty} p_n z^n \right) \left(\sum_{j=0}^{\infty} c_n (n+\sigma) z^{n+\sigma-1} \right) + \left(\sum_{k=0}^{\infty} q_n z^n \right) \left(\sum_{j=0}^{\infty} c_n z^{n+\sigma} \right) = 0. \quad (\text{B.1.4})$$

If we use the Cauchy identity for summations, namely

$$\left(\sum_{j=0}^{\infty} f_j \right) \left(\sum_{k=0}^{\infty} g_k \right) = \sum_{j=0}^{\infty} \sum_{k=0}^j f_k g_{j-k} \quad (\text{B.1.5})$$

(assuming all series converge), the solution can be rewritten as

$$\sum_{n=0}^{\infty} z^{n+\sigma-2} \left[c_n (n+\sigma)(n+\sigma-1) + \sum_{k=0}^n (p_{n-k} c_k (k+\sigma)) + \sum_{\ell=0}^n (q_{n-\ell} c_{\ell}) \right] = 0, \quad (\text{B.1.6})$$

and so the coefficients satisfy, for $n \geq 0$

$$c_n (n+\sigma)(n+\sigma-1) + \sum_{k=0}^n (p_{n-k} c_k (k+\sigma)) + \sum_{\ell=0}^n (q_{n-\ell} c_{\ell}) = 0. \quad (\text{B.1.7})$$

This allows recursive solution for c_n in terms of c_j for $j < n$. Picking $n = 0$ and insisting that $c_0 \neq 0$ gives the indicial equation for $\sigma_{1,2}$:

$$\sigma^2 + (p_0 - 1)\sigma + q_0 = 0 \quad (\text{B.1.8})$$

We impose $\sigma_1 > \sigma_2$, and there is always a series solution generated for σ_1 . We define $\delta\sigma = \sigma_1 - \sigma_2 \geq 0$. If the roots $\sigma_{1,2}$ of this equation are distinct and do not differ by an integer, then $D = 0$. If the root is repeated ($\delta\sigma = 0$) then $C = 1$ without loss of generality, and otherwise ($\delta\sigma$ a positive integer) C must be determined, with instead the coefficient $d_{\delta\sigma}$ being arbitrary. We can do a similar analysis for the series solution with a logarithmic

term. For $n = 0$ to $\sigma_1 - \sigma_2 - 1$, the coefficients d_n satisfy (B.1.7), unchanged. This then allows computation of C as

$$D = -\frac{\sum_{j=0}^{\delta\sigma-1} d_j p_{\delta\sigma-j}(j + \sigma_2) + \sum_{j=0}^{\delta\sigma-1} d_j q_{\delta\sigma-j}}{c_0(2\sigma_1 - 1) + c_0 p_0}. \quad (\text{B.1.9})$$

This requires setting $d_{\delta\sigma} = 0$. This is allowed, as choice of a different constant merely reproduces a multiple of the already determined ϕ_1 . The remaining coefficients d_n can then be determined from evaluating the higher-order terms, noting the contribution from c_n . Explicitly, we have

$$c_n = -\frac{\sum_{j=0}^{n-1} c_j p_{n-j}(\sigma_1 + j) + \sum_{j=0}^{n-1} c_j q_{n-j}}{(n + \sigma_1)(n + \sigma_1 - 1) + p_0(n + \sigma_1) + q_0} \quad (\text{B.1.10})$$

$$d_n = -\frac{\sum_{j=0}^{n-1} d_j p_{n-j}(\sigma_2 + j) + \sum_{j=0}^{n-1} d_j q_{n-j} + D \left(\sum_{j=0}^{n-\delta\sigma} c_j p_{n-\delta\sigma-j} + c_{n-\delta\sigma}(2n + 2\sigma_2 - 1) \right)}{(n + \sigma_2)(n + \sigma_2 - 1) + p_0(n + \sigma_2) + q_0} \quad (\text{B.1.11})$$

with sums understood to vanish if the upper limit of summation is less than than the lower limit. These are straightforward to implement algorithmically, being sums and products of known numbers, providing a rapid polynomial approximation of the solution to high-order rapidly.

B.1.1 Computation of Taylor/Laurent coefficients

We have assumed that we know expansions of P and Q in powers of $(z - z_0)$. This is equivalent to knowing Laurent expansions of $p(z) = P(z)/(z - z_0)$ and $q(z) = Q(z)/(z - z_0)^2$, which links to the formulation described earlier. In both cases, robust numerical implementation of Cauchy's integral formula exist when p and q are defined (locally) in the complex plane about z_0 [17]. Suppose a function p has the Laurent expansion (wlog around $z_0 = 0$)

$$p(z) = \sum_{j=-N}^{\infty} p_j z^j \quad (\text{B.1.12})$$

where N might be infinity, but for the purposes of this exercise is a finite integer. The coefficients are then explicitly given by

$$p_j = \frac{1}{2\pi i} \int_{\gamma} \frac{p(z)}{z^{j+1}} dz \quad (\text{B.1.13})$$

with γ a simple closed contour containing $z = 0$, traversed anticlockwise, with $p(z)$ analytic ($z = 0$ aside) on the interior of the contour.

Picking the contour to be the unit circle $|z| = R$, the symmetry and periodic nature of the integral allows accurate discretisation of this integral as

$$p_j \approx \frac{1}{mR^n} \sum_{j=0}^{m-1} p(R e^{2\pi i j/m}) e^{-2n\pi i j/m} \quad (\text{B.1.14})$$

with R and m chooseable parameters. Whilst it might seem choosing R as small as possible (evaluating as close as possible to the singularity) is appropriate for accuracy, it can be seen the leading factor of R^{-n} amplifies numerical errors (for example, if the integral is smaller than machine error) for higher n , and as such it makes sense to choose $R = 1$ or larger if possible, that is if p has no other singularities within this radius.

This is often the most numerically challenging part of the exercise, particularly if the ODE depends on some parameter k . Ideally, these coefficients should be computed analytically where possible. For the incompressible Rayleigh equation, this is possible if an analytic expression for U and c_0 exists, however numerical methods remove the need to vary the routine with the choice of background flow, which is useful for the construction of generic numerical routines.

B.1.2 Construction of ODE solutions, and range of validity

We have two solutions ϕ_1 and ϕ_2 that form a basis for the solutions to the differential equation in some region around z_0 . If we look for a specific solution ϕ that satisfies some conditions at a point $z = \delta$, with $\phi(\delta) = \alpha$ and $\phi'(\delta) = \beta$, then

$$\phi = \frac{\phi'_2(\delta)\alpha - \phi_2(\delta)\beta}{\phi_1(\delta)\phi'_2(\delta) - \phi_2(\delta)\phi'_1(\delta)}\phi_1(z) + \frac{\phi'_1(\delta)\alpha + \phi_1(\delta)\beta}{\phi_1(\delta)\phi'_2(\delta) - \phi_2(\delta)\phi'_1(\delta)}\phi_2(z) \quad (\text{B.1.15})$$

with series expressions available for ϕ_j and ϕ'_j .

This assumes that $z_0 - \delta$ is within the radius of convergence for the power series solutions, which is the same as the radius of convergence for the series expansions of p and q : that is, there is no other singular points within a circle of radius $|z_0 - \delta|$ around z_0 . If we want a solution valid across the boundary-layer, from $z = 0$ to $z = \delta$, we require $|z_0|, |z_0 - \delta| < |z_0 - z_{0j}|$ for all j , with z_{0j} the set of singularities of p and q away from $z = z_0$.

We demonstrate this by considering the formulation of the compressible Rayleigh equation as in (4.2.4), with

$$p(x_2) = \frac{(c_0^2)'}{c_0^2} + \frac{4C'}{C}, \quad (\text{B.1.16a})$$

$$q(x_2) = \frac{3C''}{C} + \frac{C'(c_0^2)'}{Cc_0^2} - (k_1^2 + k_3^2) - \frac{C^2}{c_0^2}. \quad (\text{B.1.16b})$$

If the background flow profile is monotonic on $(0, \delta)$ for some δ , which may be infinite, then C has at most a single zero within the boundary-layer, at the location x_2 with

$$U(x_2) = \frac{\omega}{k_1}. \quad (\text{B.1.17})$$

Both p and q are singular at this point, which we shall call x_0 . However, unless $x_2 = x_0$ is a double zero of C , both p and q have a simple pole there and we can evaluate $p_0 = 4$ and $q_0 = 0$, where p_j and q_j are the Taylor coefficients of $(x_2 - x_0)p(x_2)$ and $(x_2 - x_0)^2q(x_2)$ about $x_2 = x_0$, respectively. The indicial equation is then simply

$$\sigma^2 + 3\sigma = 0 \quad (\text{B.1.18})$$

and so $\sigma_1 = 0$ and $\sigma_2 = -3$. These roots differ by an integer, and as such we would expect D to be non-zero, though this is not always the case (as we have seen in the piecewise linear, incompressible case).

By way of illustration, consider first the *compressible* Rayleigh equation with U linear in x_2 , so that $U = U_0 + \sigma x_2$, with $\sigma = (U_\infty - U_0)/\delta$, and we will match to a uniform solution outside the boundary-layer with previous cases. Extending the definition of U to the complex plane (with coordinate z) we have transformed convective derivative

$$C(z) = i((\omega - U_0 k_1) - k_1 \sigma z). \quad (\text{B.1.19})$$

There is a single regular singular point of the Rayleigh equation (in the entire complex plane without infinity) when $C = 0$, which occurs when

$$z = z_0(k_1) = \frac{\omega - U_0 k_1}{k_1 \sigma}. \quad (\text{B.1.20})$$

Since this is unique, and p and q are otherwise analytic, the series solutions are valid for all z (though for an accurate approximation a higher numbers of terms will be required away from the critical point). This allows, for example, precise evaluation of the hard-

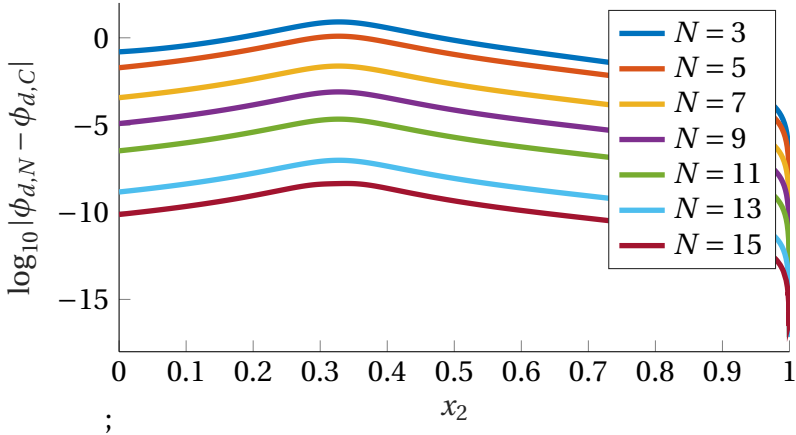
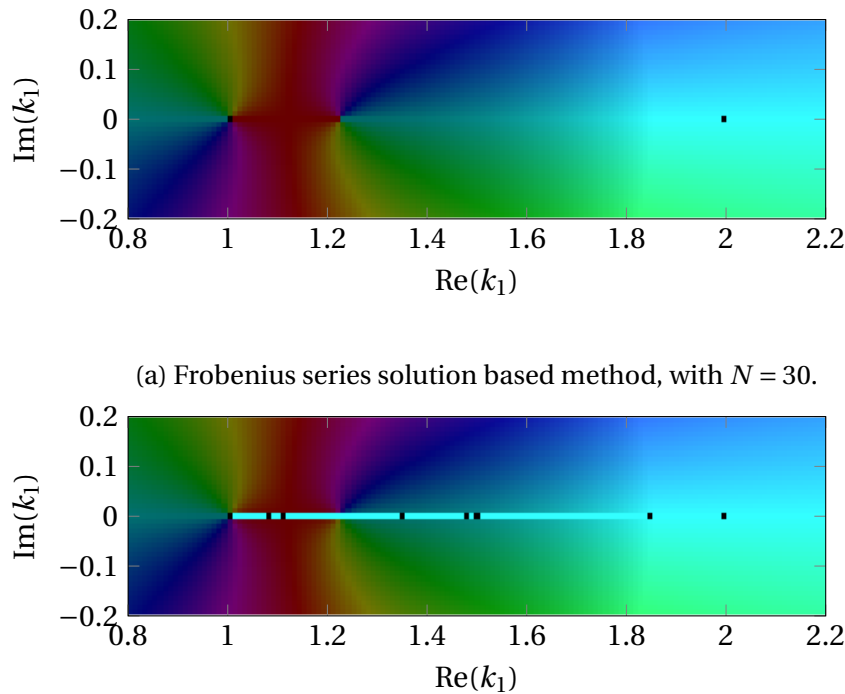


Fig. B.1.1 Considering a linear profile with $U_0 = 0.5$ and $U_\infty = 1$, scaling lengths with δ_∞ . The background speed of sound is constant, $c_0 = 2$, and frequency $\omega = 1$. For $k_1 = 1.5 + 0.1i$, near and above the critical layer, the decaying solution is computed via a series method, truncating sums after N terms. This is compared to the integrated solution with step size 1×10^{-4} , and (the logarithm of) their difference plotted across the boundary-layer (so both functions fixed identical at $x_2 = 1$). Error rapidly decreases with N . For large N , the apparent error is most likely caused by the error in the alternative method from integrating over the boundary-layer, and is more pronounced near the critical point. The series solution is very accurate even for N small, with an absolute error of around 5% in the smallest possible case $N = 3$.

wall dispersion function $D_h(k_1)$ in the vicinity of the critical-layer (which contains all k_1 such that $z_0(k_1)$ is real and lies between 0 and δ), which can be compared to the directly integrated solution and demonstrates the accuracy of this method near the critical-layer, see figures B.1.1 and B.1.2a. The method is particularly precise near the slipping edge of the critical layer, with $k_1 \approx \omega/U_0$. In the linear case there is not actually a branch cut along where the critical-layer would be, but the Frobenius method highlights the root of the dispersion relation on the real axis.

The critical-layer forms a natural branch-cut in the complex plane, which masks what is happening along the cut itself. This method allows choice of direction of this branch cut, through the log term [22], which allows isolation of the zero of the dispersion of this critical-layer in this case (though, as we can see, the critical-layer is removable if the background profile is linear and there is no geometry). This is similar to the deformation of the critical-layer seen when numerically integrating along a complex contour, as in the next section and, for example, figure 4.2.7.

We have established that this method is effective in the case of a linear profile, extending the long-wavelength analysis somewhat. What happens, however, if the background profile has some variation in shear? We consider first the simplest case of a parabolic

(a) Frobenius series solution based method, with $N = 30$.

(b) Integrated solution across boundary-layer, with step size 1/1000.

Fig. B.1.2 For the setup as in Figure B.1.1, direct investigation of the critical-layer is considered, both via the Frobenius method and by direct integration. The resulting hard-wall dispersion functions are essentially identical away from the critical layer, with discrepancy at the right-hand side of the critical layer due to numerical issues with the integration method. Further, the Frobenius method allows direct evaluation on the critical-layer itself.

profile with vanishing shear at the edge of the boundary-layer, so that U and U' are both continuous:

$$U(x_2) = U_\infty + \frac{U_\infty - U_0}{\delta^2} (x_2 - \delta)^2 \quad (\text{B.1.21})$$

displayed in figure B.1.3. The convective derivative vanishes, and we have a pair of regular singular points, when

$$z = z_0(k) = \delta \left(1 \mp \sqrt{\frac{U_\infty - \omega/k_1}{U_\infty - U_0}} \right). \quad (\text{B.1.22})$$

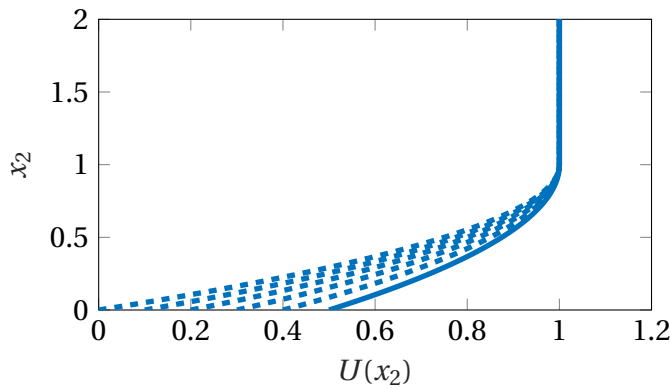


Fig. B.1.3 A smooth parabolic background profile as per (B.1.21), with lengths scaled by boundary-layer thickness δ and speeds by free-stream velocity U_∞ , allowing a single parameter in the choice of slip velocity U_0 .

The existence of two such points puts a limit on the validity of the series solution across the entirety of the boundary-layer. Importantly, if the difference between the two roots is less than the boundary-layer thickness, the solution cannot be valid across the entirety of the boundary-layer. This discrepancy is somewhat dramatically shown in figure B.1.4a. Near the right-hand end of the critical layer, with $k_1 \sim \omega/U_0$, the solution compares very favourably with the numerical solution and there are no issues of convergence. At the other end, however, the solutions are very different. This is essentially due to the presence of the second singularity being ignored in the series solution. Near the left-edge of the critical point, with $k_1 \approx \omega/U_\infty$, the two singularities are approximately equal, and so the validity of the series solution extends only a short way from the critical point, and certainly doesn't extend to $z = 0$.

We can still get a complete view of the critical-layer with a non-constant shear profile provided the profile is suitably monotonic. The issue with the parabolic profile is that, were it continued for $x_2 > \delta$, we would have another point with $U(x_2) = U(y_2)$ where x_2 lies within the boundary-layer and y_2 doesn't, corresponding to the second singular point

for fixed k_1 . If this second point z_{01} is suitably far away, $|z_0 - z_{01}| > \delta$, then the series solution converges across the entirety of the boundary-layer. For this purpose, consider the parabolic background profile $U(x_2)$ satisfying $U(\delta_j) = U_j$ with $\boldsymbol{\delta} = (\delta_0, \delta_1, \delta_\infty)$, $\mathbf{U} = (U_0, U_1, U_\infty)$, given by

$$U(x_2) = U_0 + A(x_2 - \delta_0) + B(x_2 - \delta_0)^2 \quad (\text{B.1.23})$$

with

$$B = \frac{1}{\delta_\infty - \delta_1} \left(\frac{U_\infty - U_0}{\delta_\infty - U_0} - \frac{U_1 - U_0}{\delta_1 - \delta_0} \right) \quad (\text{B.1.24a})$$

$$A = \frac{U_1 - U_0}{\delta_1 - \delta_0} - C\delta_1 \quad (\text{B.1.24b})$$

and corresponding singular points (zeros of C):

$$z_0(k) = \frac{-A + \sqrt{A^2 - 4B(U_0 - \omega/k_1)}}{2B}, \quad (\text{B.1.25a})$$

$$z_{01}(k) = \frac{-B - \sqrt{A^2 - 4B(U_0 - \omega/k_1)}}{2B}. \quad (\text{B.1.25b})$$

These poles are suitably separated for convergence

$$A^2 - 4B(U_0 - U_\infty) > B^2\delta^2. \quad (\text{B.1.26})$$

The accuracy of the Frobenius series solution, provided this condition holds, for a profile with small shear variation (so that U'' is small) is shown in figure B.1.4b. As seen before, where there is convergence of the series solution we gain a far greater degree of accuracy near, and on, the critical-layer.

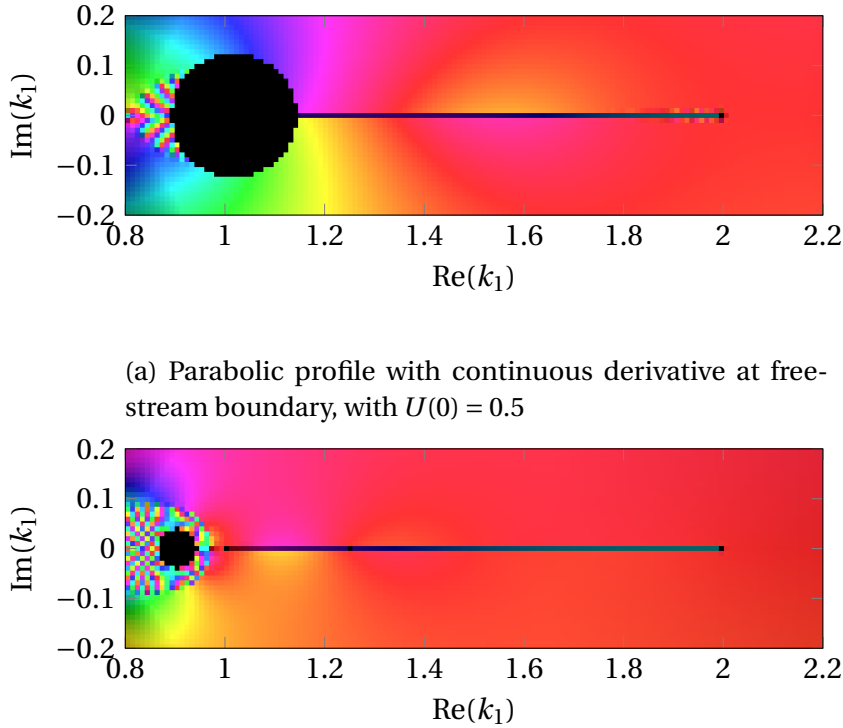


Fig. B.1.4 Phase plot of the ratio of hard-wall dispersion functions, $D_{h,\text{computed}}/D_{h,\text{frobenius}}$, with the red colour on the right of the plot indicating agreement. The black and speckled regions indicate areas where the Frobenius solution does not converge sufficiently. In both cases, lengths are scaled by boundary-layer thickness δ and speeds by U_∞ , with $c_0 = 2$ throughout. The region of agreement with the numerics is much greater for the second case, where the "hidden" singular point is further from the region $x_2 \in (0, \delta)$ for points near this critical-layer branch cut, though neither case has a successful evaluation of the dispersion function near $k_1 = \omega/U_\infty$, the "free-stream" wavenumber.